Ab Initio Investigation of the Electronic Structure and Rovibrational Spectroscopy of Group-I and II Metal Hydrides and Helides

A Thesis Presented for the Degree of Doctor of Philosophy

at

The University of Newcastle

by

Alister J. Page

Molecular Structure and Detection Group,

School of Environmental and Life Sciences,

The University of Newcastle,

New South Wales, 2308,

Australia

July, 2008

Declaration

This work contains no material which has been accepted for the award of any other degree or diploma in any university or other tertiary institution and, to the best of my knowledge and belief, contains no material previously published or written by another person, except where due reference has been made in the text. I give consent to this copy of my thesis, when deposited in the University Library, being made available for loan and photocopying subject to the provisions of the Copyright Act 1968.

(Signed) _____

Alister James Page

2008

To Mardi and my family.

Acknowledgements

I sincerely wish to thank my supervisor, Prof. Ellak I. von Nagy-Felsobuki, for his continuous encouragement, support and guidance throughout my candidature. I would also like to extend my gratitude to Dr David J. D. Wilson (La Trobe University, Australia) for his extensive assistance and a constructive, ongoing collaboration. I wish to acknowledge the receipt of an Australian Postgraduate Award at the University of Newcastle, Australia, and the Australian Research Council for funding this work.

I wish to thank staff at the Australian National University Supercomputer Facility (ANUSF), the Australian Partnership for Advanced Computing (APAC), the Australian Centre for Advanced Computing and Communications (AC^3) and Mr David Koch and Mr Aaron Scott (Faculty of Engineering, The University of Newcastle). I would particularly like to thank Mr David Huthnance for generous assistance in many aspects of computing related to my thesis.

I wish to thank the members of the Molecular Structure and Detection Group, Mr Mitchell Paul, Mr Jason Sky and Mr Anthony Morrison for providing an enjoyable environment conducive to study.

Finally, I wish to extend my deepest gratitude to Mardi, who continued to support and encourage me from start to finish. I would also like to sincerely thank my family for their continued support, and particularly my mother and father for their help and guidance throughout my candidature. "For man, unlike any other thing organic or inorganic in the universe, grows beyond his work, walks up the stairs of his concepts, emerges ahead of his accomplishments" (*John Steinbeck, The Grapes of Wrath*). This thesis was written in LaTeX.

Table of Contents

Abstract

The electronic structure and rovibrational spectroscopy of MH_2, MH_2^{n+}, $HMHe^{n+}$ and MHe_2^{n+} (M = Li, Be, Na, Mg, K, Ca; n = 1, 2) have been investigated using correlated *ab initio* ansatz.

In order to determine the efficacy of various electronic structure methods with respect to Group-I and II hydrides and helides, atomic properties of Li, Be, Na, Mg, K and Ca were calculated. Relativistically-corrected UCCSD(T) and IC-MRCI(+Q) were deemed to be the most suitable ansatz with respect to both efficiency and accuracy. The lowest $^2A_1$ and $^2\Sigma^-$ states of MH_2 were found to be purely repulsive, in agreement with previous predictions. The main factor determining the structure and stability of the excited states of MH_2 was the relative orientations and occupations of the valence p atomic orbital of M and the H_2 $1\sigma_u$ orbital. The ground states of MH_2^{n+} were found to be the result of the charge-quadrupole interaction between M^{n+} and the H_2 molecular subunit. The structures of the ground states of $HMHe^+$ were extremely fluxional with respect to the central bond angle co-ordinate. The ground state PESs of MHe_2^+ were also extremely sensitive to the *ab initio* ansatz by which they are modelled. The respective bonding of the H and He in both $HMHe^+$ and $HMHe^{2+}$ appeared to be charge-dependent in the case of Be, Mg and Ca. Despite the weak bonding observed for the Group-II hydrohelide and helide monocations, the corresponding dications each exhibit thermodynamically stable equilibria.

The solution algorithm of von Nagy-Felsobuki and co-workers was employed in the calculation of vibrational and rovibrational spectra. This algorithm employed an Eckart-Watson Hamiltonian in conjunction with rectilinear normal co-ordinates.

Vibrational and rovibrational Hamiltonian matrices were diagonalised using variational methods. This algorithm was extended so that the vibration transition moment integrals, and hence vibrational radiative properties, of linear triatomic molecules could be calculated. A method by which vibration-averaged structures are calculated was also developed and implemented.

Analytical potential energy functions (PEFs) and dipole moment functions (DMFs) of $(^1A_1)LiH_2^+$, $(^1A_1)NaH_2^+$, $(^1A_1)BeH_2^{2+}$, $(^1A_1)MgH_2^{2+}$, $(^1\Sigma_g^+)BeHe_2^{2+}$, $(^2\Sigma^+)HBeHe^{2+}$, $(^1\Sigma_g^+)MgHe_2^{2+}$ and $(^2\Sigma^+)HMgHe^{2+}$ were developed using least-square regression techniques in conjunction with discrete *ab initio* grids. Vibrational structures and spectra of these species were subsequently calculated. In addition, the rovibrational spectra of $(^1A_1)LiH_2^+$, $(^1A_1)NaH_2^+$, $(^1A_1)BeH_2^{2+}$ and $(^1A_1)MgH_2^{2+}$ were calculated. For $(^1A_1)LiH_2^+$ and $(^1A_1)LiD_2^+$, calculated rovibrational transition frequencies for $J \leq 10$ and $0 \leq K \leq 3$ were within *ca.* 0.1-0.2% of experimental values.

Publications Related to this Thesis

[1] *Ab initio properties and potential energy surface of the ground electronic state of* $BeHe_2^+$. A. J. Page, D. J. D. Wilson, E. I. von Nagy-Felsobuki, *Chem. Phys. Lett.*, (2006) **429**(1-3) 335.

[2] *Rovibrational spectra of* LiH_2^+, $LiHD^+$ *and* LiD_2^+ *determined from FCI property surfaces.* A. J. Page, E. I. von Nagy-Felsobuki, *J. Phys. Chem. A*, (2007) **111**(20) 4478.

[3] *Ab initio calculations of the ground electronic states of* $HBeHe^+$ *and* $BeHe_2^{2+}$. A. J. Page, D. J. D. Wilson, E. I. von Nagy-Felsobuki, *Chem. Phys. Lett.*, (2007) **442**(4-6) 194.

[4] *Ab initio rovibrational spectra of* BeH_2^{2+}, $BeHD^{2+}$ *and* BeD_2^{2+}. A. J. Page, E. I. von Nagy-Felsobuki, *Mol. Phys.*, (2007) **105**(19-22) 2527.

[5] *Ab initio study of ground state* MH_2, $HMHe^+$ *and* MHe_2^{2+}, *M = Mg, Ca.* A. J. Page, E. I. von Nagy-Felsobuki, *Phys. Chem. Chem. Phys.*, (2008) **10**(9) 1285.

[6] *Trends in low-lying electronic states of* XH_2 *(X = Li, Na, K).* A. J. Page, E. I. von Nagy-Felsobuki, *J. Mol. Struct. (Theochem)*, (2008) **853**(1-3) 53.

[7] *Ab initio electronic and rovibrational structure of* MgH_2^{2+} A. J. Page, E. I. von Nagy-Felsobuki, *Chem. Phys.*, (2008) **351**(1-3) 37.

[8] *Structural and energetic trends in Group-I and II Hydrohelide Cations* A. J. Page, E. I. von Nagy-Felsobuki, *Chem. Phys. Lett.*, (In press).

[9] *Ab initio rovibrational spectrum of the NaH_2^+ Ion-Quadrupole Complex* A. J. Page, E. I. von Nagy-Felsobuki, *Theor. Chem. Acc.*, (Accepted).

[10] *Ab initio vibrational spectrum of ($^2\Sigma^+$)$HMgHe^{2+}$.* A. J. Page, E. I. von Nagy-Felsobuki, *Chem. Phys. Lett.*, (Submitted).

[11] *Group-I and II hydride cations: an ab initio investigation.* A. J. Page, D. J. D. Wilson, E. I. von Nagy-Felsobuki, *J. Phys. Chem. A*, (Submitted).

Conference Proceedings Related to this Thesis

[1] *Ab initio rovibrational spectra of singly charged lithium hydrides using full configuration interaction property surfaces.* A. J. Page, E. I. von Nagy-Felsobuki, *6th Royal Australian Chemical Institute Conference on Physical Chemistry (CPC2007)*, Abstract Page PC11 P19, Adelaide, Australia (2007).

[2] *Ab initio properties and potential energy surface of the ground electronic state of* $BeHe_2^+$. A. J. Page, D. J. D. Wilson, E. I. von Nagy-Felsobuki, *6th Royal Australian Chemical Institute Conference on Physical Chemistry (CPC2007)*, Abstract Page PP26 P44, Adelaide, Australia (2007).

[3] *Ab initio rovibrational spectrum of* BeH_2^{2+} *using IC-MRCI property surfaces.* A. J. Page, E. I. von Nagy-Felsobuki, *Molecular Quantum Mechanics: Analytical Gradients and Beyond. A Conference in Honour of Peter Pulay*, Abstract Page 35, Budapest, Hungary (2007).

[4] *An ab initio study of ground state* MH_2, $HMHe^+$ *and* MHe_2^{2+}, $M = Mg$, *Ca.* A. J. Page, E. I. von Nagy-Felsobuki, *Singapore International Chemistry Conference 5 (SICC-5)*, Abstract Page 2:32, Singapore (2007).

[5] *Electronic structure and spectroscopy of* $(^1A_1)MgH_2^{2+}$. A. J. Page, E. I. von Nagy-Felsobuki, *Singapore International Chemistry Conference 5 (SICC-5)*, Abstract Page 2:40, Singapore (2007).

[6] *Rovibrational spectrum of* MgH_2^{2+} *using CCSD(T) property surfaces.* A. J. Page, E. I. von Nagy-Felsobuki, *22nd Austin Symposium on Molecular Structure*, Abstract Page TM2, Austin, Texas, USA (2008).

[7] *Molecular ion-quadrupole complexes: Group I/II ion dihydride cations.* A. J. Page, D. J. D. Wilson, E. I. von Nagy-Felsobuki, *22nd Austin Symposium on Molecular Structure*, Abstract Page P25, Austin, Texas, USA (2008).

[8] *Ab initio rovibrational spectra of ion-quadrupole complexes.* A. J. Page, E. I. von Nagy-Felsobuki, *2008 World Congress of WATOC*, Abstract Page P0027, Sydney, Australia (2008).

[9] *Ab initio trends in the structures and stabilities of MH_2^{n+} (M = Li-K, Be-Ca; n = 1, 2.* A. J. Page, D. J. D. Wilson, E. I. von Nagy-Felsobuki, *2008 World Congress of WATOC*, Abstract Page OC041, Sydney, Australia (2008).

Table of Acronyms

ANO	Atomic NO
ANO-RCC	Relativistically corrected ANO basis set
AO	Atomic orbital
aug-cc-pCVXZ	Augmented cc-pCVXZ basis set
aug-cc-pVXZ	Augmented cc-pVXZ basis set
aug-CVQZ	Augmented CVQZ basis set
BO	Born-Oppenheimer
BP	Breit-Pauli
BSSE	Basis set superposition error
CASSCF	Complete active space SCF
CBS	Complete basis set
cc	Correlation consistent
cc-pCVXZ	cc with polarisation, core and valence X-ζ basis set
cc-pVXZ	cc with polarisation, valence X-ζ basis set
CC	Coupled-cluster
CCSD	CC with single and double excitations
CCSD(T)	CCSD with perturbative treatment of triple excitations
CCSDT	CCSD with 'full' triple excitations
CCSDTQ	CCSDT with quadruple excitations
CG	Cowan-Griffin
CGTO	Contracted GTO
CI	Configuration interaction
CIS	CI with single excitations

CISD	CI with single and double excitations
CISDT	CISD with 'full' triple excitations
CISDTQ	CISDT with quadruple excitations
CVXZ	Core-valence polarisation X-ζ basis set
Darw	Relativistic Darwin correction
DFT	Density functional theory
DHF	Dirac-Hartree-Fock
DK	Douglas-Kroll
DK*n*	n^{th} order DK correction
DMS	Dipole moment surface
DMF	Dipole moment function
DUN	Dunham
DZ	Double-ζ
ECP	Effective core potential
EDUN	Exponential Dunham
ESR	Electron spin resonance
EOGL	Exponential Ogilvie
ESPF	Exponential Simons, Parr and Finlan
FCI	Full CI
FEM	Finite element method
FTIR	Fourier Transform IR
GTO	Gaussian type orbital
HEG	Harris, Engerholm and Gwinn
HF	Hartree-Fock

HOMO	Highest occupied MO
IC-MRCI	Internally contracted MRCI
IE	Ionisation energy
IE$_n$	n^{th} IE
IR	Infra-red
LUMO	Lowest unoccupied MO
MED	Maximum electron density
MEP	Minimum energy path
MCSCF	Multi-configurational SCF
MO	Molecular orbital
MP	Møller-Plesset
MP*n*	n^{th} order Møller-Plesset
MP4(SDTQ)	'Full' MP4 with single, double, triple, quadruple excitations
MRCI	Multi-reference CI
MRCISD	MRCI with single and double excitations
MV	Relativistic mass-velocity correction
NO	Natural orbital
OGL	Ogilvie
PES	Potential energy surface
PEF	Potential energy function
+Q	Davidson correction (*viz.* CISD+Q/MRCISD+Q)
QCI	Quadratic CI
QCISD	QCI with single and double excitations
QCISD(T)	QCISD with perturbative treatment of triple excitations

QZ	Quadruple-ζ
RG	Rare gas
RHF	Spin-restricted HF
ROHF	Spin-restricted open-shell HF
SCF	Self consistent field
SD	Slater determinant
SO	Spin-orbit
SPF	Simons, Parr and Finlan
SSFC	Site-site function counterpoise
STO	Slater type orbital
SVD	Singular value decomposition
TM	Transition metal
TZ	Triple-ζ
UCCSD	Spin-unrestricted CCSD
UCCSD(T)	Spin-unrestricted CCSD(T)
UCCSDT	Spin-unrestricted CCSDT
UHF	Spin-unrestricted HF
UV	Ultra-violet
VB	Valence bond
VBO	Vibration band origin
ZPE	Zero-point energy

CHAPTER 1

The Chemistry of Alkali and Alkaline-Earth Metal Hydrides and Helides

1.1. Introduction

The relationship between empirical observation and theoretical prediction in science is necessarily synergic. In no field is this relationship more evident than in quantum mechanics, and in particular, in quantum chemistry. Since the inception of quantum chemistry in the mid-20$^{\text{th}}$ century, the interplay between theory and experiment has continually advanced knowledge of molecular structure, energetics and dynamics. This is certainly the case in the area of molecular spectroscopy. Indeed, this area played host to the original success of molecular quantum mechanics itself [1].

The interplay between experiment and theory may be illustrated using H_3^+- a benchmark molecule of both quantum chemistry and rovibrational spectroscopy [2]. The first rovibrational spectrum of H_3^+ reported in the literature was an *a priori* prediction made in the 1970s by Carney and Porter [3–5]. The rovibrational states were calculated variationally, in conjunction with an analytical *ab initio* potential energy surface (PES) embedded in the nuclear Hamiltonian operator. Carney and Porter calculated the ν_1 and ν_2 fundamental frequencies to be 3185 and 2516 cm^{-1}, respectively, and also reported the lowest energies in the P, Q and R rotational branches of H_3^+. In 1980 the first infra-red (IR) rovibrational spectrum of H_3^+ was reported and assigned by Oka [6]. Oka determined the ν_2 fundamental frequency

to be 2521.3 cm^{-1}, a value *ca.* 5 cm^{-1} larger than that predicted by Carney and Porter. Oka also assigned several rovibrational transitions of H_3^+ that were generally shifted by *ca.* 5 cm^{-1} relative to the values reported by Carney and Porter. The consensus held at the time was that the variational calculation of accurate molecular rovibrational spectra was possible, but was limited by the accuracy of the molecular PES employed. To this end, Meyer, Botschwina and Burton [7] constructed a refined PES of H_3^+, ultimately yielding *ab initio* rovibrational transition frequencies to within *ca.* 2 cm^{-1} of the experimental values. Subsequent calculations in 1988 by Miller and Tennyson [8] gave transition frequencies differing from experimental values by *ca.* 0.01 cm^{-1}. These calculations, together with the calculation [9] and observation [10] of the vibrational overtone frequencies of H_3^+, ultimately assisted in the detection of H_3^+ in the Jovian atmosphere [11]. More important was the subsequent detection of H_3^+ in the interstellar medium [12]. It is now believed that H_3^+ is the initiator of the majority of interstellar chemical processes [13].

The interaction between experimental and theoretical investigation is also illustrated by He_2. This interaction is somewhat more current relative to H_3^+, since investigation into the structure and stability of He_2 is ongoing. The motivation driving the study of the He_2 'molecule' largely centers on the question of existence alone. Initial theoretical studies into the nature of He_2 were inconclusive as to whether the dimer exhibited a bound state. This was due to the similarity between the early values of the zero-point energy (ZPE) and the dissociation energy (D_e). There is continuing theoretical interest into the nature of the He_2 PES [14–30]. The helium dimer has also been investigated experimentally on numerous occasions [31–34]. These studies have recently been reviewed by Jeziorski and co-workers [35, 36] and Springall and co-workers [37]. In 2007 Jeziorski *et al.* [21] employed symmetry adapted perturbation theory to characterise the He_2 PES, reporting D_e,

R_e, D_0 and $\langle R \rangle$ of 0.94842 ± 0.0003 meV, 2.968 ± 0.006 Å, 0.149 ± 0.03 μeV and 45.6 ± 0.5 Å, respectively. The last two values are in reasonable agreement with the experimentally measured values [38] of 0.95 +0.3/-0.2 μeV and 52 ± 4 Å, respectively. Prior to the investigation of Jeziorski *et al.* [21], van Mourik *et al.* [39] reported a comparable D_e value of 0.9479 ± 0.03 meV using full configuration interaction (FCI) at the complete basis set limit (CBS). Similarly, Anderson *et al.* [29] employed quantum Monte-Carlo methods to predict D_e to be 0.9488 ± 0.09 meV. The stability of He_2 was confirmed experimentally in 1996 by Schöllkopf and Toennies [34].

The remainder of this Chapter is concerned primarily with a review of the chemistries of hydrogen and helium. Due to the scope of the documented chemistry of hydrogen, this review will deal exclusively with investigations of alkali and alkaline-earth metal hydrides of form MH_x^{n+} (M = Li, Be, Na, Mg, K, Ca; $n = 0, 1, 2$; $x = 1, 2$). Conversely, due to the relative sparsity of the investigations concerning helium chemistry, the review presented here includes a cursory survey of all investigations of small molecular helide species (*viz.* those of the main and transition metal groups), with a more detailed focus upon those investigations of species of the form $HMHe^{n+}$ and MHe_x^{n+} (M = Li, Be, Na, Mg, K, Ca; $n = 0, 1, 2$; $x = 1, 2$). Both experimental and theoretical facets of these chemistries will be considered. Thus the necessary synergy between experimental and theoretical investigation will be highlighted.

1.2. An Overview of Alkali and Alkaline-Earth Metal Hydrogen Chemistry

If abundance alone were the determining criterion, atomic hydrogen would be the most important elemental species, constituting 92.1% of the known atomic matter in the universe [13]. The roles of atomic hydrogen with respect to nascent

interstellar chemical processes are therefore elementary. For example, H_2, H_2^+ and H_3^+ have been postulated to be the initiators of more complex interstellar chemical reactions and astrophysical processes [13, 40]. *Ipso facto*, the very existence of the more complex chemistries (that not only sustain life) ultimately have their nexuses in hydrogen chemistry.

A comprehensive account of the chemistry of hydrogen is far beyond the scope of any single review. This observation is immediate from reviews such as that of Aldridge and Downs [41], who list numerous prior review articles, conference proceedings and books, each dealing with only a single aspect of hydrogen chemistry. At the turn of the 21st century the study of transition metal hydride compounds had held prominence for approximately three decades (see references [41–43] and references therein). The motivations driving this field of research ranged from organometallic chemistry of transition metals and aspects of catalysis, through to the discovery in 1984 of molecular dihydrogen complexes (see references [42, 43] and references therein). Surprisingly, little headway into the main group chemistry of hydrogen was made during this period. Accounts of main group hydrides written during the 1970s [44, 45] had remained current until relatively recently. The lethargy in the development of main group hydrogen chemistry has been attributed to various factors, including heterogeneity and the general familiarity of the compounds in question. The physical frailty of many of the species in question has also dissuaded progress, with thermal decomposition and hydrophilicity posing particular problems [41].

This has significantly changed over the last 10-15 years, with progress being made in the synthesis, characterisation and preservation of molecular main group metal hydrides. Aspects of such advances with respect to Al, Ga, In, As and Sb hydrides have been reviewed by several authors [46–50]. Unprecedented impetus

towards the study of alkali and alkaline-earth metal hydrogen chemistry, and in particular investigation into mechanisms of the bulk storage of molecular hydrogen, has also been provided from the evolution of 'hydrogen economies' [51, 52].

1.2.1. Hydrides of the Alkali Metals

Small hydrides and hydride ions of the alkali metals provide an illustrative example of the synergy between experimental and theoretical science. Available experimental and theoretical spectroscopic parameters of the ground states of LiH^{n+}, NaH^{n+}, KH^{n+} $(n = 0, 1)$ are compared in Table 1.1. The ground and excited states of LiH have received extensive theoretical and experimental attention over many decades [41]. This molecule is an exemplary species with respect to the precision available through experimental submillimeter spectroscopic techniques. For instance, observed rotational transitions [53] have resulted in an experimental Born-Oppenheimer (BO) bond length of 1.594 908 11(16) Å - a value accurate to one part in 10^8 Å. In 1993, Stwalley and Zemke [54] completed a comprehensive review of all structural and spectroscopic studies of LiH. More recent spectroscopic investigations were reviewed in 2007 by Tokunaga *et al.* [55] and in 2008 by Wu *et al.* [56]. There have been several advances made in theoretical techniques for which LiH has been invaluable as a prototypical system [57–59]. For example, Bubin and co-workers [58, 59] have reported non-BO vibrational energies of the ground states of LiH and LiH^+. Accurate PESs for several electronic states of LiH and LiH^+ are also a continual area of research [60–64]. Such advances for LiH and LiH^+ have been reviewed in 2007 by Čurík [65] and in 2004 by Magnier [63], respectively.

Despite the abundance of studies available concerned with the spectroscopy of NaH (as reviewed by Stwalley *et al.* [68] in 1991), theoretical investigations of the spectroscopic and electronic structure of NaH remain sparse. Interestingly, the NaH

PES poses significant challenges to theoretical [62, 67] and experimental [69, 74] methods alike. Sodium hydride has also been speculated to comprise a significant fraction of the interstellar gaseous medium [75, 76]. In 2003 Taylor and Newman [77] surmised that there were numerous inconsistencies between the reported theoretical and experimental literature concerning NaH. These discrepancies were illustrated by the published range of D_e values at the time, *viz.* 8751 - 17100 cm^{-1} [77]. To this end, these authors constructed a coupled-cluster with singles, doubles and perturbative triples (CCSD(T)) CBS limit PES of the ground state of NaH. Subsequent to the investigation of Taylor and Newman is that of Chen *et al.* [78], who employed a quadratic configuration interaction (QCISD/6-311G**) method to investigate the ground state equilibrium parameters of NaH. There is a scarcity of data reported in the literature concerning the ground and excited states of NaH^+. Moreover, there is a complete lack of experimental spectroscopic information in the literature. Theoretical investigations have therefore explored the chemistry of NaH^+ to this

Table 1.1 Equilibrium parameters of ground state MH and MH^+(M = Li, Na, K).

	R_e (/Å)	ω_e (/cm^{-1})	D_e (/eV)
		LiH	
Exp.	1.59490811[53]	1405.50936[54]	2.4275[54]
Theor.	1.588-1.63578[62, 66, 67]	1386-1416[62, 66, 67]	2.42-2.53[62, 66, 67]
		NaH	
Exp.	1.8874[68, 69]	1171.0946[68, 69]	1.899[68]
Theor.	1.864-1.9144[62, 66, 67]	1162-1198[62, 66, 67]	1.91-1.99[62, 66, 67]
		KH	
Exp.	2.240164[68, 70, 71]	986.6484[70]	1.7708[68]
Theor.	2.214-2.313[62, 67]	954-995[62, 67]	1.68-1.86[62, 67]
		LiH^+	
Exp.	-	-	-
Theor.	2.16-2.20[63]	417-422[63]	0.1299-0.1410[63]
		NaH^+	
Exp.	-	-	-
Theor.	2.46-3.07[72]	266-330[72]	0.020-0.103[72]
		KH^+	
Exp.	-	-	-
Theor.	2.65-5.29[73]	226-372[73]	0.022-0.136[73]

point. Magnier [72] reviewed such investigations in 2005, as well as reporting a model potential study of the lowest 48 electronic states of NaH^+.

In 1991, Stwalley *et al.* [68] reviewed spectroscopic studies of KH. This review was updated in 2007 by Khelifi *et al.* [79], who also calculated extensive listings of dynamical couplings and radiative/non-radiative lifetimes. Supplementary to these reviews is the work of Bhattacharjee and Dastidar [80], who calculated dissociative cross-sections of KH. In addition, the ground state PES of KH has been investigated on several occasions [62, 67, 81–86]. Far fewer investigations were concerned with KH^+ when reviewed by Magnier in 2006 [73]. The latter investigation [73] was also the most extensive study of KH^+ to date, in which adiabatically correlated PESs up to the K(4d) + H^+ asymptotic limit were presented.

The collision between a Li atom and H_2 is one of the simplest three-body problems. Nevertheless, due to the interplay between low-lying electronic states, the chronological reconstruction of the exact collisional mechanism is a monumental task [87]. The low-lying PESs in question have been characterised in a number of theoretical investigations [66, 87–98]. As such, certain common features of various low-lying states of LiH_2 have been established. For example, there is common agreement that the lowest state of $^2A_1$ symmetry is purely repulsive, whereas the minimum energy structure corresponds to the $^2B_2$ PES minimum. This is also the case for NaH_2 and KH_2 [97]. Over the last decade, the dynamics of NaH_2 in low-lying states have received extensive theoretical attention. In particular, the non-adiabatic dynamics between the lowest $^2A_1$ and $^2B_2$ PESs, vibronic coupling and electronic predissociation processes of NaH_2 have been modelled in several studies [91, 96, 97, 99–108]. The investigation of these phenomena has also assisted the development of semiclassical trajectory methods, such as the trajectory surface hopping model [109] and optimal control theory of pulsed laser fields [105, 107, 108].

The collisional quenching of Na($3\ ^2P$) by H_2 has also been observed in several experiments [104, 106, 110, 111]. The presence of alkali metals, such as sodium and potassium, have also been deduced from the spectra of dwarf stars and irradiated planets (see reference [112] and references therein). Moreover, substellar objects such as evolved methane brown dwarfs are hydrogen-rich [113]. In such an environment, the broadening of the spectral lines of these metals by hydrogen is expected to be a prevalent phenomenon. Pump-probe spectroscopic techniques have been utilised on several occasions to investigate the dynamics of the exciplex K* - H_2 interaction, and the associated rovibrational structures [114–117]. Far less theoretical scrutiny has been passed on KH_2. For example, only three theoretical investigations [96, 97, 118] have been reported in the literature to date. In 2007, Page and von Nagy-Felsobuki [97] characterised the structures and stabilities of the three lowest bound states of KH_2, *viz.* those of B_2, B_1 and Σ_g^+ symmetry using relativistically corrected CCSD(T) and multi-reference CI (MRCI) (see Chapter 2).

The LiH_2^+ collision complex is produced from the anisotropic interaction between the Li^+ ion and the H_2 quadrupole moment, and possesses a binding energy of *ca.* 0.28 eV [119, 120]. The nature of the scattering collision between Li^+ and H_2 has been the subject of many theoretical investigations [87, 93, 94, 119, 121–140]. Investigations concerning the PES of the ground electronic state of LiH_2^+ [119, 121–127, 133, 134, 141] have been reviewed in 2007 by Page and von Nagy-Felsobuki [139] (see Chapter 3). There is common agreement from these studies that the ground electronic state of LiH_2^+ possesses C_{2v} symmetry, with a bond angle and bond length of approximately 21° and 2.0 Å, respectively. The rovibrational structure of LiH_2^+ has also been calculated using several different *ab initio* methods, such as Møller-Plesset perturbation theory (MP2) [138], complete active space self consistent field (CASSCF)/MRCISD [137] and FCI [139]. Bieske and co-workers

[142, 143] have recently recorded IR rovibrational spectra of LiH_2^+ and LiD_2^+, which is in excellent agreement with the available *ab initio* data [139].

There has been in recent years a vigorous interplay between theory [137, 139] and experiment [142, 143] with respect to the spectroscopy of LiH_2^+ and LiD_2^+ (see references [139, 142] and references therein). This is illustrated by the comparison of selected FCI rovibrational transition frequencies for the $K = 0$ manifold of LiD_2^+ [139] with experimental values which is given in Table 1.2. It is evident that the agreement between these theoretical and experimental transition frequencies was better than *ca.* 5 cm^{-1} for all transitions listed. The largest differences arose from the highest J values considered. This indicates that the analytical FCI PES employed in the calculation of these rovibrational energies is an accurate representation of the 'true' surface. This fact is also reflected in the differences between experimental and theoretical vibration-averaged structures for both LiD_2^+ and LiH_2^+. For instance, the differences between theoretical [139] and experimental [142, 143] Li^+ - H_2 separations for these ground vibrational states are of the order of 0.010 Å.

The ground state of NaH_2^+ also results from an ion-quadrupole interaction, analogous to LiH_2^+. Subsequently, NaH_2^+ exhibits similar structural and energetic features to those of LiH_2^+. For example, the equilibrium bond length and angle of NaH_2^+ are *ca.* 2.4 Å and 18°, respectively, whilst the binding energy is *ca.* 0.13 eV. Nevertheless, there are fewer studies concerning NaH_2^+ [144–147], and theoretical investigations still lead the exploration into aspects of NaH_2^+ such as thermochemistry [148], dissociation dynamics [149] and the PES [150]. The thermochemistry of NaH_2^+ has also been characterised experimentally [149]. The literature concerning KH_2^+ is also sparse. For example, only four investigations have focused on the *ab initio* characterisation of the ground state of KH_2^+ [144, 145, 147, 149]. Although no spectroscopy of KH_2^+ has been observed experimentally, Bushnell *et al.* [149] have

Table 1.2 Comparison of selected experimental and *ab initio* rovibrational transition frequencies (/cm^{-1}) of LiD_2^+[a].

Trans.			Exp.	Theor.	Δ	Trans.			Exp.	Theor.	Δ
R Branch						*P* Branch					
$1_{0,1}$	←	$0_{0,0}$	2917.7	2920.6	2.9	$0_{0,0}$	←	$1_{0,1}$	2911.5	2914.5	3.0
$2_{0,2}$	←	$1_{0,1}$	2920.8	2923.7	2.9	$1_{0,1}$	←	$2_{0,2}$	2908.4	2911.4	3.0
$3_{0,3}$	←	$2_{0,2}$	2923.8	2926.9	3.1	$2_{0,2}$	←	$3_{0,3}$	2905.3	2908.4	3.1
$4_{0,4}$	←	$3_{0,3}$	2926.9	2930.0	3.1	$3_{0,3}$	←	$4_{0,4}$	2902.2	2905.4	3.2
$5_{0,5}$	←	$4_{0,4}$	2929.9	2933.2	3.3	$4_{0,4}$	←	$5_{0,5}$	2899.1	2902.4	3.3
$6_{0,6}$	←	$5_{0,5}$	2932.9	2936.4	3.5	$5_{0,5}$	←	$6_{0,6}$	2896.0	2899.5	3.5
$7_{0,7}$	←	$6_{0,6}$	2935.8	2939.7	3.9	$6_{0,6}$	←	$7_{0,7}$	2892.9	2896.7	3.7
$8_{0,8}$	←	$7_{0,7}$	2938.8	2943.0	4.2	$7_{0,7}$	←	$8_{0,8}$	2889.8	2893.9	4.1
$9_{0,9}$	←	$8_{0,8}$	2941.6	2946.4	4.8	$8_{0,8}$	←	$9_{0,9}$	2886.7	2891.3	4.6
$10_{0,10}$	←	$9_{0,9}$	2944.5	2949.9	5.4	$9_{0,9}$	←	$10_{0,10}$	2883.6	2888.7	5.1

[a]Experimental data from reference [143]. *Ab initio* data (FCI with augmented triple-ζ basis sets) from reference [139]. All transitions given in terms of J_{K_a,K_c} for $K = 0$.

derived experimental thermochemistry, including the dissociation energy, in the gas-phase. *Ab initio* equilibrium structures indicate that, in concurrence with LiH_2^+ and NaH_2^+, the ground state of KH_2^+ arises from the ion-quadrupole interaction between the metal ion and H_2, respectively. The equilibrium bond length and bond angle have been calculated to be *ca.* 3.1 Å and 13.7°, respectively. The increase in R_e and decrease in θ_e relative to LiH_2^+ and NaH_2^+ may be understood in terms of the larger ionic radius of K^+.

1.2.2. Hydrides of the Alkaline-Earth Metals

Small neutral hydrides of the alkaline-earth metals Be, Mg and Ca have provided ample opportunity for the comparison of experimental and theoretical data over the last three decades. This is particularly the case for spectroscopic data, which have been collated for the ground states of BeH^{n+}, MgH^{n+} and CaH^{n+} ($n = 0, 1$) and BeH_2, MgH_2 and CaH_2 in Tables 1.3 and 1.4, respectively.

There has been extensive spectroscopic and theoretical analysis of the ground and low-lying excited states of BeH, as reviewed in 2006 by Le Roy *et al.* [151]. In

Table 1.3 Equilibrium parameters of ground state MH and MH^+(M = Be, Mg, Ca).

	R_e (/Å)	ω_e (/cm^{-1})	D_e (/eV)
		BeH	
Exp.	1.342436-1.345[153, 158]	2061.41626-2071.87[153, 158]	2.035[153]
Theor.	1.33-1.34389[66, 67, 159]	2082-2148[66, 67]	1.67-2.01[62, 67]
		MgH	
Exp.	1.729682-1.729828[160, 161]	1478.2-1495.2632[160–162]	1.34-1.376808[54, 161]
Theor.	1.73-1.74859[66, 67]	1354-1532[66, 67]	1.24-1.30[66, 67]
		CaH	
Exp.	2.00083[163]	1298.3999[163]	≤1.70[54]
Theor.	1.99-2.074[67, 163–166]	1253-1284[67, 165]	1.58-1.70[67, 165]
		BeH^+	
Exp.	1.312[167]	2221.7[167]	2.348[167]
Theor.	1.31-1.33[168–172]	2146-2243[168–172]	2.279-3.139[168–172]
		MgH^+	
Exp.	1.6519[167]	1699.1[167]	2.1[173]
Theor.	1.6558-1.6542[174]	1699-1705[174]	1.78-2.03[173, 174]
		CaH^+	
Exp.	-	-	-
Theor.	1.881-2.085[175]	1467-1519[174, 175]	2.106-2.290[174, 175]

particular, BeH is part of a small set of molecules for which nearly all rovibronic transitions have been identified experimentally [152]. Le Roy *et al.* [151] have estimated that *ca.* 95% of the ground state rovibrational transitions have been assigned, *via* techniques including Fourier-Transform IR (FTIR) [151–154], matrix IR [155] and electron-spin resonance (ESR) [156]. There is generally good agreement in the spectroscopic structural parameters with those obtained from crystal structure measurements [157]. The experimental rovibrational studies of BeH have recently been complemented by accurate theoretical methods including FCI [176] and non-BO methods [177]. Other physical properties of BeH have also been investigated theoretically, including hyperfine coupling [178] and magnetic moments [179]. The rovibrational structure and associated radiative properties of BeH^+ have been studied extensively using theoretical methods [169, 171, 172, 180, 181]. Additionally, the PESs of low-lying states have been constructed in several investigations [168, 182].

Of particular importance in this respect is the recent work of Bubin *et al.*, who investigated the ground state of BeH^+ using non-BO methods. These experimental rovibrational parameters are in good agreement with the high-resolution ultra-violet (UV) emission spectrum obtained by Coxon *et al.* [183]. Far fewer investigations have focused on the dication BeH^{2+}. Nevertheless, several theoretical attempts have been made to characterise the ground state PES of BeH^{2+} [170, 184–186]. Although no spectrum of BeH^{2+}has been observed experimentally, Franzreb *et al.* [187] employed charge-stripping mass spectrometry techniques to generate BeH^{2+} in the gas-phase.

Magnesium hydride is a molecule of some astrophysical importance, as lines of the ($A^2\Pi$ - $X^2\Sigma^+$) transition are present in the absorption spectra of the sun [198, 199]. The first experimental spectroscopic characterisation of MgH was made in 1926 [200], in an attempt to identify prevalent lines in astronomical spectra. The state of theoretical and experimental spectroscopic investigation into MgH was assessed in 2004 by Shayesteh *et al.* [201]. From this review it is evident that most aspects of the MgH spectrum were exhaustively studied in the 1970s by Balfour *et al.* (see reference [201] and references therein). Nevertheless, there are several subsequent investigations of the spectrum of MgH reported in the literature [160–162, 201–203]. Prior to the work of Shayesteh *et al.* [201] is that of Huber and Herzberg [167], who in 1977 reported a nearly exhaustive review of the spectroscopy of MgH. The ground state of MgH^+ has also been the subject of several investigations of theoretical [173, 204] and experimental [205–207] nature. For example Jørgenson *et al.* [173] have modelled the photodissociation of a single MgH^+ ion using adiabatic PESs. Similarly, Dutta *et al.* [204] have calculated the collisional cross-section of the reaction between Mg and H^+ using semi-classical molecular orbital (MO) methods. This photodissociative process has also been the focus of Coulomb-crystal experi-

Table 1.4 Equilibrium parameters of ground state $(^1\Sigma_g^+)MH_2$ (M = Be, Mg, Ca).

	R_e (/Å)	Frequencies (/cm^{-1})			D_e (/eV)
		ω_1	ω_2	ω_3	
			BeH_2		
Exp.	1.3264[188]	1275-1395.2[189–191]	697.9-810[155, 189–191]	1776.1-2179[188–191]	4.2112[188]
Theor.	1.3268-1.344[155, 192]	1980-1992[193]	705-717[193]	2158-2179[193]	4.190-4.212[193]
			MgH_2		
Exp.	1.69582[194]	-	417-437[174]	1558-1589[174]	-
Theor.	1.6939-1.7108[174, 195]	1552-1715[174]	414-458[174]	1576-1756[174]	3.116-3.168[174]
			CaH_2[a]		
Exp.	-	1164-1261[174]	-	1240-1290[174]	-
Theor.	2.01-2.0682[174]	1223-1309[174]	116-207[174]	1306-1367[174]	2.679-2.713[174]

[a]Theoretical θ_e = 157 - 180° [41, 174]; experimental θ_e = 166 - 168° [196, 197].

ments [205]. Several groups [206, 207] have studied the broadening of the transitions of Mg^+ by bulk hydrogen.

The investigation into the structure and spectroscopy of CaH is a much more current area of research, with much of the investigation into the spectroscopy of CaH occurring during the last decade (see reference [208] and references therein). Techniques such as Stark and Zeeman spectroscopy [209–213] have been used extensively in this pursuit. Experimental investigations have been complemented in 1999 and 2003 by the *ab initio* calculation of rovibronic [165] and rovibrational [208] spectra of CaH, respectively. These studies were predated by IR diode laser and ESR spectroscopic investigations of CaH [163, 203] performed during the 1980s. Investigation of CaH^+ is also relatively recent, as reviewed in 2006 by Dutta *et al.* [214]. These authors investigated the charge-transfer processes involved in collisions between Ca^+ and H using adiabatic PESs. The Ca^+ line broadening in bulk hydrogen has also been modelled [206, 207], as have the ground state spectroscopic constants [175]. Boutalib *et al.* [215] have also studied several low-lying PESs using an effective core potential (ECP) method.

Neutral BeH_2 has been the subject of several theoretical investigations [66, 192, 193, 193, 216–221], with much of this work focusing upon the theoretical characterisation of equilibrium parameters [192, 193, 216–219] and the construction of accurate PESs [193, 217, 220, 221]. The rovibrational states of BeH_2 have also been recently studied using *ab initio* methods [193, 217]. In 1993 [155, 191], 2002-2003 [222, 223] and 2005 [190] the BeH_2 monomer was identified experimentally. Spectroscopic data of BeH_2 and BeD_2 were reported in 2006 by Shayesteh and Bernath [188]. The chemical trapping of H_2 by BeO has also been investigated experimentally [224]. Most recently, Sampath *et al.* [189] conducted IR spectroscopic and inelastic neutron scattering experiments on solid BeH_2. The dynamics of MgH_2

are dominated by the non-adiabatic interactions of energetically low-lying excited singlet states, which dictate the dynamics of the Mg insertion into the H_2 subunit [195]. This fact has been the primary motivation for theoretical investigation into the nature of MgH_2 and its low-lying PESs. These dynamics and the related PESs have been studied extensively using theoretical methods [174, 195, 225–231]. There is also considerable motivation for the experimental investigation into the structure and dynamics of MgH_2, particularly since magnesium hydrides have been postulated to be economical solutions to the bulk storage of molecular hydrogen [232]. Aspects of MgH_2 such as synthesis [233–237], structure [162, 194, 233, 238] and spectroscopy [194] have been the subject of several experiments. In 2007 Li and Le Roy [229] reported accurate *ab initio* rovibrational energies which were within *ca.* 1 cm^{-1} of experimental values [194].

The equilibrium bond angle of the ground electronic state of CaH_2 is still uncertain, despite a number of experimental and theoretical investigations [164, 166, 174, 197, 231, 239–242]. These theoretical investigations have indicated that the uncertainty arises due to the flat curvature of the molecular PES along the H-Ca-H bend co-ordinate. Although the equilibrium structure of CaH_2 has been determined to be non-linear in a number of rare gas matrix isolation experiments [196, 197, 243], uncertainty with respect to the bond angle remains due to the possible interference of matrix effects. Despite attempts, no gas-phase experimental structure has been determined to date [244]. Using a fully anharmonic *ab initio* PES, Koput [239] reported that CaH_2 exhibits a non-linear equilibrium structure with $\theta_e = 164.37°$. The postulated experimental bond angle is 166-168° [196, 197, 243]. However, the PES of Koput [239] possesses a barrier height with respect to $\theta = 180°$ of only 6 cm^{-1}. In the most recent theoretical investigation of the ground state of CaH_2, Page and von Nagy-Felsobuki [174] employed relativistically corrected CCSD(T) and

internally contracted MRCI (IC-MRCI) to determine a linear equilibrium structure (see Chapter 2).

The dihydrides of Be^{n+}, Mg^{n+} and Ca^{n+} result from the charge-quadrupole interaction between the metal ion and H_2, as do those of Li^{n+}, Na^{n+} and K^{n+}. However, the chemistries, PESs and structures of the alkaline-earth metal dihydride cations remain relatively unexplored compared to their alkali counterparts. For example, the ground state of BeH_2^+ has been investigated by Poshusta *et al.* [245] and Hinze *et al.* [221]. Discussion on the symmetry of the ground state of BeH_2^+ is ongoing, with some investigations indicating the existence of symmetry breaking in the two Be - H bonds [221]. This symmetry breaking has been explained qualitatively using simple MO arguments. Other theoretical studies [245, 246] have predicted equilibrium structures of C_{2v} symmetry. The ground state of BeH_2^{2+} has also received theoretical attention [221, 247–249]. Most recently, Page and von Nagy-Felsobuki [248] calculated rovibrational transition frequencies and radiative properties of BeH_2^{2+} using an IC-MRCI PES and dipole moment surface (DMS) (see Chapter 4). There have been no reported experimental data with respect to the ground state of any positively charged beryllium dihydride at present. Limited theoretical study of MgH_2^+ and MgH_2^{2+} has been reported in the literature. For example, Bauschlicher *et al.* [250] reported the first *ab initio* PES of the ground and low-lying electronic states of MgH_2^+ using MRCI. Simandiras *et al.* [251] determined the equilibrium parameters of MgH_2^{2+} using SCF and MP2. More recently, Petrie [252] investigated the Mg^{2+} cation affinity of H_2 using high-level *ab initio* techniques. In 2007 Page and von Nagy-Felsobuki [253] employed relativistically corrected CCSD(T) to construct the rovibrational spectrum of MgH_2^{2+} for low-lying vibrational and rotational states (see Chapter 6). The latter investigation is the only reported theoretical study of the rovibrational structure of MgH_2^{2+} reported

in the literature, although Ding *et al.* [254] have reported spectroscopic parameters of MgD_2^+ based on photo-fragmentation mass-spectrometric techniques. Krośnicki and co-workers have studied the CaH_2^+ complex in several investigations [255, 256]. These workers constructed adiabatic PESs of the ground state and excited states corresponding to the $(3d)^2D$ and $(4p)^2P$ Ca^+ terms, in both $C_{\infty v}$ and C_{2v} configurations. Of particular interest in the present context is the calculation of the vibrational structure and band origins of the $(3d)^2D Ca^+$-H_2 exciplex [256]. The Ca^+-H_2 complex has also been studied in Paul trap experiments [257, 258].

1.3. An Overview of Alkali and Alkaline-Earth Metal Helium Chemistry

Of all the elements helium is the least reactive, possessing a first ionisation energy (IE_1) and dipole polarisability of 24.587 eV and 0.205 $Å^3$, respectively [259]. Helium is also the second most abundant atomic substance, constituting 7.8% of the known atomic matter in the universe [13]. The inertness of atomic helium prevents many potential ligands which would fix helium in a chemical sense. Indeed, amongst the only chemical species known to exhibit traditional chemistry with neutral atomic helium is helium itself [260] (*viz.* species of the form He_n, $n \geq 2$), atomic mercury [261, 262] and C_{60} [263, 264]. Molecules of form OBeHe [265, 266], HHeF [267] and RNBeHe [268] (where R- included groups such as H-, HO-, F-, HCH_2-, $HOCH_2$ and C_6H_5-) have also been predicted to be thermodynamically stable using theoretical methods. The spectroscopy of the He-CO_2 complex has also been measured experimentally, and modelled theoretically (see references [269] and references therein). Helium cations He^{n+} ($n = 1, 2$) are, on the other hand, chemically reactive species. For any atom L, reaction $L + He^{n+} \rightarrow LHe^{n+}$ will result simply in charge transfer (*i.e.* $LHe^{n+} \rightarrow He + L^{n+}$), due to the relative magnitudes of IEs of L and He^{n+}. Chemical bonding may result however, provided that L possesses a sufficiently high

IE. Elements including oxygen, flourine, neon and argon were therefore originally considered as appropriate candidates. In 2004 Grandinetti [270] completed a comprehensive review of theoretical and experimental investigations of helium cation chemistry. This survey augments previous reviews including those of Frenking and co-workers [271–273], von Ragué-Schleyer [274] and Bauschlicher *et al.* [275].

The initial contemplation of helium chemistry came in the form of a prediction by Pauling in 1933 [276], concerning the stability of the bound states of He_2^+ and He_2^{2+}. Mass spectrometric techniques were employed in the detection of He_2^+ soon after this prediction. Investigation into both He_2^+ and He_2^{2+} is ongoing [277–281]. It is now well established that $(^2\Sigma_u^+)He_2^+$ and $(^1\Sigma_g^+)He_2^{2+}$ are strongly bound, exhibiting equilibrium bond lengths of 1.08 and 0.70 Å, respectively [270, 282]. The dissociation energies of these states are *ca.* 2.5 and 1.5 eV, respectively [283, 284]. With respect to the dissociation products $He^+ + He^+$, the ground state of He_2^{2+} is metastable, having an estimated lifetime of *ca.* 10^{-6} s using Coulomb explosion techniques [285]. Of particular interest within the context of this work are those investigations which are concerned with the rovibrational and rovibronic states of He_2^+. Such investigations were reviewed in 2008 by Raunhardt *et al.* [286]. The first experimental identification of a helide ion consisting of more than two atoms occurred in 1968 by Patterson [287], who observed He_3^+. From this investigation the dissociation energy of He_3^+ (with respect to $[He_2^+ + He]$) was determined to be 0.17 $\pm$ 0.03 eV. Subsequent theoretical and experimental investigation into He_3^+ has been reviewed in 2007 by Paidarová *et al.* [288]. The vibrational spectrum of the ground state of He_3^+ was also recently calculated by Karlický *et al.* [289].

The hydrohelide cation, HeH^+, was first detected experimentally in 1925 by Hogness and Lunn [290] in the mass spectra of ionised helium containing H_2 [270]. It has since been postulated that HeH^+ is prevalent in astronomical phenomena,

such as planetary nebula [291–294], white dwarfs [295], supernovae [296] and quasistellar objects [297]. The $X^1\Sigma^+$ ground state of HeH^+ exhibits a bond length of *ca.* 0.77 Å, and an adiabatic dissociative potential well-depth of *ca.* 1.9 eV [298, 299]. The lowest excited state, $(A^1\Sigma^+)HeH^+$, lies *ca.* 11.5 eV above the $X^1\Sigma^+$ limit, and so $(X^1\Sigma^+)HeH^+$ is essentially isolated. The relatively large permanent dipole moment of HeH^+ (brought on by the lack of inversion symmetry) renders HeH^+ unique amongst helide ionic species, in that it is amenable to high-resolution IR spectroscopic techniques [299, 300]. Current *ab initio* vibrational and rovibrational energies are therefore in excellent agreement with experimentally measured values [300–302].

The theoretical study of main group helide ions assisted in the initial elucidation of the mechanisms underpinning helium chemistry [265, 273]. Throughout the 1990s diatomic species such as MHe^+ and MHe^{2+}, where M = B - F and Al - Cl, were studied extensively [270]. Investigations into the structures and stabilities of ground and excited state MHe^+ species by Frenking and co-workers [265, 273, 303] culminated in the proposal of the 'donor-acceptor' bonding model. This model qualitatively explained the bonding trends observed for MHe^+ in terms of the electronic configuration of the ligand. The dissociative potential well-depth of the ground states of MHe^+ (M = B - F, Al - Cl) are generally less than 0.1 eV, with exceptions including M = B, N, O and Si [270]. The converse is generally the case for the low-lying excited states of the monocations. The ground states of MHe^{2+} (M = B - F, Al - Cl) are also generally strongly bound, and possess dissociative well-depths (with respect to $[M^{2+}$ + He]) ranging from *ca.* 0.2 eV (M = Cl) to *ca.* 10.5 eV (M = O). Trends observed (with respect to structure and stability) in diatomic main group helide ions are essentially observed in the analogous triatomic dihelide ions. Theoretical and experimental methods have also unravelled a surprisingly rich chemistry between the helium and the heavier rare-gas (RG) elements [270].

Transition metal (TM) helide ions pose a unique challenge to theoretical methods, due largely to the valence configuration of the TM ligand. This has been illustrated in theoretical investigations of MHe^+ (M = Sc - Cu [304–306], M = Ti, V, Cr, Fe, Co [307, 308], M = Cr, Co, Ni [308] and M = Au [309]), MHe^{2+} (M = Sc - Cu [305, 310], M = Ti [311] and M = Sc, Ti [312]) and MHe^{3+} (M = Sc [313], M = Sc - Cu [314], M = Y [315] and M = La, Eu, Gd, Yb, Lu [316]). In the case of MHe^+, these theoretical calculations indicate that TM ligands possessing a $d^n s^1$ valence configuration (Sc^+, Ti^+, Mn^+ and Fe^+) yield D_e and R_e values of *ca.* 0.004 - 0.043 eV and 3.2 - 4.1 Å, respectively, whereas TM ligands possessing a d^{n+1} valence configuration (V^+, Cr^+, Co^+, Ni^+ and Cu^+) yield D_e and R_e values of *ca.* 0.017 - 0.195 eV and 1.8 - 2.7 Å, respectively [304–306]. This differential phenomena is not present in MHe^{2+} and MHe^{3+}, since all TM dications arise from a d^{n+1} and d^n valence configuration, respectively. These conclusions are also supported by gas-phase field-ion microscopy data concerning MHe^{n+}(M = V, Fe, $n = 2, 3$) [317].

1.3.1. Helides of the Alkali Metals

In contrast to some molecular helide ions of alkaline-earth metals (*vide infra*), molecular helide ions of the alkali metals exhibit very weak bonding in the ground state [270]. This bonding may be generally classified as purely electrostatic in nature. Nevertheless, larger helium clusters doped with neutral and cationic Li, Na and K adducts have been studied both theoretically [318–321] and experimentally [322, 323]. In particular, Shindo *et al.* [322] have observed the spectral line broadening of the ($5^2P \leftarrow 4^2S$) transition of K in a gaseous helium environment. Murano *et al.* [324] have synthesised $LiHe^+$ from the reaction of LiCl and He in the gas-phase. The existence of $LiHe^+$ has also been confirmed by Scheidermann *et al.* [323], who employed molecular beam and electron impact techniques.

There are several motivations driving investigation into the nature of diatomic helide ions of the alkali metals. For instance, the interaction between He and an alkali metal cation M^+ is a archetypal example of the interaction between two closed-shell species. The solvation of alkali cations in helium and related ionic mobility studies have also provided impetus into the investigation of MHe^+ systems. There has therefore been significant theoretical interest in the construction of ground and excited state MHe^+ PESs (M = Li - Fr) [118, 273, 304, 321, 325–349]. Salient data concerning the spectroscopic properties of MHe^+ (M = Li, Na, K) are listed in Tables 1.5, 1.6 and 1.7, respectively.

It is evident from Table 1.5 that, for the ground state of $LiHe^+$, reasonable agreement has been achieved between reported experimental and theoretical equilibrium structures. For example, the 'best' approach employed (CCSD(T)/aug-cc-pV5Z [332]) and yielded R_e and D_e values *ca.* 0.07 Å and 0.002 eV larger than the experimental values [329, 347, 350]. From comparison of the CCSD(T)/cc-pV5Z and CCSD(T)/aug-cc-pV5Z data it may be inferred that the addition of diffuse functions to the cc-pV5Z basis set has a minimal effect on the ground state $LiHe^+$ PES. For example, the differences observed in R_e and D_e values are 0.001 Å and 0.0039 eV, respectively, whereas these ω_e values are in exact agreement. The MOCI calculations of Hiyama [348] indicate that the interaction of the $(3s\ ^1S)Li^+$ ion with He results in a strongly bound complex, compared to the ground state of $LiHe^+$. Nevertheless, the R_e value of this excited state is *ca.* 1.8 Å larger than that of the ground state. The ground state of $LiHe^{2+}$ resides on a purely repulsive PES as reported by both Frenking *et al.* [273] and Hughes and von Nagy-Felsobuki [351]. It is therefore anticipated that both $NaHe^{2+}$ and KHe^{2+} also exhibit unbound ground states, although no experimental or theoretical data is available to definitively support such a statement. The experimental and theoretical data concerning the ground state of $NaHe^+$ listed

Table 1.5 Equilibrium parameters of $LiHe^+$ reported in the literature.

Method	State	R_e (/Å)	D_e[a] (/eV)	ω_e (/cm^{-1})
SCF[b]	$^1\Sigma^+$	1.89	-	-
MP2[c]	$^1\Sigma^+$	2.062	0.065	208
Model Potential[d]	$^1\Sigma^+$	1.896	0.0804	272
MOCI[e]	$^1\Sigma^+$	2.00	0.079	244
CEPA[f]	$^1\Sigma^+$	1.92	-	-
CEPA2[g]	$^1\Sigma^+$	1.894	0.0810	-
QCISD(T)[h]	$^1\Sigma^+$	1.95	0.068	-
QCISD(T)[i]	$^1\Sigma^+$	1.910	0.0781	260
CCSD(T)[j]	$^1\Sigma^+$	1.898	0.0801	258.4
CCSD(T)[k]	$^1\Sigma^+$	1.897	0.08049	258.4
Expt.[l]	$^1\Sigma^+$	1.96	0.0781	-
Expt.[m]	$^1\Sigma^+$	1.96	0.0737	-
Expt.[n]	$^1\Sigma^+$	1.92	0.0781	-
MOCI[e]	$[Li^+ (3s\ ^1S)]^1\Sigma^+$	3.73	0.496	-

[a]Refers to the reactions [$LiHe^{n+} \rightarrow Li^{n+} + He$].
[b]Using a model potential; see reference [346].
[c]In conjunction with the 6-31G(*d*,*p*) basis set; see reference [273].
[d]See reference [349].
[e]In conjunction with [5*s*5*p*2*d*] (He), [5*s*4*p*2*d*] (Li), [6*s*6*p*2*d*] (Na) and [8*s*6*p*2*d*] (K) basis sets; see reference [348].
[f]In conjunction with [9*s*4*p*] (Li) and [7*s*3*p*2*d*] (He) basis sets; see reference [330].
[g]See reference [352].
[h]In conjunction with augmented 6-311G basis sets; see reference [325].
[i]In conjunction with the 6-311G+(3*df*,3*pd*) basis sets. The ω_e is calculated using MP2/6-311G+(3*df*,3*pd*); see reference [327].
[j]In conjunction with the cc-pV5Z basis set; see reference [321].
[k]In conjunction with the aug-cc-pV5Z basis set; see reference [332].
[l]See reference [329].
[m]See reference [350].
[n]See reference [347].

in Table 1.6 are indicative of an electrostatically bound complex. In particular, these data highlight the difficulties encountered in approximating a shallow molecular PES. For example, significant discrepancies are evident in the CCSD(T) values [319, 321, 336, 337] of R_e listed in Table 1.6. The PES is therefore extremely sensitive to the basis sets employed. For example, Marinetti *et al.* [321] (who employed CCSD(T)/cc-pV5Z) reported an equilibrium bond length value *ca.* 0.15 Å smaller than that of Nakayama *et al.* [319]. The latter authors also employed CCSD(T), but used the cc-pVQZ basis set for Na and the cc-pV5Z basis set for He. The equilibrium

Table 1.6 Equilibrium parameters of $NaHe^+$ reported in the literature.

Method	State	R_e (/Å)	D_e [a] (/eV)	ω_e (/cm^{-1})
SCF[b]	$^1\Sigma^+$	2.33	-	-
SCF[c]	$^1\Sigma^+$	2.415	0.033	129
Model Potential[d]	$^1\Sigma^+$	2.324	0.0408	155
EXGF[e]	$^1\Sigma^+$	2.328	0.0409	-
CASSCF[f]	$^1\Sigma^+$	2.421	0.037	138.4
MOCI[g]	$^1\Sigma^+$	2.40	0.035	114
QCISD(T)[h]	$^1\Sigma^+$	2.41	0.028	-
QCISD(T)[i]	$^1\Sigma^+$	2.334	0.0490	160
CCSD(T)[j]	$^1\Sigma^+$	2.232	0.0411	148.2
CCSD(T)[k]	$^1\Sigma^+$	2.38	0.03507	-
CCSD(T)[l]	$^1\Sigma^+$	2.307	-	-
CCSD(T)[m]	$^1\Sigma^+$	2.325	0.0408	-
Expt.[n]	$^1\Sigma^+$	2.41	0.0390	-
Expt.[o]	$^1\Sigma^+$	2.33	0.0434	-
CASSCF[f]	$^3\Sigma^+$	3.536	1.011	239.4
CASSCF[f]	$[He^+ (1s\ ^1S)]^1\Sigma^+$	3.904	0.603	206.9
MOCI[g]	$[Na^+ (3s\ ^1S)]^1\Sigma^+$	3.95	0.707	-

[a]Refers to the reactions [$NaHe^{n+} \rightarrow Na^{n+} + He$].
[b]Using a model potential; see reference [346].
[c]In conjunction with contracted ANO basis sets; see reference [304].
[d]See reference [349].
[e]See reference [338].
[f]In conjunction with the aug-cc-pVTZ basis sets; see reference [335].
[g]In conjunction with [5*s*5*p*2*d*] (He), [5*s*4*p*2*d*] (Li), [6*s*6*p*2*d*] (Na) and [8*s*6*p*2*d*] (K) basis sets; see reference [348].
[h]In conjunction with augmented 6-311G basis sets; see reference [325].
[i]In conjunction with the 6-311G+(3*df*,3*pd*) basis sets. The ω_e is calculated using MP2/6-311G+(3*df*,3*pd*); see reference [327].
[j]In conjunction with the cc-pV5Z basis set; see reference [321].
[k]In conjunction with the cc-pVQZ (Na) and cc-pV5Z (He) basis sets; see reference [319].
[l]In conjunction with the C-Huz-5 basis sets; see reference [336].
[m]In conjunction with the aug-cc-pVQZ basis sets; see reference [337].
[n]See reference [347].
[o]See reference [328].

parameters obtained from experiment are in better agreement. For example, these R_e and D_e values differ by *ca.* 0.08 Å and 0.004 eV, respectively. As was the case for $LiHe^+$, the excited Σ states of $NaHe^+$exhibit deeper energy wells than does the ground state. This is illustrated by the CASSCF calculations of Panin *et al.* [335] with respect to $(^3\Sigma^+)NaHe^+$. According to these results the $^3\Sigma^+$ state of $NaHe^+$ exhibits a potential well-depth two orders of magnitude greater than that of the ground

Table 1.7 Equilibrium parameters of KHe^+ reported in the literature.

Method	State	R_e (/Å)	D_e [a] (/eV)	ω_e (/cm^{-1})
SCF[b]	$^1\Sigma^+$	2.91	-	-
Model Potential[c]	$^1\Sigma^+$	2.825	0.0229	100
EXGF[d]	$^1\Sigma^+$	2.852	0.0290	-
SAPT[e]	$^1\Sigma^+$	2.867	0.0155	-
MOCI[f]	$^1\Sigma^+$	2.90	0.024	84
CCSD(T)[g]	$^1\Sigma^+$	2.83	0.0230	96.78
Expt.[h]	$^1\Sigma^+$	2.90	0.0217	-
Expt.[i]	$^1\Sigma^+$	2.91	0.0173	-
MOCI[f]	$[K^+ (3s\ ^1S)]^1\Sigma^+$	4.35	0.360	-

[a]Refers to the reactions $[KHe^{n+} \rightarrow K^{n+} + He]$.
[b]Using a model potential; see reference [346].
[c]See reference [349].
[d]See reference [343].
[e]See reference [341].
[f]In conjunction with [5*s*5*p*2*d*] (He), [5*s*4*p*2*d*] (Li), [6*s*6*p*2*d*] (Na) and [8*s*6*p*2*d*] (K) basis sets; see reference [348].
[g]In conjunction with the cc-pV5Z basis set; see reference [321].
[h]See reference [347].
[i]See reference [344].

state. In addition, the curvature of the $(^3\Sigma^+)NaHe^+$ CASSCF PES differs substantially from that of the ground state, as indicated by the respective values of ω_e. Table 1.7 shows that there are fewer *ab initio* investigations of the ground state of KHe^+ reported in the literature. Nevertheless, theoretical and experimental PES parameters are consistent for the ground state of KHe^+. The CCSD(T)/cc-pV5Z R_e and D_e values of Marinetti *et al.* [321] are *ca.* 0.07 Å and 0.013 eV larger than the experimental values. No excited state of KHe^+ has been observed experimentally to date. The MOCI data for the $([K^+ (3s\ ^1S)]^1\Sigma^+)KHe^+$ are consistent with that for the analogous Li and Na species however, in that this excited state exhibits a larger dissociative potential well-depth and equilibrium bond length.

Very few studies of polyatomic helide ions of the alkali metal have been reported in the literature. The study of the equilibrium structures and stabilities of species of the form MHe_2^+ is therefore ongoing. For example, Sapse *et al.* [327] com-

pleted a systematic study of the structures and stabilities of $LiHe_n^+$ and $NaHe_n^+$ (n = 1-4) using MP2 and QCISD(T) in conjunction with 6-311+G(3*df*,3*pd*) basis sets. Sapse *et al.* [327] predicted bound symmetric non-linear structures for all species investigated. More recently, in 2007 Marinetti *et al.* [321] employed CCSD(T)/aug-cc-pV5Z to predict non-linear and linear equilibrium structures of $LiHe_2^+$ and $NaHe_2^+$, respectively. From a comparison of the energies of linear and non-linear $LiHe_2^+$ equilibria, Marinetti *et al.* [321] concluded that a definitive equilibrium structure of $LiHe_2^+$ using CCSD(T)/aug-cc-pV5Z was not attainable. Marinetti *et al.* [321] also predicted a linear equilibrium structure for the ground state of KHe_2^+. The latter is the only reported data concerning KHe_2^+ available in the literature.

In a series of studies, Bodo and co-workers [353, 354] have investigated the solvation of cationic alkali metal dimers in helium. To this end, these workers developed molecular PESs for Li_2He and M_2He^+ (M = Li, Na, K) using MP4(SDTQ)/cc-pV5Z. At this level of theory M_2He^+ (M = Li, Na, K) exhibit $D_{\infty h}$ equilibrium structures. Although the method of Bodo *et al.* [353] and Sapse *et al.* [327] differ both in the approximation of correlation and the size of basis set employed, comparison between the equilibrium structures of M_2He^+ and MHe_2^+ (M = Li, Na) suggests that the latter C_{2v} species exhibit marginally larger potential well-depths. Most notably in the present context is the calculation of Bodo *et al.* [353] of 12, 7 and 5 vibrational states (M = Li, Na, K, respectively) [353] for $J = 0$. The number of bound levels for these species reflects the trend observed by Bodo *et al.*, *viz.* that the potential well-depth of M_2He^+ decreases markedly with an increasing atomic mass of M. At present, no study of dications of form MHe_2^{2+} (M = Li, Na, K) has been reported, although it is expected (from trends observed for the analogous alkaline-earth metal helide ions, *vide infra*) that such species reside on repulsive molecular PESs due to the respective trends observed in the corresponding diatomic dications. Bodo

and co-workers [355, 356] have also modelled the solvation of single Li^+, Na^+ and K^+ ions in small helium nanodroplets *via* Monte Carlo techniques.

No investigation of an alkali metal hydrohelide ion has been reported in the literature. However, the neutral HLiHe and HNaHe species have been studied on several occasions using *ab initio* methods [357–361]. In particular, Taylor and co-workers [359–361] have constructed CCSD(T) PESs for the purposes of studying the dynamics of vibrational and rovibrational energy transfer in HLiHe and HNaHe. Bodo and co-workers [357, 358] have also investigated the bound rovibrational states of HLiHe.

1.3.2. Helides of the Alkaline-Earth Metals

With respect to helium chemistry, the alkaline-earth metals exhibit a wide range of bonding characteristics, from weak van der Waals interactions through to strong covalent and ionic bonds. For many molecular systems the interaction between alkaline-earth metal cations and helium has been shown to be thermodynamically stable [270]. The hydrides and helides of the alkaline-earth metals are also of interest with respect to interstellar chemistry [175, 362]. Although there has been no reported experimental observation of a beryllium helide, the helides of the heavier alkaline-earth metals have been observed in several experiments. In particular, discussion into the structures of helium nanodroplets doped with Mg, Ca, Sr and Ba is ongoing [363–365]. Alignment effects in the CaHe($5\ ^1P_1$ - $5\ ^3P_J$) energy transfer collision have also been observed using laser scattering techniques, in which an absorption profile for the Ca-He collision complex has been identified [366, 367]. No alkaline-earth metal helide cation has been identified experimentally to date.

Extensive *ab initio* investigation of diatomic beryllium helides has been conducted. Results pertinent to this thesis are collated in Table 1.8. It is evident that

the $^2\Sigma^+$ ground state of $BeHe^+$ has been well characterised using *ab initio* methods. For example, using CCSD(T) and IC-MRCI in conjunction with augmented quadruple-ζ basis sets, Page *et al.* [368] have reported R_e, D_e and ω_e values in agreement to within 0.004 Å, 0.0001 eV and 1.6 cm^{-1}. These values of R_e and ω_e are also in reasonable agreement with the QCISD(T) data of Leung *et al.* [369]. The lowest $^2\Pi$ state has been investigated by Frenking *et al.* [273] and Leung *et al.* [369], both of which employed MP2. The data presented by these workers indicate that ($^2\Pi$)$BeHe^+$ is significantly more stable than ($^2\Sigma^+$)$BeHe^+$. Similarly, the SCF and post-SCF data of Hayes and Gole [370] and Bu and Zhong [371], respectively, indicate that the ground state of $BeHe^{2+}$ is also strongly bound.

With respect to calcium and magnesium helides, the focus has been centred on the diatomic species [252, 304, 372–377]. Appropriate data concerning the di-

Table 1.8 *Ab initio* parameters of diatomic beryllium helide cations reported in the literature.

Method	State	R_e (/Å)	D_e [a] (/eV)	ω_e (/cm^{-1})
		$BeHe^+$		
MP2[b]	$^2\Sigma^+$	3.132	0.013	68
MP2[c]	$^2\Sigma^+$	3.105	-	67
QCISD(T)[d]	$^2\Sigma^+$	2.96	-	73
CCSD(T)[e]	$^2\Sigma^+$	2.940	0.0161	75.9
IC-MRCI[e]	$^2\Sigma^+$	2.936	0.0160	74.3
MP2[b]	$^2\Pi$	1.415	0.676	-
QCISD(T)[d]	$^2\Pi$	1.38	0.7247	916
		$BeHe^{2+}$		
HF[f]	$^1\Sigma^+$	-	0.807	-
MP2[c]	$^1\Sigma^+$	1.453	0.872	829

[a]Refers to the reactions [$BeHe^{n+} \rightarrow Be^{n+} + He$].

[b]R_e and ω_e calculated in conjunction with the 6-31G(d,p) basis set. The D_e was calculated using MP4(SDTQ)/-311G(2df,2pd); see reference [273].

[c]In conjunction with the 6-311G++(3df,3pd) basis set; see reference [371].

[d]In conjunction with the 6-311++G**(3df, 3dp) (Be) and aug-cc-pVQZ (He) basis sets; see reference [369].

[e]In conjunction with the aug-CVQZ (Be) and aug-cc-pVQZ (He) basis sets; see reference [368].

[f]See reference [370].

atomic cations of magnesium and calcium with helium are summarised in Tables 1.9 and 1.10, respectively. Trends observed with respect to the $^2\Sigma^+$ and $^2\Pi$ states of $BeHe^+$ are also present in $MgHe^+$ and $CaHe^+$. For instance, it is evident from Table 1.9 that the ground $^2\Sigma^+$ state of $MgHe^+$exhibits R_e, D_e and ω_e values of *ca.* 3.5 Å, 0.01 eV and 50 cm^{-1}, whereas these parameters for the lowest $^2\Pi$ state are *ca.* 1.9 Å, 0.28 eV and 468 cm^{-1}. These ratios between R_e and D_e values for $(^2\Sigma^+)CaHe^+$ and $(^2\Pi)CaHe^+$ are also of similar magnitudes. At present, there has been no calculated harmonic frequencies of any excited state of $CaHe^+$. Page and von Nagy-Felsobuki [174] have also reported CCSD(T), IC-MRCI and quadruples-corrected IC-MRCI (IC-MRCI+Q) equilibrium parameters of $(^1\Sigma^+)CaHe^{2+}$ which

Table 1.9 *Ab initio* parameters of diatomic magnesium helide cations reported in the literature.

Method	State	R_e (/Å)	D_e[a] (/eV)	ω_e (/cm^{-1})
		$MgHe^+$		
SCF/MCPF[b]	$^2\Sigma^+$	3.565	0.009	21
MP2[c]	$^2\Sigma^+$	3.611	0.011	45
MP2[d]	$^2\Sigma^+$	3.611	0.009	46
QCISD(T)[c]	$^2\Sigma^+$	3.535	0.012	-
QCISD(T)[e]	$^2\Sigma^+$	3.56	0.008	44
CCSD(T)[f]	$^2\Sigma^+$	3.5151	0.009	49.8
IC-MRCI[f]	$^2\Sigma^+$	3.5929	0.008	47.9
IC-MRCI+Q[f]	$^2\Sigma^+$	3.5311	0.008	49.5
QCISD(T)[e]	$^2\Pi$	1.86	0.2806	468
		$MgHe^{2+}$		
MP2[d]	$^1\Sigma^+$	1.910	0.320	434
CCSD(T)[f]	$^1\Sigma^+$	1.8920	0.3327	483.8
IC-MRCI[f]	$^1\Sigma^+$	1.8919	0.3424	483.2
IC-MRCI+Q[f]	$^1\Sigma^+$	1.8923	0.3285	483.3

[a]Refers to the reactions [$MgHe^{n+} \rightarrow Mg^{n+}$ + He].
[b]See reference [304].
[c]In conjunction with the 6-311+G(3*df*, 3*pd*) basis set; see reference [327].
[d]In conjunction with the 6-311+G(3*df*, 3*pd*) basis set; see reference [378].
[e]In conjunction with the 6-311+G(2*df*) (Mg) and aug-cc-pVQZ (He) basis sets; see reference [372].
[f]Includes basis set superposition error and relativistic corrections, in conjunction with the $[9s, 8p, 5d, 2f]$ ANO-RCC (Mg) and aug-cc-pVQZ (He) basis sets; see reference [174].

Table 1.10 *Ab initio* parameters of diatomic calcium helide cations reported in the literature.

Method	State	R_e (/Å)	${D_e}^a$ (/eV)	ω_e (/cm^{-1})
		$CaHe^+$		
SCF[b]	$^2\Sigma^+$	4.1	0.006	-
CISD[c]	$^2\Sigma^+$	4.4	0.004	-
B3LYP[d]	$^2\Sigma^+$	4.01	0.006	47.6
CCSD(T)[e]	$^2\Sigma^+$	4.3086	0.004	29.9
IC-MRCI[e]	$^2\Sigma^+$	4.4231	0.005	30.2
IC-MRCI+Q[e]	$^2\Sigma^+$	4.3344	0.004	30.2
CISD[c]	$[Ca^+(3d\ ^2D)]^2\Delta$	2.9	0.017	-
CISD[c]	$[Ca^+(3d\ ^2D)]^2\Pi$	2.6	0.023	-
CISD[c]	$[Ca^+(3d\ ^2D)]^2\Sigma^+$	4.8	0.002	-
SCF[b]	$[Ca^+(4p\ ^2P)]^2\Pi$	2.4	0.090	-
CISD[c]	$[Ca^+(4p\ ^2P)]^2\Pi$	2.4	0.088	-
SCF[b]	$[Ca^+(4p\ ^2P)]^2\Sigma^+$	6.09	0.001	-
CISD[c]	$[Ca^+(4p\ ^2P)]^2\Sigma^+$	6.99	0.0009	-
CISD[c]	$[Ca^+(5s\ ^2S)]^2\Sigma^+$	2.3	0.16	-
CISD[c]	$[Ca^+(4d\ ^2D)]^2\Delta$	2.4	0.10	-
CISD[c]	$[Ca^+(4d\ ^2D)]^2\Pi$	2.4	0.16	-
		$CaHe^{2+}$		
CCSD(T)[e]	$^1\Sigma^+$	2.3576	0.1483	295.5
IC-MRCI[e]	$^1\Sigma^+$	2.3644	0.1245	298.7
IC-MRCI+Q[e]	$^1\Sigma^+$	2.3596	0.1434	295.6

[a]Refers to the reactions [$CaHe^{n+} \rightarrow Ca^{n+} + He$].
[b]SCF model potential method; see reference [379].
[c]SCF/CISD pseudopotential method; see reference [380].
[d]In conjunction with the 6-311+G($3df$) basis set; see reference [381].
[e]Including basis set superposition error and relativistic corrections, in conjunction with the $[10s, 9p, 5d, 2f]$ ANO-RCC (Ca) and aug-cc-pVQZ (He) basis sets; see reference [174].

indicate similar trends to those observed in $(^1\Sigma^+)BeHe^{2+}$ and $(^1\Sigma^+)MgHe^{2+}$ (see Chapter 6).

Investigations of the heavier (*viz.* Sr and Ba) alkaline-earth metal helides are limited. There are no reported studies of any Ra helide species. Moreover, studies of diatomic Sr and Ba helides are limited to the neutral case [382–387]. However, Fukuyama *et al.* [388, 389] have observed laser-induced flourescence of the $BaHe^+$and Ba^*He^+ exciplexes in both gaseous and liquid helium environments.

There are very few *ab initio* investigations concerning polyatomic alkaline-

earth metal helide ions in the literature. All *ab initio* data reported in the literature concerning triatomic cations of beryllium, magnesium and calcium with helium are listed in Tables 1.11, 1.12 and 1.13, respectively. Of particular interest with respect to $(^2A_1)BeHe_2^+$ is the bend mode frequency of a_1 symmetry. The *ab initio* data reported by Bu and co-workers [371, 378] and Page *et al.* [192, 368] are indicative of an extremely shallow PES and a small barrier to linearity. The latter observation is also drawn from the analytical IC-MRCI+Q PES for $(^2A_1)BeHe_2^+$ constructed by Page *et al.* [368]. Conversely, $(^1\Sigma_g^+)BeHe_2^{2+}$ resides in a deep potential well and dissociates into $[BeHe^{2+} + He]$ at *ca.* 0.8 eV, as indicated by the Hartree-Fock (HF) results of Harrison *et al.* [390]. Page *et al.* [192] employed IC-MRCI+Q to predict a dissociative potential well-depth of *ca.* 0.9 eV. The latter authors also constructed an analytical IC-MRCI+Q $(^1\Sigma_g^+)BeHe_2^{2+}$ PES. *Ab initio* calculations [192, 391] indicate that $HBeHe^+$is also strongly bound. For example, the MP2, QCISD, CCSD and CASSCF calculations of Antoniotti *et al.* [391] yielded a dissociative well-depth (with respect to $[BeH^+ + He]$) of *ca.* 0.32 eV. Similarly, Page *et al.* [192], who employed CCSD(T), IC-MRCI and IC-MRCI+Q, determined this well-depth to be *ca.* 0.37 eV.

Sapse *et al.* [327] determined the equilibrium properties of the ground state of $MgHe_n^+$ $(n = 1-4)$ using MP2 and QCISD(T) in conjunction with 6-311+G(3*df*,*pd*) basis sets. Bu and Zhong [378, 392] have also used MP2 to investigate $MgHe_n^{m+}$ $(m = 1, 2; n = 1-10)$ and $MgHe_n^+$ $(n = 1-4)$. These workers determined that the ground states of $MgHe_2^+$ and $MgHe_2^{2+}$ correspond to C_{2v} equilibrium structures. Conversely, Page and von Nagy-Felsobuki [174] predicted a $D_{\infty h}$ equilibrium structure for the ground state of $MgHe_2^{2+}$, using relativistically corrected CCSD(T) and IC-MRCI (see Chapter 6).

Investigations of polyatomic calcium helides have been limited to the neutral,

Table 1.11 *Ab initio* parameters of triatomic beryllium helide cations reported in the literature.

Method	R_e(Be-He) (/Å)	R_e(Be-H) (/Å)	θ_e (/°)	D_e[a] (/eV)	Frequencies (/cm^{-1}) ω_1	ω_2	ω_3
			(^{2}A$_1$)BeHe$_2^+$				
MP2[b]	3.085	-	61.3	0.1959	69	25	60
MP2[c]	3.020	-	60.6	0.1380	89.4	46.4	77.0
CCSD(T)[c]	2.924	-	60.1	0.1688	82.2	43.4	70.6
IC-MRCI+Q[c]	2.920	-	60.2	0.1863	67.3	23.7	68.1
			($^1\Sigma_g^+$)BeHe$_2^{2+}$				
HF[d]	1.44		180	0.768	-	-	-
CCSD(T)[e]	1.4373	-	180	0.8808	730.8	13.7	995.2
IC-MRCI[e]	1.4372	-	180	0.8811	727.1	105.2	1010
IC-MRCI+Q[e]	1.4373	-	180	0.8731	-	-	-
			($^1\Sigma^-$)HBeHe$^+$				
B3LYP[f]	1.525	1.302	180	0.33	-	-	-
MP2[f]	1.519	1.294	180	0.29	642.9	278.3	2349.5
QCISD[f]	1.529	1.304	180	0.28	-	-	-
CCSD(T)[f]	1.529	1.305	180	0.28	-	-	-
CCSD(T)[e]	1.5178	1.2998	180	0.3762	-	-	-
IC-MRCI[e]	1.5181	1.2998	180	0.3759	1038	334.2	2047
IC-MRCI+Q[e]	1.5175	1.2998	180	0.3699	-	-	-

[a]Refer to the reactions [BeHe$_n^{2+}$→ BeHe^{n+} + He] and [HBeHe$^+$→ BeH$^+$ + He], as appropriate.
[b]R_e and θ_e calculated in conjunction with the 6-311+G(3*df*,3*pd*) basis set, ω values calculated using the 6-311+G(2*d*,2*p*) basis set; see reference [371].
[c]Basis set superposition error corrected values, in conjunction with the aug-CVQZ (Be) and aug-cc-pVQZ (He) basis sets; see reference [368].
[d]See reference [390].
[e]R_e, θ_e and D_e values are corrected for basis set superposition error, calculated in conjunction with the aug-CVQZ (Be) and aug-cc-pVQZ (He) basis sets. CCSD(T) ω values are harmonic and neglect basis set superposition error correction. IC-MRCI ω values are anharmonic and include basis set superposition error correction; see reference [192].
[f]R_e, θ_e, D_e values calculated using the 6-311++G(2*df*,2*pd*) basis set. The ω_e values were calculated using the 6-31G(*d*); see reference [391].

singly and doubly positively charged species. For example, Jalbout and Solimannejad [381] have studied CaHe$_n^+$ ($n = 1 - 4$) with density functional theory (DFT) and have predicted that these species exhibit thermodynamically stable equilibria. Groenenberg and Balakrishnan [393] employed CCSD(T) to generate a PES for ($^2\Sigma^+$)HCaHe, which consisted of 3700 symmetrically distinct points. Most recently, Page and von Nagy-Felsobuki [174] investigated the ground states of HCaHe$^+$ and CaHe$_2^{2+}$ (see Chapter 6). These workers observed that both HCaHe$^+$ and CaHe$_2^{2+}$ ex-

Table 1.12 *Ab initio* parameters of triatomic magnesium helide cations reported in the literature.

Method	R_e(Mg-He) (/Å)	R_e(Mg-H) (/Å)	θ_e (/°)	D_e[a] (/eV)	Frequencies (/cm^{-1}) ω_1	ω_2	ω_3
			$(^2A_1)MgHe_2^+$				
MP2[b]	3.600	-	51.9	-	23	46	43
MP2[c]	3.602	-	52.47	0.0212	21.45	45.85	42.65
			$MgHe_2^{2+}$				
MP2[b]	1.911	-	135.9	0.2892	413	45	453
CCSD(T)[d]	1.8960	-	180.0	0.3261	446	47.2	508
IC-MRCI[d]	1.8964	-	180.0	0.3011	448	47.6	513
IC-MRCI+Q[d]	1.8936		180.0	0.3178	450	47.4	510
			$(^1\Sigma^-)HMgHe^+$				
CCSD(T)[e]	2.1665	1.6493	180.0	0.0809	664	194	1570
IC-MRCI[e]	2.1779	1.6512	180.0	0.0752	662	192	1594
IC-MRCI+Q[e]	2.1689	1.6494	180.0	0.0800	664	194	1574

[a]Refer to the reactions [$MgHe_n^{2+} \rightarrow MgHe^{n+} + He$] and [$HMgHe^+ \rightarrow MgH^+ + He$], as appropriate.
[b]In conjunction with the 6-311+G(3*df*,3*pd*) basis set; see reference [371].
[c]In conjunction with the 6-311+G(3*df*,3*pd*) basis set; see reference [327].
[d]Includes basis set superposition error and relativistic corrections, in conjunction with the $[9s, 8p, 5d, 2f]$ ANO-RCC (Mg) and aug-cc-pVQZ (He) basis sets; see reference [368].

Table 1.13 *Ab initio* parameters of triatomic calcium helide cations reported in the literature.

Method	R_e(Ca-He) (/Å)	R_e(Ca-H) (/Å)	θ_e (/°)	D_e[a] (/eV)	Frequencies (/cm^{-1}) ω_1	ω_2	ω_3
			$(^2A_1)CaHe_2^+$				
B3LYP[b]	4.05	-	57.8	0.013	62.3	33.1	54.3
			$(^2A_1)CaHe_2^{2+}$				
CCSD(T)[c]	2.3667	-	106.0	0.1435	-	-	-
IC-MRCI[c]	2.3516	-	109.9	0.1469	-	-	-
IC-MRCI+Q[c]	2.3419	-	108.1	0.1514	-	-	-
			$(^2A')HCaHe^+$				
CCSD(T)[c]	2.6271	1.9215	113.4	0.0416	-	-	-
IC-MRCI[c]	2.6441	1.9260	115.1	0.0404	-	-	-
IC-MRCI+Q[c]	2.6309	1.9210	113.3	0.0425	-	-	-

[a]Refer to the reactions [$CaHe_n^{2+} \rightarrow CaHe^{n+} + He$] and [$HCaHe^+ \rightarrow CaH^+ + He$], as appropriate.
[b]In conjunction with the 6-311+G(3*df*) basis set; see reference [381].
[c]Basis set superposition error corrected values, in conjunction with the aug-CVQZ (Ca) and aug-cc-pVQZ (He) basis sets; see reference [368].

ist as quasi-linear species. That is, the $HCaHe^+$ and $CaHe_2^{2+}$ PESs both exhibit minima corresponding to non-linear structures, but are unable to support a bound vibrational state in the bend mode. Moreover, Page and von Nagy-Felsobuki [174] calculated the barriers to linearity for $HCaHe^+$ and $CaHe_2^{2+}$ to be *ca.* 115 and 3 cm^{-1}, respectively.

1.4. Conclusions and Outline

The aims of this thesis are twofold. Firstly, trends in the hydrides, hydrohelides and helides of alkali and alkaline-earth metals will be analysed and elucidated using *ab initio* techniques. Secondly, accurate *ab initio* molecular rovibrational spectra of a subset of suitable non-linear and linear triatomic species will be generated. The algorithm by which these aims will be achieved is outlined in Figure 1.1. The investigations pursued in this thesis will in some, but not all, cases involve the *a priori* prediction of structural, energetic and spectroscopic properties of the species in question. The relevant chemistries of hydrogen and helium have been therefore reviewed in this Chapter, addressing stage (a) of Figure 1.1. Particular emphasis has been placed on the synergic relationship between experimental and theoretical investigation in fields such as molecular spectroscopy and quantum chemistry.

The remainder of this thesis may be outlined as follows. Chapter Two details methods and applications of electronic structure theory (stage (b) of Figure 1.1). In particular, MO theory, one-electron basis sets and methods of electron correlation approximation will be emphasised. *Ab initio* properties of alkali and alkaline-earth metal atoms will be benchmarked. The equilibrium properties of their respective dihydrides will also be presented and discussed. These equilibrium parameters are necessary for the development of accurate molecular property surfaces and vibrational/rovibrational spectra. Chapter Three discusses the construction and

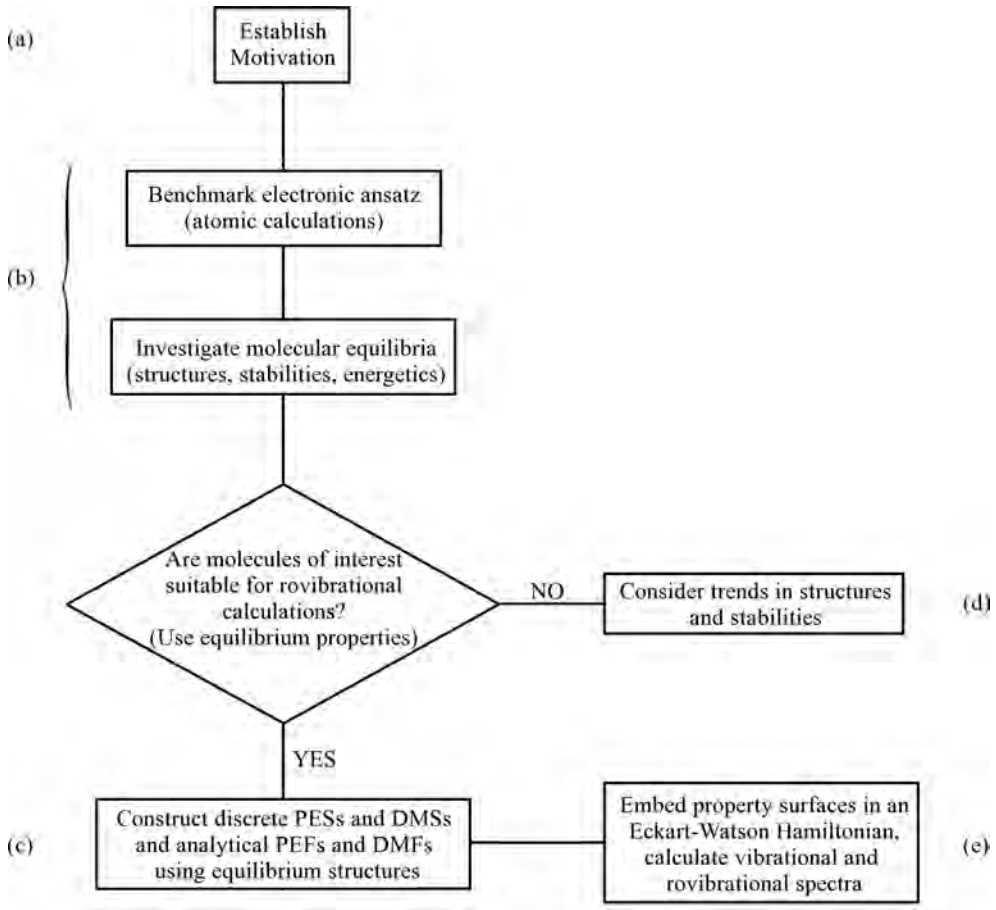

Figure 1.1 Algorithm for the *ab initio* investigation of alkali and alkaline-earth metal hydrides and helides.

analytical representation of *ab initio* molecular property surfaces (stage (c) of Figure 1.1). The generation of accurate PESs and DMSs will be discussed in detail. In particular, the PESs and DMSs of the ground states of LiH_2^+, BeH_2^{2+} and $BeHe_2^{2+}$, and analytical representations thereof, will also be presented. The solution of the nuclear Schrödinger equation (stage (e) of Figure 1.1) is discussed in Chapter Four. This solution requires the molecular PES and DMS to be embedded in the vibrational Hamiltonian operator. Eckart-Watson vibrational Hamiltonians for both non-linear and linear triatomic molecules will be given explicitly. The form of the rovibrational 'super-matrix' elements for non-linear molecules will also be given. The algorithm by which dipole transition moment integrals and hence radiative properties of non-linear molecules are calculated will be described. This

algorithm will also be extended to the linear case. Molecular rovibrational and vibrational spectra of the ground states of the isoelectronic species BeH_2^{2+} and $HBeHe^+$, respectively, will be presented in Chapter Four. Stages (c), (d) and (e) of Figure 1.1 will be applied to hydride, hydrohelide and helide cations of (Li, Na, K) and (Be, Mg, Ca) in Chapters Five and Six, respectively. The electronic structures, stabilities and energetics of these ground state species will therefore be investigated. Molecular PESs, DMSs and rovibrational spectra of suitable species will also be constructed. Chapter Seven will present the general conclusions and discussion of the main results of this thesis.

1.5. References

[1] J. M. Hollas, *Modern Spectroscopy* (Wiley and Sons, Chichester, 1996), 3rd ed.

[2] P. G. Burton and E. I. von Nagy-Felsobuki, Chem. Aust. **55**, 408 (1988).

[3] G. D. Carney and R. N. Porter, J. Chem. Phys. **65**, 3547 (1976).

[4] G. D. Carney and R. N. Porter, Phys. Rev. Lett. **45**, 537 (1980).

[5] G. D. Carney and R. N. Porter, J. Chem. Phys. **60**, 4251 (1974).

[6] T. Oka, Phys. Rev. Lett. **45**, 531 (1980).

[7] W. Meyer, P. Botschwina, and P. G. Burton, J. Chem. Phys. **84**, 191 (1986).

[8] S. Miller and J. Tennyson, J. Mol. Spec. **126**, 183 (1987).

[9] S. Miller and J. Tennyson, J. Mol. Spec. **128**, 530 (1988).

[10] M. G. Bawendi, B. D. Rehfuss, and T. Oka, J. Chem. Phys. **93**, 6200 (1990).

[11] T. Oka, Rev. Mod. Phys. **64**, 1141 (1992).

[12] T. R. Geballe and T. Oka, Nature **384**, 344 (1996).

[13] T. Oka, Proc. Nat. Acad. Sci. **103**, 12235 (2006).

[14] E. F. Laschuk, M. M. Martins, and S. Evangelisti, Int. J. Quant. Chem. **95**, 303 (2003).

[15] N. Kurita and H. Sekino, Int. J. Quant. Chem. **91**, 355 (2003).

[16] F. Ruette, M. Sanchez, R. Anez, A. Bermudez, and A. Sierraalta, J. Mol. Struct. (Theochem) **729**, 19 (2005).

[17] D. M. Ceperley and H. Partridge, J. Chem. Phys. **84**, 820 (1986).

[18] R. A. Aziz and M. J. Slaman, Z. Phys. D **25**, 343 (1993).

[19] R. A. Aziz, A. Krantz, and M. J. Slaman, Z. Phys. D **21**, 251 (1991).

[20] T. van Mourik and J. Thom H. Dunning, J. Chem. Phys. **111**, 9248 (1999).

[21] M. Jeziorski, W. Cencek, K. Patkowski, B. Jeziorski, and K. Szalewicz, J. Chem. Phys. **127**, 124303 (2007).

[22] S. M. Cybulski and R. R. Toczylowski, J. Chem. Phys. **111**, 10520 (1999).

[23] D. E. Woon, J. Chem. Phys. **100**, 2838 (1994).

[24] W. Klopper and J. Noga, J. Chem. Phys. **103**, 6127 (1995).

[25] A. R. Janzen and R. A. Aziz, J. Chem. Phys. **103**, 9626 (1995).

[26] R. Specchio, A. Famulari, and M. Raimondi, J. Mol. Struct. (THEOCHEM) **549**, 77 (2001).

[27] J. V. Burda, R. Zahradnik, P. Hobza, and M. Urban, Mol. Phys. **89**, 425 (1996).

[28] J. F. Ogilvie and F. Y. H. Wang, J. Mol. Struct. (THEOCHEM) **273**, 277 (1992).

[29] J. B. Anderson, C. A. Traynor, and B. M. Boghosian, J. Chem. Phys. **99**, 345 (1993).

[30] N. C. Bera, I. Bhattacharyya, and A. K. Das, Int. J. Quant. Chem. **107**, 824 (2007).

[31] F. Luo, G. C. McBane, G. Kim, C. F. Giese, and W. R. Gentry, J. Chem. Phys. **98**, 3564 (1993).

[32] E. S. Meyer, J. C. Mester, and I. F. Silvera, J. Chem. Phys. **100**, 4021 (1994).

[33] F. Luo, C. F. Giese, and W. R. Gentry, J. Chem. Phys. **104**, 1151 (1996).

[34] W. Schollkopf and J. P. Toennies, J. Chem. Phys. **104**, 1155 (1996).

[35] K. Patkowski, W. Cencek, M. Jeziorska, B. Jeziorski, and K. Szalewicz, J. Phys. Chem. A **111**, 7611 (2007).

[36] K. Szalewicz, K. Patkowski, and B. Jeziorski, Structure and Bonding **116**, 43 (2005).

[37] R. Springall, M. C. Per, S. P. Russo, and I. K. Snook, J. Chem. Phys. **128**, 114308 (2008).

[38] R. E. Grisenti, W. Schollkopf, J. P. Toennies, G. C. Hegerfeldt, T. Kohler, and M. Stoll, Phys. Rev. Lett. **85**, 2284 (2000).

[39] T. van Mourik and J. H. van Lenthe, J. Chem. Phys. **102**, 7479 (1995).

[40] W. Klemperer, Proc. Nat. Acad. Sci. **103**, 12232 (2006).

[41] S. Aldridge and A. J. Downs, Chem. Rev. **101**, 3305 (2001).

[42] G. J. Kubas, Chem. Rev. **107**, 4152 (2007).

[43] S. Sabo-Etienne and B. Chaudret, Chem. Rev. **98**, 2077 (1998).

[44] E. Wiberg and E. Amberger, *Hydrides of the Elements of Main Groups I-IV* (Elsevier, Amsterdam, 1971).

[45] J. C. Bailar, *Comprehensive Inorganic Chemistry* (Pergamon Press, Oxford, 1973), vol. 1, 2.

[46] A. J. Downs and C. R. Pulham, Chem. Soc. Rev. **23**, 175 (1994).

[47] A. J. Downs, Coord. Chem. Rev. **189**, 59 (1999).

[48] A. J. Downs and C. R. Pulham, Adv. Inorg. Chem. **41**, 171 (1994).

[49] S. M. Godfrey, C. A. McAuliffe, A. G. Mackie, and R. G. Norman, *Chemistry of Arsenic, Antimony and Bismuth* (Blackie Academic and Professional, London, 1998), p. 67.

[50] M. J. Taylor and P. J. Brothers, *Chemistry of Aluminium, Gallium, Indium and Thallium* (Blackie, Glasgow, 1993), p. 111.

[51] B. Sakintuna, F. Lamari-Darkrim, and M. Hirscher, Int. J. Hydrogen Energy **32**, 1121 (2007).

[52] S.-I. Orimo, Y. Nakamori, J. R. Eliseo, A. Zuttel, and C. M. Jensen, Chem. Rev. **107**, 4111 (2007).

[53] M. Bellini, P. De Natale, M. Inguscio, T. D. Varberg, and J. M. Brown, Phys. Rev. A **52**, 1954 (1995).

[54] W. C. Stwalley and W. T. Zemke, J. Phys. Chem. Ref. Data **22**, 87 (1993).

[55] S. K. Tokunaga, J. O. Stack, J. J. Hudson, B. E. Sauer, E. A. Hinds, and M. R. Tarbutt, J. Chem. Phys. **126**, 124314 (2007).

[56] C.-Y. Wu, W.-T. Luh, F. X. Gadéa, and W. C. Stwalley, J. Chem. Phys. **128**, 064303 (2008).

[57] X. Li and J. Paldus, J. Chem. Phys. **118**, 2470 (2003).

[58] S. Bubin, L. Adamowicz, and M. Molski, J. Chem. Phys. **123**, 134310 (2005).

[59] S. Bubin and L. Adamowicz, J. Chem. Phys. **125**, 064309 (2006).

[60] F. Gadéa and T. Leininger, Theor. Chim. Acta **116**, 566 (2006).

[61] J. A. Coxon and C. S. Dickinson, J. Chem. Phys. **121**, 9378 (2004).

[62] M. Dolg, Theor. Chim. Acta **93**, 141 (1996).

[63] S. Magnier, J. Phys. Chem. A **108**, 1052 (2004).

[64] F. A. Gianturco, P. G. Giorgi, H. Berriche, and F. X. Gadéa, Astron. Astrophys. Supp. Ser. **117**, 377 (1996).

[65] R. Curík and C. H. Greene, Mol. Phys. **105**, 1565 (2007).

[66] J. A. Pople, B. T. Luke, M. J. Frisch, and J. S. Binkley, J. Phys. Chem. **89**, 2198 (1985).

[67] P. Fuentealba, O. Reyes, H. Stoll, and H. Preuss, J. Chem. Phys. **87**, 5338 (1987).

[68] W. C. Stwalley, W. T. Zemke, and S. C. Yang, J. Phys. Chem. Ref. Data **20**, 153 (1991).

[69] U. Magg and H. Jones, Chem. Phys. Lett. **146**, 415 (1988).

[70] N. N. Haese, D.-J. Liu, and R. S. Altman, J. Chem. Phys. **81**, 3766 (1984).

[71] H. Odashima, D. B. Wang, F. Matsushima, S. Tsunekawa, and K. Takagi, J. Mol. Spec. **171**, 513 (1995).

[72] S. Magnier, J. Phys. Chem. A **109**, 5411 (2005).

[73] S. Magnier, Chem. Phys. **326**, 375 (2006).

[74] S. J. Duclos, Y. K. Vohra, A. L. Ruoff, S. Filipek, and B. Baranowski, Phys. Rev. B **36**, 7664 (1987).

[75] R. L. Plambeck and N. R. Erickson, Astrophys. J. **262**, 606 (1982).

[76] K. Kirby and A. Dalgarno, Astrophys. J. **224**, 444 (1978).

[77] B. K. Taylor and P. R. Newman, J. Chem. Phys. **118**, 8770 (2003).

[78] Y. L. Chen, C. H. Huang, and W. P. Hu, J. Phys. Chem. A **109**, 9627 (2005).

[79] N. Khelifi, B. Oujia, and F. X. Gadéa, J. Phys. Chem. Ref. Data **36**, 191 (2007).

[80] A. Bhattacharjee and K. R. Dastidar, Phys. Rev. A **72**, 023419 (2005).

[81] N. Geum, G.-H. Jeung, A. Derevianko, R. Cote, and A. Dalgarno, J. Chem. Phys. **115**, 5984 (2001).

[82] J.-Y. Zhang and J. Mitroy, Phys. Rev. A **76**, 022705 (2007).

[83] V. M. Garcia, R. Caballol, and J. P. Malrieu, J. Chem. Phys. **109**, 504 (1998).

[84] S. R. Langhoff, J. Charles W. Bauschlicher, and H. Partridge, J. Chem. Phys. **85**, 5158 (1986).

[85] S. H. Patil and K. T. Tang, J. Chem. Phys. **118**, 4905 (2003).

[86] N. Khelifi, B. Oujia, and F. X. Gadéa, J. Chem. Phys. **116**, 2879 (2002).

[87] H. S. Lee, Y. S. Lee, and G. H. Jeung, J. Phys. Chem. A **103**, 11080 (1999).

[88] J. M. L. Martin, Chem. Phys. Lett. **273**, 98 (1997).

[89] H. Kato, K. Hirao, I. Nishida, K. Kimoto, and K. Akagi, J. Phys. Chem. **85**, 3391 (1981).

[90] X. Wang and L. Andrews, J. Phys. Chem. A **111**, 6008 (2007).

[91] B. S. Jursic, J. Mol. Struct. (THEOCHEM) **491**, 11 (1999).

[92] P. Jankowski and B. Jeziorski, J. Chem. Phys. **111**, 1857 (1999).

[93] B. H. Cardelino, W. H. Eberhardt, and R. F. Borkman, J. Chem. Phys. **84**, 3230 (1986).

[94] P. Hobza and P. von Ragué-Schleyer, Chem. Phys. Lett. **105**, 630 (1984).

[95] W. Grochala and R. Hoffmann, J. Phys. Chem. A **104**, 9740 (2000).

[96] F. Rossi and J. Pascale, Phys. Rev. A **32**, 2657 (1985).

[97] A. J. Page and E. I. von Nagy-Felsobuki, J. Mol. Struct. (THEOCHEM) **853**, 53 (2008).

[98] J.-J. Chen, Y.-M. Hung, D.-K. Liu, H.-S. Fung, and K.-C. Lin, J. Chem. Phys. **114**, 9395 (2001).

[99] M. D. Hack and D. G. Truhlar, J. Chem. Phys. **110**, 4315 (1999).

[100] M. Hack, A. Jasper, Y. Volobuev, D. Schwenke, and D. Truhlar, J. Phys. Chem. A **103**, 6309 (1999).

[101] M. Hack, A. Jasper, Y. Volobuev, D. Schwenke, and D. Truhlar, J. Phys. Chem. A **104**, 217 (2000).

[102] M. D. Hack and D. G. Truhlar, J. Chem. Phys. **114**, 9305 (2001).

[103] D. R. Yarkony, J. Chem. Phys. **84**, 3206 (1986).

[104] P. Botschwina, W. Meyer, I. V. Hertel, and W. Reiland, J. Chem. Phys. **75**, 5438 (1981).

[105] D. Geppert, A. Hofmann, and R. de Vivie-Riedle, J. Chem. Phys. **119**, 5901 (2003).

[106] R. de Vivie-Riedle, P. Hering, and K. L. Kompa, Z. Phys. D **17**, 299 (1990).

[107] R. de Vivie-Riedle and K. Sundermann, Appl. Phys. B **71**, 285 (2000).

[108] R. de Vivie-Riedle, L. Kurtz, and A. Hofmann, Pure Appl. Chem. **3**, 525 (2001).

[109] A. W. Jasper, C. Zhu, S. Nangia, and D. G. Truhlar, Farad. Disc. **127**, 1 (2004).

[110] M. Motzkus, G. Pichler, K. L. Kompa, and P. Hering, J. Chem. Phys. **106**, 9057 (1997).

[111] M. Motzkus, G. Pichler, K. L. Kompa, and P. Hering, J. Chem. Phys. **108**, 9291 (1998).

[112] A. Burrows and M. Volobuyev, Astrophys. J. **583**, 985 (2003).

[113] N. F. Allard, F. Allard, P. H. Hauschildt, J. F. Kielkopf, and L. Machin, Astron. Astrophys. **411**, L473 (2003).

[114] T.-H. Wong, P. D. Kleiber, and K.-H. Yang, J. Chem. Phys. **110**, 6743 (1999).

[115] D.-K. Liu and K.-C. Lin, J. Chem. Phys. **107**, 4244 (1997).

[116] D.-K. Liu and K.-C. Lin, J. Chem. Phys. **105**, 9121 (1996).

[117] K.-C. Lin and H.-C. Chang, J. Chem. Phys. **90**, 6151 (1989).

[118] R. Santra and K. Kirby, J. Chem. Phys. **123**, 214309 (2005).

[119] D. J. Searles and E. I. von Nagy-Felsobuki, Phys. Rev. A **43**, 3365 (1991).

[120] C. H. Wu, J. Chem. Phys. **71**, 783 (1979).

[121] E. Bodo, F. A. Gianturco, R. Martinazzo, A. Forni, A. Famulari, and M. Raimondi, J. Phys. Chem. A **104**, 11972 (2000).

[122] E. Bodo, F. A. Gianturco, and R. Martinazzo, J. Phys. Chem. A **105**, 10994 (2001).

[123] E. Bodo, F. A. Gianturco, R. Martinazzo, and M. Raimondi, J. Phys. Chem. A **105**, 10986 (2001).

[124] R. Martinazzo, G. F. Tantardini, E. Bodo, and F. A. Gianturco, J. Chem. Phys. **119**, 11241 (2003).

[125] R. Martinazzo, E. Bodo, F. A. Gianturco, and M. Raimondi, Chem. Phys. **287**, 335 (2003).

[126] C. Sanz, E. Bodo, and F. A. Gianturco, Chem. Phys. **314**, 135 (2005).

[127] R. Davy, E. Skoumbourdis, and T. Kompanchenko, Mol. Phys. **97**, 1263 (1999).

[128] A. Russek, R. Snyder, and R. J. Furlan, Phys. Rev. A **39**, 6158 (1989).

[129] D. A. Dixon, J. L. Gole, and A. Komornicki, J. Phys. Chem. **92**, 1378 (1988).

[130] J. B. Collins, P. von Ragué-Schleyer, J. S. Binkley, J. A. Pople, and L. Radom, J. Am. Chem. Soc. **98**, 3436 (1976).

[131] E. Kochanski, Chem. Phys. Lett. **28**, 471 (1974).

[132] R. C. Raffenetti and K. Ruedenberg, J. Chem. Phys. **59**, 5978 (1973).

[133] W. A. Lester Jr, J. Chem. Phys. **54**, 3171 (1971).

[134] W. A. Lester Jr, J. Chem. Phys. **53**, 1511 (1970).

[135] N. K. Ray, J. Chem. Phys. **52**, 463 (1970).

[136] A. A. Wu and F. O. Ellison, J. Chem. Phys. **47**, 1458 (1967).

[137] W. P. Kraemer and V. Špirko, Chem. Phys. **330**, 190 (2006).

[138] V. P. Bulychev, K. M. Bulanin, and M. O. Bulanin, Opt. Spectrosc. **96**, 205 (2004).

[139] A. J. Page and E. I. von Nagy-Felsobuki, J. Phys. Chem. A **111**, 4478 (2007).

[140] D. M. Bishop and S. M. Cybulski, Chem. Phys. Lett. **230**, 177 (1994).

[141] W. Kutzelnigg, V. Staemmler, and C. Hoheisel, Chem. Phys. **1**, 27 (1973).

[142] C. Emmeluth, B. L. J. Poad, C. D. Thompson, G. H. Weddle, and E. J. Bieske, J. Chem. Phys. **126**, 204309 (2007).

[143] C. D. Thompson, C. Emmeluth, B. L. J. Poad, G. H. Weddle, and E. J. Bieske, J. Chem. Phys. **125**, 044310 (2006).

[144] J. G. Vitillo, A. Damin, A. Zecchina, and G. Ricchiardi, J. Chem. Phys. **122**, 114311 (2005).

[145] M. Barbatti, G. Jalbert, and M. A. C. Nascimento, J. Chem. Phys. **114**, 2213 (2001).

[146] J. D. Switalski, J. T. J. Huang, and M. E. Schwartz, J. Chem. Phys. **60**, 2252 (1974).

[147] I. Tamássy-Lentei and J. Szaniszló, J. Mol. Struct. (Theochem) **501-502**, 403 (2000).

[148] L. A. Curtiss and J. A. Pople, J. Phys. Chem. **92**, 894 (1988).

[149] J. E. Bushnell, P. R. Kemper, and M. T. Bowers, J. Phys. Chem. **98**, 2044 (1994).

[150] M. F. Falcetta, J. L. Pazun, M. J. Dorko, D. Kitchen, and P. E. Siska, J. Phys. Chem. **97**, 1011 (1993).

[151] R. J. Le Roy, D. R. T. Appadoo, R. Colin, and P. F. Bernath, J. Mol. Spec. **236**, 178 (2006).

[152] C. Focsa, S. Firth, P. F. Bernath, and R. Colin, J. Chem. Phys. **109**, 5795 (1998).

[153] R. Colin, C. Dreze, and M. Steinhauer, Can. J. Phys. **61**, 641 (1983).

[154] R. Colin, D. de Greef, P. Goethals, and G. Verhaegen, Chem. Phys. Lett. **25**, 70 (1974).

[155] T. J. Tague and L. Andrews, J. Am. Chem. Soc. **115**, 12111 (1993).

[156] L. B. Knight Jr., J. M. Brom Jr., and W. Weltner Jr., J. Chem. Phys. **56**, 1152 (1972).

[157] G. S. Smith, Q. C. Johnson, D. K. Smith, D. E. Cox, R. L. Snyder, R.-S. Zhou, and A. Zalkin, Solid State Commun. **67**, 491 (1988).

[158] A. Shayesteh, K. Tereszchuk, P. F. Bernath, and R. Colin, J. Chem. Phys. **118**, 1158 (2003).

[159] P. J. Bruna, G. A. Di Labio, and J. S. Wright, J. Phys. Chem. **96**, 6269 (1992).

[160] B. Lemoine, C. Demuynck, J. L. Destombes, and P. B. Davies, J. Chem. Phys. **89**, 673 (1988).

[161] A. Shayesteh, R. D. E. Henderson, R. J. Le Roy, and P. F. Bernath, J. Phys. Chem. A **111**, 12495 (2007).

[162] T. J. Tague and L. Andrews, J. Phys. Chem. **98**, 8611 (1994).

[163] D. Petitprez, B. Lemoine, C. Demuynck, J. L. Destombes, and B. Macke, J. Chem. Phys. **91**, 4462 (1989).

[164] M. Kaupp, P. von Ragué-Schleyer, H. Stoll, and H. Preuss, J. Chem. Phys. **94**, 1360 (1991).

[165] T. Leininger and G.-H. Jeung, J. Chem. Phys. **103**, 3942 (1995).

[166] T. Shunmei Fujii and S. Iwata, Chem. Phys. Lett. **251**, 150 (1996).

[167] K. P. Huber and G. Herzberg, *Constants of Diatomic Molecules*, vol. IV of *Molecular Spectra and Molecular Structure* (Van Nostrand, New York, 1979).

[168] F. B. C. Machado and F. R. Ornellas, J. Chem. Phys. **94**, 7237 (1991).

[169] F. R. Ornellas, J. Mol. Struct. (THEOCHEM) **92**, 337 (1983).

[170] F. R. Ornellas and F. B. C. Machado, J. Mol. Struct. (THEOCHEM) **282**, 43 (1993).

[171] F. R. Ornellas, J. Chem. Phys. **82**, 379 (1985).

[172] F. R. Ornellas, J. Phys. B **15**, 1977 (1982).

[173] S. Jorgensen, M. Drewsen, and R. Kosloff, J. Chem. Phys. **123**, 094302 (2005).

[174] A. J. Page and E. I. von Nagy-Felsobuki, Phys. Chem. Chem. Phys. **10**, 1285 (2008).

[175] S. Canuto, M. A. Castro, and K. Sinha, Phys. Rev. A **48**, 2461 (1993).

[176] J. Pitarch-Ruiz, J. Sánchez-Marin, and A. M. Velasco, J. Comp. Chem. (In press).

[177] S. Bubin and L. Adamowicz, J. Chem. Phys. **126**, 214305 (2007).

[178] B. Fernandez and P. Jorgensen, Chem. Phys. Lett. **232**, 463 (1995).

[179] G. H. Lushington, P. J. Bruna, and F. Grein, Z. Phys. D **36**, 301 (1996).

[180] F. R. Ornellas, W. C. Stwalley, and W. T. Zemke, J. Chem. Phys. **79**, 5311 (1983).

[181] Y. Liu, W. Sun, and W. Ren, Front. Phys. China **2**, 213 (2006).

[182] F. B. C. Machado, O. Roberto-Neto, and F. R. Ornellas, Chem. Phys. Lett. **284**, 293 (1998).

[183] J. A. Coxon and R. Colin, J. Mol. Spec. **181**, 215 (1997).

[184] F. Wang, Z. Zhu, C. Yang, and F. Jing, Chin. Phys. Lett. **15**, 715 (1998).

[185] M. Chrysos, M. E. Alikhani, and M. Jacon, Int. J. Quant. Chem. **53**, 57 (1995).

[186] P. M. W. Gill and L. Radom, Chem. Phys. Lett. **147**, 213 (1988).

[187] K. Franzreb, R. C. Sobers Jr., J. Lorincik, and P. Williams, Phys. Rev. A **71**, 024701 (2005).

[188] A. Shayesteh and P. F. Bernath, J. Chem. Phys. **124**, 156101 (2006).

[189] S. Sampath, A. I. Kolesnikov, K. M. Lantzky, and J. L. Yarger, J. Chem. Phys. **128**, 134512 (2008).

[190] X. Wang and L. Andrews, Inorg. Chem. **44**, 610 (2005).

[191] M. D. Senin, V. V. Akhachinskii, Y. E. Markushking, N. A. Chirin, L. M. Kopytin, I. P. Mikhalenko, N. M. Ermolaev, and A. V. Zabrodin, Inorg. Mater. **29**, 1416 (1993).

[192] A. J. Page, D. J. D. Wilson, and E. I. von Nagy-Felsobuki, Chem. Phys. Lett. **442**, 194 (2007).

[193] H. Li and R. J. L. Roy, J. Chem. Phys. **125**, 044307 (2006).

[194] A. Shayesteh, D. R. T. Appadoo, I. Gordon, and P. F. Bernath, J. Chem. Phys. **119**, 7785 (2003).

[195] H. Li, D. Xie, and H. Guo, J. Chem. Phys. **121**, 4156 (2004).

[196] Z. L. Xiao, R. H. Hauge, and J. L. Margrave, High Temp. Sci. **31**, 59 (1991).

[197] X. Wang and L. Andrews, J. Phys. Chem. A **108**, 11500 (2004).

[198] A. M. Boesgaard, Astrophys. J. **154**, 185 (1968).

[199] C. J. Donzelli and D. L. Ferreiro, Astron. Astrophys. Supp. Ser. **127**, 527 (1998).

[200] W. W. Watsona and P. Rudnick, Astrophys. J. **63**, 20 (1926).

[201] A. Shayesteh, D. R. T. Appadoo, I. Gordon, R. J. Le Roy, and P. F. Bernath, J. Chem. Phys. **120**, 10002 (2004).

[202] K. K. Irikura, J. Phys. Chem. Ref. Data **36**, 389 (2007).

[203] L. B. Knight Jr. and W. Weltner Jr., J. Chem. Phys. **54**, 3875 (1971).

[204] C. M. Dutta, P. Nordlander, and M. Kimura, Chem. Phys. Lett. **264**, 51 (1997).

[205] A. Bertelsen, I. S. Vogelius, S. Jorgensen, R. Kosloff, and M. Drewsen, Eur. Phys. J. D **31**, 403 (2004).

[206] T. S. Monteiro, G. Danby, I. L. Cooper, A. S. Dickinson, and E. L. Lewis, J. Phys. B **21**, 4165 (1988).

[207] P. S. Barklem and B. J. O'Mara, Mon. Not. Roy. Astron. Soc. **300**, 863 (1998).

[208] P. F. Weck, P. C. Stancil, and K. Kirby, J. Chem. Phys. **118**, 9997 (2003).

[209] J. D. Weinstein, R. de Carvalho, T. Guillet, B. Friedrich, and J. M. Doyle, Nature **395**, 148 (1998).

[210] B. Friedrich, J. D. Weinstein, R. de Carvalho, and J. M. Doyle, J. Chem. Phys. **110**, 2376 (1999).

[211] J. Chen, J. Gengler, T. C. Steimle, and J. M. Brown, Phys. Rev. A **73**, 012502 (2006).

[212] T. C. Steimle, J. Chen, and J. Gengler, J. Chem. Phys. **121**, 829 (2004).

[213] L. E. Berg, K. Ekvall, and S. Kelly, Chem. Phys. Lett. **257**, 351 (1996).

[214] Phys. Rev. A **73**, 032714 (2006).

[215] A. Boutalib, J. P. Daudey, and M. E. Mouhtadi, Chem. Phys. **167**, 111 (1992).

[216] F. E. Penotti, Int. J. Quant. Chem. **106**, 1153 (2006).

[217] J. Koput and K. A. Peterson, J. Chem. Phys. **125**, 044306 (2006).

[218] T. Hrenar, H.-J. Werner, and G. Rauhut, Phys. Chem. Chem. Phys. **7**, 3123 (2005).

[219] L. N. Vidal and P. A. M. Vazquez, Chem. Phys. **321**, 209 (2006).

[220] J. M. L. Martin and T. J. Lee, Chem. Phys. Lett. **200**, 502 (1992).

[221] J. Hinze, Mol. Phys. **96**, 711 (1999).

[222] P. F. Bernath, A. Shayesteh, K. Tereszchuk, and R. Colin, Science **297**, 1323 (2002).

[223] A. Shayesteh, K. Tereszchuk, P. F. Bernath, and R. Colin, J. Chem. Phys. **118**,

3622 (2003).

[224] C. A. Nicolaides and P. Valtazanos, Chem. Phys. Lett. **176**, 239 (1991).

[225] L. von Szentpaly, J. Phys. Chem. A **106**, 11945 (2002).

[226] P. Chaquin, A. Sevin, and H. Yu, J. Phys. Chem. **89**, 2813 (1985).

[227] R. Ahlrichs, F. Keil, H. Lischka, W. Kutzelnigg, and V. Staemmler, J. Chem. Phys. **63**, 455 (1975).

[228] G. S. Tschumper and H. F. Schaefer III, J. Chem. Phys. **108**, 7511 (1998).

[229] H. Li and R. J. Le Roy, J. Phys. Chem. A **111**, 6248 (2007).

[230] D.-K. Liu, K.-C. Lin, and J.-J. Chen, J. Chem. Phys. **113**, 5302 (2000).

[231] J.-J. Chen, M.-K. Hsiao, and K.-C. Lin, J. Chem. Phys. **123**, 121101 (2005).

[232] C. X. Shang, M. Bououdina, Y. Song, and Z. X. Guo, Int. J. Hydrogen Energy **29**, 73 (2004).

[233] J. G. McCaffrey, J. M. Parnis, G. A. Ozin, and W. H. Breckenridge, J. Phys. Chem. **89**, 4945 (1985).

[234] B. Bogdanovic, P. Bons, M. Schwickardi, and K. Seevogel, Chem. Ber. **124**, 1041 (1991).

[235] W. Knott, Z. Naturforsch. B **52**, 629 (1997).

[236] Y. Chen and J. S. Williams, J. Alloys. Compd. **217**, 181 (1995).

[237] G. Koerner, K. D. Klein, and W. Knott, Z. Naturforsch. B **47b**, 767 (1992).

[238] W. H. Zachariasen, C. E. Holley, and J. F. Stamper, Acta. Cryst. **16**, 352 (1963).

[239] J. Koput, J. Phys. Chem. A **109**, 4410 (2005).

[240] I. Bytheway, R. J. Gillespie, T.-H. Tang, and R. F. W. Bader, Inorg. Chem. **34**, 2407 (1995).

[241] R. L. DeKock, M. A. Peterson, L. K. Timmer, E. J. Baerends, and P. Verooijs, Polyhedron **9**, 1919 (1990).

[242] Y.-W. Song, J.-J. Chen, M.-K. Hsiao, K.-C. Lin, and Y.-M. Hung, J. Chem. Phys. **120**, 2774 (2004).

[243] A. F. Andresen, A. J. Maeland, and D. Slotfeldt-Ellingsen, J. Solid State Chem. **20**, 93 (1977).

[244] A. Shayesteh, K. A. Walker, I. Gordon, D. R. T. Appadoo, and P. F. Bernath, J. Mol. Struct. (THEOCHEM) **695-696**, 23 (2004).

[245] R. D. Poshusta, D. W. Klint, and A. Liberles, J. Chem. Phys. **55**, 252 (1971).

[246] A. J. Page and E. I. von Nagy-Felsobuki, unpublished, 2008.

[247] P. Valtazanos and C. A. Nicolaides, Chem. Phys. Lett. **172**, 254 (1990).

[248] A. J. Page and E. I. von Nagy-Felsobuki, Mol. Phys. **105**, 2527 (2007).

[249] D. G. Musaev and O. P. Charkin, Z. Strukt. Khim. **31**, 190 (1990).

[250] C. W. Bauschlicher, Chem. Phys. Lett. **201**, 11 (1993).

[251] E. D. Simandiras and C. A. Nicolaides, Chem. Phys. Lett. **185**, 529 (1991).

[252] S. Petrie, J. Phys. Chem. A **106**, 7034 (2002).

[253] A. J. Page and E. I. von Nagy-Felsobuki, Chem. Phys. **351**, 37 (2008).

[254] L. N. Ding, M. A. Young, P. D. Kleiber, W. C. Stwalley, and A. M. Lyyra, J. Phys. Chem. **97**, 2181 (1993).

[255] E. Czuchaj, M. Krośnicki, and H. Stoll, Mol. Phys. **98**, 419 (2000).

[256] M. Krośnicki and J. Czub, Theor. Chem. Acc. **115**, 322 (2006).

[257] M. Knoop, M. Vedel, and F. Vedel, Phys. Rev. A **58**, 264 (1998).

[258] S. Urabe, K. Hayasaka, M. Watanabe, H. Imajo, and R. Ohmukai, Jpn. J. App. Phys. **33**, 1590 (1994).

[259] D. R. Lide, *CRC Handbook of Chemistry and Physics* (CRC Press, 2007-2008), 88th ed.

[260] J. P. Toennies and A. F. Vilesov, Angew. Chem. Int. Ed. **43**, 2622 (2004).

[261] J. J. Manley, Nature **115**, 337 (1925).

[262] R. Heller, J. Chem. Phys. **9**, 154 (1941).

[263] Z. Wang, D. Liu, K. Su, H. Fan, Y. Li, and Z. Wen, Chem. Phys. **331**, 309 (2007).

[264] T. Weiske, T. Wong, W. Krotschmer, J. K. Terlouw, and H. Schwarz, Angew. Chem. Int. Ed. **31**, 183 (1992).

[265] G. Frenking, W. Koch, J. Gauss, and D. Cremer, J. Am. Chem. Soc. **110**, 8007 (1988).

[266] T. Takayanagi, H. Motegi, Y. Taketsugu, and T. Taketsugu, Chem. Phys. Lett. **454**, 1 (2008).

[267] M. W. Wong, J. Am. Chem. Soc. **122**, 6289 (2000).

[268] P. Antoniotti, N. Bronzolino, and F. Grandinetti, J. Phys. Chem. A **107**, 2974 (2003).

[269] H. Ran and D. Xie, J. Chem. Phys. **128**, 124323 (2008).

[270] F. Grandinetti, Int. J. Mass. Spec. **237**, 243 (2004).

[271] G. Frenking and D. Cremer, Structure and Bonding **73**, 17 (1990).

[272] G. Frenking, W. Koch, and J. F. Liebman, *From Atoms to Molecules: Isoelectronic Analogues* (VCH Publishers, New York, 1989).

[273] G. Frenking, W. Koch, D. Cremer, J. Gauss, and J. F. Liebman, J. Phys. Chem.

93, 3397 (1989).

[274] P. von Ragué-Schleyer, Adv. Mass. Spec. **10A**, 287 (1986).

[275] C. W. Bauschlicher, S. R. Langhoff, and H. Partridge, *Organometallic Ion Chemistry* (1996), vol. 15, p. 47.

[276] L. Pauling, J. Chem. Phys. **1**, 56 (1933).

[277] J. Xie, B. Poirier, and G. I. Gellene, J. Chem. Phys. **122**, 184310 (2005).

[278] A. Ruzsinszky, J. P. Perdew, G. I. Csonka, O. A. Vydrov, and G. E. Scuseria, J. Chem. Phys. **126**, 104102 (2007).

[279] J. Xie, B. Poirier, and G. I. Gellene, J. Chem. Phys. **119**, 10678 (2003).

[280] N. C. Bera, I. Bhattacharyya, and A. K. Das, Int. J. Quant. Chem. **107**, 1067 (2007).

[281] N. Yu and W. H. Wing, Phys. Rev. Lett. **59**, 2055 (1987).

[282] L. Wolniewicz, J. Phys. B **32**, 2257 (1999).

[283] H. Yagisawa, H. Sato, and T. Watanabe, Phys. Rev. A **16**, 1352 (1977).

[284] H. Hogreve, Mol. Phys. **98**, 249 (2000).

[285] A. Belkacem, E. P. Kanter, R. E. Mitchell, Z. Vager, and B. J. Zabransky, Phys. Rev. Lett. **63**, 2555 (1989).

[286] M. Raunhardt, M. Schafer, N. Vanhaecke, and F. Merkt, J. Chem. Phys. **128**, 164310 (2008).

[287] P. L. Patterson, J. Chem. Phys. **48**, 3625 (1968).

[288] I. Paidarová, R. Polák, B. Pauliková, F. Karlický, K. Oleksy, D. Hrivňák, F. X. Gadéa, and R. Kalus, Chem. Phys. (In press).

[289] F. Karlicky, B. Lepetit, R. Kalus, I. Paidarova, and F. X. Gadéa, J. Chem. Phys. **128**, 124303 (2008).

[290] T. R. Hogness and E. G. Lunn, Phys. Rev. **26**, 44 (1925).

[291] J. Dabrowski and G. Herzberg, Trans. N. Y. Acad. Sci. II **38**, 14 (1977).

[292] J. H. Black, Astrophys. J. **222**, 125 (1978).

[293] W. Roberge and A. Dalgarno, Astrophys. J. **255**, 489 (1982).

[294] C. Cecchi-Pestellini and A. Dalgarno, Astrophys. J. **413**, 611 (1993).

[295] V. P. Gaur, G. C. Joshi, and M. C. Pande, Astrophys. Space Sci. **197**, 57 (1992).

[296] S. Miller, J. Tennyson, and A. Dalgarno, Nature **355**, 420 (1992).

[297] V. K. Dubrovich and A. A. Lipovka, Astrophys. Space Sci. **296**, 307 (1995).

[298] D. M. Bishop and L. M. Cheung, J. Mol. Spec. **75**, 462 (1979).

[299] P. Bernath and T. Amano, Phys. Rev. Lett. **48**, 20 (1982).

[300] S. Bubin, M. Stanke, D. Kędziera, and L. Adamowicz, Phys. Rev. A **76**, 022512

(2007).

[301] M. Stanke, D. Kędziera, S. Bubin, and L. Adamowicz, Phys. Rev. A **77**, 022506 (2008).

[302] E. A. Engel, N. Doss, G. J. Harris, and J. Tennyson, Mon. Not. Roy. Astron. Soc. **357**, 471 (2005).

[303] G. Frenking, W. Koch, F. Reichel, and D. Cremer, J. Am. Chem. Soc. **112**, 4240 (1990).

[304] H. Partridge, C. W. Bauschlicher, and S. R. Langhoff, J. Phys. Chem. **96**, 5350 (1992).

[305] D. J. D. Wilson, C. J. Marsden, and E. I. von Nagy-Felsobuki, Phys. Chem. Chem. Phys. **5**, 252 (2003).

[306] C. W. Bauschlicher and S. R. Langhoff, Int. Rev. Phys. Chem. **9**, 149 (1990).

[307] H. Partridge and C. W. Bauschlicher, J. Phys. Chem. **98**, 2301 (1994).

[308] J. Niu, B. K. Rao, P. Jena, and M. Manninen, Phys. Rev. B **51**, 4475 (1995).

[309] P. Pyykkö, J. Am. Chem. Soc. **117**, 2067 (1995).

[310] D. J. D. Wilson, C. J. Marsden, and E. I. von Nagy-Felsobuki, J. Phys. Chem. A **106**, 7348 (2002).

[311] M. Hotakka, T. Kindstedt, P. Pyykkö, and B. Roos, Mol. Phys. **52**, 223 (1984).

[312] J. Klos, M. F. Rode, J. E. Rode, G. Chalasinski, and M. M. Szczesniak, Eur. Phys. J. D **31**, 429 (2004).

[313] S. Petrie, Chem. Phys. Lett. **399**, 475 (2004).

[314] D. J. D. Wilson, C. J. Marsden, and E. I. von Nagy-Felsobuki, Chem. Phys. **284**, 555 (2002).

[315] R. Wesendrup, M. Pernpointner, and P. Schwerdtfeger, Phys. Rev. A **60**, R3347 (1999).

[316] M. Dolg, H. Stoll, and H. Preuss, J. Mol. Struct. (Theochem) **251**, 327 (1991).

[317] E. W. Müller and T. T. Tsong, Prog. Surf. Sci. **4**, 1 (1974).

[318] C. DiPaola, F. Sebastianelli, E. Bodo, B. Baccarelli, F. Gianturco, and M. Yurtsever, J. Chem. Theor. Comp. **1**, 1045 (2005).

[319] A. Nakayama and K. Yamashita, J. Chem. Phys. **112**, 10966 (2000).

[320] D. E. Galli, M. Buzzacchi, and L. Reatto, J. Chem. Phys. **115**, 10239 (2001).

[321] F. Marinetti, E. Coccia, E. Bodo, F. A. Gianturco, E. Yurtsever, M. Yurtsever, and E. Yildirim, Theor. Chim. Acta **118**, 53 (2007).

[322] F. Shindo, J. F. Babb, K. Kirby, and K. Yoshino, J. Phys. B **40**, 2841 (2007).

[323] A. A. Scheidemann, V. V. Kresin, and H. Hess, J. Chem. Phys. **107**, 2839 (1997).

[324] Y. Murano, G. Izawa, K. Yoshihara, M. Takahashi, M. Kishimoto, and S. Suzuki, Int. J. Mass Spec. Ion Phys. **41**, 179 (1976).

[325] S. Bililign, M. Gutowski, J. Simons, and W. H. Breckenridge, J. Chem. Phys. **100**, 8212 (1994).

[326] M. Krauss, P. Maldonado, and A. C. Wahl, J. Chem. Phys. **54**, 4944 (1971).

[327] A.-M. Sapse, A. Dumitra, and D. C. Jain, J. Clust. Sci. **14**, 21 (2003).

[328] L. A. Viehland, Chem. Phys. **85**, 291 (1984).

[329] I. R. Gatland, W. F. Morrison, H. W. Ellis, M. G. Thackston, E. W. McDaniel, M. H. Alexander, L. A. Viehland, and E. A. Mason, J. Chem. Phys. **66**, 5121 (1977).

[330] P. C. Hariharan and V. Staemmler, Chem. Phys. **15**, 409 (1976).

[331] L. A. Viehland, Chem. Phys. **78**, 279 (1976).

[332] P. Soldán, E. P. F. Lee, J. Lozeille, J. N. Murrell, and T. G. Wright, Chem. Phys. Lett. **343**, 429 (2001).

[333] P. E. Siska, J. Chem. Phys. **85**, 7497 (1986).

[334] M. T. Elford, I. Roeggen, and H. R. Skullerud, J. Phys. B **32**, 1873 (1999).

[335] A. I. Panin, A. N. Petrov, and Y. G. Khait, J. Mol. Struct. (THEOCHEM) **490**, 189 (1999).

[336] P. Soldán, E. P. F. Lee, and T. G. Wright, J. Chem. Soc. Farad. Trans. **94**, 3307 (1998).

[337] P. Soldán, E. P. F. Lee, and T. G. Wright, Mol. Phys. **97**, 139 (1999).

[338] G. R. Ahmadi, J. Almlof, and I. Roeggen, Chem. Phys. **199**, 33 (1995).

[339] L. A. Viehland, J. Lozeille, P. Soldán, E. P. F. Lee, and T. G. Wright, J. Chem. Phys. **119**, 3729 (2003).

[340] R. Moszynski, P. E. S. Wormer, and L. A. Viehland, J. Phys. B **27**, 4933 (1994).

[341] R. Moszynski, B. Jeziorski, G. H. F. Diercksen, and L. A. Viehland, J. Chem. Phys. **101**, 4697 (1994).

[342] L. A. Viehland, J. Lozeille, P. Soldán, E. P. F. Lee, and T. G. Wright, J. Chem. Phys. **121**, 341 (2004).

[343] I. Roeggen, H. R. Skullerud, and M. T. Elford, J. Phys. B **29**, 1913 (1996).

[344] H. R. Skullerud, T. H. Lovaas, and K. Tsurugida, J. Phys. B **32**, 4509 (1999).

[345] J. K.-C. Lau, C. H. S. Wong, P. S. Ng, F. M. Siu, N. L. Ma, and C. W. Tsang, Chem. Eur. J. **9**, 3383 (2003).

[346] R. Ahlrichs, H. J. Bohm, S. Brode, K. T. Tang, and J. P. Toennies, J. Chem. Phys.

88, 6290 (1988).

[347] A. D. Koutselos, E. A. Mason, and L. A. Viehland, J. Chem. Phys. **93**, 7125 (1990).

[348] M. Hiyama, S. Nanbu, and S. Iwata, Chem. Phys. Lett. **192**, 443 (1992).

[349] W. Breckenridge, V. L. Ayles, and T. G. Wright, Chem. Phys. **333**, 77 (2007).

[350] P. Polak-Dingels, M. S. Rajan, and E. A. Gislason, J. Chem. Phys. **77**, 3983 (1982).

[351] J. M. Hughes and E. I. von Nagy-Felsobuki, Eur. Phys. J. D **6**, 185 (1999).

[352] U. E. Senff and P. G. Burton, Mol. Phys. **58**, 637 (1986).

[353] E. Bodo, E. Yurtsever, M. Yurtsever, and F. A. Gianturco, J. Chem. Phys. **124**, 074320 (2006).

[354] E. Bodo, F. A. Gianturco, E. Yurtsever, and M. Yurtsever, Mol. Phys. **103**, 3223 (2005).

[355] E. Coccia, E. Bodo, and F. A. Gianturco, Europhys. Lett. **82**, 23001 (6pp) (2008).

[356] E. Coccia, E. Bodo, F. Marinetti, F. A. Gianturco, E. Yildrim, M. Yurtsever, and E. Yurtsever, J. Chem. Phys. **126**, 124319 (2007).

[357] E. Bodo, F. A. Gianturco, R. Martinazzo, F. Paesani, and M. Raimondi, J. Chem. Phys. **113**, 11071 (2000).

[358] F. A. Gianturco, S. Kumar, S. K. Pathak, M. Raimondi, M. Sironi, J. Gerratt, and D. L. Cooper, Chem. Phys. **215**, 227 (1999).

[359] B. K. Taylor and R. J. Hinde, J. Chem. Phys. **111**, 973 (1999).

[360] B. K. Taylor and R. J. Hinde, J. Chem. Phys. **122**, 074308 (2005).

[361] B. K. Taylor, J. Chem. Phys. **121**, 7725 (2004).

[362] C. Reyle, R.-D. Scholz, M. Schultheis, A. C. Robin, and M. Irwin, Mon. Not. Roy. Astron. Soc. **373**, 705 (2006).

[363] J. Reho, U. Merker, M. R. Radcliff, K. K. Lehmann, and G. Scoles, J. Chem. Phys. **112**, 8409 (2000).

[364] Y. Ren and V. V. Kresin, Phys. Rev. A **76**, 043204 (2007).

[365] F. Stienkemeier, F. Meier, and H. O. Lutz, J. Chem. Phys. **107**, 10816 (1997).

[366] K. C. Lin, P. D. Kleiber, J. X. Wang, W. C. Stwalley, and S. R. Leone, J. Chem. Phys. **89**, 4771 (1988).

[367] M. O. Hale and S. R. Leone, J. Chem. Phys. **79**, 3352 (1983).

[368] A. J. Page, D. J. D. Wilson, and E. I. von Nagy-Felsobuki, Chem. Phys. Lett. **429**, 335 (2006).

[369] A. W. K. Leung and W. H. Breckenridge, J. Chem. Phys. **111**, 9197 (1999).

[370] E. F. Hayes and J. L. Gole, J. Chem. Phys. **55**, 5132 (1971).

[371] X. Bu and C. Zhong, Chem. Phys. Lett. **392**, 181 (2004).

[372] A. W. K. Leung, R. R. Julian, and W. H. Breckenridge, J. Chem. Phys. **111**, 4999 (1999).

[373] D. Bellert and W. Breckenridge, Chem. Rev. **102**, 1595 (2002).

[374] K. L. Burns, D. Bellert, A. W.-K. Leung, and W. H. Breckenridge, J. Chem. Phys. **114**, 7877 (2001).

[375] K. L. Burns, D. Bellert, A. W.-K. Leung, and W. H. Breckenridge, J. Chem. Phys. **114**, 2996 (2001).

[376] E. Czuchaj, M. Krosnicki, and H. Stoll, Chem. Phys. **292**, 101 (2003).

[377] E. Czuchaj, F. Rebentrost, H. Stoll, and H. Preuss, Chem. Phys. **182**, 191 (1991).

[378] X. Bu, C. Zhong, and A. F. Jalbout, Chem. Phys. Lett. **387**, 410 (2004).

[379] T. S. Monteiro, I. L. Cooper, A. S. Dickinson, and E. L. Lewis, J. Phys. B **19**, 4087 (1986).

[380] E. Czuchaj, F. Rebentrost, H. Stoll, and H. Preuss, Chem. Phys. **207**, 51 (1993).

[381] A. F. Jalbout and M. Solimannejad, J. Mol. Struct. (Theochem) **640**, 21 (2003).

[382] C. C. Lovallo and M. Klobukowski, Chem. Phys. Lett. **373**, 439 (2003).

[383] C. C. Lovallo and M. Klobukowski, J. Chem. Phys. **120**, 246 (2004).

[384] R.-H. Xie and J. Gong, Phys. Rev. Lett. **95**, 263202 (2005).

[385] J.-Z. Tang, M. Kimura, and I. Shimamura, Chem. Phys. Lett. **256**, 327 (2005).

[386] E. Czuchaj, F. Rebentrost, H. Stoll, and H. Preuss, Chem. Phys. **196**, 37 (1995).

[387] E. Czuchaj, F. Rebentrost, H. Stoll, and H. Preuss, Chem. Phys. **177**, 107 (1993).

[388] Y. Fukuyama, Y. Moriwaki, and Y. Matsuo, Phys. Rev. A **75**, 032725 (2007).

[389] Y. Fukuyama, Y. Moriwaki, and Y. Matsuo, Phys. Rev. A **69**, 042505 (2004).

[390] S. W. Harrison, L. J. Massa, and P. Solomon, Chem. Phys. Lett. **16**, 57 (1972).

[391] P. F. Paola Antoniotti and F. Grandinetti, Int. J. Mass. Spec. **228**, 415 (2003).

[392] X. Bu and C. Zhong, J. Mol. Struct. (Theochem) **726**, 99 (2005).

[393] G. C. Groenenboom and N. Balakrishnan, J. Chem. Phys. **118**, 7380 (2003).

CHAPTER 2

Atomic and Molecular Applications of Electronic Structure Methods

2.1. Introduction

The formulation of quantum mechanics has had a dramatic impact upon the field of chemistry. As advances in the theory and implementation of quantum chemistry are made, the accuracy and efficiency with which atomic and molecular properties are calculated has increased. Concomitantly, there has been an increase in the size of molecular system amenable to theoretical modelling. Accurate prediction (*a priori*) of the properties of molecular systems containing hundreds of atoms is now possible [1]. However, the highest levels of theory are still realistically applicable only to electron-sparse molecules.

There are several motivations for the theoretical investigation of alkali and alkaline-earth metal dihydrides. For instance, the ubiquity of atomic and molecular hydrogen throughout the interstellar media of the early (and present) universe would suggest that primordial chemistry, and hence the early chemical evolution of the universe, may have been dominated by the formation/decomposition processes of simple metal hydrides [2–4]. As such, there has been extensive theoretical investigation into the nature of LiH_2 [5–13] and BeH_2 [14–17].

The heavier alkali and alkaline-earth metal dihydrides are of interest due to the natures of the respective PESs. NaH_2 is of particular theoretical interest, since it exhibits an archetypal example of an electronically non-adiabatic process

(that is, one in which the electronic state changes non-radiatively). For example, the exciplex (^2P)Na-H_2 undergoes electronic-to-rotational-and-vibrational energy transfer according to [18],

$$\begin{aligned}(^2P)\mathrm{Na} + (^1\Sigma_g^+)\mathrm{H_2}(v, J) &\rightarrow (^2S_{1/2})\mathrm{Na} + (^1\Sigma_g^+)\mathrm{H_2}(v', J') \\ &\rightarrow (^1\Sigma^+)\mathrm{NaH}(v'', J'') + (^2S_{1/2})\mathrm{H}\end{aligned}$$

This reaction is prototypical of many reactions of a metal with a covalent molecule, and therefore has been studied extensively [8, 19–27]. Similarly, the dynamics of the formation of MgH_2 (*viz.* by the insertion of Mg into the H_2 subunit) are also dominated by non-adiabatic transitions between low-lying singlet states [28]. The reaction,

$$(^1S_0)\mathrm{Mg} + (^1\Sigma_g^+)\mathrm{H_2} \rightarrow (^1\Sigma_g^+)\mathrm{MgH_2}$$

is also endoergic, since theoretical calculations [29, 30] indicate that $(^1\Sigma_g^+)MgH_2$ lies energetically above the asymptotic limit of $(^1S_0)$Mg + $(^1\Sigma_g^+)H_2$. These facts have spawned numerous investigations into the ground state of MgH_2 [29, 31–37]. In addition, MgH_2 has been postulated to be a possible candidate for the bulk storage of molecular hydrogen [38].

Although bonding in the alkaline-earth metal dihydrides is ionic in nature, variation in the H-M-H bond angle is observed with increasing atomic number (with respect to M). For example, BeH_2 [14–17] and MgH_2 [28, 29, 31–34] are linear, whereas SrH_2 and BaH_2 are predicted to be bent [39]. There is uncertainty as to the equilibrium bond angle of the ground state of CaH_2 despite significant theoretical and experimental scrutiny [34, 39–45]. Although KH_2 is of interest with respect to chemical processes present in brown dwarfs [46, 47], only two theoretical investigations of KH_2 have been reported in the literature to date [13, 48].

The aim of the present Chapter is to give a cursory review of approximate MO based methods of electronic structure in the context of atomic and electron-sparse molecular systems. As such, SCF theory and correlated wave function methods including CI and CC will be discussed. The use of Gaussian type orbitals (GTOs) in electronic structure calculations will also be reviewed, with an emphasis placed upon GTO basis sets for alkali and alkaline-earth metals. Such levels of theory will be benchmarked using the ground state properties of Li, Be, Na, Mg, K and Ca. Equilibrium molecular properties of the neutral dihydrides of these elements will subsequently be investigated. Knowledge of equilibrium molecular parameters serves two purposes in the present context (*i.e.* Figure 1.1). Firstly, molecular candidates suitable for vibrational and rovibrational calculations may be assessed by considering the relative structures and stabilities of the species in question. Secondly, a knowledge of these equilibrium molecular parameters is necessary if accurate descriptions of molecular property surfaces (*i.e.* PESs and DMSs) are to be attained.

2.2. The Dirac Equation

Dirac [49–51] proposed that the time-independent quantum mechanics of a free particle are described (in atomic units) by the eigenfunction satisfying,

$$i\hbar = \hat{H} \left| \Psi \left(\mathbf{r} \right) \right\rangle \tag{2.1}$$

where $\mathbf{r}$ are a set of arbitrary position co-ordinates,

$$\hat{H} = c\alpha \cdot \mathbf{p} + \beta mc^2 \tag{2.2}$$

and α and β are the Hermitian Dirac matrices. It follows that a relativistic particle in a central field is described by the four-spinor $|\Psi\rangle \equiv |\Psi(\mathbf{r})\rangle$ such that,

$$\left(E - c\alpha \cdot \mathbf{p} - \beta mc^2 - \hat{V}(\mathbf{r})\right)|\Psi\rangle = 0 \tag{2.3}$$

for some potential operator $\hat{V}(\mathbf{r})$. Extending equation (2.3) to an n-electron atomic system requires a Hamiltonian of the form [52–55],

$$\hat{H} = \hat{h}_{\mathrm{D}}(\mathbf{r}_i) + \sum_{i<j}^{n} \hat{g}_{ij} \tag{2.4}$$

where $\hat{h}_{\mathrm{D}}(\mathbf{r}_i)$ is the one electron Dirac operator,

$$\hat{h}_{\mathrm{D}}(\mathbf{r}_i) = \sum_{i}^{n} \left(c\alpha_i \cdot \mathbf{p}_i + (\beta - 1)c^2 - V_i\right) \tag{2.5}$$

and $\hat{g}_{ij}$ is the two electron operator [56],

$$\hat{g}_{ij} = \frac{1}{|\mathbf{r}_i - \mathbf{r}_j|} \tag{2.6}$$

The latter appears in the Coulombic and exchage operators. The Breit-Pauli (BP) Hamiltonian truncates the n-electron relativistic Hamiltonian to first-order in $\left(\frac{v}{c}\right)^2$. This Hamiltonian is of form,

$$\hat{H}_{\mathrm{BP}} = \hat{H}_0 + \hat{H}_{\mathrm{Darw}} + \hat{H}_{\mathrm{MV}} + \hat{H}_{\mathrm{SO}} \tag{2.7}$$

Here, $\hat{H}_0$ is the non-relativistic Hamiltonian, $\hat{H}_{\mathrm{Darw}}$ is the one- and two- electron Darwin correction, $\hat{H}_{\mathrm{MV}}$ is the relativistic mass-velocity correction, $\hat{H}_{\mathrm{SO}}$ is the spin-orbit coupling correction, $\mathbf{S}_i$, $\mathbf{r}_i$ and $\mathbf{p}_i$ are the instantaneous spin, position and

momentum vectors of electron i, respectively, $\mathbf{r}_{ij}$ is the instantaneous distance between electrons i and j and Z is the nuclear charge.

Several Hamiltonians have simplified $\hat{H}_{\mathrm{BP}}$ by the exclusion of various terms. For instance, the Hamiltonian of Zeigler, Snijders and Baerends [57] assumes the relativistic nature of the electron to be dominated by the $\hat{H}_{\mathrm{MV}}$, $\hat{H}_{\mathrm{Darw}}$ and $\hat{H}_{\mathrm{SO}}$ in equation (2.7). Similarly, the Hamiltonian employed by Cowan and Griffin (CG) [58] consists of these three terms, however the spin-orbit coupling is neglected in the SCF wave function. An alternative approach was employed by Douglas, Kroll and Hess (DK) [59, 60]. The DK Hamiltonian employs a 'no-pairs' approach, using external projection operators corresponding to a particle in the field of a nucleus. The BP, CG and DK Hamiltonians can be readily extended to molecular systems, for which $\hat{H}_{\mathrm{MV}}$, $\hat{H}_{\mathrm{Darw}}$ and $\hat{H}_{\mathrm{SO}}$ are incorporated as a truncated perturbation to the total energy (*i.e.* DKn). Collins *et al.* [61] have shown that the DK Hamiltonian is a reliable alternative to the Dirac HF (DHF) method for molecular systems containing heavy atoms, provided that spin-orbit coupling is small.

2.3. The Time-Independent Schrödinger Equation

Equation (2.1) collapses to the time-independent non-relativistic Schrödinger equation [62–65] in the limit $c \to \infty$,

$$\hat{H}_0 \left|\Psi\right\rangle = E \left|\Psi\right\rangle \tag{2.8}$$

where, in the n-electron atomic case,

$$\hat{H}_0 = -\frac{1}{2}\sum_{i=1}^{n} \nabla_i^2 - \sum_{i=1}^{n} \frac{Z}{\mathbf{r}_i} + \sum_{i=1}^{n}\sum_{i<j} \hat{g}_{ij} \tag{2.9}$$

Similarly, for an N-nuclei n-electron molecular system,

$$\hat{H}_0 = -\sum_{I=1}^{N} \frac{1}{M_I}\nabla_I^2 \; + \; \sum_{i=1}^{n} \hat{h}_i + \sum_{i=1}^{n}\sum_{i<j} \hat{g}_{ij} + \sum_{I=1}^{N}\sum_{I<J} \frac{Z_I Z_J}{|\mathbf{R}_I - \mathbf{R}_J|} \tag{2.10}$$

where $\hat{h}_i$ is the one-electron operator,

$$\hat{h}_i = -\frac{1}{2}\nabla_i^2 + \sum_{I=1}^{N} \frac{Z_I}{|\mathbf{R}_I - \mathbf{r}_i|} \tag{2.11}$$

The first terms of equations (2.10) and (2.11) are the nuclear and electronic kinetic energy operators respectively, and the fourth term of equation (2.10) is the potential energy operator corresponding to the repulsion between nuclei I and J. The mass and instantaneous position vectors of nucleus I are denoted by M_I and $\mathbf{R}_I$, respectively.

2.4. The Born-Oppenheimer Approximation

By employing the BO approximation equation (2.10) may be recast so that,

$$\hat{H}_0 \left|\Psi\right\rangle = \left(\hat{H}_{\text{nuc}} + \hat{H}_{\text{elec}}\right) \left|\Psi\right\rangle = E \left|\Psi\right\rangle \tag{2.12}$$

Thus it is possible to consider the motion of the electrons in the field of stationary nuclei. The electronic energy is then parametrically dependent on a particular nuclear geometry. In equation (2.12),

$$\hat{H}_{\text{nuc}} = -\sum_{I=1}^{N} \frac{1}{M_I}\nabla_I^2 + \sum_{I=1}^{N}\sum_{I<J} \frac{Z_I Z_J}{|\mathbf{R}_I - \mathbf{R}_{J,}|} \tag{2.13}$$

and,

$$\hat{H}_{\text{elec}} = \sum_{i=1}^{n} \hat{h}_i + \sum_{i=1}^{n} \sum_{i<j} \hat{g}_{ij} + \hat{V}_{\text{nuc}} \tag{2.14}$$

where $\hat{V}_{\text{nuc}}$ is the potential operator defined at a particular molecular geometry.

The assumption that the nuclei exhibit only small amplitudes of vibration is implicit within the BO formulation [66]. However, Born [67, 68] provided a more general formulation applicable to any nuclear geometry, making no assumptions with respect to the amplitude of nuclear motions. This allows the nuclear and electronic motions to be rigorously decoupled.

2.5. Self Consistent Field Theory

All MO approximations to the solutions of equation (2.12) are based on the SCF method [69–71]. The SCF wave function for an N-nuclei n-electron molecular system (with all MOs doubly occupied) is a single Slater determinant (SD),

$$|\Phi_{\text{SD}}\rangle = \frac{1}{\sqrt{N!}} \sum_{P} (-1)^p \hat{P} \prod_{i,j}^{n} \gamma_i(j) \tag{2.15}$$

Here $\hat{P}$ is a permutation operator and $\{\phi_i\}$ and $\{\alpha, \beta\}$ are orthonormal such that $\gamma_i(j) = \phi_i(j)\alpha_i(j)$ or $\gamma_i(j) = \phi_i(j)\beta_i(j)$ for spin functions α and β. The explicit form of the spatial component of $\gamma_i(j)$, $\phi_i(j)$, will be discussed in subsequent sections (*vide infra*). By construction $|\Phi_{\text{SD}}\rangle$ necessarily satisfies the Pauli exclusion principle. Self consistent field theory assumes that $|\Psi\rangle \equiv |\Phi_{\text{SD}}\rangle$ and so,

$$E_{\text{SCF}} = \left\langle \Phi_{\text{SD}} \left| \hat{H}_0 \right| \Phi_{\text{SD}} \right\rangle \tag{2.16}$$

The variational diagonalisation of the electronic Hamiltonian in the atomic orbital (AO) basis yields the spectrum of SCF energies. In the case of closed-shell atomic

and molecular systems, this is achieved by solving the Roothaan-Hall equations [72, 73],

$$\mathbf{FC} = \mathbf{SC}\epsilon \tag{2.17}$$

where **F**, **C** and **S** are, respectively, the Fock, atomic orbital coefficient and one-electron overlap integral matrices and ϵ are the SCF energies. The latter are the expectation values of the canonical SCF orbitals, $\phi_i^{'}$, in the AO basis. Spin-restricted HF (RHF) MOs obtained by the solution of equation (2.17) are eigenfunctions of $\langle S^2 \rangle$ by construction. This is not the case for the spin-unrestricted HF (UHF) open-shell formulation due to Pople and Nesbet [71], in which different spatial orbitals are assigned to electrons with different spins. The use of two distinct sets of spatial orbitals in this manner leads to lower SCF energies, and so the UHF wave function is superior to the RHF wave function in this respect. However, the restrictions placed on $|\Phi_{\mathrm{SD}}\rangle$ with respect to spin and spatial symmetries observed in RHF theory are not present in UHF theory. The value of $\langle S^2 \rangle$ in the UHF MO basis may therefore become prohibitively large, a phenomenon known as spin contamination.

There are several advantages obtained in the use of the HF method for the calculation of atomic and molecular properties. For example, the HF method is a conceptually simple and size extensive variational method known to yield total electronic energies that are in error by less than 1%. In addition, important physical molecular properties, such as equilibrium bond lengths, dipole moments, electric polarisabilities, force constants and electronic excitation energies are generally reproduced (with respect to experiment) to within 5-10% using the HF method [74]. SCF orbitals are also suitable zero-order wave functions for both variational and perturbative correlated methods [75].

Nevertheless, there are unattractive features of SCF based electronic wave functions. For example, SCF wave functions fail to accurately predict properties of

systems possessing substantial electron correlation since, by construction, electron correlation is neglected in $|\Phi_{\mathrm{SD}}\rangle$. Similarly, because SCF theory is a single-reference method, it is often inadequate when applied to molecular dissociation (for example H_2 [76]) and systems possessing strong multi-configurational character (for example O_3 [77]).

The latter shortcoming of SCF theory is alleviated by taking into account different arrangements of electrons in the initial description of the electronic wave function. This equates to the use of multiple Slater determinants as a starting point in the solution of the HF equations. For such a set of Slater determinants $\{|\Phi_{\mathrm{SD}}\rangle_i\}$, the multi-reference SCF (MCSCF) wave function $|\Psi_{\mathrm{MCSCF}}\rangle$ is optimised using the orbital rotation operator $e^{-\kappa}$ thus,

$$|\Psi_{\mathrm{MCSCF}}\rangle = e^{-\kappa} \sum_i A_i \, |\Phi_{\mathrm{SD}}\rangle_i \tag{2.18}$$

In the optimisation of $|\Psi_{\mathrm{MCSCF}}\rangle$, both the CI coefficients A_i and $|\Phi_{\mathrm{SD}}\rangle_i$ are optimised with respect to the parameters of $e^{-\kappa}$ [74].

An inherent difficulty in the optimisation of MCSCF wave functions is an appropriate choice of $\{|\Phi_{\mathrm{SD}}\rangle_i\}$; that is, the active space. Ideally, the active space should represent the most important chemical and physical aspects of the system in question [78]. The CASSCF method [76, 79] considers all possible electronic excitations over the chosen set of active determinants. The restricted active space SCF method [80–82] further partitions this set into several subsets, each of which is individually optimised.

The optimisation of CASSCF wave functions is demanding for even a limited number of active determinants. Knowles *et al.* [83–85] developed a CASSCF solution algorithm quadratically convergent in both A_i and $\{|\Phi_{\mathrm{SD}}\rangle_i\}$. MCSCF, CASSCF and

restricted active space SCF routines are present in many available *ab initio* quantum chemistry codes [86–91].

2.6. Electron Correlation Methods

Optimised SCF orbitals correspond to the most accurate atomic and molecular electronic energies and wave functions for a given single Slater determinant, disregarding the effects of electron correlation. An analogous statement is true with respect to an optimised MCSCF wave function and the corresponding set $\{|\Phi_{\mathrm{SD}}\rangle_i\}$. While the effects of correlation are included implicitly in a MCSCF wave function (in that several electronic configurations are included in the optimisation of $|\Psi_{\mathrm{MCSCF}}\rangle$), neither SCF nor MCSCF provide an explicit description of electron correlation. The correlation energy for a particular one-electron basis set is defined as,

$$E_{\mathrm{CORR}} = E - E_{\mathrm{SCF}} \tag{2.19}$$

Post SCF electronic structure methods attempt to recover E_{CORR}, and generally use either a single- or multi-reference SCF wave function as a starting point (although the latter is not necessary). Although there are a number of *ab initio* correlated methods, the present discussion will be limited to the CI and CC methods.

2.6.1. The Configuration Interaction Method

The CI wave function $|\Psi_{\mathrm{CI}}\rangle$ is constructed as a linear combination of Slater determinants $|\Phi_i\rangle$,

$$|\Psi_{\mathrm{CI}}\rangle = \sum_i C_i \, |\Phi_i\rangle \tag{2.20}$$

where C_i are linear coefficients. Here $|\Phi_i\rangle$ represents both SCF [92, 93] and MCSCF [94–96] wave functions. The FCI wave function includes all possible substitutions out of this reference wave function into unoccupied orbitals of order one, two, three, four and so on. As such, the FCI wave function recovers E_{CORR} in its entirety for the one-electron basis set employed. The trial FCI wave function is of the form,

$$|\Psi_{\mathrm{FCI}}\rangle = C_0 |\Phi_0\rangle + \sum_{i}^{\mathrm{occ}} \sum_{a}^{\mathrm{virt}} C_i^a |\Phi_i^a\rangle + \sum_{i<j}^{\mathrm{occ}} \sum_{a<b}^{\mathrm{virt}} C_{ij}^{ab} \left|\Phi_{ij}^{ab}\right\rangle + \sum_{i<j<k}^{\mathrm{occ}} \sum_{a<b<c}^{\mathrm{virt}} C_{ijk}^{abc} \left|\Phi_{ijk}^{abc}\right\rangle + \ldots \tag{2.21}$$

where $|\Phi_0\rangle$ is optimised SCF/MCSCF reference wave function. The determinantal coefficients of equation (2.21) are variationally optimised by minimising the expectation value of the electronic energy.

The number of determinants to be evaluated in a FCI calculation using n_i electrons of spin i with m basis functions is,

$$N = \binom{m}{n_\alpha}\binom{m}{n_\beta} \tag{2.22}$$

It is immediate that for all but the smallest systems with few basis functions that a FCI wave function is impractical. Several methods that circumvent this problem have been developed recently, such as the intrinsic scaling method [97–101] (which estimates the correlation energy using an extrapolation scheme) and the sparse FCI method [102] (which utilises the sparse nature of the FCI vectors in the determinantal basis to reduce computational demands). A more common approach is to employ truncated CI methods, in which the excitations from $|\Phi_0\rangle$ are restricted to a certain order. For instance, the singly and doubly excited CI wave function (CISD)

is of form,

$$|\Psi_{\mathrm{CISD}}\rangle = C_0\,|\Phi_0\rangle + \sum_{i}^{\mathrm{occ}}\sum_{a}^{\mathrm{virt}} C_i^a\,|\Phi_i^a\rangle + \sum_{i<j}^{\mathrm{occ}}\sum_{a<b}^{\mathrm{virt}} C_{ij}^{ab}\,\left|\Phi_{ij}^{ab}\right\rangle \tag{2.23}$$

The computational expense of the truncated single-reference CI methods scales as n^{2k+2}, where k is the highest order of excitation in the truncation. Hence single-reference CISD, CISD with triple excitations (CISDT) and CISDT with quadruple excitations (CISDTQ) scale as n^6, n^8 and n^{10} respectively. The optimisation of MRCI wave functions is a substantially larger problem in dimension, for which various contraction schemes have been developed [103, 104]. FCI routines are included in several quantum chemistry codes [86, 88], as are routines allowing arbitrary CI excitation from single-reference reference wave functions [89, 105].

Several attempts to correct the lack of size-extensivity of truncated CI wave functions have been made. One commonly used correction is that due to Langhoff and Davidson [106], which is defined as,

$$E_{\mathrm{Dav}} = (1 - C_0^2)E_{\mathrm{CORR}}^{\mathrm{CISD}} \tag{2.24}$$

where $E_{\mathrm{CORR}}^{\mathrm{CISD}}$ is the correlation energy calculated using CISD. E_{Dav} can also be interpreted as the correction for the lack of quadruple or higher excitations in the CI truncation (*i.e.* CISD+Q) [74].

2.6.2. The Coupled-Cluster Method

The CC wave function $|\Psi_{\mathrm{CC}}\rangle$ is a non-linear exponential parameterisation of the HF reference wave function [107–109],

$$|\Psi_{\mathrm{CC}}\rangle = e^{\hat{T}} |\Phi_0\rangle \tag{2.25}$$

where the non-Hermitian cluster operator $\hat{T}$,

$$\hat{T} = \hat{T}_1 + \hat{T}_2 + \ldots \tag{2.26}$$

consists of the first, second and third excitation operators. As such, CC wave functions are size-extensive but non-variational. Truncation of equation (2.26) yields various single-reference truncated CC methods the nomenclature of which follows that of CI (*i.e.* CCS, CCSD, CCSDT, CCSDTQ, ...,). The computational expense of these truncated CC methods scales as does the corresponding truncated CI method. However, any truncated CC wave function is both more efficient and compact than its CI counterpart. For instance, the CCSD wave function takes the form [74],

$$\begin{aligned} |\Psi_{\mathrm{CCSD}}\rangle \;=\; & |\Phi_0\rangle + \hat{T}_1 |\Phi_0\rangle + \left(\hat{T}_2 + \frac{1}{2}\hat{T}_1^2\right) |\Phi_0\rangle \\ & + \left(\hat{T}_1\hat{T}_2 + \frac{1}{6}\hat{T}_1^3\right) |\Phi_0\rangle + \left(\frac{1}{2}\hat{T}_2^2 + \frac{1}{2}\hat{T}_2\hat{T}_1^2 + \frac{1}{24}\hat{T}_1^4\right) |\Phi_0\rangle + \ldots \end{aligned} \tag{2.27}$$

Multi-reference CC wave functions are generally considered in terms of three broad categories, *viz.* valence-universal, state-universal and state-specific. These methods have recently been extended to arbitrary orders of excitation [110–112], but will not

be pursued further in the present work.

The accurate calculation of molecular properties using a CC wave function generally requires the inclusion of (at least) triples excitation from $|\Phi_0\rangle$, which is feasible only for relatively small systems. For this reason, a number of methods which approximate the triples contribution to the wave function have been developed [113, 114]. The most popular of these is the CCSD(T) method [113], in which the connected triples are incorporated as a perturbation to the CCSD wave function. The CCSD(T) method scales as n^7, and can approximate up to 90% of the full triples correction to the CCSD wave function [74]. In addition, molecular properties such as equilibrium structures, atomisation energies and conformational barrier energies calculated using CCSD(T) and CCSDT have been shown to be in excellent agreement for a range of molecules [74]. There are many implementations of single-reference CCSD and CCSD(T) available [86–90, 115]. Codes able of calculating arbitrary CC excitations for single-reference wave functions have also been developed [89, 105].

2.7. One-Electron Basis Sets

Electronic structure methods have been discussed in Sections 2.5 and 2.6 in the context of AOs and MOs for atomic and molecular systems, respectively. The AOs are typically constructed from GTOs centred on the nuclei [116],

$$G_{ijk}\left(\mathbf{r}_A, \alpha\right) = x^i y^j z^k e^{-\alpha \mathbf{r}_A^2} \tag{2.28}$$

where i, j and k are non-negative integers, α is a positive real number and $\mathbf{r}_A$ is the position of the electron relative to the nucleus A. The AOs constructed using a single GTO (primitive AOs) fail to model the hydrogenic orbital accurately for

both small and large values of r. However, this problem is overcome by employing a linear combination of several GTOs (a contracted GTO (CGTO)) [117],

$$\chi_n^{\mathrm{CGTO}} = \sum_j d_{nj} G\left(\mathbf{r}_A, \alpha\right) \tag{2.29}$$

This contraction can be general (in which all primitive GTOs of a given angular momentum on an atomic center are allowed to contribute to all CGTOs of that angular momentum) or segmented (in which each primitive GTO contributes to a single CGTO).

AOs may also be constructed using Slater type orbitals (STOs) as opposed to GTOs. A STO is defined as,

$$S_{ijk}\left(\mathbf{r}_A, \alpha\right) = x^i y^j z^k e^{-\alpha \mathbf{r}_A} \tag{2.30}$$

and therefore explicitly resembles the hydrogenic wave function. The STOs provide a more accurate and compact description of an AO than do GTOs. However, the calculation of the various integrals required for atomic and molecular properties is significantly more efficient when using CGTOs as opposed to STOs [118]. This is therefore the procedure employed by the majority of quantum chemistry codes [86–91]. Recent developments in STOs have however made STOs a genuine alternative to GTOs in atomic and molecular calculations [119–121]. Since STOs are not used in the present work they will not be discussed further.

A MO is constructed as a linear combination of a set of AOs $\{\chi_\nu\}$,

$$\phi_i\left(\mathbf{r}\right) = \sum_\nu c_{i\nu} \chi_\nu \tag{2.31}$$

Ideally, an AO basis set would be infinite (and hence complete) in which case the

optimised MOs would define the HF limit. The quality of an *ab initio* calculation is largely determined by the quality of the finite basis set, and therefore, by the quality of the one-electron basis functions used. Basis sets should satisfy three criteria, *viz.* that a basis set should provide an adequate description of electron correlation, systematically cover all of co-ordinate space and be as compact as possible [122].

One-electron basis sets are organised in terms of the number of functions prescribed to each AO on the neutral atom. For instance, the single-ζ (minimal) basis set is one which describes each AO using a single function, a double-ζ (DZ) basis set is one which describes each AO using two functions, and so on. The radial flexibility of a basis set can be increased by increasing the number of functions employed. Similarly, the angular flexibility of a basis set can be increased through the addition of functions of higher angular momentum (polarisation functions). Even tempered basis sets are constructed systematically through utilising an approximately constant ratio between orbital exponents of orbitals with the same angular momentum [123, 124]. Well tempered basis sets are constructed in the same way, with the exception that the valence orbitals are preferentially covered [125].

There is myriad basis sets concerning the alkali and alkaline-earth elements available in the literature, such as the split-valence basis sets of Pople and co-workers [126–129]. Also, the correlation-consistent (aug)-cc-p(C)VXZ ($X = D, T, Q, 5$) basis sets for Li, Be, Na, Mg and Ca have been developed by several workers [130–133], based on the earlier work of Dunning *et al.* [134–137]. Similar core-valence correlation basis sets (CVXZ, $X = D, T, Q, 5$) have been developed for all alkali and alkaline-earth elements by Iron *et al.* [138]. The latter family of basis sets were optimised using CI. A correlation-consistent basis set is constructed so that each correlating orbital is represented by a single primitive GTO, chosen so that the contribution to the correlation energy is maximised. All correlating orbitals with similar

contributions to the correlation energy are subsequently added together [130]. This hierarchical construction has led correlation-consistent basis sets to be amongst the most widely employed basis sets in the literature.

An alternative choice is to use atomic natural orbital (ANO) basis sets, whose construction is based around the expectation values of the one-electron density matrix for the occupied HF and virtual correlated orbitals. The atomic natural orbitals (ANOs) of Almlöf and Taylor [139, 140] have been extended to all alkali and alkaline-earth elements by Roos *et al.* [141]. The latter ANO-RCC basis sets incorporate scalar relativistic effects through the use of a DK Hamiltonian in conjunction with multi-reference correlated methods.

2.8. Application to Atomic Calculations

2.8.1. Computational Procedure

In order to ascertain the effectiveness of the various *ab initio* methods discussed in Section 2.6, a range of properties of the ground state atoms Li, Be, Na, Mg, K and Ca have been calculated. Since the bonding in several of the molecular systems under investigation in this thesis is dominated by charge-induced dipole interactions, the properties that have been considered presently are those pertinent to such dispersive forces. As such, IE_1, electronic polarisabilities (α) and energies of low-lying electronic transitions for the ground state Li, Na and K have been calculated using various correlated methods. The open-shell RHF (ROHF), spin-unrestricted CC (UCCSD(T), UCCSDT), CASSCF, IC-MRCI, IC-MRCI+Q methods will be considered in conjunction with the ANO-RCC [141] contracted basis sets. Explicitly, these basis sets are defined as $[8s7p4d2f]$ (Li), $[9s8p5d2f]$ (Be), $[9s8p5d4f]$ (Na), $[9s8p6d2f]$ (Mg), $[10s9p5d3f]$ (K) and $[10s9p6d2f]$ (Ca) contrac-

tions. The atomic properties of Li and Be have also been investigated using FCI, in conjunction with the CVXZ [138] and ANO-RCC [141] basis sets. All basis sets employed in this thesis are included in Appendix A. For an $(1, 2, \ldots, n)s^{1,2}(2, \ldots, k)p^6$ electronic configuration, multi-reference methods employed an active space consisting of $(n+1)s$ and $(k+1)p$ functions. The impact of relativistic effects on these atomic properties will also be investigated. Where possible, comparison has been made between the results of this work and prior theoretical and experimental data.

2.8.2. FCI Calculations of Li and Be

The convergence of various atomic properties of Li and Be as a function of basis set has been considered using all-electron FCI. The conclusions reached from this comparison will be extrapolated to all other alkali and alkaline-earth metals considered here. Table 2.1 details the comparison between the values of IE_1, α and the $^2P_J \leftarrow {}^2S_{1/2}$ and $^3P_J \leftarrow {}^1S_0$ transition frequencies for Li and Be, respectively. The basis sets considered here include the three largest ANO-RCC contractions [141] and the CVXZ basis sets (X = T, Q, 5) [138]. The latter are defined as $[6s5p3d1f]$ (X = T), $[8s7p5d3f1g]$ (X = Q) and $[10s9p7d5f3g1h]$ (X = 5) contractions. Also given in Table 2.1 are FCI atomic properties of Be calculated using the aug-CVQZ basis set [142], which consists of the $[8s7p5d3f1g]$ basis set augmented with diffuse $(1s1p1d1f1g)$ functions added in an even tempered manner.

With respect to Li, Table 2.1 illustrates that the ANO-RCC basis sets are more efficient and stable than are the CVXZ basis sets, for X=T, Q, 5. For example, the addition of $(1s1p1d1f)$ functions to the $[6s5p2d]$ contraction increases the IE_1 value by 0.0035 eV. A further addition of diffuse $(1s1p1d1f1g)$ functions increases the IE_1 value by another 0.0006 eV. The basis set convergence for the CVXZ basis sets is less noticeable. For example, the difference between IE_1 for X = T and X = Q

Table 2.1 Differences between FCI and experimental[a] atomic properties for Li and Be.

Basis Set	IE$_1$ (/eV)	Li α ($/a_0^3$)	$^2P_J \leftarrow {}^2S_{1/2}$ (/eV)	Time[b] (/(h:m:s))
$[6s5p2d]$[c]	−0.0080	−0.1	−0.0041	00:00:00.47
$[7s6p3d1f]$[c]	−0.0045	−0.1	−0.0012	00:00:02.38
$[8s7p4d2f1g]$[c]	−0.0039	0.3	−0.0012	00:00:27.10
CVTZ[d]	−0.0128	−2.1	−0.0027	00:00:01.37
CVQZ[d]	−0.0031	−1.3	−0.0009	00:00:58.99
CV5Z[d]	0.0010	−1.1	−0.0003	00:17:29.65
Basis Set	IE$_1$ (/eV)	Be α ($/a_0^3$)	$^3P_J \leftarrow {}^1S_0$ (/eV)	Time[b] (/(h:m:s))
$[7s6p3d]$[c]	−0.0138	−0.3	0.0009	00:00:37.79
$[8s7p4d1f]$[c]	−0.0093	−0.1	0.0004	00:05:20.00
$[9s8p5d2f1g]$[c]	−0.0079	−0.1	0.0009	00:29:47.88
CVTZ[d]	−0.0196	−1.0	0.0221	00:00:25.44
CVQZ[d]	−0.0057	−1.0	0.0110	00:37:43.26
aug-CVQZ[e]	−0.0056	0.0	−0.0004	03:09:57.96
CV5Z[d]	−0.0027	−0.5	0.0048	14:37:14.54

[a]Experimental data: IE$_1$ see reference [143]; α see reference [144]; transitions see reference [143].
[b]CPU time for a single energy calculation, performed on an Intel 64 bit 1.6GHz Core 2 duo CPU, 4GB RAM, 500GB disk space. All data calculated using MOLPRO [86].
[c]ANO-RCC basis set; see reference [141].
[d]See reference [138].
[e]See reference [4].

is 0.0097 eV, whereas the difference between IE$_1$ for X =Q and $X = 5$ is 0.0041 eV, with the latter value being the most accurate with respect to experiment. Similar trends with respect to the calculated values of the $^3P_J \leftarrow {}^2S_{1/2}$ transition frequency are observed. For example, data in Table 2.1 indicate that for $X = 5$, convergence has not yet been achieved. Due to the relative size of the CV5Z computation (largely due to the presence of the contracted $3g$ and $1h$ functions), further augmentation of the CV5Z contraction would be computationally prohibitive. Conversely, $^3P_J \leftarrow {}^2S_{1/2}$ transition frequency values calculated using the $[7s6p3d1f]$ and $[8s7p4d2f1g]$ transition frequencies are identical, and differ from the $[6s5p2d]$ value by 0.0029 eV. With respect to α, all three ANO-RCC basis sets provide more accurate values, with

respect to experiment, than the CVTZ, CVQZ and CV5Z basis sets for Li.

The CVXZ basis sets generally provide a more accurate value of IE_1 than do the ANO-RCC basis sets for Be. For example, from Table 2.1 it is evident that the IE_1 values calculated using the CVQZ, aug-CVQZ and CV5Z basis sets are all in closer agreement with experiment than that calculated using the [9s8p5d2f1g] ANO-RCC basis set. Nevertheless, the difference between the [8s7p4d1f] and [9s8p5d2f1g] ANO-RCC basis sets is only 0.0014 eV. Conversely, the α values for Be calculated using the ANO-RCC basis sets are superior to those calculated using the CVXZ basis sets. The single exception is the aug-CVQZ basis set, which gives an α value in exact agreement with experiment. This is attributed to the presence of the added diffuse (1s1p1d1f1g) functions. The disparate computation times between the [9s8p5d2f1g] ANO-RCC and aug-CVQZ basis sets is also illustrated in Table 2.1. The [7s6p3d], [8s7p4d1f] and [9s8p5d2f1g] ANO-RCC contractions for Be yield $^3P_J \leftarrow {}^1S_0$ transition frequencies converged to 0.0005 eV. No such convergence is observed with respect to the CVTZ, CVQZ and CV5Z contractions.

2.8.3. Relativistic Energy Corrections of Li, Be, Na, Mg, K and Ca

The inclusion of relativistic effects (not including spin-orbit effects) for alkali and alkaline-earth metals is anticipated to be significant, particularly for those in the second and third rows. Relativistic effects have been investigated for Li, Be, Na, Mg, K and Ca using both the CG and DK schemes. In particular, the mass-velocity and Darwin correction terms, as will as ROHF(CG) ROHF(DKn) (n = 2, 4 and 6) corrected energies have been calculated. The investigation of relativistic effects on atomic energies has been limited to the ROHF level, since Harrison [145] has shown that scalar relativistic effects are largely independent of the *ab initio* method employed. The use of ROHF here also facilitates comparison with numerical DHF

results [146]. These data are presented in Table 2.2.

The mass-velocity and Darwin correction terms for Li, Be, Na, Mg, K and Ca increase in magnitude with increasing atomic number as anticipated. In particular, the presence of a fully-occupied $2p$ shell creates a noticeable difference between 1st and 2nd row mass-velocity correction terms. For example, the mass-velocity correction for Na is two orders of magnitude greater than that for Be. This difference between the 2nd and 3rd row elements is smaller in a relative sense.

The CG corrections to the non-relativistic energy are perturbative and are therefore not upper-bounds to the DHF energy. This is illustrated by the ROHF(CG) energies for Na, Mg, K and Ca, for which the ROHF(CG) energy is lower than the corresponding DHF energies. The differences between the ROHF(CG) and DHF energies for K and Ca are very pronounced, the former values being *ca.* 31 and

Table 2.2 Relativistic ROHF energy corrections (/E_h) for Li, Be, Na, Mg, K and Ca.

	Li	Be	Na
ROHF[a]	-7.43268712	-14.5728580	-161.822586
Mass-velocity[b]	-0.00419850	-0.0149795	-1.317747
Darwin[b]	0.00346026	0.0120053	0.874815
ROHF(CG)[b]	-7.43342536	-14.5758321	-162.265519
ROHF(DK2)	-7.43338399	-14.5755048	-162.067248
ROHF(DK4)	-7.43338401	-14.5755051	-162.067457
ROHF(DK6)	-7.43338401	-14.5755051	-162.067457
DHF[c]	-7.43353	-14.57591	-162.07777
	Mg	K	Ca
ROHF[a]	-199.555777	-598.390534	-675.757213
Mass-velocity[b]	-2.002654	-46.135736	-60.768194
Darwin[b]	1.282932	11.862628	14.989167
ROHF(CG)[b]	-200.275499	-632.663642	-721.536240
ROHF(DK2)	-199.920722	-601.457945	-679.628294
ROHF(DK4)	-199.921080	-601.464058	-679.636510
ROHF(DK6)	-199.921081	-601.464076	-679.636537
DHF[c]	-199.93488	-601.52556	-679.70984

[a]Non-relativistic value. All data calculated in conjunction with the largest ANO-RCC basis set [141] for each metal using Molpro [86].

[b]Calculated using the CG scheme; see reference [58].

[c]Numerical value; see reference [146].

42 E_h lower than the latter, respectively. This trend is anticipated however, due to the inclusion of DK relativistic effects in the construction of the ANO-RCC basis sets.

For Li and Be, convergence with respect to the ROHF(DKn) energies is obtained essentially at $n = 2$, since the difference between ROHF(DK2) and ROHF(DK6) is of the order of 1 μE_h. For Na and Mg, the order of truncation must be increased to $n = 4$ in order to achieve convergence in the ROHF(DKn) energies. The ROHF(DK2), ROHF(DK4) and ROHF(DK6) energies for Na and Mg are converged to within *ca.* 0.1 and 1 mE_h, respectively, whereas for K and Ca these methods are converged to within *ca.* 18 and 27 μE_h, respectively. Discussion of the effects of relativistic corrections with respect to atomic ionisation energies, dipole polarisabilities and electronic transitions is included in following sections (*vide infra*).

2.8.4. Ground State Properties of Li, Be, Na, Mg, K and Ca

Ab initio and experimental values of IE_1 and P state transition frequencies for M and M^+ (M = Li, Be, Na, Mg, K and Ca) are compared in Table 2.3. *Ab initio* values of α for Li, Be, Na, Mg, K and Ca are compared to experimental values in Table 2.4. All *ab initio* values in Tables 2.3 and 2.4 have been reported in terms of mean relative errors ($\overline{\Delta}$), mean absolute errors ($\overline{\Delta}_{\text{abs}}$), standard deviations ($\sigma$) and maximum absolute errors (Δ_{max}) from experiment. The error in a calculation is defined as $\Delta_i = (IE_1)_i^{\text{calc.}} - (IE_1)_i^{\text{expt.}}$. Complete lists of IE_1 values, transition frequencies for M and M^+, and α values for M are given in Appendix B.

Despite the appropriateness of using both ROHF and CASSCF wave functions as a zero-order approximation to the atomic wave function, data from Tables 2.3 and 2.4 suggest that these methods perform relatively poorly for all species in

Table 2.3 Comparison of calculated IE_1 and transition frequency[a] values (/eV) for M and M^+ with experiment (M=Li, Be, Na, Mg, K and Ca).

	M[c]				M^+[c]			
Method[b]	$\overline{\Delta}$	$\overline{\Delta}_{\text{abs.}}$	σ	$\Delta_{\text{max.}}$	$\overline{\Delta}$	$\overline{\Delta}_{\text{abs.}}$	σ	$\Delta_{\text{max.}}$
ROHF	1.23	2.33	10.30	35.00	1.04	4.08	16.54	56.57
ROHF(DK2)	1.23	2.34	10.29	34.97	1.04	4.07	16.54	56.56
UCCSD(T)	-0.01	-0.03	0.04	0.12	0.00	-0.07	0.07	0.21
UCCSD(T)(DK2)	-0.01	-0.02	0.03	0.10	0.00	-0.07	0.08	0.24
UCCSDT	-0.01	-0.04	0.04	0.12	0.00	-0.08	0.07	0.21
UCCSDT(DK2)	-0.01	-0.02	0.03	0.10	0.00	-0.08	0.08	0.24
CASSCF	0.46	-1.22	1.16	3.12	0.02	-0.12	1.52	2.93
CASSCCF(DK2)	-0.36	-1.79	1.31	3.87	-0.07	-0.99	1.25	2.88
IC-MRCI	-0.02	-0.08	0.07	0.20	-0.01	-0.34	0.85	3.03
IC-MRCI(DK2)	-0.02	-0.06	0.06	0.17	0.00	-0.09	0.09	0.25
IC-MRCI+Q	-0.01	-0.04	0.04	0.13	0.00	-0.07	0.07	0.21
IC-MRCI+Q(DK2)	-0.01	-0.03	0.04	0.11	0.00	-0.07	0.08	0.24

[a]Corresponding to the $^2P_J \leftarrow {}^2S_{1/2}$ (M) and $^3P_J \leftarrow {}^1S_0$ (M^+) (M = Li, Na, K), and $^3P_J \leftarrow {}^1S_0$ (M) and $^2P_J \leftarrow {}^2S_{1/2}$ (M^+) (M = Be, Mg, Ca). All transitions averaged over the J quantum number where appropriate.

[b]In conjunction with the largest ANO-RCC basis set for each metal. All data calculated using Molpro [86].

[c]See text for definition of $\overline{\Delta}$, $\overline{\Delta}_{\text{abs.}}$, σ and $\Delta_{\text{max.}}$. See reference [143] for experimental data.

question, regardless of relativistic corrections. From Table 2.3 for example, Δ_{max}, $\overline{\Delta}$ and $\overline{\Delta}_{\text{abs}}$ for ROHF are observed to be generally two orders of magnitude larger than those of all correlated methods considered. The values of these statistical metrics with reference to the CASSCF method employed are generally one order of magnitude greater than the correlated methods considered. With respect to α, the ROHF and ROHF(DK2) values of $\Delta_{\text{max.}}$ listed in Table 2.4 correspond to K values. The experimental α value of K is 292.9 a_0^3 [147], and so the errors in these calculated values are of a similar magnitude to the value itself.

The values of $\overline{\Delta}$, $\overline{\Delta}_{\text{abs}}$, σ and Δ_{max} in Tables 2.3 and 2.4 for both M and M^+ using CC indicate that little benefit is gained from the computation of the full triples term in the CC expansion. It may be inferred therefore that convergence is achieved using SD(T) excitation in the CC expansion with respect to all atomic properties in question. It is also evident from values of Δ_{max} that the inclusion of

Table 2.4 Comparison of calculated and experimental α values ($/a_0^3$) for Li, Be, Na, Mg, K and Ca.

Method[a]	$\overline{\Delta}$	$\overline{\Delta}_{\text{abs.}}$	σ	$\Delta_{\text{max.}}$
ROHF	0.16	26.18	33.93	94.07
ROHF(DK2)	0.15	24.50	31.54	87.62
UCCSD(T)	0.00	1.39	7.54	15.92
UCCSD(T)(DK2)	-0.01	-0.16	5.97	10.07
UCCSDT	0.00	1.77	7.39	16.12
UCCSDT(DK2)	0.00	0.27	5.89	10.53
CASSCF	0.08	21.24	36.12	93.07
CASSCF(DK2)	0.06	18.57	33.68	85.62
IC-MRCI	0.01	3.21	12.19	27.48
IC-MRCI(DK2)	0.00	1.63	10.25	21.37
IC-MRCI+Q	0.00	0.83	8.08	15.79
IC-MRCI+Q(DK2)	-0.01	0.27	8.65	15.79

[a]In conjunction with the largest ANO-RCC basis set [141] for each metal. See text for definition of $\overline{\Delta}$, $\overline{\Delta}_{\text{abs.}}$, σ and $\Delta_{\text{max.}}$. Comparison made using experimental (Li [148], Na [149], K [147], Ca [147]) and theoretical (Be [147], Mg [150]) values. All data calculated using MOLPRO [86].

the DK2 correction slightly improves the agreement between calculated and experimental P state transition frequencies and IE_1 values for the neutral species. The converse is true for the monocations, since the inclusion of the DK2 correction in the UCCSD(T)/UCCSDT wave function increases Δ_{max} from 0.21 to 0.24 eV. The effects of scalar relativistic correction are more noticeable with respect to calculated values of α. For example, the inclusion of the DK2 correction in the UCCSD(T), UCCSDT and IC-MRCI wave functions improves these Δ_{max} values by *ca.* 5-6 a_0^3.

There is little difference between the overall performance of the CC and IC-MRCI with respect the P state transition frequencies and IE_1 values of Li, Be, Na, Mg, K and Ca. This fact is implied from the differences in $\overline{\Delta}$, $\overline{\Delta}_{\text{abs}}$, σ and Δ_{max} values calculated using these two methods. Nevertheless, it is observed that in the case of the cations the Δ_{max} values using CCSD(T), CCSDT and IC-MRCI are 0.21, 0.21 and 3.03 eV, respectively. This discrepancy is alleviated upon the inclusion of +Q corrections in the latter method. For example, the Δ_{max} value for the neutral and ionic species atoms using IC-MRCI+Q are 0.07 and 2.82 eV lower than the

IC-MRCI values, respectively. The inclusion of relativistic corrections in the IC-MRCI and IC-MRCI+Q wave functions improves the values of all statistical metrics employed for both the neutral and ionic species. The only exception is the $\Delta_{\max}$ value using IC-MRCI+Q for the cations, which is increased from 0.21 to 0.24 eV upon addition of the DK2 correction.

With respect to $\overline{\Delta}$, $\overline{\Delta}_{\text{abs.}}$, σ and $\Delta_{\text{max.}}$, Table 2.4 shows that IC-MRCI and IC-MRCI(DK2) perform more poorly than do either UCCSD(T) and UCCSDT. This suggests that triplet (or higher) excitation from the reference determinant is necessary for α to be modelled accurately. Inclusion of +Q corrections to the IC-MRCI wave function provides a significant improvement in the calculated values of α. For example, it is evident that $\overline{\Delta}$, $\overline{\Delta}_{\text{abs.}}$, σ and $\Delta_{\text{max.}}$ using IC-MRCI+Q are 0.01, 2.38, 4.11 and 11.69 a_0^3 smaller than those for IC-MRCI, respectively.

Although inclusion of the DK2 correction in the UCCSD(T), UCCSDT and IC-MRCI wave functions significantly improves $\overline{\Delta}$, $\overline{\Delta}_{\text{abs.}}$, σ and $\Delta_{\text{max.}}$ for α, the same inclusion in the IC-MRCI+Q wave function has a more tempered effect. For example, the values of $\overline{\Delta}$ and $\overline{\Delta}_{\text{abs.}}$ for IC-MRCI+Q(DK2) are lowered by 0.01 and 0.56 a_0^3 with respect to IC-MRCI+Q, whereas σ for IC-MRCI+Q(DK2) is raised by 0.57 a_0^3 with respect to IC-MRCI+Q. There is no difference in the maximum deviation from experiment upon inclusion of the DK2 correction to the IC-MRCI+Q wave function.

2.9. Application to Molecular Calculations

2.9.1. Computational Procedure

The ROHF, UCCSD(T), CASSCF, IC-MRCI and IC-MRCI+Q methods have been employed to determine equilibrium properties of MH_2 (M = Li, Be, Na,

Mg, K, Ca). These properties include R_e, θ_e, D_e, and harmonic vibration frequencies. Although this section discusses only the correlated methods listed above, ROHF and CASSCF data are listed in Appendix B.

The CASSCF, UCCSD(T), IC-MRCI and IC-MRCI+Q methods each employed an optimised ROHF reference wave function. These methods have been used in conjunction with the largest ANO-RCC contracted basis set for each metal and the aug-cc-pVQZ basis set for hydrogen. The performance, with respect to ground state metal hydride, helide and hydrohelide cations, of the hydrogen and helium aug-cc-pVQZ basis sets has been established in a number of investigations [4, 14, 34, 142, 151]. Relativistic effects have been accounted for in all calculations using the DK2 correction to the one-electron Hamiltonian. All ground state wave functions were constructed in the C_s symmetry framework, as were the $^2\Sigma_g^+$ excited state wave functions of LiH_2, NaH_2 and KH_2. For the $^2B_2$ and $^2B_1$ excited states of LiH_2, NaH_2 and KH_2, it was necessary that C_{2v} symmetry be enforced on the molecular wave functions (*vide infra*). The molecular CASSCF wave functions included the $1s$, $2s$, $2p$ orbitals of H, $1-3s$, $2p$, $3p$ orbitals of Li and Be, $1-4s$, $2-4p$, $3d$ orbitals of Na and Mg and the $1-4s$, $2-4p$, $3d$ orbitals of K and Ca. Subsequent CI calculations included all electrons for LiH_2, BeH_2, NaH_2 and MgH_2, whereas for KH_2 and CaH_2, the $1s$, $2s$, $2p$ orbitals of K and Ca were excluded in the correlated calculation. The effects of basis set superposition error (BSSE) with respect to the equilibrium properties of BeH_2, MgH_2 and CaH_2 have also been investigated. Where possible, comparison has been made between the results of this work with previous theoretical and experimental values.

In cases for which molecular hessians could not be constructed (*viz.* for multi-reference and BSSE-corrected wave functions), harmonic frequencies were calculated in the approximation of uncoupled normal modes. This entailed the construction of a

discrete potential energy grid (typically consisting of 30-40 points within 0.2 a_0 of the equilibrium geometry), which was subsequently represented using a quadratic power series [152] and embedded in the one-dimensional vibrational Schrödinger equation. The Schrödinger equation was then solved numerically using an in-house FORTRAN code, which employs a finite-element method and gaussian quadrature [66]. The source code for all programs employed in this thesis are included in Appendix C. Comparison between the harmonic frequencies obtained in this manner and those generated using MOLPRO indicate an error generally no greater than 5-10 cm^{-1}, a value largely insignificant in the context of the present work.

2.9.2. Application to LiH_2 NaH_2 and KH_2

Values of R_e, θ_e and harmonic vibration frequencies ω_1, ω_2 and ω_3 for the lowest lying bound $^2B_2$, $^2B_1$ and $^2\Sigma_g^+$ states of MH_2 (M = Li, Na, K) calculated using UCCSD(T) are presented in Table 2.5. The relative energies of these states, with respect to the $[(^2S_{1/2})M+(^1\Sigma_g^+)H_2]$ asymptotic limit, are also given in Table 2.5. For the $^2B_2$ states of MH_2 (M = Li, Na, K), comparison between the results of this work and previous theoretical values is given in Table 2.6. Complete lists of ROHF, UCCSD(T), CASSCF, IC-MRCI and IC-MRCI+Q properties for the states of MH_2 (M = Li, Na, K) are given in Appendix B. Due to symmetry restrictions upon the CASSCF/IC-MRCI wave function (as implemented in MOLPRO), harmonic frequencies of the $^2B_2$, $^2B_1$ and $^2\Sigma_g^+$ states of MH_2 (M = Li, Na, K) have not been calculated.

The $^2A_1$ PESs of LiH_2, NaH_2 and KH_2 were found to be purely repulsive, in agreement with previously established results [24]. This was also established for the first excited $^2\Sigma^-$ state. The first excited $^2B_2$ states of LiH_2, NaH_2 and KH_2 were therefore the lowest bound states. These states are known to arise from an

Table 2.5 Low-lying electronic states of MH_2 (M = Li, Na, K) using UCCSD(T)[a].

State	Energy[b] (/eV)	R_e(M-H) (/Å)	R_e(H-H) (/Å)	θ_e (/°)	Frequencies (/cm^{-1}) ω_1	ω_2	ω_3
			LiH_2				
$^2B_2$	1.0413	1.7127	0.8374	28.3	899	2732	1372
$^2B_1$	1.5150	1.9205	0.7516	22.6	591	4276	810
$^2\Sigma_g^+$	2.6117	1.7463	3.4926	180.0	909	325	1837
			NaH_2				
$^2B_2$	1.5295	2.0810	0.7945	22.0	672	3313	1008
$^2B_1$	1.8033	2.2332	0.7484	19.3	469	4311	508
$^2\Sigma_g^+$	3.2167	2.0953	4.1906	180.0	838	131	1114
			KH_2				
$^2B_2$	1.2399	2.5324	0.7736	17.6	454	3685	836
$^2B_1$	1.4065	2.7382	0.7459	15.7	319	4347	468
$^2\Sigma_g^+$	3.2825	2.5330	5.0659	180.0	677	130	907

[a]In conjunction with the largest ANO-RCC basis set [141] for Li, Na, K and the aug-cc-pVQZ basis set for H. All data include the DK2 correction and were calculated using MOLPRO [86].
[b]Relative to the $(^2S_{1/2})$M+$(^1\Sigma_g^+)H_2$ asymptotic limit, with $R_e(H_2) = 0.7420$ Å.

in-plane interaction between the *np* orbital of the metal and the H_2 σ_u MO. An analogous out-of-plane interaction leads to bound $^2B_1$ excited states for LiH_2, NaH_2 and KH_2. In particular, from Table 2.5 this interaction results in states 0.4737 (LiH_2), 0.2738 (NaH_2) and 0.1666 (KH_2) eV higher in energy than the respective $^2B_2$ states. The insertion of the metal into the H_2 bond also results in bound species, but is relatively unfavourable in an energetic sense. For example, the $^2\Sigma_g^+$ states of LiH_2, NaH_2 and KH_2 are 1.5704, 1.6872 and 2.0426 eV higher in energy than the respective $^2B_2$ states. In addition, ω_2 values for LiH_2, NaH_2 and KH_2 indicate that the PES curvature in the symmetric bend mode co-ordinate is relatively small.

The Laplacian concentration of the $^2B_2$, $^2B_1$ and $^2\Sigma_g^+$ states of MH_2 are illustrated in Figure 2.1 for M = Li. For ($^2B_2$,$^2B_1$)LiH_2 the Laplacian concentrations,

$$\nabla^2 = \frac{\partial^2}{\partial x^2} + \frac{\partial^2}{\partial y^2} + \frac{\partial^2}{\partial z^2} \tag{2.32}$$

are concomitant with the data in Table 2.5, with particular reference to the value

Table 2.6 *Ab initio* properties of the $^2B_2$ states of MH_2 (M = Li, Na, K)[a].

	Energy[b] (/eV)	R_e(M-H) (/Å)	R_e(H-H) (/Å)	θ_e (/°)	Frequencies (/cm^{-1}) ω_1	ω_2	ω_3
			LiH_2				
UCCSD(T)	1.0413	1.7127	0.8374	28.3	899	2732	1372
IC-MRCI	1.0217	1.6972	0.8399	28.7			
IC-MRCI+Q	1.0186	1.6967	0.8407	28.7			
HF[c]		1.9	0.79	24.0			
Pseudo-MO[d]		1.9	0.74	25.1			
MP2[e]		1.752	0.804	27.3			
MCSCF[f]		2.0	0.79	22.8			
DFT/B3LYP[g]		1.720					
MRCI[h]		1.70	0.83	28.3			
			NaH_2				
UCCSD(T)	1.5295	2.0810	0.7945	22.0	672	3313	1008
IC-MRCI	1.6605	2.0954	0.7821	21.5			
IC-MRCI+Q	1.5932	2.0842	0.7925	21.9			
PNO-CEPA[i]	1.64	2.11	0.79	21.7			
MCSCF/CI[j]	1.59	2.11	0.79	21.7			
MP2[k]	1.700	2.11	0.79	21.7			
MRCID[l]		2.11	0.79	21.7	588		
			KH_2				
UCCSD(T)	1.2399	2.5324	0.7736	17.6	454	3685	836
IC-MRCI	1.1795	2.5992	0.7645	16.9			
IC-MRCI+Q	1.2658	2.5663	0.7675	17.2			

[a]Using the largest ANO-RCC basis set [141] for Li, Na, K and the aug-cc-pVQZ basis set for H, in conjunction with the DK2 correction. Harmonic frequencies were not determined using multi-reference wave functions, due to symmetry considerations. All data calculated using MOLPRO [86].

[b]Relative to the $(^2S_{1/2})$M+$(^1\Sigma_g^+)H_2$ asymptotic limit with $R_e(H_2) = 0.7420$ Å.

[c]R_e(H-H) = 0.79 Å is assumed; see reference [153].

[d]Pseudo-potential MO method. R_e(H-H) = 0.74 Åis assumed; see reference [13].

[e]In conjunction with a 6-311g(2d,2p) basis set; see reference [11].

[f]In conjunction with a STO-3G basis set; see reference [154].

[g]In conjunction with a 6-311++G** basis set; see reference [12].

[h]In conjunction with [9*s*8*p*4*d*3*f*] (Li) and [4*s*3*p*] (H) basis sets; see reference [5].

[i]In conjunction with [12*s*7*p*3*d*] (Na) and [6*s*2*p*] (H) basis sets; see reference [24].

[j]In conjunction with [8*s*6*p*1*d*] (Na) and [5*s*2*p*] (H) basis sets; see reference [23].

[k]Analytical diabatic two-state fit to MP2 data, in conjunction with 2*s*2*p*2*d* augmented cc-pCVDZ (Na) and 1*s*1*p*1*d* augmented cc-pCVTZ (H) basis sets; see reference [19].

[l]In conjunction with [12*s*7*p*3*d*] (Na) and [6*s*2*p*] (H) basis sets; see reference [25].

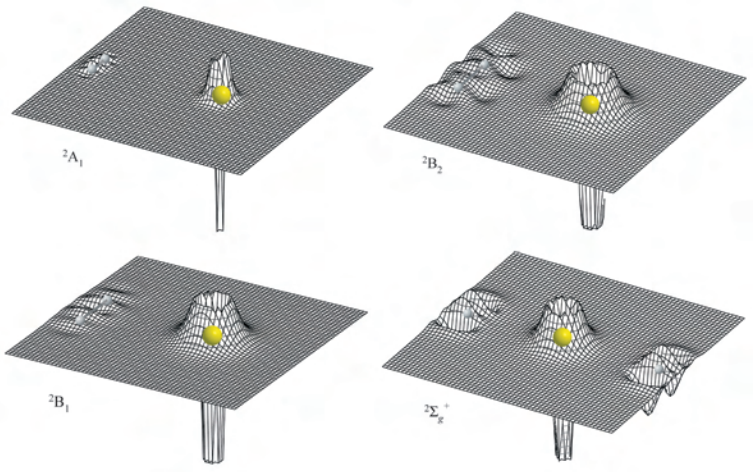

Figure 2.1 Laplacian concentrations for the $^2A_1$, $^2B_2$, $^2B_1$ and $^2\Sigma_1^+$ states of LiH_2.

of R_e(H-H). For example, the UCCSD(T) R_e(H-H) values for these states are larger than the UCCSD(T) $R_e(H_2)$ value by 95.4 and 9.6 mÅ, respectively. Furthermore, the UCCSD(T) ω_2 values for $(^2B_2)LiH_2$ and $(^2B_1)LiH_2$, which essentially correspond to the H - H stretch vibration, are 1667 and 123 cm^{-1} lower than the CCSD/aug-cc-pVQZ $\omega(H_2)$ value, the latter being 4399 cm^{-1}. Similar observations are made with respect to the $^2B_2$, $^2B_1$ states of NaH_2 and KH_2.

It is observed from Table 2.6 that for $(^2B_2)LiH_2$ and $(^2B_2)NaH_2$ the single- and multi-reference methods employed in this work yield equilibrium structures in good agreement. For instance, R_e(Li-H) using UCCSD(T) is larger than the IC-MRCI and IC-MRCI+Q values by 15.5 and 16.0 mÅ, respectively. The inclusion of +Q corrections to the $(^2B_2)NaH_2$ IC-MRCI wave function has a noticeable effect, decreasing the R_e(Na-H) value by 11.2 mÅ. There is concomitant agreement between single- and multi-reference values of R_e(H-H) and θ_e for both species. The MRCI R_e(Li-H) value of Sug Lee *et al.* [5] is larger than the IC-MRCI and IC-MRCI+Q values by *ca.* 10 mÅ. Similarly, the MRCI θ_e value of Sug Lee *et al.* [5] is 0.4° smaller than the IC-MRCI and IC-MRCI+Q values. The single- and multi-reference values of R_e(Na-H) of this work are significantly smaller than available published data,

generally differing by *ca.* 20-30 mÅ.

No data concerning the equilibrium structure of the $^2B_2$ state of KH_2 has been reported in the literature. Nevertheless, it is evident from Table 2.6 that UCCSD(T), IC-MRCI and IC-MRCI+Q give reasonably consistent equilibrium structures. For example, the value of R_e(K-H) using UCCSD(T) is smaller than the IC-MRCI and IC-MRCI+Q values by 66.8 and 33.9 mÅ, respectively. Conversely, the UCCSD(T) value of R_e(H-H) is larger than the IC-MRCI and IC-MRCI+Q values by 9.1 and 6.1 mÅ, respectively.

The differences between the UCCSD(T) and IC-MRCI results regarding the equilibrium structures of $(^2B_2)NaH_2$ and $(^2B_2)KH_2$ may arise from several factors. Firstly, the magnitude of the non-dynamical correlation, which is not accounted for within the UCCSD(T) wave function, is expected to increase with increasing atomic number. Secondly, the IC-MRCI method employed in this work is truncated at second-order (*viz.* IC-MRCISD). Higher order expansion terms, which may prove significant with respect to molecular geometries are therefore ignored. However, approximation to these terms are made through the use of the (T) correction to the UCCSD wave function and the +Q correction to the IC-MRCI wave function. The UCCSD(T) and IC-MRCI+Q are therefore expected to yield better agreement with respect to observables such as equilibrium structures and fundamental frequencies.

2.9.3. Application to BeH_2 MgH_2 and CaH_2

Ab initio values of R_e and harmonic vibration frequencies ω_1, ω_2 and ω_3 for $(^1\Sigma_g^+)BeH_2$, $(^1\Sigma_g^+)MgH_2$ and $(^1\Sigma_g^+)CaH_2$ are presented in Table 2.7. The potential

well-depths for the dissociative reactions,

$$(^1\Sigma_g^+)\mathrm{MH_2} \rightarrow (^2\Sigma^+)\mathrm{MH} + (^2S_{1/2})\mathrm{H} \tag{2.33}$$

$$(^1\Sigma_g^+)\mathrm{MH_2} \rightarrow (^1S_0)\mathrm{M} + 2\mathrm{H} \tag{2.34}$$

(where M = Be, Mg, Ca) are also given in Table 2.7.

From Table 2.7 the correlated methods employed in this work yield $(^1\Sigma_g^+)\mathrm{BeH_2}$ and $(^1\Sigma_g^+)\mathrm{MgH_2}$ equilibrium structures in excellent agreement with the experimental gas-phase values [28, 36, 155]. For instance, the largest differences between experiment and the values of this work are 0.7 and 4.32 mÅ, respectively, both of which correspond to the IC-MRCI values. Moreover, the equilibrium bond lengths of $(^1\Sigma_g^+)\mathrm{MgH_2}$ agree with the IC-MRCI CBS limit values of Li *et al.* [28] to within 18.1 mÅ, and the IC-MRCI+Q/CBS values of Li and Le Roy [35] to within 4.0 mÅ. The differences between $R_e(\mathrm{MgH_2})$ values of this work and the CCSDT and CISDTQ values of Tschumper and Schaefer [33] are slightly larger, being at most 19.3 mÅ. No experimental equilibrium bond length for the ground state of $\mathrm{CaH_2}$ has been reported to date. It is evident however that compared to the CCSD(T) value of Koput [40], the values of this work are larger by *ca.* 10 mÅ. As expected, the ROHF and CASSCF equilibrium bond lengths were consistently larger than the UCCSD(T) and IC-MRCI values for $(^1\Sigma_g^+)\mathrm{BeH_2}$, $(^1\Sigma_g^+)\mathrm{MgH_2}$ and $(^1\Sigma_g^+)\mathrm{CaH_2}$ (see Appendix B). Similarly, the inclusion of +Q corrections to the IC-MRCI wave function consistently shortened the equilibrium bond length (with respect to IC-MRCI) $(^1\Sigma_g^+)\mathrm{BeH_2}$, $(^1\Sigma_g^+)\mathrm{MgH_2}$ and $(^1\Sigma_g^+)\mathrm{CaH_2}$. The ground state of $\mathrm{CaH_2}$ is predicted to be linear with all methods employed in this work. This is in agreement with CASSCF [41] and CISD+Q [43] values. However, previous CCSD(T) [40], MP2 [42] and HF [44] calculations indicate a bent equilibrium $\mathrm{CaH_2}$ structure. This is

Table 2.7 *Ab initio* properties of the $^1\Sigma_g^+$ ground states of MH_2 (M = Be, Mg, Ca).

	R_e (/Å)	D_e[a] (/kJmol^{-1})		Frequencies (/cm^{-1})		
Method		1	2	ω_1	ω_2	ω_3
		BeH_2				
UCCSD(T)[b]	1.3267	406.20	616.31	2049	719	2258
IC-MRCI[b]	1.3271	406.82	616.04	1998	730	2241
IC-MRCI+Q[b]	1.3269	406.08	616.28	1997	731	2243
CCSD(T)[c]	1.3307			2052.22	717.18	2254.75
IC-MRCI+Q[d]	1.3307	406.32		1983.16	710.67	2169.83
FCI/cc-pVQZ[c]	1.3310					
Expt.[e]	1.3264					2178.87
		MgH_2				
UCCSD(T)[b]	1.6954	304.47	436.58	1611	435	1631
IC-MRCI[b]	1.6915	301.28	435.16	1680	465	1868
IC-MRCI+Q[b]	1.6935	305.75	441.08	1607	455	1809
CCSD(T)[f]				1625.3	457.5	1651.7
CCSDT[g]	1.7108			1601.8	438.0	1628.4
CISDTQ[g]	1.7108			1601.6	438.0	1628.2
IC-MRCI/CBS[h]	1.7096	305.66	445.43	1552.4	437.7	1575.6
IC-MRCI+Q/CBS[i]	1.69549	304.70	438.28	1627.07	437.43	1629.50
Expt.[j]	1.69582				437	1588.67
		CaH_2				
UCCSD(T)[b]	2.0548	260.21	426.18	1258	111	1327
IC-MRCI[b]	2.0629	251.97	434.75	1438	128	1326
IC-MRCI+Q[b]	2.0566	257.14	432.34	1359	125	1285
CCSD(T)[k]	2.0452			1223	116.1	1298.5

[a] $D_e(1)$ and $D_e(2)$ refer to equations (2.33) and (2.34), respectively.

[b] This work, in conjunction with the largest ANO-RCC basis sets for Be, Mg and Ca, and the aug-cc-pVQZ basis set for H. All calculations include DK2 correction and were calculated using Molpro.

[c] CCSD(T) and FCI values calculated using the cc-pCV5Z and cc-pVQZ basis sets, respectively; see reference [15].

[d] In conjunction with the aug-cc-pV5Z basis set; see reference [16].

[e] See reference [155].

[f] In conjunction with the ECP10MWB effective core potential; see reference [156].

[g] In conjunction with the cc-pVQZ basis set; see reference [33].

[h] See reference [28].

[i] See reference [35].

[j] Using experimental B_0 value [36] and theoretical α_i value [28]. Experimental R_0 value is 1.703327 Å; see reference [36].

[k] In conjunction with cc-pCV5Z (Ca) and cc-pV5Z (H) basis sets; see reference [40]. The predicted value of θ_e using this method is 164.37 °.

in agreement with the experimentally measured structures [39, 45], which were determined using cold rare-gas matrix isolation techniques. Koput [40] reported that in the HCaH bend co-ordinate, the ground state CaH_2 PES possesses a barrier to linearity of only 6 cm^{-1}.

For $(^1\Sigma_g^+)BeH_2$, the single- and multi-reference potential well-depths for equation (2.33) are in agreement with previous *ab initio* values to within 0.5 $kJmol^{-1}$. The potential well-depths of $(^1\Sigma_g^+)MgH_2$ calculated in this work are also in agreement with previous *ab initio* data. For instance, for equations (2.33) and (2.34) the values of this work are in agreement with the IC-MRCI/CBS values of Li *et al.* [28] to within *ca.* 4 and 10 $kJmol^{-1}$, respectively. There are no experimental or correlated *ab initio* dissociation energy data available in the literature for the ground state of CaH_2. Nevertheless, the methods employed in this work predict the potential well-depth to be *ca.* 69 - 76 $kJmol^{-1}$ larger the CASSCF value of Fujii and Iwata [41]. Similarly, these methods predict this potential well-depth to be *ca.* 100 - 110 $kJmol^{-1}$ larger than the HF value of DeKock *et al.* [44].

There is excellent agreement between the $(^1\Sigma_g^+)BeH_2$ CCSD(T) harmonic frequencies of Koput [15] and those of this work. In particular, the UCCSD(T) results in Table 2.7 differ from the former by no more than *ca.* 4 cm^{-1}. Similarly, for the multi-reference methods employed, there is good agreement with respect to the IC-MRCI+Q data of Li and Le Roy[16]. For example, the differences between these IC-MRCI+Q values for ω_1 and ω_2 are *ca.* 14 and 21 cm^{-1}. For ω_3 this difference is larger, being *ca.* 73 cm^{-1}. For $(^1\Sigma_g^+)MgH_2$ the UCCSD(T) values of ω_1, ω_2 and ω_3 differ from the CC and CI values of Tschumper and Schaefer [33] by at most *ca.* 9, 4 and 3 cm^{-1}, respectively. It should be noted here that the latter CCSDT and CISDTQ values are converged with respect to the level of excitation employed. With respect to the multi-reference harmonic frequencies for $(^1\Sigma_g^+)MgH_2$,

the magnitude of the differences between the results of this work and prior theoretical values can be understood in terms of the relative PES curvatures. For the ground state of CaH_2 there is generally good agreement between UCCSD(T) data and the CCSD(T) values of Koput [40]. For instance, the largest differences for ω_1, ω_2 and ω_3 are *ca.* 25, 6 and 30 cm^{-1}, respectively.

2.9.4. Basis Set Superposition Error

Increasing the number of basis functions or adding higher angular momentum functions in molecular calculations may result in an erroneous improvement of the basis set on one nucleus by that centred on neighbouring nuclei, a phenomenon commonly known as BSSE. In particular, vacant orbitals on one atomic centre may spuriously account for basis set deficiencies on a neighbouring atom [157]. The 'apparent' interaction energy will therefore contain an additive contribution to the 'pure' interaction energy. In this sense, BSSE is a measure of the completeness of a particular basis set [151]. The BSSE may also be influenced by the inclusion of core correlation in a valence only basis set [158]. Although BSSE is relatively unnoticeable in covalently and ionically bonded molecules, the BSSE in van der Waals systems (such as molecular helide ions) is often comparable to the total binding energy of the system itself [74]. The counterpoise correction method [159] negates BSSE by the calculation of fragment atomic/molecular energies in the combined molecular basis set. Generalisations of this counterpoise scheme have been proposed [160, 161]. In particular, the site-site function counterpoise (SSFC) method [160], which provides a many-body extension to the counterpoise scheme, defines the corrected energy to be,

$$\Delta E^{\mathrm{SSFC}} = E\left(\mathrm{IJK}\ldots\right) - \sum_{I} E\left(\mathrm{I}G_{\mathrm{JKL}\ldots}\right) \tag{2.35}$$

where $E\,(\mathrm{IJK}\ldots)$ is the molecular energy and $E\,(\mathrm{I}G_{\mathrm{JKL}\ldots})$ is the molecular energy using the molecular basis set whilst ignoring nuclei JKL.... The SSFC correction has been used to good effect on several van der Waals systems, such as He_2 and He_3 [160] $BeHe_2^+$ [142, 162, 163], MH_2, $HMHe^+$ and MHe_2^{2+} where M = Be, Mg and Ca [14, 34].

Equilibrium properties including R_e, potential well-depths and harmonic vibration frequencies of $(^1\Sigma_g^+)BeH_2$, $(^1\Sigma_g^+)MgH_2$ and $(^1\Sigma_g^+)CaH_2$ have been calculated using SSFC-corrected UCCSD(T), IC-MRCI and IC-MRCI+Q. These data are presented in Table 2.8, in terms of differences from the uncorrected values given in Table 2.7. ROHF and CASSCF data have also been calculated, and are included in Appendix B.

It is evident from Table 2.8 that the SSFC correction to the equilibrium structure of $(^1\Sigma_g^+)BeH_2$ is almost negligible, since each of the UCCSD(T), IC-MRCI and IC-MRCI+Q values of R_e change by less than 1 mÅ. The difference in these respective energies upon inclusion of the SSFC correction is approximately of the order of 0.1 - 1.0 mE_h. These differences manifest themselves primarily in the calculated potential well-depths for $(^1\Sigma_g^+)BeH_2$. Similar observations are made with respect to $(^1\Sigma_g^+)MgH_2$. For instance, SSFC-corrected UCCSD(T), IC-MRCI and IC-MRCI+Q energies are *ca.* 0.1 - 0.7 mE_h higher than the uncorrected analogues. The differences in R_e using these corrected methods are slightly larger, being of the order of 1 mÅ. The effects of the SSFC correction are more noticeable for $(^1\Sigma_g^+)CaH_2$. In particular, the R_e values calculated using UCCSD(T), IC-MRCI and IC-MRCI+Q are increased by 8.64, 5.31 and 5.92 mÅ, respectively. The SSFC-corrected energies of $(^1\Sigma_g^+)CaH_2$ using these methods are *ca.* 1 - 3 mE_h larger than the uncorrected energies. This is also reflected in the differences between corrected and uncorrected potential well-depths. For example, the SSFC correction decreases the IC-MRCI and

Table 2.8 BSSE corrections to equilibrium properties of $(^1\Sigma_g^+)MH_2$ (M = Be, Mg, Ca)[a].

	ΔEnergy (/mE$_h$)	ΔR_e (/mÅ)	ΔD_e[b] (/kJmol^{-1})		Frequencies (/cm^{-1})		
			1	2	$\Delta\omega_1$	$\Delta\omega_2$	$\Delta\omega_3$
			BeH_2				
UCCSD(T)	0.11891	0.12	−0.30	−0.31	−80	22	−2
IC-MRCI	1.46648	0.16	−0.79	0.15	−26	23	17
IC-MRCI+Q	-0.26161	0.12	−1.97	−1.73	−16	−9	−40
			MgH_2				
UCCSD(T)[c]	0.70552	2.61	−0.87	−1.88	−20	−4	1
IC-MRCI[c]	0.17840	2.45	−0.68	−0.46	35	−50	−111
IC-MRCI+Q[c]	0.15750	2.47	−0.35	−6.38	32	−3	−135
			CaH_2				
UCCSD(T)[c]	1.72443	8.64	1.59	2.32	−6	10	−23
IC-MRCI[c]	3.51676	5.31	6.53	−15.75	−129	−6	41
IC-MRCI+Q[c]	2.11513	5.92	4.16	−11.24	−88	−4	20

[a]BSSE was treated within the SSFC scheme [160]. All calculations include DK2 correction and employ the largest ANO-RCC basis sets for Be, Mg and Ca, and the aug-cc-pVQZ basis set for H. All calculations performed using MOLPRO.
[b]$D_e(1)$ and $D_e(2)$ refer to equations (2.33) and (2.34), respectively.
[c]BSSE corrected data; see reference [34].

IC-MRCI+Q atomisation energy values of $(^1\Sigma_g^+)CaH_2$ by 15.75 and 11.24 kJmol^{-1}, respectively.

The most noticeable effect of the SSFC correction for $(^1\Sigma_g^+)BeH_2$, $(^1\Sigma_g^+)MgH_2$ and $(^1\Sigma_g^+)CaH_2$ occurs with respect to the respective PES curvatures. This is evident from the values of $\Delta\omega_1$, $\Delta\omega_2$ and $\Delta\omega_3$ given in Table 2.8. As expected, the effects of BSSE are generally the largest for ω_1 and ω_3, which correspond to the fundamental frequencies in the symmetric breathe and asymmetric stretch modes of vibration, respectively. For example, using UCCSD(T) the value of ω_1 for $(^1\Sigma_g^+)BeH_2$ decreases by *ca.* 80 cm^{-1} upon inclusion of the SSFC correction. Similarly, for $(^1\Sigma_g^+)MgH_2$ the SSFC-corrected IC-MRCI and IC-MRCI+Q values of ω_3 are *ca.* 111 and 134 cm^{-1} lower than the uncorrected values. For $(^1\Sigma_g^+)CaH_2$, the IC-MRCI and IC-MRCI+Q values of ω_1 are decreased by *ca.* 128 and 87 cm^{-1} using the SSFC correction, respectively.

2.10. Conclusion

The application of the Dirac and Schrödinger equations has been reviewed with respect to atomic and molecular electronic structure. Exact solutions to both the atomic and molecular Schrödinger equation are achievable for only the simplest systems. Within the Born-Oppenheimer approximation, the molecular Schrödinger equation is simplified greatly. The use of MO-based electronic structure methods may also be employed to approximate the solutions to the Schrödinger equation. However, for results of chemical accuracy the use of MO-based correlated methods are required.

Both SCF and post-SCF methods have been applied to the ground states of Li, Be, Na, Mg, K and Ca and the respective monocations. In particular, properties including IE_1, α and electronic transition frequencies have been calculated using ROHF, UCCSD(T), UCCSDT, CASSCF, IC-MRCI and IC-MRCI+Q. The relativistic ANO-RCC basis sets [141] were found to provide a relatively efficient and accurate description of the ground state electronic wave functions of these atoms. The CG [58] and DK [59, 60] relativistic schemes have also been investigated with respect to these properties. While the CG scheme was found to be unreliable, the inclusion of the DK2 relativistic correction was shown to generally improve atomic properties. Excitations greater than singles and doubles in the correlated methods were found to be beneficial with respect to calculated atomic properties. For instance, IE_1 and α calculated using CC methods were found to have converged at the SD(T) level of excitation. Similarly, the +Q correction to the IC-MRCI wave function improved the values of IE_1, α and the electronic transition frequencies considered.

The structures and stabilities of MH_2 (M = Li, Be, Na, Mg, K, Ca) have been investigated using the methods listed previously. The DK2 correction was included

in all molecular calculations. From a comparison of equilibrium molecular structures using these correlated methods it was observed that excitations beyond singles and doubles were necessary for reliable results. To this end, IC-MRCI+Q was generally the most suitable method for the calculation of molecular properties. Nevertheless, UCCSD(T) also provided accurate results which were often in excellent agreement with the IC-MRCI+Q values.

The effects of BSSE on $(^1\Sigma_g^+)BeH_2$, $(^1\Sigma_g^+)MgH_2$ and $(^1\Sigma_g^+)CaH_2$ were investigated by the use of the SSFC correction scheme [160]. The magnitude of the SSFC correction to the molecular energy increased with increasing atomic number, as expected. A concomitant increase in the correction to the equilibrium bond lengths and dissociative potential well-depths was also observed. The inclusion of the SSFC correction produced a marked effect on the calculated molecular properties. In particular, corrected harmonic frequencies were observed to differ from the uncorrected values by up to *ca.* 100 cm^{-1}.

The correlated methods discussed in this Chapter have been subsequently employed throughout the remainder of this thesis for MH_2^{n+}, $HMHe^{n+}$ and MHe_2^{n+} ($n = 1, 2$, M = Li, Be, Na, Mg, K, Ca).

2.11. References

[1] C. Y. Yam, S. Yokojima, and G. H. Chen, Phys. Rev. B **68**, 153105 (2003).

[2] C. Sanz, E. Bodo, and F. A. Gianturco, Chem. Phys. **314**, 135 (2005).

[3] F. A. Gianturco, P. G. Giorgi, H. Berriche, and F. X. Gadea, Astron. Astrophys. Suppl. Ser. **117**, 377 (1996).

[4] A. J. Page and E. I. von Nagy-Felsobuki, J. Phys. Chem. A **111**, 4478 (2007).

[5] H. S. Lee, Y. S. Lee, and G. H. Jeung, J. Phys. Chem. A **103**, 11080 (1999).

[6] H. Kato, K. Hirao, I. Nishida, K. Kimoto, and K. Akagi, J. Phys. Chem. **85**, 3391 (1981).

[7] X. Wang and L. Andrews, J. Phys. Chem. A **111**, 6008 (2007).

[8] B. S. Jursic, J. Mol. Struct. (THEOCHEM) **491**, 11 (1999).

[9] P. Jankowski and B. Jeziorski, J. Chem. Phys. **111**, 1857 (1999).

[10] B. H. Cardelino, W. H. Eberhardt, and R. F. Borkman, J. Chem. Phys. **84**, 3230 (1986).

[11] P. Hobza and P. von Ragué-Schleyer, Chem. Phys. Lett. **105**, 630 (1984).

[12] W. Grochala and R. Hoffmann, J. Phys. Chem. A **104**, 9740 (2000).

[13] F. Rossi and J. Pascale, Phys. Rev. A **32**, 2657 (1985).

[14] A. J. Page, D. J. D. Wilson, and E. I. von Nagy-Felsobuki, Chem. Phys. Lett. **442**, 194 (2007).

[15] J. Koput and K. A. Peterson, J. Chem. Phys. **125**, 044306 (2006).

[16] H. Li and R. J. Le Roy, J. Chem. Phys. **125**, 044307 (2006).

[17] F. E. Penotti, Int. J. Quant. Chem. **106**, 1153 (2006).

[18] A. W. Jasper, C. Zhu, S. Nangia, and D. G. Truhlar, Farad. Disc. **127**, 1 (2004).

[19] M. D. Hack and D. G. Truhlar, J. Chem. Phys. **110**, 4315 (1999).

[20] M. Hack, A. Jasper, Y. Volobuev, D. Schwenke, and D. Truhlar, J. Phys. Chem. A **103**, 6309 (1999).

[21] M. Hack, A. Jasper, Y. Volobuev, D. Schwenke, and D. Truhlar, J. Phys. Chem. A **104**, 217 (2000).

[22] M. D. Hack and D. G. Truhlar, J. Chem. Phys. **114**, 9305 (2001).

[23] D. R. Yarkony, J. Chem. Phys. **84**, 3206 (1986).

[24] P. Botschwina, W. Meyer, I. V. Hertel, and W. Reiland, J. Chem. Phys. **75**, 5438 (1981).

[25] R. de Vivie-Riedle, P. Hering, and K. L. Kompa, Z. Phys. D **17**, 299 (1990).

[26] R. de Vivie-Riedle and K. Sundermann, Appl. Phys. B **71**, 285 (2000).

[27] R. de Vivie-Riedle, L. Kurtz, and A. Hofmann, Pure Appl. Chem. **3**, 525 (2001).

[28] H. Li, D. Xie, and H. Guo, J. Chem. Phys. **121**, 4156 (2004).

[29] J. A. Pople, B. T. Luke, M. J. Frisch, and J. S. Binkley, J. Chem. Phys. **89**, 2198 (1985).

[30] R. Ahlrichs, F. Keil, H. Lischka, W. Kutzelnigg, and V. Staemmler, J. Chem. Phys. **63**, 455 (1975).

[31] L. von Szentpaly, J. Phys. Chem. A **106**, 11945 (2002).

[32] P. Chaquin, A. Sevin, and H. Yu, J. Phys. Chem. **89**, 2813 (1985).

[33] G. S. Tschumper and H. F. Schaefer III, J. Chem. Phys. **108**, 7511 (1998).

[34] A. J. Page and E. I. von Nagy-Felsobuki, Phys. Chem. Chem. Phys. **10**, 1285 (2008).

[35] H. Li and R. Le Roy, J. Phys. Chem. A **111**, 6248 (2007).

[36] A. Shayesteh, D. R. T. Appadoo, I. Gordon, and P. F. Bernath, J. Chem. Phys. **119**, 7785 (2003).

[37] A. Shayesteh, D. R. T. Appadoo, I. Gordon, and P. F. Bernath, Can. J. Chem. **82**, 947 (2004).

[38] C. X. Shang, M. Bououdina, Y. Song, and Z. X. Guo, Int. J. Hydrogen Energy **29**, 73 (2004).

[39] X. Wang and L. Andrews, J. Phys. Chem. A **108**, 11500 (2004).

[40] J. Koput, J. Phys. Chem. A **109**, 4410 (2005).

[41] T. S. Fujii and S. Iwata, Chem. Phys. Lett. **251**, 150 (1996).

[42] I. Bytheway, R. J. Gillespie, T. H. Tang, and R. F. W. Bader, Inorg. Chem. **34**, 2407 (1995).

[43] M. Kaupp, P. von Ragué-Schleyer, and H. Stoll, J. Chem. Phys. **94**, 1360 (1991).

[44] R. L. DeKock, M. A. Peterson, L. K. Timmer, E. J. Baerends, and P. Verooijs, Polyhedron **9**, 1919 (1990).

[45] Z. L. Xiao, R. H. Hauge, and J. L. Margrave, High Temp. Sci. **31**, 59 (1991).

[46] A. Burrows and M. Volobuyev, Astrophys. J. **583**, 985 (2003).

[47] N. F. Allard, F. Allard, P. H. Hauschildt, J. F. Kielkopf, and L. Machin, Astron. Astrophys. **411**, L473 (2003).

[48] R. Santra and K. Kirby, J. Chem. Phys. **123**, 214309 (2005).

[49] P. A. M. Dirac, Proc. Roy. Soc. A **117**, 610 (1928).

[50] P. A. M. Dirac, Proc. Roy. Soc. A **118**, 351 (1928).

[51] P. A. M. Dirac, Proc. Roy. Soc. London Ser. A **123**, 714 (1928).

[52] P. Pyykko, Chem. Rev. **88**, 563 (1988).

[53] I. P. Grant, *Methods of Computational Chemistry* (Plenum Press, New York, 1987), vol. 2, p. 1.

[54] K. Balasubramanian and K. S. Pitzer, Adv. Chem. Phys. **67**, 287 (1987).

[55] K. Balasubramanian, *Encyclopedia of Computational Chemistry* (John Wiley & Sons, New York, 1998), vol. 4, p. 2471.

[56] T. Nakajima, T. Yanai, and K. Hirao, J. Comp. Chem. **23**, 847 (2002).

[57] T. Zeigler, J. G. Snijders, and E. J. Baerends, J. Chem. Phys. **74**, 1271 (1981).

[58] R. D. Cowan and D. C. Griffin, J. Opt. Soc. Am. **66**, 1010 (1976).

[59] M. Douglas and N. M. Kroll, Ann. Phys. (N.Y.) **82**, 89 (1974).

[60] B. A. Hess, Phys. Rev. A **33**, 3742 (1986).

[61] C. L. Collins, K. G. Dyall, and H. F. Schaefer III, J. Chem. Phys. **102**, 2024 (1995).

[62] E. Schrödinger, Ann. Phys. **79**, 361 (1926).

[63] E. Schrödinger, Ann. Phys. **79**, 734 (1926).

[64] E. Schrödinger, Ann. Phys. **80**, 8 (1926).

[65] E. Schrödinger, Ann. Phys. **80**, 29 (1926).

[66] D. J. Searles and E. I. von Nagy-Felsobuki, *Ab Initio Calculations of Vibrational Band Origins* (Elsevier, New York, 1991).

[67] M. Born, Gott. Nachr. Math. Phys. **KI**, 1 (1951).

[68] M. Born and K. Huang, *Dynamical Theory of Crystal Lattices* (Oxford University Press, London, 1954).

[69] V. Fock, Z. Phys. **61**, 126 (1930).

[70] P. A. M. Dirac, Proc. Camb. Phil. Soc. **26**, 376 (1930).

[71] J. A. Pople and R. K. Nesbet, J. Chem. Phys. **22**, 571 (1954).

[72] C. C. J. Roothan, Rev. Mod. Phys. **23**, 69 (1951).

[73] G. G. Hall, Proc. Roy. Soc. London Ser. A **205**, 541 (1954).

[74] T. Helgaker, P. Jorgensen, and J. Olsen, *Molecular Electronic Structure Theory* (John Wiley & Sons, Chichester, 2000).

[75] W. A. Goddard, Phys. Rev. **157**, 81 (1967).

[76] B. O. Roos, *Lecture Notes in Quantum Chemistry* (Springer-Verlag, Berlin, 1992), p. 177.

[77] O. Hino, T. Kinoshita, G. K. L. Chan, and R. J. Bartlett, J. Chem. Phys. **124**, 114311 (2006).

[78] A. C. Wahl and G. Das, *Methods of Electronic Structure Theory* (1977), vol. 3, p. 51.

[79] B. O. Roos, Adv. Chem. Phys. **69**, 399 (1987).

[80] H. J. A. Jensen, P. Jorgensen, and T. Helgaker, Chem. Phys. Lett. **162**, 355 (1989).

[81] J. Olsen, B. O. Roos, P. Jorgensen, and H. J. A. Jensen, J. Chem. Phys. **89**, 2185 (1988).

[82] P. Malmqvist, A. Rendell, and B. O. Roos, J. Phys. Chem. **94**, 5477 (1990).

[83] H. J. Werner and P. J. Knowles, J. Chem. Phys. **82**, 5053 (1985).

[84] P. J. Knowles and H. J. Werner, Chem. Phys. Lett. **115**, 259 (1985).

[85] H. J. Werner, Adv. Chem. Phys. **69**, 1 (1987).

[86] H.-J. Werner, P. J. Knowles, R. Lindh, F. R. Manby, M. Schütz, P. Celani, T. Korona, G. Rauhut, R. D. Amos, A. Bernhardsson, et al., MOLPRO, *version 2006.1*

(2006), see http://www.molpro.net.

[87] C. Angeli, K. L. Bak, V. Bakken, O. Christiansen, R. Cimiraglia, S. Coriani, P. Dahle, E. K. Dalskov, T. Enevoldsen, B. Fernandez, et al., DALTON, *a molecular electronic structure program, Release 2.0, Revision 0* (2005), see http://www.kjemi.uio.no/software/dalton/dalton.html.

[88] M. W. Schmidt, K. K. Baldridge, J. A. Boatz, S. T. Elbert, M. S. Gordon, J. H. Jensen, S. Koseki, N. Matsunaga, K. A. Nguyen, S. Su, et al., *General atomic and molecular electronic structure system*, J. Comp. Chem. 14, 1347, (1993), see http://www.msg.ameslab.gov/GAMESS.

[89] T. Straatsma, E. Aprà, T. Windus, E. Bylaska, W. de Jong, S. Hirata, M. Valiev, M. Hackler, L. Pollack, R. Harrison, et al., NWCHEM, *A Computational Chemistry Package for Parallel Computers, Version 5.0* (2006), see http://www.emsl.pnl.gov/docs/nwchem.

[90] M. J. Frisch, G. W. Trucks, H. B. Schlegel, G. E. Scuseria, M. A. Robb, J. R. Cheeseman, J. A. Montgomery, Jr., T. Vreven, K. N. Kudin, J. C. Burant, et al., GAUSSIAN 03*, revision C.01* (2004), see http://www.gaussian.com.

[91] Y. Shao, L. Fusti-Molnar, Y. Jung, J. Kussmann, C. Ochsenfeld, S. T. Brown, A. T. B. Gilbert, L. V. Slipchenko, S. V. Levchenko, D. P. O'Neill, et al., Phys. Chem. Chem. Phys. **8**, 3172 (2006).

[92] P. G. Lykos and R. G. Parr, J. Chem. Phys. **24**, 1166 (1956).

[93] P. G. Lykos and R. G. Parr, J. Chem. Phys. **25**, 1301 (1956).

[94] W. Thiel, J. Am. Chem. Soc. **103**, 1413 (1981).

[95] W. Thiel, J. Am. Chem. Soc. **103**, 1420 (1981).

[96] A. Schweig and W. Thiel, J. Am. Chem. Soc. **103**, 1425 (1981).

[97] L. Bytautus and K. Ruedenberg, J. Chem. Phys. **121**, 10852 (2004).

[98] L. Bytautus and K. Ruedenberg, J. Chem. Phys. **121**, 10905 (2004).

[99] L. Bytautus and K. Ruedenberg, J. Chem. Phys. **121**, 10919 (2004).

[100] L. Bytautus and K. Ruedenberg, J. Chem. Phys. **122**, 154110 (2005).

[101] L. Bytautus and K. Ruedenberg, J. Chem. Phys. **124**, 174304 (2006).

[102] Z. Rolik, A. Szabados, and P. R. Surjan, J. Chem. Phys. **128**, 144101 (2008).

[103] H. J. Werner and P. J. Knowles, J. Chem. Phys. **89**, 5803 (1988).

[104] P. J. Knowles and H. J. Werner, Chem. Phys. Lett. **145**, 514 (1988).

[105] M. Kallay, MRCC*, a string-based quantum chemical program suite* (2001), J. Chem. Phys., 115, 2645 (2001), see http://www.mrcc.hu.

[106] S. R. Langhoff and E. R. Davidson, Int. J. Quant. Chem. **8**, 8 (1974).

[107] F. Coester, Nucl. Phys. **7**, 421 (1958).

[108] F. Coester and H. Kümmel, Nucl. Phys. **17**, 477 (1960).

[109] J. Čížek, J. Chem. Phys. **45**, 4256 (1966).

[110] F. A. Evangelista, W. D. Allen, and H. F. Schaefer III, J. Chem. Phys. **125**, 154113 (2006).

[111] F. A. Evangelista, W. D. Allen, and H. F. Schaefer III, J. Chem. Phys. **127**, 024102 (2007).

[112] T. D. Crawford, C. D. Sherill, and E. F. Valeev, J. Comp. Chem. **28**, 1610 (2006).

[113] K. Raghavachari, G. W. Trucks, J. A. Pople, and M. Head-Gordon, Chem. Phys. Lett. **157**, 479 (1989).

[114] J. A. Pople, M. Head-Gordon, and K. Raghavachari, J. Chem. Phys. **87**, 5968 (1987).

[115] J. Stanton, J. Gauss, J. Watts, P. Szalay, R. Bartlett, A. Auer, D. Bernholdt, O. Christiansen, M. Harding, M. Heckert, et al., ACES II, see http://www.aces2.de.

[116] S. F. Boys, Proc. Roy. Soc. London Ser. A **200**, 542 (1950).

[117] S. Huzinaga, J. Chem. Phys. **42**, 1293 (1965).

[118] T. H. Dunning and P. J. Hay, *Modern Theoretical Chemistry* (Plenum Press, New York, 1977), vol. 3, p. 1.

[119] I. Ema, J. G. de la Vega, G. Ramírez, R. López, J. F. Rico, H. Meissner, and J. Paldus, J. Comp. Chem. **24**, 859 (2003).

[120] D. P. Chong, E. van Lenthe, S. van Gisbergen, and E. J. Baerends, J. Comp. Chem. **25**, 1030 (2004).

[121] E. van Lenthe and E. J. Baerends, J. Comp. Chem. **24**, 1142 (2003).

[122] T. H. Dunning, K. A. Peterson, and D. E. Woon, *Encyclopedia of Computational Chemistry* (John Wiley & Sons, New York, 1998), vol. 1, p. 88.

[123] R. D. Bardo and K. Ruedenberg, J. Chem. Phys. **59**, 5956 (1973).

[124] R. C. Raffenetti, J. Chem. Phys. **59**, 5936 (1973).

[125] S. Huzinaga, M. Klobukowski, and H. Tatewski, Can. J. Chem. **71**, 3951 (1979).

[126] J. P. Blaudeau, M. P. McGrath, L. A. Curtiss, and L. Radom, J. Chem. Phys. **107**, 5016 (1997).

[127] J. A. Pople, J. Chem. Phys. **72**, 650 (1980).

[128] W. J. Hehre, R. Ditchfield, and J. A. Pople, J. Chem. Phys. **56**, 2257 (1972).

[129] R. Krishnan, J. S. Binkley, R. Seeger, and J. A. Pople, J. Chem. Phys. **72**, 650 (1980).

[130] T. H. Dunning, J. Chem. Phys. **90**, 1007 (1989).

[131] J. Koput and K. Peterson, J. Phys. Chem. A **106**, 9595 (2002).

[132] D. E. Woon and T. H. Dunning (Unpublished).

[133] D. Feller, unofficial basis sets, see http://gnode2.pnl.gov/bse/portal.

[134] D. E. Woon and T. H. Dunning, J. Chem. Phys. **100**, 2975 (1994).

[135] D. E. Woon and T. H. Dunning, J. Chem. Phys. **98**, 1358 (1993).

[136] D. E. Woon and T. H. Dunning, J. Chem. Phys. **103**, 4572 (1995).

[137] R. A. Kendall, T. H. Dunning, and R. J. Harrison, J. Chem. Phys. **96**, 6796 (1991).

[138] M. A. Iron, M. Oren, and J. M. L. Martin, Mol. Phys. **101**, 1345 (2003).

[139] J. Almlof and P. R. Taylor, Adv. Chem. Phys. **22**, 301 (1991).

[140] J. Almlof and P. R. Taylor, J. Chem. Phys. **86**, 4070 (1987).

[141] B. O. Roos, V. Veryazov, and P. Widmark, Theor. Chem. Acc. **111**, 345 (2004).

[142] A. J. Page, D. J. D. Wilson, and E. I. von Nagy-Felsobuki, Chem. Phys. Lett. **429**, 335 (2006).

[143] J. E. Sansonetti and W. C. Martin, J. Phys. Chem. Ref. Data **34** (2005).

[144] D. R. Lide, *CRC Handbook of Chemistry and Physics* (CRC Press, 2007-2008), 88th ed.

[145] J. Harrison, Chem. Rev. **100**, 679 (2000).

[146] J. P. Desclaux, At. Nuc. Data Tables **12**, 311 (1973).

[147] T. M. Miller and N. Bederson, Adv. At. Mol. Phys. **13**, 1 (1977).

[148] A. Miffre, M. Jacquey, M. Buchner, G. Trenec, and J. Vigue, Phys. Rev. A **73**, 011603 (2006).

[149] C. R. Ekstrom, J. Schmiedmayer, M. S. Chapman, T. D. Hammond, and D. E. Pritchard, Phys. Rev. A **51**, 3883 (1995).

[150] M. W. J. Bromley and J. Mitroy, Phys. Rev. A **65**, 062505 (2002).

[151] D. J. D. Wilson, Ph.D. thesis, The University of Newcastle, Australia (2003).

[152] D. J. Searles and E. I. von Nagy-Felsobuki, Comp. Phys. Comm. **67**, 527 (1992).

[153] M. Krauss, J. Res. Natl. Bur. Stand., Sect. A **72**, 553 (1968).

[154] K. Mizutani, Y. Kuribara, K. Hayachi, and S. Matsumoto, Bull. Chem. Soc. Jap. **52**, 2185 (1979).

[155] A. Shayesteh, K. Tereszchuk, P. Bernath, and R. Colin, J. Chem. Phys. **118**, 3622 (2003).

[156] T. Hrenar, H. J. Werner, and G. Rauhut, Phys. Chem. Chem. Phys. **7**, 3123 (2005).

[157] C. W. Bauschlicher Jr, S. R. Langhoff, and P. R. Taylor, Sci. Tech. Aerosp. Rep.

Abstr. **27**, No. N89 (1989).

[158] P. R. Taylor, *Lecture Notes in Quantum Chemistry* (Springer-Verlag, 1992), vol. 58, p. 325.

[159] S. F. Boys and F. Bernardi, Mol. Phys. **19**, 553 (1970).

[160] B. Wells and S. Wilson, Chem. Phys. Lett. **101**, 429 (1983).

[161] P. Valiron and I. Mayer, Chem. Phys. Lett. **275**, 46 (1997).

[162] X. Bu and C. Zhong, Chem. Phys. Lett. **392**, 181 (2004).

[163] X. Bu, C. Zhong, and A. F. Jalbout, Chem. Phys. Lett. **387**, 410 (2004).

CHAPTER 3

Ab Initio Property Surfaces of Triatomic Molecules

3.1. Introduction

The calculation of *ab initio* rovibrational energies and radiative properties of a molecule requires detailed knowledge of the molecular PES and DMS, respectively. Moreover, functional forms of the molecular PES and DMS are required for rovibrational calculations. To this end, some parametrisation of the *ab initio* property surface (in terms of the $3N$-6(5) internal nuclear co-ordinates) must be performed.

One common approach is to employ a Taylor series expansion in a set of chosen co-ordinates [1]. This is defined in terms of the derivatives of the molecular property of interest. Such an approach is conceptually simple and therefore easily implemented. Moreover, a Taylor series expansion is applicable to all molecules, and is limited in accuracy by the order at which the expansion is truncated. The topology of the molecular property surface also affects the accuracy of the Taylor series expansion. The portion of the molecular property surface which is modelled accurately is therefore often restricted. For example, the property surfaces of weakly bound molecular systems (such as those under investigation in the present work) are particularly difficult to describe using this method.

Alternatively, molecular property surfaces may be constructed by fitting an explicit mathematical expression to a discrete grid of *ab initio* points. Such an expression may either be an interpolative or analytical function [2]. For instance,

Sutcliffe and Tennyson [3, 4] have employed interpolative Legendre polynomials, whereas Carter and Handy [5–10] have employed Morse-type functions in order to approximate the potential functions of triatomic molecules. Kraemer and Špirko [11] have employed Legendre polynomials in the approximation of the potential energy functions (PEFs) and dipole moment functions (DMFs) of LiH_2^+ and HeH_2^+. Malik *et al.* [12] have compared the use of Hermite and Lagrange interpolation with that of cubic spline functions for approximating potential functions used in the one-dimensional Schrödinger equation. The latter authors concluded that the efficacy of any interpolative potential function depends largely on the quality and nature of the discrete *ab initio* grid itself, regardless of the interpolation scheme employed. It is therefore recommended that any interpolative potential function relies on an extensive and dense *ab initio* grid [13]. This is illustrated by the work of Li and Le Roy [14, 15], who constructed analytical PEFs of BeH_2 and MgH_2 using cubic spline interpolation over non-uniform direct-product energy grids consisting of 6864 and 9030 symmetrically unique points, respectively.

Conversely, a molecular property surface may be represented analytically using a least-squares fitted function, such as a power series expansion or Padé approximant function. This approach has been used extensively by von Nagy-Felsobuki and co-workers [13, 16] for the potential functions of triatomic molecules. Power series expansions have also been employed with respect to molecular DMFs of triatomic molecules. For instance, Carney and Porter [17, 18] and Wang *et al.* [16, 19–22] have employed power series expansions of rectlinear normal co-ordinates to generate analytical DMFs. Jensen [23] and Kadziora and Shavitt [24] have generated molecular DMFs using power series expansions of internal co-ordinates and trigonometric functions thereof. In a similar fashion, Gabriel *et al.* [25] constructed a DMF for

H_2O using power series expansions of internal displacement co-ordinates. Following a systematic study of DMFs of H_2O, Lynas-Gray *et al.* [26] concluded that the most reliable DMF was that obtained using the scheme of Gabriel *et al.* [25]. A similar conclusion was reached by Sudarko [27], who compared the use of power series expansions of rectilinear normal co-ordinates and internal displacement co-ordinates for the DMF of the ground state of CHe_2^{3+}.

An advantage of both approaches outlined above is that the topology of the molecular property surface is defined explicitly by the discrete grid of *ab initio* points. This allows a greater portion of the surface to be modelled accurately. A global surface may therefore be achieved for a sufficiently large set of discrete points, although this may be computationally prohibitive. Nevertheless, the construction of a molecular property surface using a fitting scheme is not a 'black box' process. In addition, least-squares fitting methods are often numerically sensitive with respect to the number and position of the discrete points on the hypersurface. In an effort to alleviate this problem, von Nagy-Felsobuki and co-workers [2, 13, 28] have employed singular value decomposition (SVD) [29, 30] in the optimisation of the PEF and DMF parameters. Fitted molecular property surfaces also require physical inspection in order to ensure that the surface concurs with the anticipated physical properties of the system in question. Thus a more intensive effort is usually necessary for their construction.

The present Chapter is concerned with the analytical representation of discrete *ab initio* molecular property hypersurfaces of triatomic molecular systems (*i.e.* stage (c) of Figure 1.1). Existing least-squares fitting algorithms [2] will be employed in conjunction with power series and Padé approximant analytical functions for the PEFs of $(^1A_1)LiH_2^+$ [31] and $(^1A_1)BeH_2^{2+}$ [32] and $(^1\Sigma_g^+)BeHe_2^{2+}$ [33].

The DMFs of these species will also be constructed using power series expansions in the manner of Gabriel *et al.* [25]. The use of SVD analysis in the optimisation of PEF coefficients will also be illustrated using $(^1A_1)BeH_2^+$ [32].

The set of molecules considered in this Chapter followed two primary motivations. Firstly, $(^1A_1)LiH_2^+$and $(^1A_1)BeH_2^{2+}$are isoelectronic and therefore comparison of the topologies of these ground state PESs is of interest. Secondly, comparison between the PESs of $(^1A_1)BeH_2^{2+}$and $(^1\Sigma_g^+)BeHe_2^{2+}$ will assist in highlighting the differences exhibited by hydride and helide bonding with respect to the Be^{2+} cation.

The FORTRAN PES and DMS fitting/visualisation programs of Searles and von Nagy-Felsobuki [2, 34, 35] (fit_powpad, fit_dipcs, g_plot_pes_1 and dms_plot respectively) have been modified in this work and employed to generate analytical PEFs and DMFs of triatomic molecules. All plotting codes employ the NAG FORTRAN plotting routines [36]. The source code for all programs employed in this thesis is provided in Appendix C.

3.2. Potential Energy Surfaces and their Analytical Representation

3.2.1. Potential Energy Functions using Least-Squares Regression

The construction of an analytical PEF based on a discrete grid of *ab initio* points is generally approached so as to minimise the number of points on the PES, without compromising the accuracy of the PEF. It is therefore desirable to include points coincident with potential energy integral quadrature points in the discrete PES. The numerical quadrature method used throughout this work is that of Harris, Engerholm and Gwinn (HEG) [37] and employs up to 8000 quadrature points in the diagonalisation of the rovibrational Hamiltonian. This ensures conver-

gence in the lowest-lying vibrational eigenvectors and eigenvalues [13]. By using the HEG quadrature scheme, generally only $50 - 100$ points are required in the discrete *ab initio* PES. The initial distribution of discrete points are placed along each normal co-ordinate, thus ensuring that there is a concentration of points in the vicinity of the PES minimum.

An analytical PEF is constructed employing the following criteria [2, 13]:

1. The PEF should have a quantum mechanical basis;
2. The PEF real plane convergence properties should suggest a physically reasonable region of acceptability;
3. The PEF should accommodate several different types of experimental data;
4. The evaluation and analysis of the expansion coefficients should be systematic and amenable to numerical regression procedures;
5. The error in the PEF should not exceed that associated with the *ab initio* method employed for the PES, and;
6. The PEF should be consistent with the anticipated physical properties of the molecule in question (*viz.* be smooth throughout the domain of interest and exhibit monotonically increasing dissociative barriers).

These criteria, in conjunction with the least-squares method of von Nagy-Felsobuki and co-workers [2, 13, 28], will be employed in the generation of molecular PEFs throughout this work.

The accuracy and physical quality of a molecular PEF depend on both the expansion co-ordinate employed and the functional form of the PEF itself. The expansion variables employed in the present work include the Simons-Parr-Finlan

(SPF) [38], Ogilvie (OGL) [39] and Dunham (DUN) [40, 41] and the exponential analogues thereof (denoted ESPF, EOGL and EDUN, respectively [13, 42]). These expansion variables are defined as,

$$\rho_i^{\mathrm{SPF}} = \frac{r_i - r_i^0}{r_i} \tag{3.1}$$

$$\rho_i^{\mathrm{OGL}} = \frac{2(r_i - r_i^0)}{r_i + r_i^0} \tag{3.2}$$

$$\rho_i^{\mathrm{DUN}} = \frac{r_i - r_i^0}{r_i^0} \tag{3.3}$$

$$\rho_i^{\mathrm{ESPF}} = 1 - \exp(-\rho_i^{\mathrm{SPF}}) \tag{3.4}$$

$$\rho_i^{\mathrm{EOGL}} = 1 - \exp(-\rho_i^{\mathrm{OGL}}) \tag{3.5}$$

$$\rho_i^{\mathrm{EDUN}} = 1 - \exp(-\rho_i^{\mathrm{DUN}}) \tag{3.6}$$

where r_i and r_i^0 are the instantaneous and equilibrium bond lengths, respectively. Consequently, these expansion variables have a quantum mechanical basis and therefore satisfy criterion one [2].

The power series expansion of the variables (3.1-3.6) is of form,

$$\begin{aligned} V(\rho_1, \rho_2, \rho_3) = V_0 &+ \sum_{i=1}^{3} C_i^{(1)} \rho_i + \sum_{i=1}^{3}\sum_{j=1}^{3} C_{ij}^{(2)} \rho_i \rho_j \\ &+ \sum_{i=1}^{3}\sum_{j=1}^{3}\sum_{k=1}^{3} C_{ijk}^{(3)} \rho_i \rho_j \rho_k + \sum_{i=1}^{3}\sum_{j=1}^{3}\sum_{k=1}^{3}\sum_{l=1}^{3} C_{ijkl}^{(4)} \rho_i \rho_j \rho_k \rho_l + \ldots \end{aligned} \tag{3.7}$$

where the coefficients $C_i^{(1)}, C_{ij}^{(2)}, C_{ijk}^{(3)}, C_{ijkl}^{(4)}, \ldots$ are optimised variationally. The Padé approximant expansion of these variables is defined in a similar fashion,

$$V(\rho_1, \rho_2, \rho_3) = P(m, n) = \frac{\sum_{i,j,k=0}^{m} C_{ijk} \rho_1^i \rho_2^j \rho_3^k}{\sum_{i',j',k'=0}^{n} C_{i'j'k'} \rho_1^{i'} \rho_2^{j'} \rho_3^{k'}} \tag{3.8}$$

where $i+j+k \leq m$ and $i'+j'+k' \leq n$. As with the power series expansion (3.7), the coefficients C_{ijk} and $C_{i'j'k'}$ of equation (3.8) are optimised variationally. Padé approximants have been found to be generally more accurate with respect to the discrete *ab initio* PES [13]. As such, Padé approximants are expected to be more likely to satisfy criterion five.

For a discrete PES grid consisting of N *ab initio* points, the least-squares model for determining the coefficients of a PEF is defined as,

$$V_i^{\text{fit}} \approx \sum_{i=1}^{N} \beta_{ij} C_j \tag{3.9}$$

where $\mathbf{V}^{\text{fit}}$ is a $N \times 1$ matrix, β is a $N \times M$ matrix (for which β_{ij} contains the j^{th} independent basis function at the i^{th} point on the discrete PES) and C_j is a $M \times 1$ matrix (for which C_j contains the j^{th} coefficient of the PEF), such that $M < N$. It is required that $\mathbf{C}$ minimises the value of $(\chi^2)^{1/2}$,

$$\left(\chi^2\right)^{1/2} = \left[\sum_{i=1}^{N} \left(V_i^{\text{fit}} - V_i^{\text{ai}}\right)^2\right]^{1/2} \tag{3.10}$$

where $\mathbf{V}^{\text{ai}}$ is a $N \times 1$ matrix containing the *ab initio* points of the discrete PES.

3.2.2. Singular Value Decomposition Analysis

It is necessary, but not sufficient, that the coefficients $\mathbf{C}$ that define a PEF provide a minimum value of $(\chi^2)^{1/2}$. The coefficients $\mathbf{C}$ must also define a physically acceptable PEF in the domain of interest, according to criterion six. Determining such coefficients is notoriously difficult, particularly for higher order power series and Padé expansions. Indeed, the near-rank deficiencies in least-squares fitting

algorithms impact greatly on the suitability of a molecular PEF. This fact has been illustrated by von Nagy-Felsobuki and co-workers [28] and Carney and Porter [17, 43], with respect to the ground state of H_3^+. The optimisation of $\mathbf{C}$ may be assisted by employing the matrix factorisation technique of SVD [13, 28–30].

Re-writing equation (3.9) in matrix notation gives,

$$\mathbf{V}^{\text{fit}} \approx \beta\mathbf{C} \tag{3.11}$$

The residuals χ^2 are now of form,

$$\chi^2 = \left(\mathbf{V}^{\text{ai}} - \beta\mathbf{C}\right)^T \left(\mathbf{V}^{\text{ai}} - \beta\mathbf{C}\right) \tag{3.12}$$

Equation (3.11) is equivalent to the set of diagonal equations,

$$\mathbf{V}' \approx \mathbf{S}\mathbf{C}' \tag{3.13}$$

where $\mathbf{S} = \mathbf{U}^T\beta\mathbf{W}$ for orthogonal $N\times N$ and $M\times M$ matrices $\mathbf{U}$ and $\mathbf{W}$, respectively. The singular values of β, σ_j, are the diagonal entries of $\mathbf{S}$ and are such that $\sigma_j \geq 0$ for $j = 1, 2, \ldots, M$. Provided that $\sigma_j \neq 0\ \forall j$, the coefficients of the PEF using SVD are defined as,

$$C'_j = \frac{V'_j}{\sigma_j} \tag{3.14}$$

and the residuals may then be re-written,

$$\chi^2 = (\mathbf{c} - \mathbf{S}\mathbf{d})^T (\mathbf{c} - \mathbf{S}\mathbf{d}) \tag{3.15}$$

where $\mathbf{c} = \mathbf{U}^T\mathbf{V}^{\mathrm{ai}}$ and $\mathbf{d} = \mathbf{W}\beta$. The minimum residual is defined as,

$$\chi^{2*} = \sum_{i=1}^{N} c_i^2 \tag{3.16}$$

which may be obtained using the solution vector,

$$\beta = \mathbf{W}^T\mathbf{d} \tag{3.17}$$

where,

$$d_i = \frac{c_i}{\sigma_i} \tag{3.18}$$

Those entries for which $C'_j >> V'_j$ correspond to the j^{th} column of $\mathbf{V}^T$, the latter being a linear combination of parameters which is poorly determined by the data. In such cases treating σ_j as zero results in an increase of χ^2,

$$\chi^2 = \chi^{2*} + c_j^2 \tag{3.19}$$

As such, the use of SVD analysis with respect to PEF coefficients $\mathbf{C}$ results in a less precise fit. This is generally accompanied by a more acceptable PEF topology, devoid of fitting 'artefacts' *etc.*

3.2.3. Potential Energy Surface of $(^1\mathbf{A}_1)\mathbf{LiH}_2^+$

The LiH_2^+ complex arises from the anisotropic interaction between the charge of the Li^+ ion and the H_2 quadrupole moment [31, 44]. This fact is reflected in the binding energies of the complex, being *ca.* 0.28 eV. In addition, the ground state of LiH_2^+ exhibits a C_{2v} equilibrium structure with a bond angle of *ca.* 21° and

bond lengths of *ca.* 2.0 Å. LiH_2^+ is also an electron-sparse system (possessing only 4 electrons) and is therefore amenable to the most advanced *ab initio* methods available. As such, many theoretical investigations have scrutinised the nature of the the LiH_2^+ PES [11, 31, 45–62].

For example, Lester [47, 48] constructed a 150-point *ab initio* HF PES using the basis sets of Huzinaga [63]. Similarly, Russek *et al.* [55] calculated a 120-point HF PES for classical trajectory studies involving the LiD_2^+ collision complex. Kutzelnigg *et al.* [64] highlighted that the electron correlation within the H_2 fragment was not constant for collinear Li^+-H_2 collisions, inferring that the PESs of Lester [47, 48] and Russek *et al.* [55] may be deficient in the corresponding regions of the PES. Furthermore, Kutzelnigg *et al.* [64] incorporated electron correlation using a paired natural orbital-independent electron pair approximation to construct a 300-point PES. Kochanski [50] constructed a LiH_2^+ PES which included electron correlation *via* the use of an Epstein-Nesbet partition of the molecular Hamiltonian. As neither of these methods employed by Kutzelnigg *et al.* [64] or Kochanski [50] were variational, Searles and von Nagy-Felsobuki [44] constructed a 170-point CISD PES. Gianturco and co-workers [58–61] employed multi-reference valence bond theory and MRCI in the construction of a ground state LiH_2^+ PES, to elucidate the nature of the reaction dynamics present in the LiH_2^+ collision complex. Bulychev *et al.* [62] employed an MP2 PES for first reported calculation of LiH_2^+ spectroscopic properties. More recently, Kraemer and Špirko [11] employed MRCI and CCSD(T) in the construction of a ground state LiH_2^+ PES and DMS for a similar purpose. Similarly, Page and von Nagy-Felsobuki [31] employed FCI to construct an 83-point PES and 47-point DMS, for the calculation of rovibrational spectra of LiH_2^+.

Page and von Nagy-Felsobuki [31] have investigated the $^1A_1$ ground state of

LiH_2^+ using full CI (FCI) (as implemented in MOLPRO [65]), in conjunction with the CVTZ (Li) [66] and aug-cc-pVTZ (H) basis sets [67]. All electrons were correlated in the FCI calculation. At this level of theory, θ_e and R_e of the $^1A_1$ ground state of LiH_2^+ were determined to be 21.4° and 2.027 Å, respectively. In addition, the potential well-depth (D_e) for the $[LiH_2^+ \rightarrow (^1S_0)Li^+ + (^1\Sigma_g^+)H_2]$ dissociation channel was calculated to be 0.266 eV. This well-depth agreed favorably with the previously calculated values of 0.263 eV (MP2) [62], 0.255 eV (CCSD) [56] and 0.258 eV (CISD) [44]. With respect to experiment, D_0 has been measured to be 0.282 ± 0.199 eV [68]. Any comparison with the corresponding experimental D_e and these calculated values would be futile, due to the magnitude of error in the experimental measurement. The FCI PES of $(^1A_1)LiH_2^+$ ultimately consisted of 83 discrete points, and is given in Table 3.1.

In order to determine the most suitable analytical PEF for $(^1A_1)LiH_2^+$, both power series and Padé approximant functions were fitted to the FCI PES grid given in Table 3.1. All power series expansions were restricted to 7^{th} order and all Padé approximant functions were restricted to 6^{th} order. As such, all constructed analytical PEFs were uniquely defined. The $(\chi^2)^{1/2}$ values of all power series and Padé approximant PEFs for LiH_2^+ are summarised in Table 3.2.

Page and von Nagy-Felsobuki [31] determined that the most suitable PEF for $(^1A_1)LiH_2^+$ was the $P(5,5)$ Padé approximant function of the OGL variable, with the singular value σ_{67} set to zero using SVD analysis. This PEF exhibited a $(\chi^2)^{1/2}$ value of 2.41×10^{-5} E_h. The optimised coefficients of the $P(5,5)$ OGL PEF are given in Table 3.3. Two-dimensional (2D) energy projections are shown in terms of normal co-ordinates in Figure 3.1. The normal co-ordinates for both non-linear ($\mathbf{t}$) and linear ($\mathbf{w}$) triatomic molecules are discussed at greater length in Chapter Four.

Table 3.1 Discrete FCI PES grid of $(^1A_1)LiH_2^+$.

$R_{H\text{-}Li}$ $(/a_0)$	$R_{Li\text{-}H}$ $(/a_0)$	$R_{H\text{-}H}$ $(/a_0)$	Energy $(/E_h)$	$R_{H\text{-}Li}$ $(/a_0)$	$R_{Li\text{-}H}$ $(/a_0)$	$R_{H\text{-}H}$ $(/a_0)$	Energy $(/E_h)$
3.83100	3.83100	1.42145	-8.4592693576	4.69037	4.69037	0.67719	-8.1674063038
6.83897	6.83897	2.53752	-8.3703799204	4.28652	4.28652	0.59799	-8.0393733235
6.43839	6.43839	2.38889	-8.3835889480	2.80438	2.80438	0.68784	-8.1715878650
6.82991	6.82991	3.23186	-8.3243877113	2.43686	2.43686	0.69294	-8.1528838555
6.86663	6.86663	1.84317	-8.4297060444	5.10637	5.10637	0.61751	-8.0738740517
6.44126	6.44126	3.77758	-8.3034349629	5.29910	5.29910	0.76126	-8.2616495634
6.07765	6.07765	4.32329	-8.2922498430	3.73646	3.73646	0.82138	-8.3149684049
6.03782	6.03782	2.24026	-8.3975064955	2.44052	2.44052	0.62351	-8.0522017249
5.63724	5.63724	2.09163	-8.4118264159	3.65563	4.21159	0.55644	-7.9498197072
6.02999	6.02999	2.93460	-8.3439437712	4.21159	3.65563	0.55644	-7.9498197072
6.06671	6.06671	1.54591	-8.4497981595	3.54587	4.15530	1.13141	-8.4363299759
6.83952	6.83952	3.92621	-8.2982852563	4.31902	3.38259	1.32805	-8.4532116681
6.91267	6.91267	1.14883	-8.4344756003	3.03031	4.69315	3.24040	-8.3243874568
4.03129	4.03129	1.49576	-8.4581568426	4.50049	3.38671	3.81030	-8.3079311595
3.63071	3.63071	1.34713	-8.4579170014	3.51743	2.57620	1.45493	-8.4368263051
4.23158	4.23158	1.57008	-8.4552110789	4.39111	4.03734	1.60108	-8.4535426846
3.43043	3.43043	1.27282	-8.4532516555	5.78042	4.18201	2.41559	-8.3847724523
4.63215	4.63215	1.71870	-8.4456059386	4.31247	5.32283	2.04005	-8.4184731759
3.02985	3.02985	1.12419	-8.4289442190	3.22701	5.49285	2.73472	-8.3557206021
3.82597	3.82597	1.76862	-8.4446022239	2.53501	4.47731	2.29455	-8.3701143746
3.84434	3.84434	1.07427	-8.4266629293	2.65113	3.06939	1.13662	-8.4214242807
3.82927	3.82927	2.11579	-8.4166367030	3.75919	4.37255	1.98723	-8.4263675648
3.86589	3.86589	0.72710	-8.2301460081	4.02447	5.03048	3.20563	-8.3348073307
3.86074	3.86074	2.81014	-8.3608440940	3.70181	3.35006	0.90873	-8.3668529510
4.22827	4.22827	2.26442	-8.4035899716	3.70067	2.76659	2.51449	-8.3643969853
4.26492	4.26492	0.87573	-8.3493940661	4.13245	2.52052	4.87989	-8.2560043492
3.43064	3.43064	1.96716	-8.4261296902	4.26119	3.53112	0.81630	-8.3082411500
5.43331	5.43331	2.01596	-8.4191259348	2.22870	2.22870	0.82693	-8.2470905876
3.86074	3.86074	2.81014	-8.3608440940	6.23446	6.23446	2.31322	-8.3906018800
4.01934	4.01934	4.19883	-8.3017914790	4.29254	4.29254	5.58752	-8.2885498546
2.64897	2.64897	0.55895	-7.9396943209	5.97269	1.69394	4.40189	-8.1176177832
3.47427	4.18782	1.58197	-8.4530969326	1.69394	5.97269	4.40189	-8.1176177832
3.11767	4.54471	1.98720	-8.4184828720	2.68891	2.68891	2.36425	-8.3480641012
2.76122	4.90164	2.52181	-8.3613594122	2.60397	2.60397	2.98428	-8.2812949953
2.40502	5.25863	3.11999	-8.2969088683	2.92718	2.92718	3.75294	-8.2797763175
3.67827	1.18202	2.59194	-7.9263116291	3.65655	0.80496	2.89787	-7.3751162742
3.98482	6.48206	3.11061	-8.3343537876	5.37194	1.09505	4.33504	-7.7442257247
2.52848	2.52848	0.50231	-7.7811405279	3.04181	0.61825	2.45629	-6.8369494113
5.28775	5.28775	0.90013	-8.3601088553	3.23626	3.23626	0.63516	-8.1047786916
4.96904	4.96904	0.78123	-8.2802967056	2.64049	2.64049	0.69782	-8.1757216687
7.03561	7.03561	2.61048	-8.3642161707	3.05300	3.05300	0.63815	-8.1070594477
2.40053	2.40053	0.60865	-8.0219057248				

Table 3.2 $(\chi^2)^{1/2}$ values (/E_h) of least-squares fitted PEFs for $(^1A_1)LiH_2^+$.

m	n	Number of Coefficients	SPF	OGL	DUN	ESPF	EOGL	EDUN
				Power Series				
3		13	5.97−02[a]	2.18−01	8.61−01	3.71−01	4.04−02	2.79−01
4		22	4.29−02	4.61−02	4.29−01	1.54−01	3.18−02	7.28−02
5		34	2.47−02	6.11−03	1.41−01	5.02−02	2.06−02	8.59−03
6		50	8.72−03	1.13−03	3.45−02	4.66−02	9.28−03	2.82−03
7		70	3.35−03	2.62−04	7.64−03	6.81+01	3.70−03	1.56−04
				Padé Approximant				
4	4	43	2.46−03	6.49−04	3.79−03	8.31−03	2.02−03	1.02−03
4	5	55	6.37−04	1.41−04	3.58−04	2.49−02	6.41−04	1.19−04
5	4	55	3.04−03	4.16−04	3.81−04	2.45−02	7.81−04	2.06−04
5	5	67	1.10−03	1.99−05	4.14−05	2.65−02	1.48−04	1.41−05
4	6	71	3.01−04	1.82−05	2.52−05	1.95−00	4.42−03	1.12−05
6	4	71	4.71−04	1.82−05	2.09−05	3.47−02	4.83−04	1.09−05
5	6	83	4.97−07	3.61−07	9.74−07	2.03−00	1.29−06	1.43−07
6	5	83	3.05−06	2.26−07	9.29−07	5.57−02	3.95−07	2.04−07

[a]5.97-02 denotes 5.97×10^{-2}.

Table 3.3 $P(5,5)$ FCI PEF of $(^1A_1)LiH_2^+$.

Expansion Variable	Expansion Coefficient[a]		Expansion Variable	Expansion Coefficient[a]	
	Numerator	Denominator		Numerator	
1	−8.45927	1.00000	$\rho_1\rho_3^3 + \rho_2\rho_3^3$	−0.48684	−0.04225
$\rho_1 + \rho_2$	−0.35389	−0.04182	$\rho_1^2\rho_2^2$	−0.91369	−0.11575
ρ_3	7.44789	0.88041	$\rho_1^2\rho_3^2 + \rho_2^2\rho_3^2$	0.68407	0.07702
$\rho_1^2 + \rho_2^2$	−0.32568	−0.05002	$\rho_1^2\rho_2\rho_3 + \rho_1\rho_2^2\rho_3$	−0.35578	−0.04157
ρ_3^2	−0.50382	−0.10126	$\rho_1\rho_2\rho_3^2$	−1.02203	−0.11737
$\rho_1\rho_2$	−0.61305	−0.06228	$\rho_1^5 + \rho_2^5$	0.35384	0.04218
$\rho_2\rho_3 + \rho_1\rho_3$	2.85792	0.33865	ρ_3^5	−0.31153	−0.03004
$\rho_1^3 + \rho_2^3$	−0.91065	−0.09652	$\rho_1^4\rho_2 + \rho_1\rho_2^4$	−1.60778	−0.18455
ρ_3^3	−2.66822	−0.25257	$\rho_1^4\rho_3 + \rho_2^4\rho_3$	−0.09778	−0.00883
$\rho_1^2\rho_2 + \rho_1\rho_2^2$	0.29928	0.03978	$\rho_1\rho_3^4 + \rho_2\rho_3^4$	0.28490	0.02592
$\rho_1^2\rho_3 + \rho_2^2\rho_3$	0.86255	0.11254	$\rho_1^3\rho_2^2 + \rho_1^2\rho_2^3$	0.85707	0.10306
$\rho_1\rho_3^2 + \rho_2\rho_3^2$	0.29797	0.03376	$\rho_1^3\rho_3^2 + \rho_2^3\rho_3^2$	−1.39617	−0.17138
$\rho_1\rho_2\rho_3$	−2.20076	−0.28353	$\rho_1^2\rho_3^3 + \rho_2^2\rho_3^3$	0.78176	0.09533
$\rho_1^4 + \rho_2^4$	−0.86984	−0.11424	$\rho_1^3\rho_2\rho_3 + \rho_1\rho_2^3\rho_3$	2.23376	0.26369
ρ_3^4	0.50820	0.02310	$\rho_1\rho_2\rho_3^3$	−1.59244	−0.19373
$\rho_1^3\rho_2 + \rho_1\rho_3^2$	2.48456	0.29230	$\rho_1^2\rho_2^2\rho_3$	−1.44861	−0.17276
$\rho_1^3\rho_3 + \rho_2^3\rho_3$	−0.99427	−0.11856	$\rho_1^2\rho_2\rho_3^2 + \rho_1\rho_2^2\rho_3^2$	0.52514	0.06629
$(\chi^2)^{1/2} = 2.41 \times 10^{-5}$ E_h					

[a]All coefficients given in E_h.

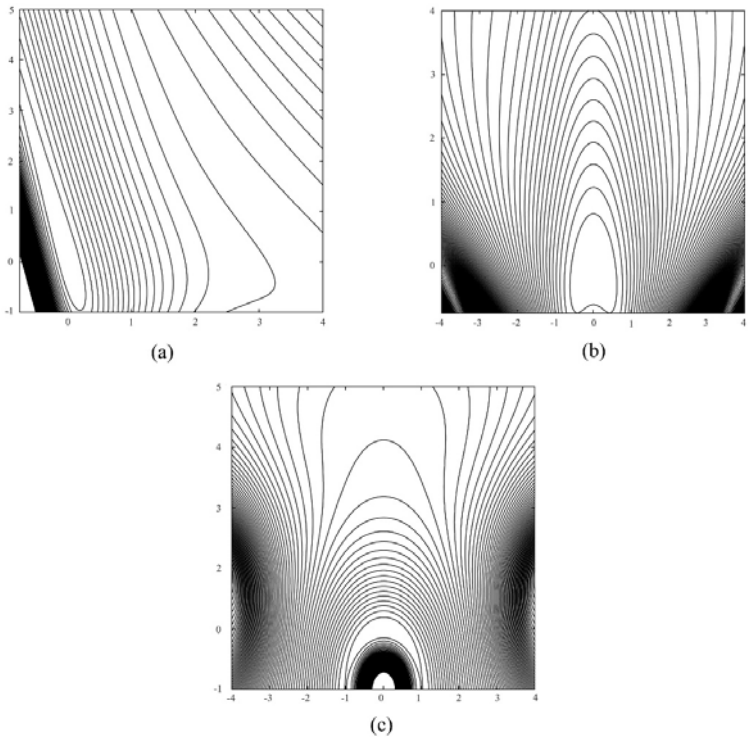

Figure 3.1 Two-dimensional projections of the $(^1A_1)LiH_2^+$ $P(5,5)$ OGL PEF in terms of normal co-ordinates: (a) t_2 (x) versus t_1 (y); (b) t_3 (x) versus t_1 (y); (c) t_3 (x) versus t_2 (y). Contours spaced at 25 kJ mol^{-1}.

3.2.4. Potential Energy Surface of $(^1\mathbf{A}_1)\mathbf{BeH}_2^{2+}$

The BeH_2^{2+} complex shares several similarities with the isolelectronic LiH_2^+ collision complex. Most notably, BeH_2^{2+} is the result of the anisotropic interaction between the Be^{2+} charge state and the H_2 quadrupole moment [32]. The physical properties of the ground state of BeH_2^{2+} therefore bear resemblance to those of LiH_2^+. For example, the binding energy of BeH_2^{2+} is *ca.* 2.38 eV, whereas the C_{2v} equilibrium structure exhibits a bond angle and bond lengths of *ca.* 29° and 1.6 Å, respectively. It is interesting then that fewer efforts to characterise the BeH_2^{2+} PES have been reported in the literature. For example, Musaev and Charkin [69] con-

structed a ground state PES employing MP3 and a 3-21G* basis set. Similarly, Valtazanos and Nicolaides [70] employed MRCISD in conjunction with an augmented Dunning-Hay double-ζ basis set [71] to investigate the ground state PES of BeH_2^{2+}. More recently, Page and von Nagy-Felsobuki [32], used IC-MRCI [32] and CCSD(T) [72] combined with augmented quadruple-ζ basis sets to calculate a ground state PES and DMS for BeH_2^{2+} (see Chapter 6).

Page and von Nagy-Felsobuki [32] have constructed a discrete PES of $(^1A_1)BeH_2^{2+}$, employing IC-MRCI (as implemented in MOLPRO [65]) in conjunction with the aug-CVQZ (Be) [66, 73] and aug-cc-pVQZ (H) [67, 74] basis sets. The SSFC method [75] was employed for all points on the discrete PES in order to account for BSSE. The IC-MRCI wave function included single and double excitations from an optimised CASSCF wave function, and all electrons were included in the correlated calculation. The CASSCF wave function spanned the $1s$, $2s$, $2p$, $3s$, $3p$, $3d$, $4s$ and $4p$ AOs of beryllium and the $1s$, $2s$, $2p$ and $3s$ AOs of hydrogen. The CASSCF orbital set was based on a closed-shell HF determinant. The equilibrium structure of the ground state of BeH_2^{2+} employing this method was shown to exhibit a bond angle of 29.4° and a bond length of 1.609 Å. Ultimately, the IC-MRCI PES grid consisted of 89 points, as is evident from Table 3.4. All points on the discrete PES grid were within ± 3.0 a_0 from the equilibrium geometry.

The IC-MRCI discrete PES of Page and von Nagy-Felsobuki [32] given in Table 3.4 has been fitted with several power series and Padé approximant expansions in an effort to determine the most suitable analytical PEF. As for the ground state of LiH_2^+, the highest power series and Padé approximant orders employed for BeH_2^{2+} were 7^{th} order and 6^{th} order, respectively. The coefficients of each PEF were therefore uniquely defined. The $(\chi^2)^{1/2}$ values of these power series and Padé ap-

Table 3.4 Discrete IC-MRCI PES grid of $(^1A_1)BeH_2^{2+}$.

$R_{\text{H-Be}}$ ($/a_0$)	$R_{\text{Be-H}}$ ($/a_0$)	$R_{\text{H-H}}$ ($/a_0$)	Energy ($/E_h$)	$R_{\text{H-Li}}$ ($/a_0$)	$R_{\text{Li-H}}$ ($/a_0$)	$R_{\text{H-H}}$ ($/a_0$)	Energy ($/E_h$)
3.04011	3.04011	1.54159	-14.916075510	3.89199	1.79208	2.46735	-14.765305690
1.47698	1.47698	0.74895	-14.250605820	2.30926	3.10939	1.57149	-14.893646870
1.86776	1.86776	0.94711	-14.670265840	3.82138	3.48011	1.87962	-14.896326340
2.10223	2.10223	1.06601	-14.789572380	2.99280	4.02502	2.03340	-14.891642240
2.33670	2.33670	1.18490	-14.857698060	3.33676	2.76989	1.34691	-14.906682780
2.57117	2.57117	1.30380	-14.894437900	2.55441	3.57789	1.43545	-14.902684020
2.80564	2.80564	1.42269	-14.911510300	3.81689	2.30955	2.98521	-14.820350680
3.27458	3.27458	1.66049	-14.912682660	2.40822	3.67771	2.55216	-14.851276630
3.50905	3.50905	1.77938	-14.904239030	3.71074	3.71074	1.53663	-14.901975980
3.74352	3.74352	1.89828	-14.892681330	2.65469	2.65469	0.80756	-14.735966990
3.97799	3.97799	2.01717	-14.879316060	2.29923	2.29923	0.81955	-14.719883710
4.21246	4.21246	2.13607	-14.865041770	4.41219	4.41219	3.78795	-14.786788500
4.60325	4.60325	2.33423	-14.840851780	2.15478	2.15478	1.73684	-14.811055510
3.16118	3.16118	0.17469	-10.781028200	1.02399	3.27071	2.40411	-14.077840610
3.14192	3.14192	0.31138	-13.179738470	3.47026	1.78181	2.08950	-14.780391400
3.09340	3.09340	0.72145	-14.653377520	4.91086	2.96185	2.72738	-14.850913580
3.05930	3.05930	1.13152	-14.882316130	1.14517	2.59131	1.67326	-14.316566960
3.03611	3.03611	1.95166	-14.902247780	3.79618	2.36981	1.62454	-14.892985220
3.04735	3.04735	2.36173	-14.877312790	3.50512	2.75950	3.39342	-14.818784560
3.07367	3.07367	2.77181	-14.852499830	2.62420	3.77798	3.92803	-14.795461120
3.11470	3.11470	3.18188	-14.831414550	2.87993	2.87993	0.75574	-14.692310670
3.16984	3.16984	3.59195	-14.814876980	2.35624	2.35624	2.52837	-14.789492480
4.47418	1.60859	3.13851	-14.672244170	2.43192	2.43192	2.21710	-14.834779650
4.11557	1.96593	2.56524	-14.804123230	3.85698	1.60971	2.55250	-14.690872750
3.90043	2.18057	2.25101	-14.851528100	1.72143	4.58712	3.16704	-14.718836160
3.68530	2.39534	1.97229	-14.884326660	2.00966	3.45601	1.95518	-14.842464170
3.47021	2.61020	1.74618	-14.904593600	4.47117	1.60019	3.30501	-14.659819230
2.89678	3.18346	1.56564	-14.915175220	1.81570	4.30681	3.48912	-14.724483480
2.46695	3.61360	1.89005	-14.892425700	4.37686	1.74169	2.80058	-14.738974840
2.25215	3.82872	2.15344	-14.863925780	4.24623	4.24623	1.67659	-14.882738730
2.03746	4.04385	2.45736	-14.821818470	4.61836	4.61836	1.64155	-14.871352880
1.68000	4.40245	3.02019	-14.706319290	1.99256	1.99256	2.47493	-14.652814810
3.23079	3.23079	1.98240	-14.900683490	1.98261	1.98261	3.05526	-14.584536230
2.86003	2.86003	1.10078	-14.875710100	2.79310	3.11934	1.06792	-14.865907430
3.05634	3.41469	1.67588	-14.912221850	3.43657	2.88528	1.91154	-14.902895770
3.05975	2.62974	1.49967	-14.910756120	3.66474	2.89299	2.19395	-14.886481960
2.67685	3.39458	2.00349	-14.894897710	3.30207	0.44123	2.89322	-10.906211240
3.25738	2.90373	0.92368	-14.809846970	2.04374	4.64840	5.07472	-14.724912450
3.05472	3.48534	2.11077	-14.892704120	3.29114	3.29114	4.27540	-14.796205750
3.04597	2.34103	0.95009	-14.809426100	3.44571	3.44571	4.95885	-14.785011090
3.50481	3.50481	2.30978	-14.878249620	4.70064	2.15994	5.36578	-14.735202470
3.79539	3.79539	2.63013	-14.853117440	2.41566	4.82350	5.96405	-14.748454000
2.64587	2.64587	1.70407	-14.899621920	3.17080	6.03714	3.59477	-14.813337430
2.74103	2.74103	1.07412	-14.867087610	5.22111	5.22111	1.94802	-14.842490780
2.50874	2.50874	2.69250	-14.807831450				

proximant functions, in conjunction with the SPF, OGL, DUN expansion variables (and their exponential analogues) are provided in Table 3.5.

The most suitable PEF was ultimately determined to be the $P(6,5)$ Padé expansion of the OGL variable, setting $\sigma_{65,67-69,71-83} = 0$ with SVD analysis. This PEF exhibited a $(\chi^2)^{1/2}$ value of 2.37×10^{-5} E_h. The coefficients of the $P(6,5)$ OGL PEF are listed in Table 3.6, and 2D constant energy projections are shown in Figure 3.2. For the purposes of comparison, a $P(6,5)$ OGL function has been generated without the assistance of SVD, and is also included in Figure 3.2. From Table 3.5 it is clear that the $(\chi^2)^{1/2}$ value for the latter PEF is 3.71×10^{-6} E_h, and as such exceeds the accuracy of the SVD $P(6,5)$ OGL defined in Table 3.6. However, the irregularities exhibited by this non-SVD PEF observed in Figure 3.2 indicate that this PEF is unsuitable for use in the numerical solution of the nuclear Schrödinger eigenvalue problem.

Table 3.5 $(\chi^2)^{1/2}$ values ($/E_h$) of least-squares fitted PEFs for $(^1A_1)BeH_2^{2+}$.

m	n	Number of Coefficients	SPF	OGL	DUN	ESPF	EOGL	EDUN
Power Series								
3		13	1.35−01[a]	8.34−01	2.97−00	4.58−01	1.41−01	1.04−00
4		22	2.27−02	3.34−01	1.35−00	1.64−01	1.63−02	4.35−01
5		34	1.07−02	6.99−02	8.67−01	1.35+02	6.98−03	1.12−01
6		50	2.66−03	1.04−02	5.24−01	1.36+02	2.11−03	1.85−02
7		70	3.03−04	5.07−04	1.33−01	1.37+02	2.46−04	1.07−03
Padé Approximant								
4	4	43	8.13−03	6.80−02	1.02−02	5.73−02	3.50−02	1.89−02
4	5	55	2.45−04	3.11−04	9.29−03	1.39+02	2.89−04	2.83−04
5	4	55	2.23−04	1.95−04	8.65−03	1.36+02	3.42−04	2.87−04
5	5	67	3.48−05	3.57−05	1.35−03	1.37+02	4.63−05	4.48−05
4	6	71	1.09−04	2.07−05	5.97−04	1.37+02	2.70−05	6.12−05
6	4	71	9.33−05	1.12−04	3.88−04	1.37+02	1.34−04	4.77−05
5	6	83	3.32−05	7.62−06	3.70−06	1.37+02	1.81−05	5.87−06
6	5	83	1.30−05	1.17−05	3.71−06	1.37+02	8.35−06	8.99−06

[a] 1.35-01 denotes 1.35×10^{-1}.

Table 3.6 $P(6,5)$ OGL PEF of $(^1A_1)BeH_2^{2+}$.

Expansion Variable	Expansion Coefficient[a] Numerator	Denominator	Expansion Variable	Expansion Coefficient[a] Numerator	Denominator
1	-14.91608	1.00000	$\rho_1^4\rho_3 + \rho_2^4\rho_3$	1.13607	0.09062
$\rho_1 + \rho_2$	-1.02216	-0.06851	$\rho_1\rho_3^4 + \rho_2\rho_3^4$	0.39635	0.02892
ρ_3	9.42432	0.63179	$\rho_1^3\rho_2^2 + \rho_1^2\rho_2^3$	-0.99972	-0.06327
$\rho_1^2 + \rho_2^2$	-3.20434	-0.22909	$\rho_1^3\rho_3^2 + \rho_2^3\rho_3^2$	2.00360	0.12824
ρ_3^2	2.52618	0.14997	$\rho_1^2\rho_3^3 + \rho_2^2\rho_3^3$	1.98883	0.12973
$\rho_1\rho_2$	2.28407	0.14949	$\rho_1^3\rho_2\rho_3 + \rho_1\rho_2^3\rho_3$	-0.58792	-0.03691
$\rho_2\rho_3 + \rho_1\rho_3$	-2.46649	-0.16167	$\rho_1\rho_2\rho_3^3$	-5.00373	-0.32754
$\rho_1^3 + \rho_2^3$	-1.49899	-0.08402	$\rho_1^2\rho_2^2\rho_3$	1.21895	0.07156
ρ_3^3	-4.70489	-0.29012	$\rho_1^2\rho_2\rho_3^2 + \rho_1\rho_2^2\rho_3^2$	-0.11261	-0.00868
$\rho_1^2\rho_2 + \rho_1\rho_2^2$	0.72998	0.05343	$\rho_1^6 + \rho_2^6$	0.10293	
$\rho_1^2\rho_3 + \rho_2^2\rho_3$	-1.08487	-0.06287	ρ_3^6	-0.01779	
$\rho_1\rho_3^2 + \rho_2\rho_3^2$	0.18929	0.01186	$\rho_1^5\rho_2 + \rho_1\rho_2^5$	-0.23762	
$\rho_1\rho_2\rho_3$	1.66527	0.09003	$\rho_1^5\rho_3 + \rho_2^5\rho_3$	-0.09470	
$\rho_1^4 + \rho_2^4$	-0.92384	-0.07711	$\rho_1\rho_3^5 + \rho_2\rho_3^5$	-0.00615	
ρ_3^4	-0.10542	-0.01785	$\rho_1^4\rho_2^2 + \rho_1^2\rho_2^4$	0.05226	
$\rho_1^3\rho_2 + \rho_1\rho_3^2$	1.54007	0.10829	$\rho_1^4\rho_3^2 + \rho_2^4\rho_3^2$	0.02930	
$\rho_1^3\rho_3 + \rho_2^3\rho_3$	4.71765	0.30947	$\rho_1^2\rho_3^4 + \rho_2^2\rho_3^4$	-0.01047	
$\rho_1\rho_3^3 + \rho_2\rho_3^3$	0.59241	0.03577	$\rho_1^4\rho_2\rho_3 + \rho_1\rho_2^4\rho_3$	0.13711	
$\rho_1^2\rho_2^2$	-0.21197	-0.02674	$\rho_1\rho_2\rho_3^4$	0.12887	
$\rho_1^2\rho_3^2 + \rho_2^2\rho_3^2$	0.61249	0.03784	$\rho_1^3\rho_2^3$	0.30481	
$\rho_1^2\rho_2\rho_3 + \rho_1\rho_2^2\rho_3$	-2.25794	-0.15816	$\rho_1^3\rho_3^3 + \rho_2^3\rho_3^3$	-0.10560	
$\rho_1\rho_2\rho_3^2$	-1.86607	-0.10698	$\rho_1^3\rho_2^2\rho_3 + \rho_1^2\rho_2^3\rho_3$	-0.03784	
$\rho_1^5 + \rho_2^5$	-1.34577	-0.08630	$\rho_1^3\rho_2\rho_3^2 + \rho_1\rho_2^3\rho_3^2$	0.20543	
ρ_3^5	0.21380	0.01335	$\rho_1^2\rho_2\rho_3^3 + \rho_1\rho_2^2\rho_3^3$	-0.01800	
$\rho_1^4\rho_2 + \rho_1\rho_2^4$	0.46964	0.03409	$\rho_1^2\rho_2^2\rho_3^2$	-0.53313	
$(\chi^2)^{1/2} = 2.37 \times 10^{-5}$ E_h					

[a]All coefficients given in E_h.

3.2.5. Potential Energy Surface of $(^1\Sigma_g^+)BeHe_2^{2+}$

Small beryllium helide cations have been the focus of several *ab initio* investigations [33, 73, 76–85]. However, these investigations have dwelt upon the singly and double charged diatomics, and hence studies of $BeHe_2^{2+}$ are rare. For instance, Harrison *et al.* [77] predicted $BeHe_2^{2+}$ to be linear and bound by 74.04 kJ mol^{-1} (with respect to dissociation into $BeHe^{2+}$ + He), using HF. To date, the only study of $BeHe_2^{2+}$ reported using a correlated level of theory is that of Page *et al.* [33], who

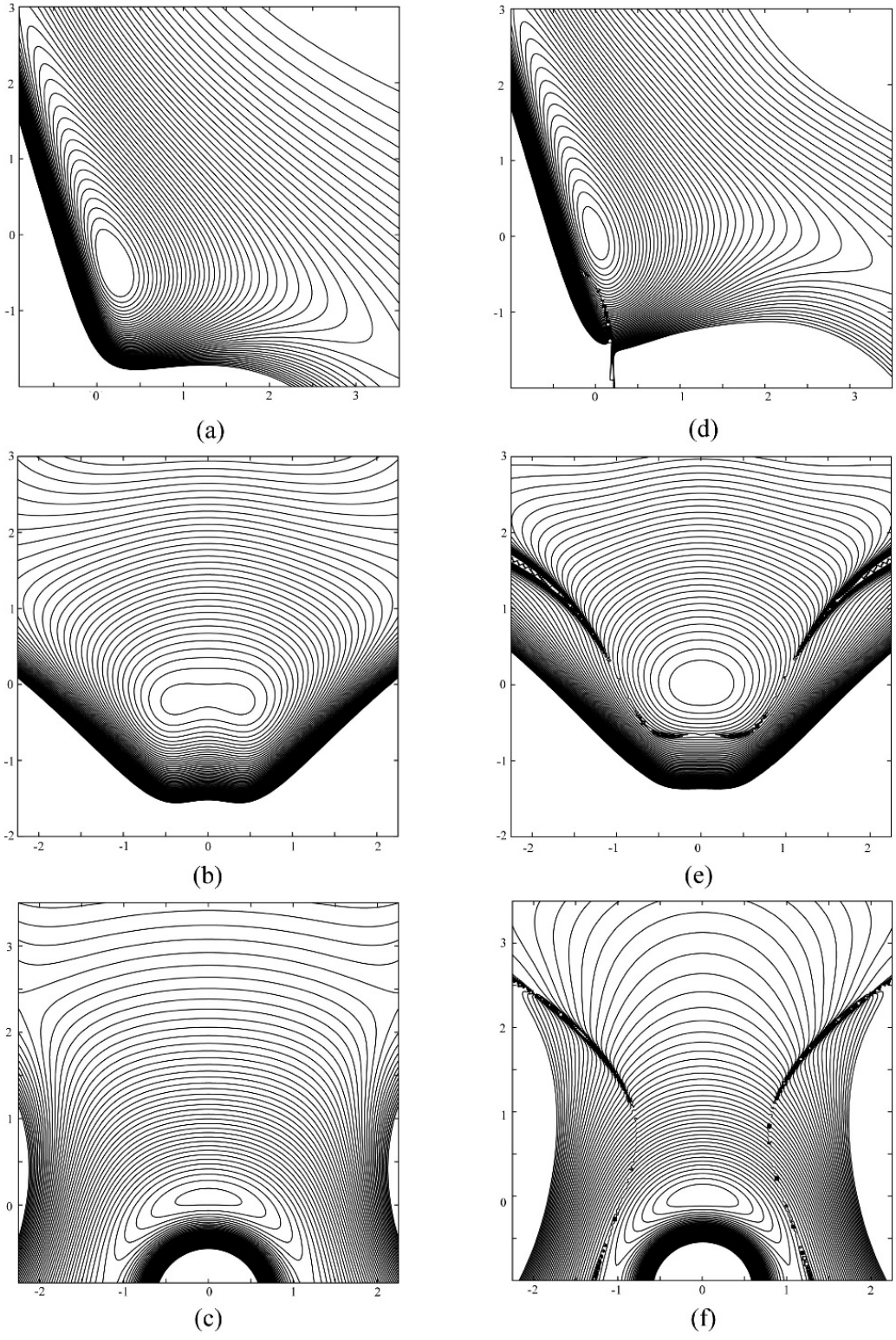

Figure 3.2 The removal of fitting artefacts using SVD for the $(^1A_1)BeH_2^{2+}$ $P(6,5)$ OGL PEF. Figures (a,b,c) and (d,e,f) were constructed with and without SVD, respectively: (a,d) t_2 (x) versus t_1 (y); (b,e) t_3 (x) versus t_1 (y); (c,f) t_3 (x) versus t_2 (y). Contours spaced at 10 kJ mol^{-1}.

employed both IC-MRCI and CCSD(T) in order to characterise the ground state PES of $BeHe_2^{2+}$. This investigation is also the only published PES of the ground state of $BeHe_2^{2+}$ available.

Page *et al.* [33] have employed all-electron IC-MRCI to construct a PES of the $(^1\Sigma_g^+)$ ground state of $BeHe_2^{2+}$. In a similar fashion to the IC-MRCI method for BeH_2^{2+}, the IC-MRCI wave function was based upon an optimised CASSCF, which spanned the beryllium $1s$, $2s$, $2p$, $3s$, $3p$, $3d$, $4s$ and $4p$ AOs of beryllium and the $1s$, $2s$, $2p$ and $3s$ AOs of helium, respectively. In addition, all He $1s$ AO density was excluded from the CASSCF optimisation and included in the subsequent IC-MRCI calculation. Employing this method yielded an equilibrium Be - He bond length of 1.4372 Å, a value which was in excellent with the all-electron CCSD(T) value of 1.4373 Å [33]. Similar consistency was observed with respect to the potential well-depth for the $[(^1\Sigma_g^+)BeHe_2^{2+} + (^1\Sigma^+)BeHe^{2+} + He]$ dissociation channel. For example, the IC-MRCI well-depth was 85.01 kJ mol^{-1}, a value 0.03 kJ mol^{-1} larger than the corresponding CCSD(T) well-depth. The final PES grid reported by Page *et al.* [33] consisted of 87 points, as is evident from Table 3.7.

Several power series and Padé approximant representations to the $(^1\Sigma_g^+)BeHe_2^{2+}$ IC-MRCI grid have been constructed in conjunction with expansion variables (3.1-3.6). In all cases the number of coefficients did not exceed 87, and so each PEF was uniquely defined. The $(\chi^2)^{1/2}$ values for all constructed PEFs for $(^1\Sigma_g^+)BeHe_2^{2+}$ are detailed in Table 3.8. The (6,5) Padé expansion of the EOGL variable with $\sigma_{60,62-74} = 0$ using SVD analysis was ultimately determined to be the most appropriate representation of the $(^1\Sigma_g^+)BeHe_2^{2+}$ IC-MRCI PES grid. The $(\chi^2)^{1/2}$ of this PEF was calculated to be 3.14×10^{-5} E_h. This PEF is shown in Figure 3.3 (as 2D constant energy contour plots) and defined in Table 3.9.

Table 3.7 Discrete IC-MRCI PES grid of $(^1\Sigma_g^+)BeHe_2^{2+}$.

$R_{\text{He-Be}}$ $(/a_0)$	$R_{\text{Be-He}}$ $(/a_0)$	$R_{\text{He-He}}$ $(/a_0)$	Energy $(/\text{E}_h)$	$R_{\text{He-Be}}$ $(/a_0)$	$R_{\text{Be-He}}$ $(/a_0)$	$R_{\text{He-He}}$ $(/a_0)$	Energy $(/\text{E}_h)$
2.71591	2.71591	5.43182	-19.52603671	1.68694	2.85333	4.54028	-19.37072327
2.79819	2.79819	5.59638	-19.52553894	3.14348	2.31371	5.43182	-19.51117754
2.63363	2.63363	5.26725	-19.52543837	3.24291	2.25985	5.43182	-19.50562774
2.88047	2.88047	5.76095	-19.52420944	3.07866	2.57598	5.43182	-19.52153072
2.55134	2.55134	5.10269	-19.52337011	3.62797	2.15922	5.43182	-19.48915187
2.96276	2.96276	5.92551	-19.52226392	3.73077	2.56531	5.43182	-19.50996624
2.46906	2.46906	4.93813	-19.51949227	2.64798	3.93849	5.43182	-19.50770917
2.71826	2.71826	5.43182	-19.52603918	2.60158	2.96486	5.43182	-19.52354042
2.72120	2.72120	5.43182	-19.52602406	2.63924	3.26210	5.43182	-19.51893547
2.72531	2.72531	5.43182	-19.52601887	2.54311	2.91370	5.43182	-19.52333586
2.73058	2.73058	5.43182	-19.52600819	2.37800	3.19110	5.43182	-19.51391549
2.73701	2.73701	5.43182	-19.52598805	2.35211	3.30786	5.43182	-19.51052594
2.74459	2.74459	5.43182	-19.52595811	2.35318	3.74665	5.43182	-19.50300304
2.82898	2.60284	5.43182	-19.52501346	2.56559	3.73097	5.43182	-19.50996757
2.94204	2.48977	5.43182	-19.52182636	2.64829	3.93871	5.43182	-19.50770768
3.05511	2.37671	5.43182	-19.51611174	3.01943	3.85290	5.75147	-19.50625160
2.66905	3.22912	5.84323	-19.51980750	3.07173	3.46608	4.92677	-19.51114662
2.88408	2.34087	5.02041	-19.51645909	4.59991	3.36283	7.29181	-19.49225245
2.68383	3.77822	6.25464	-19.51041507	3.97113	2.44197	6.26687	-19.50378765
2.96837	1.89736	4.60900	-19.45149460	3.71498	3.71498	7.07746	-19.49628924
2.75927	4.34963	6.66605	-19.50332278	3.17801	3.17801	6.25464	-19.51539412
2.89060	4.93561	7.07746	-19.49809476	1.86381	1.86381	2.96335	-19.35987805
3.53873	3.53873	7.07746	-19.50229912	2.94915	2.94915	3.78617	-19.51734956
2.94187	2.94187	5.43182	-19.52264652	4.36155	4.36155	8.72311	-19.47961465
1.58523	3.84658	5.43182	-19.29289278	4.77297	4.77297	9.54593	-19.47307931
1.89309	1.89309	3.78617	-19.37694776	2.15057	3.28125	5.43182	-19.49416286
3.06165	3.06165	5.43182	-19.51908469	1.01990	4.41192	5.43182	-18.26171837
3.84658	1.58523	5.43182	-19.29289278	1.89309	1.89309	3.78617	-19.37694777
3.95014	3.95014	7.90029	-19.48923086	0.76241	3.02376	3.78617	-16.81446823
3.20197	3.20197	5.43182	-19.51420267	5.49223	3.23088	8.72311	-19.49042738
3.36026	3.36026	5.43182	-19.50835492	1.99665	4.25799	6.25464	-19.45551912
3.29151	6.13449	7.90029	-19.48788590	2.37283	2.37283	4.60900	-19.51207840
3.53410	3.53410	5.43182	-19.50202247	2.20504	2.20504	3.78617	-19.48783987
3.91999	3.91999	5.43182	-19.48969238	3.64703	3.64703	4.60900	-19.49724202
4.05717	3.06119	5.43182	-19.50269265	4.21548	4.21548	6.25464	-19.48249670
3.77139	2.67089	5.43182	-19.51021565	4.67970	4.67970	8.72311	-19.47432464
4.54106	4.54106	8.72311	-19.47642575	4.29885	4.29885	7.90029	-19.48083729
2.03022	5.35614	5.43182	-19.45513297	1.86790	3.56391	5.43182	-19.43277909
3.30340	5.18816	7.07746	-19.49008305	4.00051	0.60849	4.60900	-15.11324227
5.04106	0.91969	5.43182	-17.81978975	1.32775	2.45842	3.78617	-19.03352481
3.40322	4.75413	8.15735	-19.49045734	2.66554	6.05757	8.72311	-19.49579411
2.71144	2.03474	4.74619	-19.48393244	3.69266	2.56198	6.25464	-19.51076846
3.05256	1.48772	4.54028	-19.22626577	2.35628	3.48695	5.84323	-19.50761709
2.18695	2.55924	4.74619	-19.50388349				

Table 3.8 $(\chi^2)^{1/2}$ values (/E_h) of least-squares fitted PEFs for $(^1\Sigma_g^+)BeHe_2^{2+}$.

m	n	Number of Coefficients	SPF	OGL	DUN	ESPF	EOGL	EDUN
				Power Series				
3		13	9.40−02[a]	6.34−01	2.54−00	1.29−01	5.22−02	8.32−01
4		22	0.13−01	7.62−02	1.08−00	1.48−02	4.58−03	1.48−01
5		34	1.45−03	3.87−03	6.30−01	3.86−03	1.14−03	1.12−02
6		50	1.93−04	1.91−04	5.26−02	7.22−04	1.92−04	7.04−04
7		70	2.55−05	3.11−05	6.37−03	7.56−04	2.60−05	3.19−05
				Padé Approximant				
4	4	43	1.58−02	1.78−04	7.38−03	3.81−04	1.79−03	2.12−04
4	5	55	3.73−05	1.45−04	7.20−05	2.81−04	3.90−05	4.62−05
5	4	55	1.38−02	6.83−04	7.40−05	6.49−05	3.99−05	4.52−05
5	5	67	2.81−05	3.05−05	2.99−05	2.69−04	2.88−04	2.26−04
4	6	71	4.57−04	2.24−05	3.24−05	7.21−04	1.60−05	1.71−05
6	4	71	6.55−05	1.80−04	3.28−05	2.66−04	3.47−05	2.95−05
5	6	83	2.06−05	1.98−05	1.22−04	7.22−04	2.18−05	1.79−05
6	5	83	2.54−05	8.62−04	2.13−04	2.63−04	1.57−05	6.03−05

[a]9.40-01 denotes 9.40×10^{-1}.

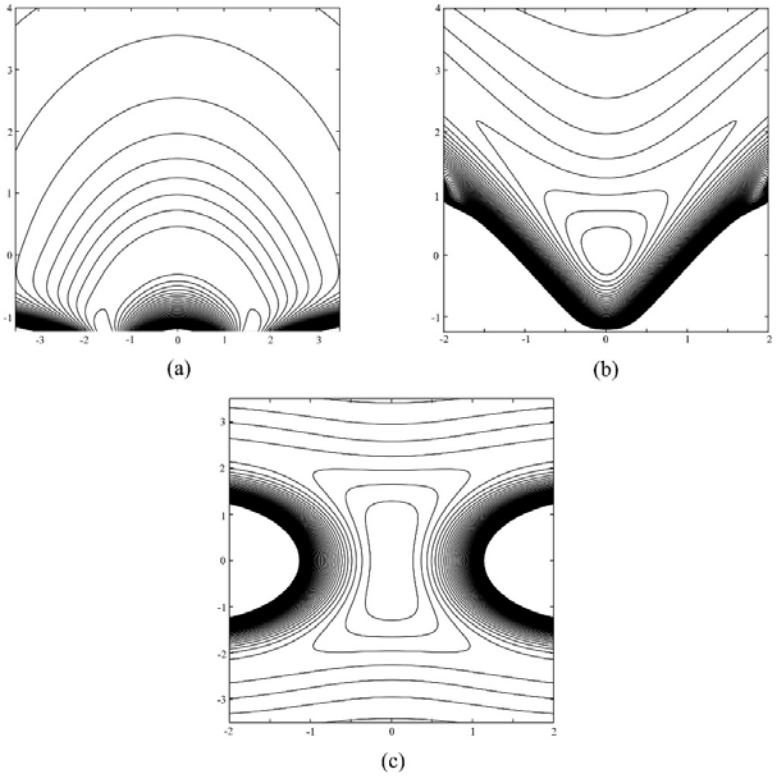

Figure 3.3 Two-dimensional projections of the $(^1\Sigma_g^+)BeHe_2^{2+}$ $P(6,5)$ EOGL PEF in terms of normal co-ordinates: (a) w_2 (x) versus w_1 (y); (b) w_4 (x) versus w_1 (y); (c) w_4 (x) versus w_2 (y). Contours spaced at 20 kJ mol^{-1}.

Table 3.9 $P(6,5)$ EOGL PEF of $(^1\Sigma_g^+)BeHe_2^{2+}$.

Expansion Variable	Expansion Coefficient[a] Numerator	Denominator	Expansion Variable	Expansion Coefficient[a] Numerator	Denominator
1	-19.52604	1.00000	$\rho_1^4\rho_3 + \rho_2^4\rho_3$	-7.18650	-0.43336
$\rho_1 + \rho_2$	-4.40797	-0.22578	$\rho_1\rho_3^4 + \rho_2\rho_3^4$	0.78428	-0.08608
ρ_3	0.40751	0.02094	$\rho_1^3\rho_2^2 + \rho_1^2\rho_2^3$	-14.58210	-0.76239
$\rho_1^2 + \rho_2^2$	16.48308	0.82882	$\rho_1^3\rho_3^2 + \rho_2^3\rho_3^2$	12.68413	0.78984
ρ_3^2	2.67425	0.13766	$\rho_1^2\rho_3^3 + \rho_2^2\rho_3^3$	3.68697	0.18136
$\rho_1\rho_2$	-3.59749	-0.18490	$\rho_1^3\rho_2\rho_3 + \rho_1\rho_2^3\rho_3$	-0.40923	0.00284
$\rho_2\rho_3 + \rho_1\rho_3$	5.43041	0.27809	$\rho_1\rho_2\rho_3^3$	-4.04024	0.61158
$\rho_1^3 + \rho_2^3$	3.14949	0.17353	$\rho_1^2\rho_2^2\rho_3$	-7.23348	-0.15025
ρ_3^3	1.21177	0.08483	$\rho_1^2\rho_2\rho_3^2 + \rho_1\rho_2^2\rho_3^2$	-8.95313	-0.96199
$\rho_1^2\rho_2 + \rho_1\rho_2^2$	-0.35043	-0.02135	$\rho_1^6 + \rho_2^6$	0.38433	
$\rho_1^2\rho_3 + \rho_2^2\rho_3$	-1.31870	-0.06028	ρ_3^6	2.69251	
$\rho_1\rho_3^2 + \rho_2\rho_3^2$	1.81088	0.06559	$\rho_1^5\rho_2 + \rho_1\rho_2^5$	0.49693	
$\rho_1\rho_2\rho_3$	2.22829	0.13046	$\rho_1^5\rho_3 + \rho_2^5\rho_3$	-0.06548	
$\rho_1^4 + \rho_2^4$	-10.77248	-0.52919	$\rho_1\rho_3^5 + \rho_2\rho_3^5$	-4.58678	
ρ_3^4	0.38225	0.09426	$\rho_1^4\rho_2^2 + \rho_1^2\rho_2^4$	0.61811	
$\rho_1^3\rho_2 + \rho_1\rho_3^2$	-3.52795	-0.17849	$\rho_1^4\rho_3^2 + \rho_2^4\rho_3^2$	0.65711	
$\rho_1^3\rho_3 + \rho_2^3\rho_3$	-11.24971	-0.58127	$\rho_1^2\rho_3^4 + \rho_2^2\rho_3^4$	-2.74239	
$\rho_1\rho_3^3 + \rho_2\rho_3^3$	3.47149	0.03194	$\rho_1^4\rho_2\rho_3 + \rho_1\rho_2^4\rho_3$	-3.09822	
$\rho_1^2\rho_2^2$	5.32976	0.30232	$\rho_1\rho_2\rho_3^4$	12.48466	
$\rho_1^2\rho_3^2 + \rho_2^2\rho_3^2$	-2.67013	-0.05480	$\rho_1^3\rho_2^3$	-0.03286	
$\rho_1^2\rho_2\rho_3 + \rho_1\rho_2^2\rho_3$	8.18626	0.35440	$\rho_1^3\rho_3^3 + \rho_2^3\rho_3^3$	2.49649	
$\rho_1\rho_2\rho_3^2$	4.87906	0.46193	$\rho_1^3\rho_2^2\rho_3 + \rho_1^2\rho_2^3\rho_3$	2.11778	
$\rho_1^5 + \rho_2^5$	-0.14747	-0.00926	$\rho_1^3\rho_2\rho_3^2 + \rho_1\rho_2^3\rho_3^2$	1.49386	
ρ_3^5	3.63463	0.18002	$\rho_1^2\rho_2\rho_3^3 + \rho_1\rho_2^2\rho_3^3$	0.38420	
$\rho_1^4\rho_2 + \rho_1\rho_2^4$	-0.51621	-0.01034	$\rho_1^2\rho_2^2\rho_3^2$	-9.71455	
$(\chi^2)^{1/2} = 3.14 \times 10^{-5}$ E_h					

[a]All coefficients given in E_h.

3.3. Dipole Moment Surfaces and their Analytical Representation

3.3.1. Dipole Moment Functions using Least-Squares Regression

As for discrete *ab initio* PESs, it is desirable to minimise the size of a discrete *ab initio* DMS without jeopardising the accuracy and applicability of the final DMF. The number and position of points comprising an *ab initio* DMS is therefore critical. For this reason it is preferable to construct a discrete DMS in conjunction with an

accompanying PES. This approach has been employed in the present work. It is also recommended that extensive, preferably augmented, one-electron basis sets are employed in the construction of the discrete *ab initio* DMS grid, since the error in calculated dipole moments using HF has been determined to be of the magnitude of $0.1 - 0.2$ D [86–88]. Post HF methods generally yield dipole moments closer to experiment.

In the manner of von Nagy-Felsobuki and co-workers [2, 89–92] *ab initio* DMSs are calculated in this work by decomposing the total molecular dipole moment operator thus,

$$\hat{\mu} = \mu_x \mathbf{i} + \mu_y \mathbf{j} + \mu_z \mathbf{k} \tag{3.20}$$

By enforcing the Eckart frame upon the molecule (Figure 3.4), $\mu_z \equiv 0$. Consequently, $\hat{\mu}$ is defined entirely by the x and y components of the dipole moment.

Having constructed an *ab initio* DMS grid, the DMF is constructed in a similar manner to the construction of a PEF, *viz.* by a least-squares fitting technique. However, Sudarko *et al.* [89–91] have shown that by expressing the molecular dipole moment in terms of internal displacement co-ordinates ($\rho_1 = R_1 - R_1^0$, $\rho_1 = R_2 - R_2^0$ and $\rho_1 = \theta - \theta^0$), as opposed to normal co-ordinates, the least-squares fitting process is more tractable. As such, this approach will be employed in the present work. The

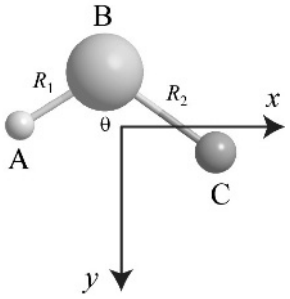

Figure 3.4 The Eckart framework for a C_s triatomic molecule, with the origin at the centre-of-mass.

DMF is then defined as a power series,

$$\mu_{\alpha}^{\text{fit}}\left(\rho_1,\rho_2,\rho_3\right)=\sum_{i,j,k}^{n}C_{ijk}(\rho_1)^i(\rho_2)^j(\rho_3)^k \tag{3.21}$$

where α is either x or y, and n is the order of the expansion. The $\left(\chi^2\right)^{1/2}$ value for the fitted DMF is defined in an analogous manner to equation (3.10),

$$\left(\chi^2\right)_{\alpha}^{1/2}=\left[\sum_{i=1}^{M}\left(\mu_{\alpha,i}^{\text{fit}}-\mu_{\alpha,i}^{\text{ai}}\right)^2\right]^{1/2} \tag{3.22}$$

where M is the number of discrete points on the *ab initio* DMS, and $\mu_{\alpha,i}^{\text{ai}}$ is the i^{th} *ab initio* point on the $\alpha-$component of the DMS. As for *ab initio* PEFs, a minimal $\left(\chi^2\right)^{1/2}$ value is only one criterion by which the utility of a DMF is gauged. An *ab initio* DMF must also predict physically realistic properties for the molecule in question. For example, a DMF should be close to linearity in the vicinity of the equilibrium geometry, as for most molecules the electrical anharmonicity is expected to be small in this region.

3.3.2. Dipole Moment Surface of $(^1\mathbf{A}_1)\mathbf{LiH}_2^+$

Page and von Nagy-Felsobuki [31] have employed the FCI method described in Section 3.2.1 in order to calculate a 47-point discrete DMS for $(^1\text{A}_1)\text{LiH}_2^+$. This DMS grid, provided in Table 3.10, included points within the domains 1.341 Å$\leq R_1 \leq$ 3.161 Å, 0.327 Å$\leq R_2 \leq$ 2.907 Å, and $5.396^\circ \leq \theta \leq 91.054^\circ$.

The DMFs of $(^1\text{A}_1)\text{LiH}_2^+$ have been constructed using least-squares fitted power series expansions of ρ_1, ρ_2 and ρ_3. For μ_x and μ_y the power series expansions were restricted to 6^{th} and 5^{th} orders, respectively, thereby ensuring the uniqueness of

Table 3.10 Discrete FCI DMS grid of $(^1A_1)LiH_2^+$.

$R_{H\text{-}Li}$ (/Å)	$R_{Li\text{-}H}$ (/Å)	θ (/deg.)	μ_y (/a.u.)	μ_x (/a.u.)	$R_{H\text{-}Li}$ (/Å)	$R_{Li\text{-}H}$ (/Å)	θ (/deg.)	μ_y (/a.u.)	μ_x (/a.u.)
2.027	2.027	21.383	-0.2262	0.0000	2.843	0.579	16.777	-0.2633	0.0566
2.133	2.133	21.383	-0.2424	0.0000	1.935	0.426	17.293	-0.3534	0.0485
1.921	1.921	21.383	-0.2110	0.0000	3.161	0.896	18.707	-0.1715	0.0431
2.239	2.239	21.383	-0.2595	0.0000	2.255	1.869	5.396	-0.2651	0.0058
1.815	1.815	21.383	-0.1969	0.0000	2.187	1.334	91.054	-0.0618	0.0806
2.451	2.451	21.383	-0.2959	0.0000	1.958	1.464	42.791	-0.1004	0.0724
1.603	1.603	21.383	-0.1726	0.0000	1.959	1.773	13.665	-0.2265	0.0076
2.025	2.025	26.728	-0.2034	0.0000	2.130	2.662	39.538	-0.1918	-0.0561
2.034	2.034	16.063	-0.2509	0.0000	1.989	2.314	26.961	-0.2053	-0.0315
2.026	2.026	32.075	-0.1837	0.0000	1.403	1.624	21.351	-0.1572	-0.0150
2.046	2.046	10.792	-0.2754	0.0000	1.341	2.369	20.892	-0.0650	-0.0654
2.043	2.043	42.684	-0.1560	0.0000	1.708	2.907	20.955	-0.1092	-0.0700
2.238	2.238	31.063	-0.2157	0.0000	2.282	2.817	21.317	-0.2775	-0.0387
2.257	2.257	11.786	-0.3096	0.0000	3.059	2.213	21.227	-0.2478	0.0572
1.815	1.815	33.322	-0.1584	0.0000	2.324	2.136	21.372	-0.2529	0.0138
2.875	2.875	21.383	-0.3745	0.0000	1.861	1.363	21.238	-0.1376	0.0342
2.043	2.043	42.684	-0.1560	0.0000	2.382	1.792	55.637	-0.1234	0.0622
2.127	2.127	62.977	-0.1433	0.0000	1.604	2.484	43.277	-0.0917	-0.0933
1.402	1.402	12.112	-0.1717	0.0000	2.286	1.790	14.152	-0.2171	0.0224
2.133	2.133	9.415	-0.2970	0.0000	1.876	2.199	14.266	-0.2408	-0.0143
2.272	2.272	81.210	-0.1512	0.0000	2.029	2.046	14.347	-0.2588	-0.0007
1.423	1.423	52.161	-0.1232	0.0000	2.783	1.273	20.432	-0.0262	0.0680
2.702	2.702	6.933	-0.4137	0.0000	2.594	1.461	20.883	-0.0676	0.0693
1.610	0.327	16.757	-0.4711	0.0281					

each DMF. $(\chi^2)^{1/2}$ values of all constructed LiH_2^+ DMFs are provided in Table 3.11. The most satisfactory representations of the discrete μ_x and μ_y DMS components were the 5th and 6th order power series, which exhibited $(\chi^2)^{1/2}$ values of 5.47×10^{-3} and 1.87×10^{-9} a.u., respectively [31]. No artefacts (such as singularities, *etc.*) were visible in either component DMF, and so no SVD analysis was required. Expansion coefficients of the μ_x and μ_y component DMFs are listed in Table 3.12 and 2D projections (in terms of ρ_1, ρ_2 and ρ_3) are shown in Figures 3.5 and 3.6.

Table 3.11 $(\chi^2)^{1/2}$ values (/a.u.) of least-squares fitted μ_x and μ_y DMFs for $(^1A_1)$ LiH_2^+.

	μ_x		μ_y	
Power Series Order	Number of Coefficients	$(\chi^2)^{1/2}$	Number of Coefficients	$(\chi^2)^{1/2}$
2	3	2.34−01[a]	7	9.22−01
3	7	8.04−02	13	5.83−01
4	13	1.40−02	22	6.35−02
5	22	3.58−03	34	5.47−03
6	34	1.87−09		

[a]2.34-01 denotes 2.34×10^{-1}.

Table 3.12 Expansion coefficients (/a.u.) of the $(^1A_1)LiH_2^+$ DMF.

	μ_y			μ_x			
Term	Coefficient	Term	Coefficient	Term	Coefficient	Term	Coefficient
C_{000}	5.7601−01[a]	C_{220}	−9.4638−02	C_{100}	1.8861−01	C_{302}	−1.1685−02
C_{100}	3.4804−05	C_{202}	−1.6226−02	C_{200}	2.0763−03	C_{311}	−2.4483−03
C_{001}	1.8903−01	C_{112}	2.1411−01	C_{101}	−4.7736−03	C_{212}	−2.4611−02
C_{200}	4.7607−01	C_{103}	2.1319−03	C_{300}	−5.2909−02	C_{203}	2.7818−02
C_{110}	4.9100−05	C_{004}	9.5231−01	C_{210}	−2.4306−02	C_{104}	−2.7099−02
C_{101}	5.3544−02	C_{500}	8.2286−10	C_{201}	1.6578−02	C_{600}	1.6356−06
C_{002}	−1.1176−02	C_{410}	2.6332−07	C_{102}	6.0459−02	C_{510}	1.6919−04
C_{300}	−5.9663−03	C_{401}	−3.7635−05	C_{400}	−1.3197−02	C_{501}	−1.5990−03
C_{210}	2.7333−04	C_{320}	−2.9354−04	C_{310}	−1.9791−02	C_{420}	−1.1817−02
C_{201}	1.5931−02	C_{302}	−3.8223−02	C_{301}	−1.4453−02	C_{402}	6.6305−03
C_{111}	6.1169−06	C_{311}	−2.7398−04	C_{211}	−1.1477−03	C_{411}	−1.7546−03
C_{102}	−6.0344−02	C_{203}	−1.2935−04	C_{202}	1.9869−02	C_{321}	−1.1988−02
C_{003}	−4.3103−01	C_{221}	4.9197−02	C_{103}	1.0788−02	C_{312}	−5.0470−05
C_{400}	−4.4142−06	C_{212}	−1.0932−07	C_{500}	2.9653−03	C_{303}	1.8402−02
C_{310}	2.4548−02	C_{113}	−4.0974−01	C_{410}	−1.0368−02	C_{204}	−2.9648−02
C_{301}	2.7332−02	C_{104}	8.7353−03	C_{401}	4.2567−03	C_{213}	1.8880−02
C_{211}	−1.2785−05	C_{005}	−2.6951−03	C_{320}	5.0693−03	C_{105}	3.4407−02
$(\chi^2)^{1/2}$ 5.47×10^{-3} a.u.				$(\chi^2)^{1/2}$ 1.87×10^{-9} a.u.			

[a]5.7601-01 denotes 5.7601×10^{-1}.

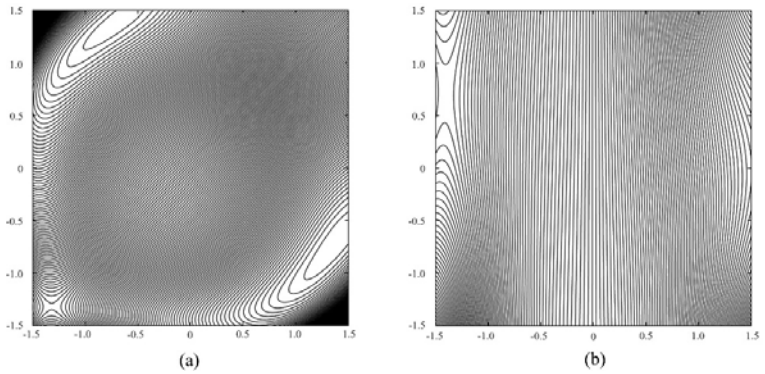

Figure 3.5 Two-dimensional constant dipole projections of μ_x for $(^1\mathrm{A}_1)\mathrm{LiH}_2^+$: (a) ρ_2 (x) versus ρ_1 (y); (b) ρ_3 (x) versus ρ_1 (y). See text for definition of ρ_i.

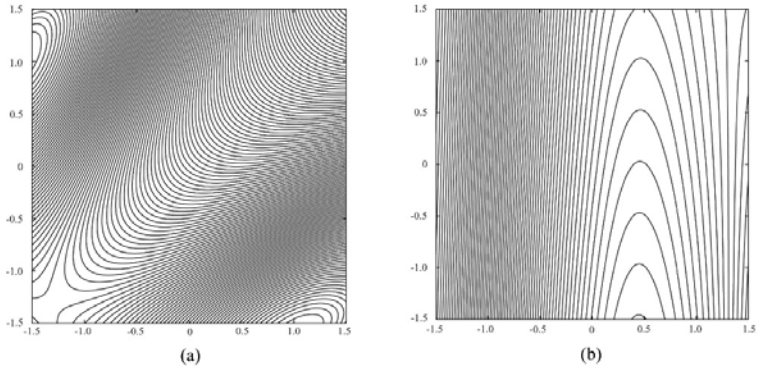

Figure 3.6 Two-dimensional constant dipole projections of μ_y for $(^1\mathrm{A}_1)\mathrm{LiH}_2^+$: (a) ρ_2 (x) versus ρ_1 (y); (b) ρ_3 (x) versus ρ_1 (y). See text for definition of ρ_i.

3.3.3. Dipole Moment Surface of $(^1\mathbf{A}_1)\mathbf{BeH}_2^{2+}$

Page and von Nagy-Felsobuki [32] have constructed a 73-point DMS for $(^1\mathrm{A}_1)\mathrm{BeH}_2^{2+}$, employing the IC-MRCI method described in Section 3.2.3. This discrete DMS grid is shown in Table 3.13.

In order to obtain the most accurate analytical DMF, power series expansions of up to 8^{th} and 7^{th} orders for μ_x and μ_y, respectively, were constructed. The $(\chi^2)^{1/2}$ of these DMFs are given in Table 3.14. It is evident from Table 3.14 that the most accurate μ_x and μ_y DMFs, in terms of the values of $(\chi^2)^{1/2}$, are the 7^{th} and 6^{th} order power series expansions of ρ_1, ρ_2 and ρ_3, respectively [32]. In both cases, no SVD was required for physically acceptable DMFs. Contour projections of the 7^{th} order

Table 3.13 Discrete IC-MRCI DMS grid of $(^1A_1)BeH_2^{2+}$.

$R_{\text{H-Be}}$ (/Å)	$R_{\text{Be-H}}$ (/Å)	θ (/deg.)	μ_y (/a.u.)	μ_x (/a.u.)	$R_{\text{H-Be}}$ (/Å)	$R_{\text{Be-H}}$ (/Å)	θ (/deg.)	μ_y (/a.u.)	μ_x (/a.u.)
1.609	1.609	29.374	-0.1980	0.0000	2.008	2.008	40.546	0.1490	0.0000
0.782	0.782	29.374	-0.3340	0.0000	1.400	1.400	37.571	-0.1176	0.0000
0.988	0.988	29.374	-0.2822	0.0000	1.450	1.450	22.598	-0.3209	0.0000
1.237	1.237	29.374	-0.2380	0.0000	1.328	1.328	64.908	0.0125	0.0000
1.361	1.361	29.374	-0.2221	0.0000	2.060	0.948	28.394	0.8006	-0.4151
1.485	1.485	29.374	-0.2091	0.0000	1.950	1.268	29.082	0.2277	-0.3010
1.733	1.733	29.374	-0.1877	0.0000	2.022	1.842	29.361	-0.1366	-0.0882
1.857	1.857	29.374	-0.1765	0.0000	1.836	1.381	29.248	-0.0007	-0.2098
1.981	1.981	29.374	-0.1626	0.0000	1.766	1.466	23.185	-0.2298	-0.1067
2.105	2.105	29.374	-0.1434	0.0000	1.723	1.495	29.343	-0.1473	-0.1076
2.229	2.229	29.374	-0.1158	0.0000	2.020	1.222	51.434	0.6894	-0.5661
2.436	2.436	29.374	-0.0384	0.0000	1.619	1.392	29.339	-0.1569	-0.1054
1.619	1.619	21.314	-0.3714	0.0000	1.964	1.964	23.899	-0.3507	0.0000
1.607	1.607	37.496	-0.0557	0.0000	1.405	1.405	17.497	-0.3980	0.0000
1.613	1.613	45.599	0.0562	0.0000	1.217	1.217	20.533	-0.3266	0.0000
1.627	1.627	53.602	0.1411	0.0000	1.724	1.537	15.948	-0.4550	-0.0421
1.648	1.648	61.432	0.2035	0.0000	1.836	0.943	28.660	0.4411	-0.3449
1.677	1.677	69.024	0.2479	0.0000	2.599	1.567	28.970	0.7462	-0.4389
2.763	2.763	21.503	-0.5025	0.0000	1.612	1.239	13.700	-0.2902	-0.0695
1.742	1.742	81.013	0.2934	0.0000	2.009	1.254	14.895	0.1201	-0.1625
1.222	1.645	29.236	-0.0467	0.1886	1.855	1.460	64.312	0.3949	-0.3111
1.584	2.130	29.237	0.1034	0.2555	1.389	1.999	73.203	-0.3823	0.6972
1.352	1.893	19.164	-0.0916	0.1542	1.524	1.524	15.079	-0.4806	0.0000
1.533	1.685	29.361	-0.1753	0.0720	1.247	1.247	64.895	-0.0411	0.0000
1.419	1.798	29.287	-0.0594	0.1767	1.287	1.287	54.237	-0.0485	0.0000
1.305	1.912	29.146	0.1435	0.2722	2.041	0.852	28.113	0.8907	-0.4177
1.192	2.026	28.928	0.4186	0.3537	1.063	1.829	28.908	0.2977	0.3157
1.078	2.140	28.617	0.7568	0.4199	2.247	2.247	22.772	-0.4306	0.0000
1.710	1.710	35.733	-0.0567	0.0000	2.444	2.444	20.474	-0.5986	0.0000
1.513	1.513	22.191	-0.3358	0.0000	1.478	1.651	19.837	-0.3571	0.0501
1.617	1.807	29.355	-0.1539	0.0911	1.819	1.527	33.791	-0.0228	-0.1627
1.274	1.946	43.675	0.4282	0.4416	1.939	1.531	36.766	0.1203	-0.2458
1.417	1.796	36.150	0.0554	0.2234	1.747	0.233	20.602	-0.1964	-0.0574
0.542	1.731	27.036	0.5222	0.3243	1.443	2.354	28.997	0.5529	0.3957
1.616	1.844	36.920	0.0191	0.1411	2.178	1.040	28.489	0.8824	-0.4386
0.606	1.371	28.282	0.0386	0.2360	2.064	1.154	28.835	0.5251	-0.3777
1.855	1.855	38.479	0.0431	0.0000					

μ_x and 6$^{\text{th}}$ order μ_y component DMFs are shown (in terms of ρ_1, ρ_2 and ρ_3) in Figures 3.7 and 3.8. The expansion coefficients of these component DMFs are given in Table 3.15. It is observed from these figures that both μ_x and μ_y component DMFs exhibit little electrical anharmonicity near the equilibrium geometry and appear free of fitting 'artefacts'.

Table 3.14 $(\chi^2)^{1/2}$ values (/a.u.) of least-squares fitted μ_x and μ_y DMFs for $(^1\text{A}_1)\text{BeH}_2^{2+}$.

	μ_x		μ_y	
Power Series Order	Number of Coefficients	$(\chi^2)^{1/2}$	Number of Coefficients	$(\chi^2)^{1/2}$
3	7	9.69−02[a]	13	9.87−01
4	13	3.63−02	22	4.02−01
5	22	2.72−03	34	8.81−02
6	34	2.98−04	50	1.93−03
7	50	2.09−04	70	3.12−03
8	70	2.45−04		

[a]9.69-02 denotes 9.69×10^{-2}.

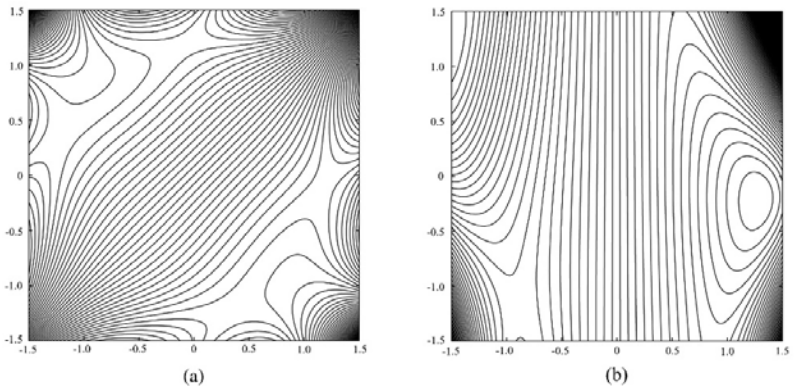

Figure 3.7 Two-dimensional constant dipole projections of μ_x for $(^1\text{A}_1)\text{BeH}_2^{2+}$: (a) ρ_1 (x) versus ρ_2 (y); (b) ρ_3 (x) versus ρ_1 (y). See text for definition of ρ_i.

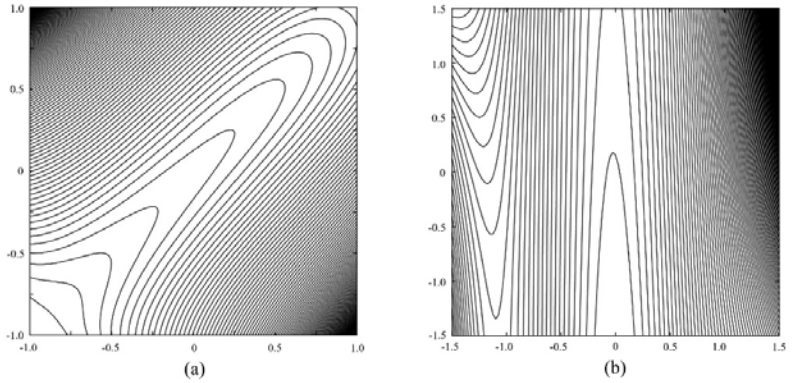

Figure 3.8 Two-dimensional constant dipole projections of μ_y for $(^1A_1)BeH_2^{2+}$: (a) ρ_1 (x) versus ρ_2 (y); (b) ρ_3 (x) versus ρ_1 (y). See text for definition of ρ_i.

Table 3.15 Expansion coefficients (/a.u.) of the $(^1A_1)BeH_2^{2+}$ DMF.

μ_y				μ_x			
Term	Coefficient	Term	Coefficient	Term	Coefficient	Term	Coefficient
C_{000}	−1.9785−01[a]	C_{320}	−7.6746−01	C_{100}	−4.7669−01	C_{420}	7.2177−02
C_{100}	4.6987−02	C_{302}	2.1220−07	C_{200}	2.8722−02	C_{402}	−9.5335−04
C_{001}	4.2125−02	C_{311}	−3.6687−01	C_{101}	−3.9169−02	C_{411}	−2.0170−02
C_{200}	8.1544−04	C_{203}	1.2003−07	C_{300}	−4.9537−03	C_{321}	5.6877−02
C_{110}	−2.6161−01	C_{221}	−5.0516−03	C_{210}	−6.4700−02	C_{312}	−4.1378−03
C_{101}	1.2602−02	C_{212}	9.1135−02	C_{201}	−1.6734−02	C_{303}	5.4358−05
C_{002}	1.9629−02	C_{113}	3.2781−02	C_{102}	−2.3849−02	C_{204}	2.9089−02
C_{300}	1.2384−05	C_{104}	−2.4155−04	C_{400}	2.6845−02	C_{213}	8.9626−02
C_{210}	−3.1056−01	C_{005}	1.5258−02	C_{310}	−1.1085−02	C_{105}	2.1205−02
C_{201}	−1.7456−03	C_{600}	1.3234−11	C_{301}	8.6212−02	C_{700}	−1.5940−08
C_{111}	7.3568−01	C_{510}	−1.8330−09	C_{211}	−8.6367−02	C_{610}	2.3260−05
C_{102}	−1.3343−02	C_{501}	−2.4411−06	C_{202}	−1.1288−02	C_{601}	−8.9100−04
C_{003}	9.9008−01	C_{420}	5.0314−04	C_{103}	9.7242−02	C_{520}	1.3414−02
C_{400}	−1.7538−01	C_{402}	4.7228−03	C_{500}	3.8935−02	C_{502}	−4.6429−02
C_{310}	4.0481−02	C_{411}	−5.2549−04	C_{410}	2.3628−02	C_{511}	1.7686−02
C_{301}	−2.7936−05	C_{330}	1.6460−01	C_{401}	3.1176−02	C_{430}	−5.0784−03
C_{211}	−4.9042−02	C_{303}	−2.2387−09	C_{320}	1.2522−01	C_{403}	−2.6465−07
C_{220}	−1.4005−01	C_{321}	7.3146−03	C_{302}	−7.6399−03	C_{421}	−7.0568−03
C_{202}	−3.7047−06	C_{312}	7.1429−01	C_{311}	−4.6766−02	C_{412}	−4.3735−02
C_{112}	−8.9059−01	C_{222}	5.3077−03	C_{212}	3.6597−03	C_{322}	−1.6238−02
C_{103}	3.3709−02	C_{213}	−2.1718−02	C_{203}	4.9557−02	C_{313}	−9.9257−02
C_{004}	−2.0064−00	C_{204}	9.3845−02	C_{104}	−1.4223−01	C_{304}	2.5777−03
C_{500}	1.3103−06	C_{114}	−2.7215−02	C_{600}	−8.5364−04	C_{214}	−8.5103−02
C_{410}	−2.0794−02	C_{105}	−2.2443−06	C_{510}	9.4859−02	C_{205}	3.7157−04
C_{401}	4.5322−03	C_{006}	−2.3833−04	C_{501}	7.4018−02	C_{106}	7.6394−05
$(\chi^2)^{1/2}$ 1.93×10^{-3} a.u.				$(\chi^2)^{1/2}$ 2.09×10^{-4} a.u.			

[a]-1.978543-01 denotes -1.978543×10^{-1}.

3.3.4. Dipole Moment Surface of $(^1\Sigma_g^+)BeHe_2^{2+}$

An *ab initio* DMS grid of $(^1\Sigma_g^+)BeHe_2^{2+}$ has been constructed using the IC-MRCI method of Page *et al.* [33] described in Section 3.2.5. This DMS grid was constructed using a 57-point subset of the 87 points comprising the IC-MRCI PES [33], and is given in Table 3.16.

Table 3.16 Discrete IC-MRCI DMS grid of $(^1\Sigma_g^+)BeHe_2^{2+}$.

$R_{\text{He-Be}}$ (/Å)	$R_{\text{Be-He}}$ (/Å)	θ (/deg.)	μ_y (/a.u.)	μ_x (/a.u.)	$R_{\text{H-Li}}$ (/Å)	$R_{\text{Li-H}}$ (/Å)	θ (/deg.)	μ_y (/a.u.)	μ_x (/a.u.)
1.437	1.437	180.000	0.0000	0.0000	1.716	1.196	161.276	-0.2977	-0.4928
1.481	1.481	180.000	0.0000	0.0000	1.629	1.363	147.592	-0.5497	-0.2702
1.394	1.394	180.000	0.0000	0.0000	1.974	1.358	118.064	-1.0904	-0.7750
1.307	1.307	180.000	0.0000	0.0000	1.401	2.084	109.554	-1.2604	-0.9443
1.438	1.438	175.232	-0.0004	-0.0786	1.377	1.569	154.692	-0.4250	0.1892
1.440	1.440	172.853	0.0002	-0.1180	1.397	1.726	133.707	-0.8153	0.3661
1.442	1.442	170.481	-0.0002	-0.1574	1.346	1.542	169.003	-0.1808	0.1850
1.445	1.445	168.116	-0.0002	-0.1969	1.258	1.689	154.223	-0.4211	0.4202
1.448	1.448	165.762	0.0002	-0.2365	1.245	1.750	146.864	-0.5424	0.5091
1.452	1.452	163.420	0.0002	-0.2762	1.598	2.039	113.071	-1.3941	0.6203
1.497	1.377	180.000	-0.1120	0.0000	1.625	1.834	97.621	-1.5964	-0.3839
1.557	1.318	180.000	-0.2233	0.0000	2.101	1.292	154.742	-0.4695	-0.8522
1.617	1.258	180.000	-0.3335	0.0000	1.966	1.966	144.561	0.0000	-0.9069
1.412	1.709	164.275	-0.2859	0.2999	1.682	1.682	159.506	0.0002	-0.4213
1.526	1.239	147.651	-0.4900	-0.2706	2.308	2.308	180.000	0.0000	0.0000
1.420	1.999	150.452	-0.5836	0.6291	1.138	1.736	180.000	0.5479	0.0000
1.530	2.612	127.511	-1.1743	1.3115	0.540	2.335	180.000	1.4131	0.0000
1.620	1.620	125.016	-0.0002	-1.0357	0.403	1.600	180.000	0.5615	0.0000
1.694	1.694	116.033	0.0002	-1.2701	2.906	1.710	180.000	-1.2704	0.0000
1.778	1.778	107.849	-0.0002	-1.5172	0.784	0.784	180.000	0.0000	0.0000
1.870	1.870	100.436	-0.0002	-1.7764	1.256	1.256	152.433	0.0000	-0.3765
2.074	2.074	87.710	0.0002	2.3248	1.167	1.167	118.303	0.0001	-0.7375
2.147	1.620	98.504	-1.6497	-0.9175	0.988	1.886	180.000	0.8019	0.0000
1.074	2.834	81.258	-0.9218	-2.4210	2.117	0.322	180.000	-1.1084	0.0000
2.668	0.487	110.495	-0.5709	-2.0356	0.703	1.301	180.000	0.3152	0.0000
1.435	1.077	180.000	-0.2833	0.0000	1.411	3.206	180.000	1.8553	0.0000
1.157	1.354	180.000	0.1564	0.0000	1.954	1.356	180.000	-0.6143	0.0000
0.893	1.510	180.000	0.4515	0.0000	1.247	1.845	180.000	0.5854	0.0000
1.663	1.224	168.816	-0.1789	-0.4105					

Several power series representations of the $(^1\Sigma_g^+)BeHe_2^{2+}$ IC-MRCI DMS grid have been constructed. Due to symmetry considerations these DMFs have been constructed under C_s symmetry. Subsequently, the maximum order of expansion yielding uniquely defined coefficients is reduced. Listed in Table 3.17 are $(\chi^2)^{1/2}$ values of the μ_x and μ_y component DMFs of $(^1\Sigma_g^+)BeHe_2^{2+}$. It is immediate from this table that the only representations of the $(^1\Sigma_g^+)BeHe_2^{2+}$ DMS exhibiting sufficient accuracy are the 5^{th} order expansions for both the μ_x and μ_y component DMFs, which are defined by 56 coefficients. These coefficients are given in Table 3.18. Contour projections, in terms of the internal displacement co-ordinates, are shown in Figures 3.9 and 3.10. From these figures it is evident that both component DMFs exhibit satisfactory topological features over the domains featured. Therefore no SVD analysis was required in this case.

Table 3.17 $(\chi^2)^{1/2}$ values (/a.u.) for μ_x and μ_y as a function of expansion order for $(^1\Sigma_g^+)BeHe_2^{2+}$.

	μ_x		μ_y	
Power Series Order	Number of Coefficients	$(\chi^2)^{1/2}$	Number of Coefficients	$(\chi^2)^{1/2}$
2	10	2.74+00[a]	10	4.34+00
3	20	2.03+00	20	2.66+00
4	35	1.11+00	35	1.42+00
5	56	9.20−04	56	1.16−03

[a] 2.74+00 denotes 2.74×10^0.

Table 3.18 Expansion coefficients (/a.u.) of the $(^1\Sigma_g^+)BeHe_2^{2+}$ DMF.

μ_y				μ_x			
Term	Coefficient	Term	Coefficient	Term	Coefficient	Term	Coefficient
C_{000}	6.7005−05[a]	C_{031}	1.4220+01	C_{000}	−7.5307−05	C_{031}	−1.3449+01
C_{100}	−1.1974−05	C_{202}	−3.6092−01	C_{100}	−9.3582−01	C_{202}	4.3278−01
C_{010}	6.5906−04	C_{112}	3.8472−01	C_{010}	9.3514−01	C_{112}	−3.3039−01
C_{001}	1.8693−02	C_{022}	6.6307−01	C_{001}	−1.0951−03	C_{022}	−6.8870−01
C_{200}	−1.4779−02	C_{103}	−4.9453−03	C_{200}	−3.2516−01	C_{103}	6.6304−03
C_{110}	−1.7801−02	C_{013}	7.9706−03	C_{110}	2.4762−02	C_{013}	−8.0641−03
C_{020}	−5.4398−03	C_{004}	1.0558−06	C_{020}	3.4165−01	C_{004}	−1.7122−06
C_{101}	−2.7483−01	C_{500}	4.1545−02	C_{101}	6.7171−01	C_{500}	2.6317−03
C_{011}	6.1671−01	C_{410}	1.2041−02	C_{011}	−4.0488−01	C_{410}	−2.3727−01
C_{002}	8.4352−04	C_{320}	6.4279−02	C_{002}	−4.3769−04	C_{320}	−2.2047−01
C_{300}	−3.1207−02	C_{230}	2.3811−01	C_{300}	2.1137−01	C_{230}	−8.5220−02
C_{210}	−1.5410−01	C_{140}	1.7511−01	C_{210}	1.2182−01	C_{140}	−5.4770−02
C_{120}	−1.1984−01	C_{050}	−4.2496−03	C_{120}	1.8095−01	C_{050}	2.8070−02
C_{030}	−1.0192−02	C_{401}	−1.3566+01	C_{030}	−1.7464−01	C_{401}	1.4290+01
C_{201}	−1.5405+00	C_{311}	3.7346+00	C_{201}	2.2281+00	C_{311}	−6.8836+00
C_{111}	4.8706+00	C_{221}	1.0820+01	C_{111}	−4.1467+00	C_{221}	−1.2489+01
C_{021}	6.4530+00	C_{131}	3.1377+00	C_{021}	−6.6786+00	C_{131}	−4.8713+00
C_{102}	−6.6689−02	C_{041}	4.1863+00	C_{102}	1.1803−01	C_{041}	−6.0614+00
C_{012}	1.7462−01	C_{302}	−6.0211−01	C_{012}	−1.5842−01	C_{302}	6.5737−01
C_{003}	9.5540−05	C_{212}	5.6611−02	C_{003}	−7.5785−05	C_{212}	−2.6847−02
C_{400}	1.6071−02	C_{122}	6.1245−01	C_{400}	2.7393−02	C_{122}	−6.3240−01
C_{310}	−1.8248−01	C_{032}	4.2464−01	C_{310}	−5.3465−02	C_{032}	−4.8495−01
C_{220}	−3.6221−02	C_{203}	−1.1992−02	C_{220}	9.7394−02	C_{203}	1.3855−02
C_{130}	1.3458−01	C_{113}	6.4767−03	C_{130}	2.0900−02	C_{113}	−5.8595−03
C_{040}	2.0414−02	C_{023}	1.2713−02	C_{040}	−4.1516−02	C_{023}	−1.4016−02
C_{301}	−4.3266+00	C_{104}	−8.6299−05	C_{301}	5.0659+00	C_{104}	1.0706−04
C_{211}	5.0959+00	C_{014}	1.0757−04	C_{211}	−3.0716+00	C_{014}	−1.1564−04
C_{121}	1.0314+01	C_{005}	1.5239−08	C_{121}	−6.7779+00	C_{005}	−2.3868−08
$(\chi^2)^{1/2}$ 1.16×10^{-3} a.u.				$(\chi^2)^{1/2}$ 9.20×10^{-4} a.u.			

[a] 6.7005-05 denotes 6.7005×10^{-5}.

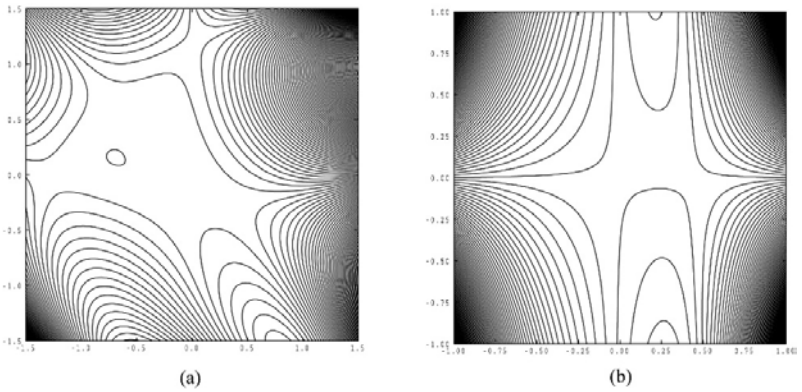

Figure 3.9 Two-dimensional constant dipole projections of μ_x for $(^1\Sigma_g^+)\mathrm{BeHe}_2^{2+}$: (a) ρ_1 (x) versus ρ_2 (y); (b) ρ_3 (x) versus ρ_1 (y). See text for definition of ρ_i.

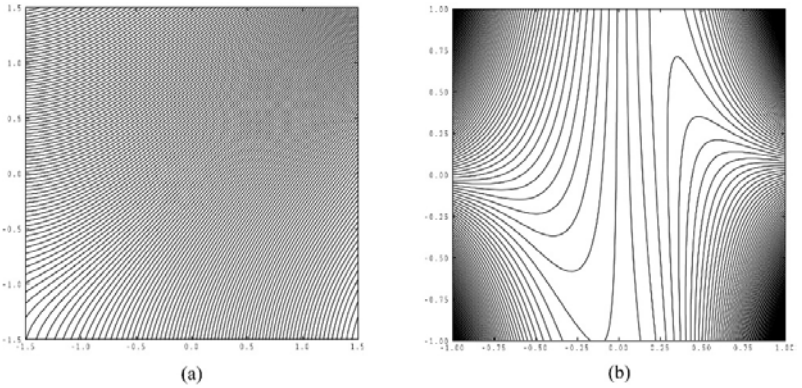

Figure 3.10 Two-dimensional constant dipole projections of μ_y for $(^1\Sigma_g^+)\mathrm{BeHe}_2^{2+}$: (a) ρ_1 (x) versus ρ_2 (y); (b) ρ_3 (x) versus ρ_1 (y). See text for definition of ρ_i.

3.4. Conclusion

The construction of molecular PEFs and DMFs employing least-squares fitting methods has been reviewed. Particular emphasis has been placed upon the approach employed by von Nagy-Felsobuki and co-workers [2, 13], which includes the use of SVD analysis in alleviating the near-rank deficiencies in the optimisation of PEF and DMF coefficients.

These methods were subsequently applied to the $^1\mathrm{A}_1$ ground states of the isoelectronic species LiH_2^+ and BeH_2^{2+} and the $^1\Sigma_g^+$ ground state of BeHe_2^{2+}, in or-

der to generate accurate PEFs. Discrete PESs of these species were calculated, consisting of 83 (FCI), 89 (IC-MRCI) and 87 (IC-MRCI) points, respectively. The most appropriate analytical representation to the discrete $(^1A_1)LiH_2^+$ FCI PES was a $P(5,5)$ Padé approximant with the OGL expansion variable with $\sigma_{67} = 0$ using SVD. This PEF yielded a $(\chi^2)^{1/2}$ value with respect to the FCI grid of 2.41×10^{-5} E_h. The most appropriate PEF for the ground state of BeH_2^{2+} was the $P(6,5)$ Padé approximant with the OGL expansion variable. More extensive SVD was required in this case however, with $\sigma_{65,67-69,71-83} = 0$ giving a $(\chi^2)^{1/2}$ value of 2.37×10^{-5} E_h with respect to the calculated IC-MRCI PES grid. Neglecting SVD analysis in the optimisation of this $P(6,5)$ OGL function gave a more accurate PEF in a statistical sense. However, it was illustrated that the latter PEF was not appropriate, due to the topology of the potential energy in the region of the equilibrium geometry. A $P(6,5)$ Padé approximant with the EOGL expansion variable was determined to be the most appropriate representation of the $^1\Sigma_g^+$ ground state of $BeHe_2^{2+}$. The technique of SVD analysis was also applied to the latter PEF, with $\sigma_{60,62-74} = 0$ yielding a $(\chi^2)^{1/2}$ value of 3.14×10^{-5} E_h.

Discrete 47-, 73- and 47-point DMS grids of $(^1A_1)LiH_2^+$, $(^1A_1)BeH_2^{2+}$ and $(^1\Sigma_g^+)BeHe_2^{2+}$ were constructed using FCI, IC-MRCI and IC-MRCI, respectively. It was subsequently determined that the 5^{th} and 6^{th} order power series expansions of internal displacement co-ordinates were the most suitable for the μ_x and μ_y DMS components of $(^1A_1)LiH_2^+$. Similarly, the most appropriate analytical DMFs for $(^1A_1)BeH_2^{2+}$ were found to be the 7^{th} and 6^{th} order expansions of internal displacement co-ordinates, for μ_x and μ_y, respectively. Analytical representations to μ_x and μ_y of $(^1\Sigma_g^+)BeHe_2^{2+}$ were constructed under C_s symmetry, and so the maximum power series expansion order was restricted to 5. It was subsequently

determined that the most appropriate power series representation of both μ_x and μ_y of $(^1\Sigma_g^+)BeHe_2^{2+}$ was the 5^{th} order expansion, which did not necessitate SVD analysis in the optimisation of the DMF term coefficients. All component DMFs constructed here exhibited statistical accuracies exceeding those of the respective *ab initio* methods employed for the corresponding DMSs.

3.5. References

[1] O. Christiansen, T. A. Ruden, K. Ruud, and T. Helgaker, J. Chem. Phys. **116**, 8334 (2002).

[2] D. J. Searles and E. I. von Nagy-Felsobuki, Comp. Phys. Comm. **67**, 527 (1992).

[3] B. T. Sutcliffe, *Methods in Computational Chemistry* (Plenum Press, New York, 1992), vol. 4.

[4] J. Tennyson, S. Miller, and J. R. Henderson, *Methods in Computational Chemistry* (Plenum Press, New York, 1992), vol. 4.

[5] S. Carter and N. C. Handy, Comp. Phys. Rep. **5**, 117 (1986).

[6] S. Carter and N. C. Handy, J. Chem. Phys. **87**, 4294 (1987).

[7] S. Carter and N. C. Handy, Mol. Phys. **52**, 1367 (1984).

[8] S. Carter and N. C. Handy, Mol. Phys. **53**, 1033 (1984).

[9] S. Carter and N. C. Handy, Mol. Phys. **57**, 175 (1984).

[10] S. Carter and N. C. Handy, Mol. Phys. **47**, 1445 (1982).

[11] W. P. Kraemer and V. Špirko, Chem. Phys. **330**, 190 (2006).

[12] D. J. Malik, J. Eccles, and D. Secrest, J. Comp. Phys. **38**, 157 (1980).

[13] D. J. Searles and E. I. von Nagy-Felsobuki, *Ab Initio Calculations of Vibrational Band Origins* (Elsevier, New York, 1991).

[14] H. Li and R. J. L. Roy, J. Chem. Phys. **125**, 044307 (2006).

[15] H. Li and R. J. Le Roy, J. Phys. Chem. A **111**, 6248 (2007).

[16] D. J. Searles and E. I. von Nagy-Felsobuki, *Lecture Notes in Chemistry* (Springer-Verlag, Berlin, 1993), vol. 61.

[17] G. D. Carney and R. N. Porter, J. Chem. Phys. **65**, 3547 (1976).

[18] G. D. Carney and R. N. Porter, J. Chem. Phys. **60**, 4251 (1974).

[19] F. Wang, D. J. Searles, and E. I. von Nagy-Felsobuki, J. Mol. Struct. (THEOCHEM) **272**, 73 (1992).

[20] F. Wang, D. J. Searles, and E. I. von Nagy-Felsobuki, Chem. Phys. **172**, 247 (1993).

[21] F. Wang, D. J. Searles, and E. I. Von Nagy-Felsobuki, J. Phys. Chem. **96**, 6158 (1992).

[22] F. Wang, D. J. Searles, and E. I. Von Nagy-Felsobuki, Theor. Chim. Acta **88**, 131 (1994).

[23] P. Jensen, J. Mol. Spec. **132**, 429 (1988).

[24] G. S. Kedziora and I. Shavitt, J. Chem. Phys. **106**, 8733 (1997).

[25] W. Gabriel, E.-A. Reinsch, P. Rosmus, S. Carter, and N. C. Handy, J. Chem. Phys. **99**, 897 (1993).

[26] A. E. Lynasgray, S. Miller, and J. Tennyson, J. Mol. Spec. **169**, 458 (1988).

[27] Sudarko, Ph.D. thesis, The University of Newcastle, Australia (2000).

[28] F. Wang, D. J. Searles, and E. I. von Nagy-Felsobuki, J. Chin. Chem. Soc. **39**, 339 (1992).

[29] G. E. Forsythe, M. A. Malcolm, and C. B. Moler, *Computer Methods for Mathematical Computations* (Prentice-Hall, Elglewood Cliffs, 1977).

[30] J. H. Wilkinson, *Numerical Software: Needs and Availability* (Academic Press, New York, 1978).

[31] A. J. Page and E. I. von Nagy-Felsobuki, J. Phys. Chem. A **111**, 4478 (2007).

[32] A. J. Page and E. I. von Nagy-Felsobuki, Mol. Phys. **105**, 2527 (2007).

[33] A. J. Page, D. J. D. Wilson, and E. I. von Nagy-Felsobuki, Chem. Phys. Lett. **442**, 194 (2007).

[34] D. J. Searles, F. Wang, J. A. Hayward, J. M. Hughes, D. J. D. Wilson, A. J. Page, and E. I. von Nagy-Felsobuki, G_PLOT_PES_1 (Unpublished, 2008).

[35] D. J. Searles, F. Wang, J. A. Hayward, J. M. Hughes, D. J. D. Wilson, A. J. Page, and E. I. von Nagy-Felsobuki, DMS_PLOT (Unpublished, 2008).

[36] NAG Graphics Library, Mark 4. See http://www.nag.com.

[37] D. O. Harris, G. G. Engerholm, and W. D. Gwinn, J. Chem. Phys. **43**, 1515 (1965).

[38] G. Simons, R. G. Parr, and J. M. Finlan, J. Chem. Phys. **59**, 3229 (1973).

[39] J. F. Ogilvie, Proc. Roy. Soc. London Ser. A **A378**, 387 (1981).

[40] J. L. Dunham, Phys. Rev. **41**, 713 (1932).

[41] J. L. Dunham, Phys. Rev. **41**, 721 (1932).

[42] J. N. Huffaker, J. Chem. Phys. **64**, 3175 (1976).

[43] G. D. Carney and R. N. Porter, Phys. Rev. Lett. **45**, 537 (1980).

[44] D. J. Searles and E. I. von Nagy-Felsobuki, Phys. Rev. A **43**, 3365 (1991).

[45] A. J. Wu and F. O. Ellison, J. Chem. Phys. **47**, 1458 (1967).

[46] N. K. J. Ray, J. Chem. Phys. **52**, 463 (1970).

[47] W. A. Lester Jr, J. Chem. Phys. **54**, 3171 (1971).

[48] W. A. Lester Jr, J. Chem. Phys. **53**, 1511 (1970).

[49] R. C. Raffenetti and K. J. Ruedenberg, Chem. Phys. **59**, 5978 (1973).

[50] E. Kochanski, Chem. Phys. Lett. **28**, 471 (1974).

[51] J. B. Collins, P. von Ragué-Schleyer, J. S. Binkley, J. A. Pople, and L. J. Radom, J. Am. Chem. Soc. **98**, 3436 (1976).

[52] P. Hobza and P. von Ragué-Schleyer, Chem. Phys. Lett. **105**, 630 (1984).

[53] B. H. Cardelino, W. H. Eberhardt, and R. F. J. Borkman, J. Chem. Phys. **84**, 3230 (1986).

[54] D. A. Dixon, J. L. Gole, and A. J. Komornicki, J. Phys. Chem. **92**, 1378 (1988).

[55] A. Russek, R. Snyder, and R. J. Furlan, Phys. Rev. A **39**, 6158 (1989).

[56] R. Davy, E. Skoumbourdis, and T. Kompanchenko, Mol. Phys. **97**, 1263 (1999).

[57] H. S. Lee, Y. S. Lee, and G. H. Jeung, J. Phys. Chem. A **103**, 11080 (1999).

[58] E. Bodo, F. A. Gianturco, R. Martinazzo, and M. Raimondi, J. Phys. Chem. A **105**, 10986 (2001).

[59] R. Martinazzo, G. F. Tantardini, E. Bodo, and F. A. Gianturco, J. Chem. Phys. **119**, 11241 (2003).

[60] R. Martinazzo, E. Bodo, F. A. Gianturco, and M. Raimondi, Chem. Phys. **287**, 335 (2003).

[61] C. Sanz, E. Bodo, and F. A. Gianturco, Chem. Phys. **314**, 135 (2005).

[62] V. P. Bulychev, K. M. Bulanin, and M. O. Bulanin, Opt. Spectrosc. **96**, 205 (2004).

[63] S. Huzinaga, J. Chem. Phys. **42**, 1293 (1965).

[64] W. Kutzelnigg, V. Staemmler, and C. Hoheisel, Chem. Phys. **1**, 27 (1973).

[65] H.-J. Werner, P. J. Knowles, R. Lindh, F. R. Manby, M. Schütz, P. Celani, T. Korona, G. Rauhut, R. D. Amos, A. Bernhardsson, et al., MOLPRO, *version 2006.1* (2006), see http://www.molpro.net.

[66] M. A. Iron, M. Oren, and J. M. L. Martin, Mol. Phys. **101**, 1345 (2003).

[67] T. H. Dunning, J. Chem. Phys. **90**, 1007 (1989).

[68] C. H. Wu, J. Chem. Phys. **71**, 783 (1979).

[69] D. G. Musaev and O. P. Charkin, Z. Strukt. Khim. **31**, 190 (1990).

[70] P. Valtazanos and C. A. Nicolaides, Chem. Phys. Lett. **172**, 254 (1990).

[71] T. H. Dunning and P. J. Hay, *Methods of Electronic Structure Theory* (Plenum Press, New York, 1977).

[72] A. J. Page and E. I. von Nagy-Felsobuki, unpublished, 2008.

[73] A. J. Page, D. J. D. Wilson, and E. I. von Nagy-Felsobuki, Chem. Phys. Lett. **429**, 335 (2006).

[74] D. E. Woon and T. H. Dunning, J. Chem. Phys. **100**, 2975 (1994).

[75] B. Wells and S. Wilson, Chem. Phys. Lett. **101**, 429 (1983).

[76] E. F. Hayes and J. L. Gole, J. Chem. Phys. **55**, 5132 (1971).

[77] S. W. Harrison, L. J. Massa, and P. Solomon, J. Chem. Phys. **59**, 263 (1973).

[78] A. W. K. Leung and W. H. Breckenridge, J. Chem. Phys. **111**, 9197 (1999).

[79] D. Bellert and W. H. Breckenridge, Chem. Rev. **102**, 1595 (2002).

[80] H. Partridge, J. R. Stallcop, and E. Levin, J. Chem. Phys. **115**, 6471 (2001).

[81] C. C. Lovallo and M. Klobukowski, Chem. Phys. Lett. **373**, 439 (2003).

[82] U. Kleinekathöfer, M. Lewerenz, and M. Mladenovic, Phys. Rev. Lett. **83**, 4717 (1999).

[83] S. W. Harrison, L. J. Massa, and P. Solomon, Chem. Phys. Lett. **16**, 57 (1972).

[84] X. Bu and C. Zhong, Chem. Phys. Lett. **392**, 181 (2004).

[85] X. Bu, C. Zhong, and A. F. Jalbout, Chem. Phys. Lett. **387**, 410 (2004).

[86] N. Oliphant and R. J. Bartlett, J. Chem. Phys. **100**, 6550 (1994).

[87] S. Green, Adv. Chem. Phys. **25**, 179 (1974).

[88] G. D. Kedziora and I. Shavitt, J. Chem. Phys. **106**, 8733 (1997).

[89] Sudarko, J. M. Hughes, and E. I. von Nagy-Felsobuki, Aust. J. Phys. **53**, 665 (2000).

[90] Sudarko and E. I. von Nagy-Felsobuki, J. Mol. Spec. **208**, 161 (2001).

[91] Sudarko, Ph.D. thesis, The University of Newcastle, Australia (2000).

[92] D. J. D. Wilson and E. I. von Nagy-Felsobuki, Mol. Phys. **103**, 507 (2005).

CHAPTER 4

Ab Initio Vibrational and Rovibrational Spectra of Triatomic Molecules

4.1. Introduction

Theoretical approximations of the vibrational and rovibrational spectra of polyatomic molecules began with the BO approximation [1, 2]. By employing this approximation the electronic energy is parametrically dependent on a particular set of nuclear co-ordinates. Provided that the molecular PES is known, it is (in principle) possible to calculate the complete spectrum of rovibrational eigenvalues for a species within the BO approximation. Variational rovibrational Hamiltonians for three- [3], four- [4–12], five- [13] and six-atom [14] molecular systems have been reported in the literature. More recently, general N-atom molecular vibrational Hamiltonians have been developed by Mátyus *et al.* [15], Yurchenko *et al.* [16] and Pesonen [17].

Modern rovibrational calculations for polyatomic molecules generally have their beginnings in the Hamiltonians of Eckart [18], Wilson and Howard [19], Darling and Dennison [20] and Watson [21, 22]. The assumption that the nuclear motion of polyatomic molecules consists of small amplitude vibrations coupled with near rigid rotations about some well defined vibration-averaged equilibrium geometry is implicit in these approaches. Amongst the first great successes of *ab initio* rovibrational calculations of polyatomic molecules was the ground state of H_3^+ [23–30]. In 1978 Carney *et al.* [23] reviewed model Hamiltonians with an emphasis on the convergence of different solution methodologies with respect to the final rovibrational

spectra. A number of other pertinent reviews can be found in the literature. These include the works of Carter and Handy [31–35], Jensen and Bunker [36–38], Bačić and Light [39], Searles and von Nagy-Felsobuki [40, 41], Sutcliffe [42], Tennyson and co-workers [43–45], Hubac and Svrcek [46] and Schwenke [11, 47, 48].

The molecular rovibrational Hamiltonian is most conveniently classified in terms of the co-ordinate system employed in its construction. One general class of rovibrational Hamiltonians consists of those expressed in a subset of curvilinear internal co-ordinates, such as internal/valence [25, 49–53], scattering [27, 54–60] and Radau hyperspherical co-ordinates [61–63]. The 'MORBID' (Morse Oscillator-Rigid Bender Internal Dynamics) Hamiltonian of Jensen and co-workers [64–67] also lies in this category. Hamiltonians of this form provide an advantage in that the complete eigenspectrum of any polyatomic molecule can be approximated in principle. However, suitable choices of basis sets, matrix element computations and diagonalisation techniques must be made for the problem to remain computationally tractable. As such, a rovibrational Hamiltonian of this form is realistically suitable only for small species, *viz.* tri- and tetra-atomic species [15].

Another broad class of rovibrational Hamiltonians follows from the work of Watson [21, 22], who developed general non-linear and linear Hamiltonians using rectilinear normal co-ordinates within the Eckart framework [18]. The main appeal of the Eckart-Watson Hamiltonians is that they may be applied to an arbitrary molecular structure or bonding arrangement. The need for molecule-specific co-ordinate systems is therefore alleviated. In addition, the vibration-rotation coupling terms in the Hamiltonian are minimised, due to the use of the Eckart framework. The latter fact has ramifications for both the size of rovibrational basis set required for converged solutions and the time required for the diagonalisation of the Hamiltonian matrix. Nevertheless, Eckart-Watson Hamiltonians fail to describe large amplitude

vibrational motions, due to the nature of the co-ordinates employed in their construction.

Based on the work of Carney and Porter [23, 24, 68, 69] with respect to D_{3h} and C_{2v} triatomic molecules, Searles and von Nagy-Felsobuki [70] and Wang *et al.* [71] developed normal co-ordinate vibrational Hamiltonians for C_s and linear triatomic molecules, respectively. The latter vibrational Hamiltonians are employed throughout this work.

The remainder of this Chapter is dedicated to the discussion and implementation of the vibrational solution algorithm of von Nagy-Felsobuki and co-workers [40], for both non-linear and linear triatomic molecules (*i.e.* stage (e) of Figure 1.1). This algorithm requires both a detailed knowledge of the equilibrium structure and an embedded analytical PEF and DMF. These have been discussed in Chapters Two and Three, respectively. Aspects including the construction of one-dimensional (1D) and 3D vibrational eigenvectors, the numerical quadrature scheme and the calculation of kinetic energy, angular momenta and potential energy matrix integrals will be discussed in this Chapter. A method for calculating the vibration-averaged structures of triatomic molecules will also be developed. The calculation of transition dipole moment integrals will be reviewed in the context of the calculation of *ab initio* vibrational spectra. The form of the rovibrational 'super-matrix' elements for non-linear molecules will be discussed, as will rovibrational transition dipole moment integrals [72]. All aspects of these algorithms will be illustrated using the $^1A_1$ and $^1\Sigma_g^+$ ground states of BeH_2^{2+} and $BeHe_2^{2+}$, respectively.

4.2. Solution Algorithm: Overview

Throughout this thesis, the solutions of the vibrational and rovibrational Schrödinger equation have been obtained using the solution algorithm of von Nagy-

Felsobuki and co-workers (see Figure 4.1). The individual stages of this algorithm are dealt with at greater length in subsequent sections of this Chapter, but are outlined briefly at this point:

1. *Ab initio* property surfaces (*viz.* the PEF and DMF) of the species in question are constructed using the linear regression techniques described in Chapter Three;

2. The analytical PEF is embedded in the 1D Schrödinger equation, which is solved variationally using a finite-element method (FEM) (see §4.3);

3. The eigenvectors of the 1D Schrödinger equation are employed as a configurational basis for the 3D trial vibrational eigenvectors. The analytical PEF is embedded in the 'full' vibrational Hamiltonian, which is then diagonalised using the 3D trial wave functions (see §4.4, §4.4.1-3);

4. The analytical DMF is embedded in the 3D Schrödinger equation. Vibrational dipole transition moment matrix elements are then determined as the expectation values of the dipole moment operator in the vibrational eigenvector basis (see §4.4.6);

5. Elements of the rotational constant, centrifugal distortion and Coriolis coupling matrices spanned by the optimised 3D eigenvectors are calculated (see §4.5);

6. Trial rovibrational wave functions are constructed using the 3D eigenvectors in conjunction with rotational basis functions. The latter are constructed as $\pm$ combinations of symmetric-top eigenfunctions, $\left|R^{\pm}_{JKm}\right\rangle$. The rovibrational 'super-matrix' is then constructed and diagonalised to yield rovibrational eigenvalues (see §4.5.1), and;

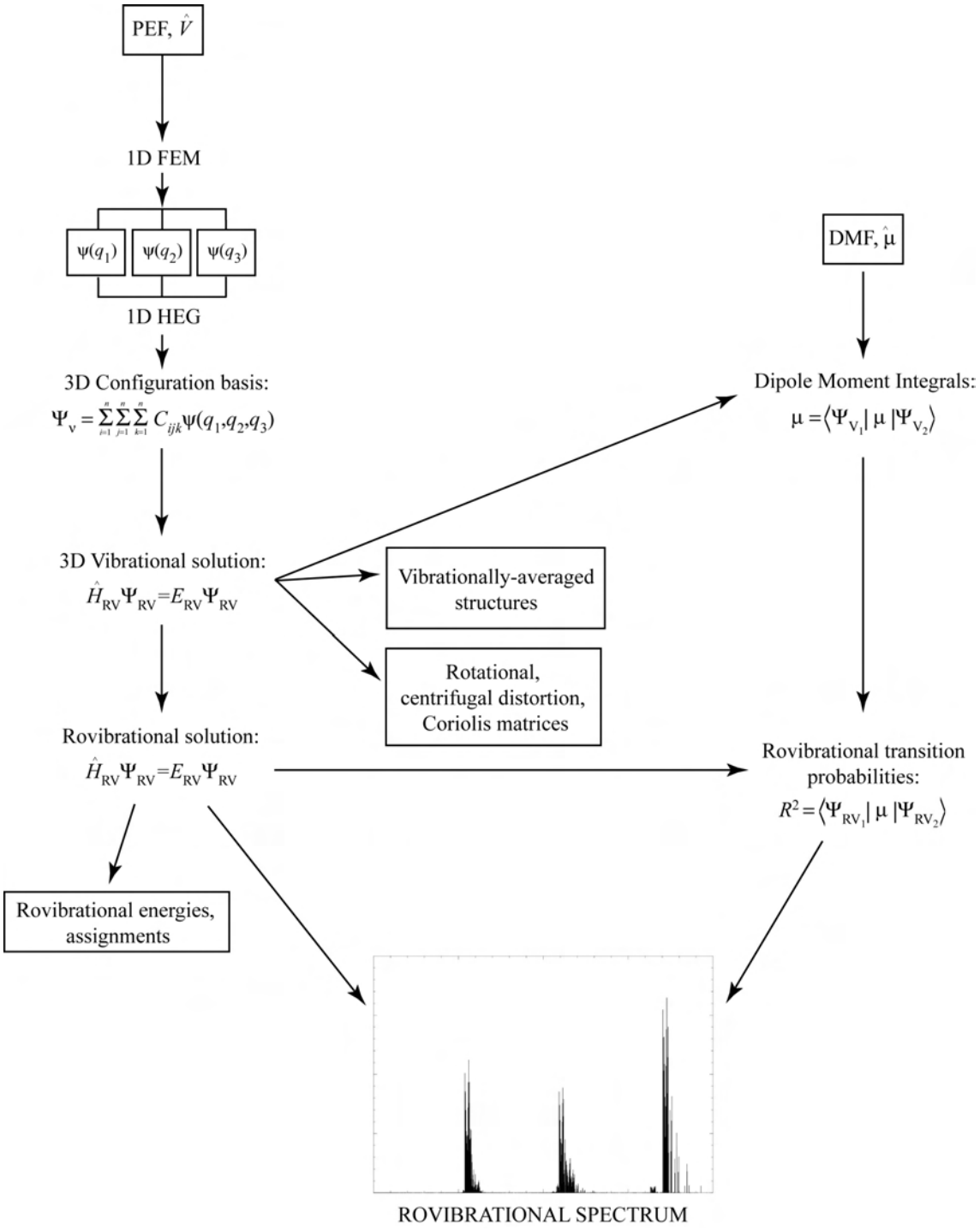

Figure 4.1 The rovibrational spectrum solution algorithm of von Nagy-Felsobuki and co-workers.

7. Rovibrational dipole transition moment matrix elements are calculated using the embedded DMF. Radiative properties, such as rovibrational transition probabilities and spectral line intensities are then calculated in the space-fixed framework (see §4.5.2).

The latter three aspects of this algorithm are currently applicable only to non-linear molecules. For all spectroscopic quantities reported in this thesis, cgs units will be employed.

4.3. The One-Dimensional Vibrational Wave Function

Closed-form solutions to the nuclear Schrödinger equation can only be obtained for contrived potential operators, such as the finite-square well, the harmonic potential and the Morse potential [40]. In general however, the nuclear Schrödinger equation cannot be solved analytically. To this end, the 1D FEM approach of von Nagy-Felsobuki and co-workers [73], which employs the Ritz-Rayleigh method [74], has been employed in this thesis.

The general 1D vibrational Schrödinger equation is of form,

$$\left\{ \frac{\partial^2}{\partial q_i^2} + \hat{U}_w^{(3)}(q_i) + \hat{V}(q_i) \right\} \psi_j(q_i) = \lambda_j \psi_j(q_i) \tag{4.1}$$

where $\frac{\partial}{\partial q_i}$, $\hat{U}_w^{(3)}(q_i)$ and $\hat{V}(q_i)$ are the kinetic energy, 3$^{\text{rd}}$ order Watson and potential operators in the arbitrary normal co-ordinate q_i, respectively, and ψ_j and λ_j are the j^{th} eigenfunction and eigenvalue, respectively. It is noted here that $\hat{U}_w \equiv 0$ for linear molecules. In the cases of non-linear and linear molecules, $\mathbf{q} \equiv \mathbf{f}$ and $\mathbf{q} \equiv \mathbf{w}$, respectively. These two sets of normal co-ordinates are shown in Figures 4.2 and 4.3, respectively.

The FEM solves equation (4.1) variationally by dividing a specified domain

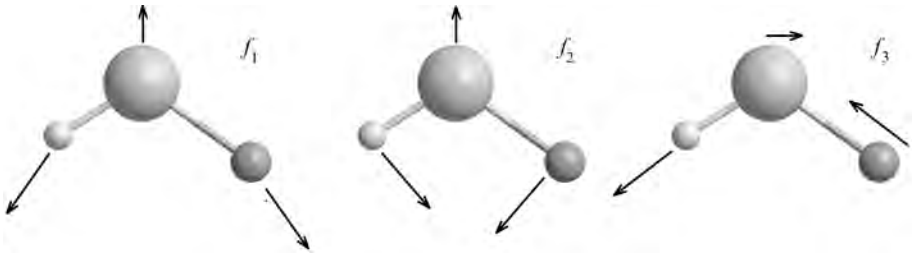

Figure 4.2 The vibrational **f** co-ordinates of a C_s triatomic molecule [70].

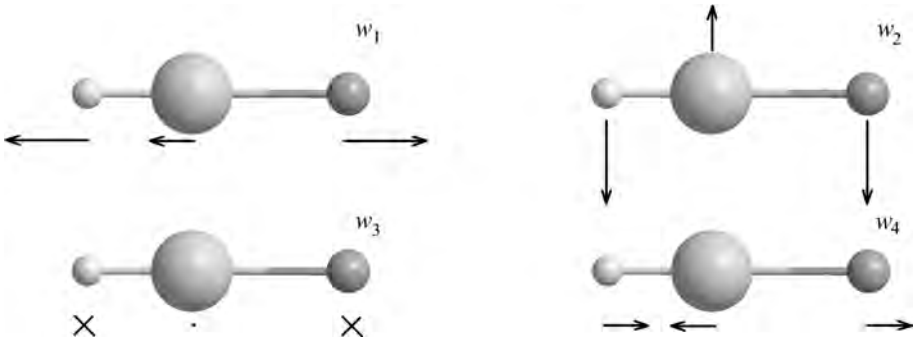

Figure 4.3 The vibrational **w** co-ordinates of a linear triatomic molecule [75], shown in the xz plane.

of $\hat{V}(q_i)$ into a number of 'finite-elements', over each of which the eigenvalue problem is solved using a trial function $\Phi_j(q_i)$, constructed as a combination of localised basis functions. These basis functions, $\phi(q_i)$, are identically zero for all elements other than that being considered. As such, the eigenfunction ψ_j may be written as,

$$\psi_j(q_i) \approx \Phi_j(q_i) = \sum_{k=1}^{16} c_{jk}\phi_k(q_i) \tag{4.2}$$

Throughout this thesis, ϕ have been chosen as Hermite cubic polynomials. For an

element of size h, the latter are defined as [73],

$$\phi_1^h = 1 - 3\left(\frac{Q_i^h}{h}\right)^2 + 2\left(\frac{Q_i^h}{h}\right)^3 \tag{4.3}$$

$$\phi_2^h = Q_i^h - 2\left(\frac{\left(Q_i^h\right)^2}{h}\right) + \left(\frac{\left(Q_i^h\right)^3}{h^2}\right) \tag{4.4}$$

$$\phi_3^h = 3\left(\frac{Q_i^h}{h}\right)^2 - 2\left(\frac{Q_i^h}{h}\right)^3 \tag{4.5}$$

$$\phi_4^h = -\left(\frac{\left(Q_i^h\right)^2}{h}\right) + \left(\frac{\left(Q_i^h\right)^3}{h^2}\right) \tag{4.6}$$

Thus continuity of ϕ, Φ and the first derivatives thereof is imposed [40]. Substitution of equation (4.2) into equation (4.1) yields a residual,

$$r(\Phi_j) = \left[\frac{\partial}{\partial q_i} + \hat{U}_w^{(3)}(q_i) + \hat{V}(q_i)\right]\Phi_j - \lambda_j \Phi_j \tag{4.7}$$

the value of which must be minimised. If Φ_j is such that the corresponding Rayleigh quotient,

$$R(\Phi_j) = \frac{\int \left(\Phi_j'\right)^2 dq_i + \int \Phi_j \left(\hat{U}_w^{(3)} + \hat{V}\right)\Phi_j dq_i}{\int \Phi_j^2 dq_i} \tag{4.8}$$

is minimised, then ψ_j is an eigenfunction of equation (4.1). It is convenient to express $\Phi_j(q_i)$ as a piece-wise continuous polynomial,

$$\Phi_j^h(q_i) = \sum_{k=1}^{16} c_{jk}^h \phi_k^h(q_i) \tag{4.9}$$

Equation (4.8) is defined over the finite-element $q_i^h = [0, h]$ as,

$$R(\Phi_j) = \frac{\sum_{k=1}^{16}\sum_{l=1}^{16} c_{jk}^h c_{jl}^h \int_0^h \left((\phi_k')^h(\phi_l')^h + \phi_k^h\left(\hat{U}_w^{(3)} + \hat{V}\right)\phi_l^h\right) dq_i^h}{\sum_{k=1}^{16}\sum_{l=1}^{16} c_{jk}^h c_{jl}^h \int_0^h \phi_k^h \phi_l^l dq_i^h} \tag{4.10}$$

or equivalently,

$$\mathbf{R}^h = \frac{(\mathbf{C}^h)^T \mathbf{A}^h \mathbf{C}^h}{(\mathbf{C}^h)^T \mathbf{M}^h \mathbf{C}^h} \tag{4.11}$$

where $(\mathbf{C}^h)^T = [C^h_{1j}, C^h_{2j}, C^h_{3j}, \ldots, C^h_{nj}]$ is the transpose of the matrix containing the expansion parameters defined on q^h_i and j refers to the j^{th} eigenfunction. The matrix $\mathbf{M}^h$ is the local mass matrix, the elements of which are defined as,

$$\left[M^h_{kl}\right] = \int_0^h \Phi^h_j \Phi^h_k dq^h_i = \frac{h}{420} \begin{bmatrix} 156 & 22h & 54 & -13h \\ 22h & 4h^2 & -3h & -3h^2 \\ 54 & 13h & 156 & -22h \\ -13h & -3h^2 & -22h & 4h^2 \end{bmatrix} \tag{4.12}$$

The elements $\left[A^h_{kl}\right]$ of the matrix $\mathbf{A}^h$ are defined on q^h_i as,

$$\left[A^h_{kl}\right] = \left[K^h_{kl}\right] + \left[P^h_{kl}\right] = \int_0^h \left[(\Phi'_k)^h (\Phi'_l)^h + \Phi^h_k \left(\hat{U}^{(3)}_w + \hat{V}\right) \Phi^h_l\right] dq^h_i \tag{4.13}$$

where,

$$\left[K^h_{kl}\right] = \frac{1}{30h} \begin{bmatrix} 36 & 22h & 54 & -13h \\ 22h & 4h^2 & 13h & -3h^2 \\ 54 & 13h & 156 & -22h \\ -13h & -3h^2 & -22h & 4h^2 \end{bmatrix} \tag{4.14}$$

and,

$$\left[P^h_{kl}\right] = \left[P^h_{kl}\right] = \left[\int_0^h \Phi^h_k \left(\hat{U}^{(3)}_w + \hat{V}\right) \Phi^h_l dq^h_i\right] \tag{4.15}$$

respectively.

The elemental matrices $\mathbf{K}^h$ and $\mathbf{M}^h$ are evaluated successively on each interval q^h_i and are combined to form sparse 'global' matrices $\mathbf{K}$ and $\mathbf{M}$. The latter contain the appropriate overlapping contributions from adjacent finite-elements.

The subsequent global Rayleigh quotient matrix **R** is solved using a diagonalisation procedure developed by Doherty *et al.* [76]. It has been established [77, 78] that convergence to within double-precision accuracy in the eigenfunctions and eigenvalues of equation (4.1) is attained with the use of 1000 finite-elements. This convention has therefore been employed in this thesis. Moreover, the decay of $\psi_j(q_i)$ (to at most $1 \times 10^{-7}\ a_0^{1/2}$) in the classically forbidden regions of the chosen 1D domains have been ensured. All solutions to the 1D vibrational Schrödinger equation reported in this thesis have been calculated using FORTRAN programs of von Nagy-Felsobuki and co-workers (oneda_pade_cs, vib41_cc_new) [79], given in Appendix C.

4.3.1. One-Dimensional Vibrational Eigenvectors of $(^1\mathrm{A}_1)\mathrm{BeH}_2^{2+}$

The 1D vibrational states of $(^1\mathrm{A}_1)\mathrm{BeH}_2^{2+}$ have been calculated using the FEM procedure outlined in the previous section. The analytical PEF employed here is that of Page and von Nagy-Felsobuki [80], described in Chapter 3. The domains employed for the numerical integration procedure in the t_1, t_2 and t_3 normal co-ordinates are [-2.0 a_0, 3.0 a_0], [-0.9 a_0, 3.5 a_0] and [-2.25 a_0, 2.25 a_0], respectively. The vibrational energies, E_{t_i}, of the lowest 20 t_1, t_2 and t_3 normal modes of $(^1\mathrm{A}_1)\mathrm{BeH}_2^{2+}$ are listed in Table 4.1. The explicit form of the normal co-ordinates of non-linear molecules are discussed at greater length in §4.4. To illustrate the appropriate decay of the 1D vibrational eigenfunctions in the classically forbidden regions of the PEF, the five lowest t_1 eigenfunctions are given in Appendix D.

4.3.2. One-Dimensional Vibrational Eigenvectors of $(^1\Sigma_g^+)\mathrm{BeHe}_2^{2+}$

The 1D vibrational eigenfunctions and eigenvalues of the $^1\Sigma_g^+$ ground state of BeHe_2^{2+} have been calculated using the FEM, in conjunction with the $P(6,5)$ EOGL

Table 4.1 One-dimensional eigenvalues (/cm^{-1}) of (^{1}A$_1$)BeH$_2^{2+}$ relative to the PEF minimum[a].

v	$E_{f_1}(v)$	$E_{f_2}(v)$	$E_{f_3}(v)$
1	519.5	1152.5	219.6
2	1985.5	4074.9	903.0
3	3427.7	6827.7	1850.0
4	4846.4	9417.7	2886.9
5	6241.7	11858.0	3992.5
6	7613.8	14132.9	5146.0
7	8962.9	16269.2	6336.2
8	10289.0	18265.1	7556.1
9	11592.3	20126.3	8801.0
10	12872.8	21858.9	10067.8
11	14138.0	23469.6	11354.4
12	15366.1	24966.0	12659.6
13	16579.0	26356.7	13982.5
14	17769.4	27651.0	15322.5
15	18937.4	28858.6	16679.4
16	20082.9	29989.4	18053.1
17	21206.1	31056.7	19443.5
18	22307.5	32092.9	20857.0
19	23389.8	33162.7	22274.9
20	24464.0	34322.7	23716.2

[a]PEF minimum = -14.90871403 E$_h$.

PEF of the $^1\Sigma_g^+$ ground state of BeHe$_2^{2+}$. The latter was developed in Chapter 3. The integration domains employed in the w_1 and w_3 vibrational normal co-ordinates are [-1.25 a_0, 4.0 a_0] and [-1.5 a_0, 1.5 a_0], respectively, whereas in the w_2 bend co-ordinate domains of [-3.5 a_0, 3.5 a_0] are employed. These domains guaranteed all 1D eigenfunctions decayed appropriately. The lowest 20 1D vibrational eigenvalues (E_{w_i}) of ($^1\Sigma_g^+$)BeHe$_2^{2+}$ for each vibrational co-ordinate are given in Table 4.2. The explicit form of the normal co-ordinates of linear molecules are discussed at greater length in §4.4.

Table 4.2 One-dimensional eigenvalues (/cm^{-1}) of ($^1\Sigma_g^+$)BeHe$_2^{2+}$, relative to the PEF minimum[a].

v	$E_{w_1}(v)$	$E_{w_2/w_3}(v)$	$E_{w_4}(v)$
1	363.5	52.6	505.0
2	1077.0	184.9	1530.0
3	1772.3	355.5	2584.5
4	2449.3	545.6	3667.1
5	3108.1	750.0	4776.7
6	3748.6	965.5	5912.1
7	4370.8	1189.6	7072.6
8	4974.7	1420.7	8257.3
9	5560.1	1657.5	9465.5
10	6127.0	1899.0	10696.5
11	6675.4	2144.3	11949.9
12	7205.1	2392.8	13224.9
13	7716.0	2643.8	14521.2
14	8208.0	2896.7	15838.3
15	8681.1	3151.2	17175.8
16	9135.1	3406.8	18533.2
17	9569.9	3663.1	19910.3
18	9985.4	3919.8	21306.6
19	10381.5	4176.7	22721.9
20	10758.2	4433.3	24155.8

[a]PEF minimum = -19.52603610 E$_h$.

4.4. Normal Co-ordinate Vibrational Hamiltonians for Triatomic Molecules

Using the BO approximation, the nuclear rovibrational quantum mechanical Hamiltonian may be written as,

$$\hat{H}^{\mathrm{RV}} = \hat{H}^{\mathrm{vib}} + \hat{H}^{\mathrm{rot}} + \hat{H}^{\mathrm{cor}} + \hat{V} \tag{4.16}$$

where $\hat{H}^{\mathrm{vib}}$, $\hat{H}^{\mathrm{rot}}$ and $\hat{H}^{\mathrm{cor}}$ are the operators describing the vibration, rotation and the vibration-rotation coupling of the nuclei, respectively. The electronic potential for a given set of nuclear co-ordinates is denoted by $\hat{V}$. The use of a normal co-ordinate Hamiltonian, such as that employed throughout this thesis, necessitates a

two-stage approach to solving the nuclear Schrödinger equation,

$$\hat{H}^{\mathrm{RV}}\Psi^{\mathrm{RV}} = E^{\mathrm{RV}}\Psi^{\mathrm{RV}} \tag{4.17}$$

This two-stage approach entails firstly the partitioning of $\hat{H}^{\mathrm{RV}}$ in equation (4.17) into operators corresponding to purely vibrational and rotational motion. The second stage involves the combination of these separate solution sets and the subsequent solution of equation (4.17) using the 'full' rovibrational Hamiltonian (equation (4.16)). A detailed account of the use of this normal co-ordinate approach has been reported by Searles and von Nagy-Felsobuki [40, 41].

4.4.1. The Non-Linear Case

For a non-linear triatomic molecule, the most general form of $\hat{H}^{\mathrm{vib}}$ corresponds to that for a molecule of C_s symmetry [70],

$$\begin{aligned}\hat{H}^{\mathrm{vib}} &= \sum_{\alpha}\hat{T}_{\alpha} + \hat{T}_l + \hat{U}_w^{(3)} + \hat{V} \\ &= -\frac{\hbar^2}{2\mu_{C_s}}\left\{\sum_{k=1}^{3}\frac{\partial^2}{\partial f_k^2} + \frac{\mu_{C_s}}{\mathbf{I}'(f_1)}\left(f_2\frac{\partial}{\partial f_3} - f_3\frac{\partial}{\partial f_2}\right)^2\right\} - \frac{\hbar^2}{8}\sum_{\alpha}\mu_{\alpha\alpha} + \hat{V}\end{aligned} \tag{4.18}$$

Here, $\hat{T}_{\alpha}$ and $\hat{T}_l$ correspond to the vibrational kinetic energy and vibrational angular momentum operators, α runs over x, y and z co-ordinates and $\mathbf{I}'(f_1)$ is the effective inertial tensor,

$$\mathbf{I}'(f_1) = \frac{m_1m_2m_3\mu_{C_s}R_1^2}{M\lambda^2} + \frac{2R_1\mu_{C_s}(m_1m_2m_3)^{1/2}}{M^{1/2}\lambda} + \mu_{C_s}f_1^2 \tag{4.19}$$

The C_s Hamiltonian of equation (4.18) is defined in terms of the rectilinear $\mathbf{f}$ co-ordinates [70] (see Figure 4.2). In the case of a C_{2v} species, equation (4.18) collapses to the C_{2v} $\mathbf{t}$ co-ordinate Hamiltonian of Carney *et al.* [25] and so $\mathbf{f} \equiv \mathbf{t}$. The Watson operator may be expanded as a Taylor series [21],

$$\mu_{\alpha\alpha} = \mathbf{I^{e^{-1}}} + \mathbf{I^{e^{-1}}a_w I^{e^{-1}}} + \frac{3}{4}\mathbf{I^{e^{-1}}a_w I^{e^{-1}}a_w I^{e^{-1}}} - \frac{1}{2}\mathbf{I^{e^{-1}}a_w I^{e^{-1}}a_w I^{e^{-1}}a_w I^{e-1}} + \ldots \tag{4.20}$$

such that [41],

$$\mathbf{I^{e^{-1}}} = \frac{1}{4(R_1 b + R_2 c)^2 a^2 \lambda^2 \mu_{C_s}} \begin{bmatrix} 2\mu_{C_s}(\mu_{C_s} - \alpha) & -2\mu_{C_s}\beta & 0 \\ -2\mu_{C_s}\beta & 2\mu_{C_s}(\mu_{C_s} - \alpha) & 0 \\ 0 & 0 & \mu_{C_s}^2 - \alpha^2 - \beta^2 \end{bmatrix} \tag{4.21}$$

The $\mathbf{a_w}$ matrix is defined as,

$$\mathbf{a_w} = \mathbf{a_{w_1}} + \mathbf{a_{w_2}} + \mathbf{a_{w_3}} \tag{4.22}$$

where,

$$\mathbf{a_{w_1}} = \gamma R_1 (R_1 b + R_2 c) 2\gamma a \begin{bmatrix} \mu_{C_s} - \alpha & \beta & 0 \\ \beta & \mu_{C_s} - \alpha & 0 \\ 0 & 0 & 2\mu_{C_s} \end{bmatrix} \tag{4.23}$$

$$\mathbf{a_{w_2}} = 2\lambda a \begin{bmatrix} \frac{(R_2^2 - R_1^2)a}{R_2} & -(R_1 c + R_2 b) & 0 \\ -(R_1 c + R_2 b) & \frac{(R_2^2 - R_1^2)a}{R_2} & 0 \\ 0 & 0 & 0 \end{bmatrix} \tag{4.24}$$

and,

$$\mathbf{a_{w_3}} = 2\lambda a \begin{bmatrix} R_1c + R_2b & \frac{(R_2^2 - R_1^2)a}{R_2} & 0 \\ \frac{(R_2^2 - R_1^2)a}{R_2} & -(R_1c + R_2b) & 0 \\ 0 & 0 & 0 \end{bmatrix} \tag{4.25}$$

Here, $a, b, c, R_1, R_2, R_3, \mu_{C_s}, \alpha, \beta, \gamma$ and λ are mass and structural parameters derived by Carney *et al.* [23] and von Nagy-Felsobuki and co-workers [40, 41]. These parameters, and therefore the form of $\hat{H}^{\text{vib}}$, are symmetry dependent. The 'collapsing' of the mass and structural parameters of $\hat{H}^{\text{vib}}$ is shown explicitly in Table 4.3.

4.4.2. The Linear Case

According to Amat and Henry [81], linear triatomic molecules possess four normal vibrational co-ordinates, including a single doubly degenerate bending and two non-degenerate stretching vibrational co-ordinates. For a linear triatomic molecule, the vibrational motion is dependent only on two of the Euler angles which are required to specify the direction of molecular axis in the space-fixed frame of reference. The absence of the third Euler angle means that the commutation relations of the angular momenta operators developed for non-linear systems [21, 22, 82] no longer hold. Additionally, the elements of $\mathbf{I}'$ in the linear case may be such that $\mathbf{I}'^{-1}$ can become singular. From these considerations, an Eckart-Watson Hamiltonian for linear triatomic molecules must be derived in a co-ordinate system which alleviates these unique problems.

Wang *et al.* [71] derived a 4D Eckart-Watson vibrational Hamiltonian for linear triatomic molecules analogous to equation (4.18) in normal co-ordinates $\mathbf{w}$

Table 4.3 Structural and mass parameters of non-linear triatomic molecules as a function of molecular symmetry.

Parameter	C_s (A-B-C)	C_{2v} (A-B-A)	D_{3h} (A-A-A)
R^a	$R_1 \neq R_3 \neq R_3$	$R_1, R_2 \neq R_3$	R_1
M^b	$m_A + m_B + m_C$	$2m_A + m_B$	$3m_A$
a^c	$\cos\theta_1$	$\cos\left(\frac{\theta}{2}\right)$	$\frac{\sqrt{3}}{2}$
b^c	$\sin\theta_1$	$\sin\left(\frac{\theta}{2}\right)$	$\frac{1}{2}$
c^c	$\sin\theta_2$	$\sin\left(\frac{\theta}{2}\right)$	$\frac{1}{2}$
λ	$\left\{\frac{1}{R_1^2}\left[\frac{R_2^2}{m_A^2} + \frac{(R_1 b + R_2 c)^2}{m_B^2} + \frac{R_1^2}{m_C^2}\right]\right\}^{-1/2}$	$\left[\frac{1}{m_A^2} + \frac{4b^2}{m_B^2} + \frac{1}{m_C^2}\right]^{-1/2}$	$\frac{m_A}{\sqrt{3}}$
$\mu_{\text{symm.}}{}^d$	$\frac{\lambda^2}{R_1^2}\left[\frac{R_2^2}{m_A} + \frac{(R_1 b + R_2 c)^2}{m_B} + \frac{R_1^2}{m_C}\right]$	$\lambda^2\left[\frac{1}{m_A} + \frac{4b^2}{m_B} + \frac{1}{m_C}\right]$	M
α	$\frac{\lambda^2}{R_1^2}\left[\frac{R_1^2 a^2 - R_2^2 c^2}{m_A} + \frac{(R_1 b + R_2 c)^2}{m_B} + \frac{R_1^2 a^2 - R_1^2 b^2}{m_C}\right]$	$\lambda^2\left[\frac{\cos\theta}{m_A} - \frac{4b^2}{m_B} + \frac{\cos\theta}{m_C}\right]$	0
β	$\frac{2\lambda^2 a}{R_1}\left[\frac{R_1 b}{m_C} - \frac{R_2 c}{m_A}\right]$	$\lambda^2 \sin\theta\left[\frac{1}{m_C} - \frac{1}{m_A}\right]$	0
γ^2	$\frac{m_A m_B m_C}{4a^2\lambda^4(R_1 b + R_2 c)}$	$\left[1 - \frac{\alpha^2}{\mu_{C_{2v}}^2} - \frac{\beta^2}{\mu_{C_{2v}}^2}\right]$	0

[a] R_1,R_2 and R_3 correspond to inter-nuclear distance vectors between nuclei 1st and 2nd , 2nd and 3rd and 1st and 3rd nuclei respectively.

[b] M is the total mass of nuclei A, B and C.

[c] θ is the inter-nuclear A-B-C bond angle. θ_1 and θ_2 are sub-angles thereof; see reference [41].

[d] $\mu_{\text{symm.}}$ is the reduced mass.

(see Figure 4.3). This Hamiltonian is defined as,

$$\begin{aligned}\hat{H}^{\text{vib}} &= \sum_{\alpha} \hat{T}_{\alpha} + \hat{T}_{l} + \hat{V} \\ &= -\frac{\hbar^2}{2\mu_{\text{symm.}}} \left\{ \sum_{k=1}^{4} \frac{\partial^2}{\partial w_k^2} \; + \; \frac{\mu_1}{\mathbf{I}'(w_1)} \left[\left(w_2 \frac{\partial}{\partial w_4} - w_4 \frac{\partial}{\partial w_2} \right)^2 \right. \right. \\ &\qquad \left. \left. + \left(w_3 \frac{\partial}{\partial w_4} - w_4 \frac{\partial}{\partial w_3} \right)^2 \right] \right\} + \hat{V}\end{aligned} \tag{4.26}$$

where $\mathbf{I}'(w_1)$ is defined as,

$$\mathbf{I}'(w_1) = \left[\left(I^0 \right)^{1/2} + \mu_1^{1/2} w_1 \right]^2 \tag{4.27}$$

such that,

$$I^0 = \frac{m_1 m_2 R_1^2 + m_2 m_3 R_2^2 + m_1 m_3 R_3^2}{M} \tag{4.28}$$

and,

$$\mu_{\text{symm.}} = \frac{m_1 m_2 m_3 M I^0}{m_1^2 m_2^2 R_1^2 + m_2^2 m_3^2 R_2^2 + m_1^2 m_3^2 R_3^2} \tag{4.29}$$

The lack of the Watson operator is noted in equation (4.26). The corresponding 1D vibrational Schrödinger equation (equation (4.1)) lacks this Watson operator accordingly.

By constraining the vibrational motion of the molecule to a single plane (*viz.* the xz plane) [82], Wang *et al.* [75] redefined the vibrational motion of the system entirely by three of the four $\mathbf{w}$ co-ordinates (w_1, w_2 and w_4). By setting $w_3 \equiv 0$ the number of rotational degrees of freedom is increased from two to three. Consequently, the commutation relations of the angular momenta operators for non-

linear molecules [21, 22, 82] now hold. Equation (4.26) is simplified accordingly,

$$\begin{aligned}\hat{H}^{\text{vib}} &= \sum_{\alpha} \hat{T}_{\alpha} + \hat{T}_{l} + \hat{V} \\ &= -\frac{\hbar^2}{2\mu_{\text{symm.}}} \left\{ \sum_{k=1}^{3} \frac{\partial^2}{\partial w_k^2} + \frac{\mu_1}{\mathbf{I}'(w_1)} \left[\left(w_2 \frac{\partial}{\partial w_3} - w_2 \frac{\partial}{\partial w_3} \right)^2 \right] \right\} + \hat{V}\end{aligned} \tag{4.30}$$

where w_4 in equation (4.26) is replaced by w_3 in equation (4.30) for simplicity of notation.

4.4.3. The Vibrational Wave Function

Within the approach of von Nagy-Felsobuki and co-workers [40, 41], the vibrational wave functions of both non-linear and linear triatomic molecules consist of three dimensions. In particular, they are constructed as configuration products of optimised 1D eigenfunctions,

$$\Psi_v^{\text{vib}}(\psi_i(q_1), \psi_j(q_2), \psi_k(q_3)) = \sum_{i=1}^{n_1} \sum_{j=1}^{n_2} \sum_{k=1}^{n_3} c_{ijk} \psi_i(q_1) \psi_j(q_2) \psi_k(q_3) \tag{4.31}$$

where n_a denote the number of 1D basis functions employed in co-ordinate a, respectively. The wave functions Ψ_v^{vib} correspond to non-linear and linear species for $\mathbf{q} = \mathbf{f}$ and $\mathbf{q} = \mathbf{w}$, respectively. For all molecules considered in this thesis, the expansion of Ψ_v^{vib} in the solution of the vibrational Schrödinger equation is limited such that $n_1 = n_2 = n_3 = 20$. It follows that each vibrational eigenfunction consists of an 8000 term CI expansion. The convergence of the eigenvalues of Ψ_v^{vib} to within the residual error of the analytical PEF has been established for a number of molecules [77, 78, 83] using this algorithm.

The manner of the construction of Ψ_v^{vib} provides a convenient assignment

scheme. The configuration weight of the j^{th} configuration in the i^{th} eigenfunction of $\hat{H}^{\text{vib}}$ is defined as [41],

$$(\%\text{weight})_{ij} = \left[\frac{C_{ij}^2}{\sum_{k=1}^{8000} C_{ik}^2}\right]^{1/2} \times 100 \tag{4.32}$$

Equation (4.32) allows the dominant character of a vibrational eigenfunction to be gauged. Additionally, the corresponding configuration density is defined as [72],

$$(\%\text{density})_{ij} = \left[\frac{|C_{ij}|}{\sum_{k=1}^{8000} C_{ik}^2}\right]^{1/2} \times 100 \tag{4.33}$$

This provides another metric by which the character of the optimised 3D vibrational eigenvectors may be determined.

4.4.4. Numerical Evaluation of Matrix Integrals

The explicit form of the vibrational kinetic energy, angular momentum and truncated Watson operator matrix elements may be given in terms of Ψ_v^{vib}. Defining $\left|\Psi^{\text{vib}}(\psi_i(q_1), \psi_j(q_2), \psi_k(q_3)\right\rangle = |ijk\rangle$, the kinetic energy matrix elements are of form,

$$\sum_{\alpha=1}^{3}\left[-\frac{\hbar^2}{\mu_{\text{symm}}}\left\langle ijk\left|\frac{\partial^2}{\partial q_\alpha^2}\right|lmn\right\rangle\right] \tag{4.34}$$

which may be expressed in terms of the 1D basis functions,

$$-\frac{\hbar^2}{\mu_{\text{symm}}}\left[\langle j|m\rangle\langle k|n\rangle\left\langle i\left|\frac{\partial^2}{\partial q_1^2}\right|l\right\rangle + \langle i|l\rangle\langle k|n\rangle\left\langle j\left|\frac{\partial^2}{\partial q_2^2}\right|m\right\rangle + \langle i|l\rangle\langle j|m\rangle\left\langle k\left|\frac{\partial^2}{\partial q_3^2}\right|n\right\rangle\right] \tag{4.35}$$

and by orthonormality the kinetic energy matrix elements are,

$$-\frac{\hbar^2}{\mu_{\text{symm}}}\left[\delta_{jm}\delta_{kn}\left\langle i\left|\frac{\partial^2}{\partial q_1^2}\right|l\right\rangle + \delta_{il}\delta_{kn}\left\langle j\left|\frac{\partial^2}{\partial q_2^2}\right|m\right\rangle + \delta_{il}\delta_{jm}\left\langle k\left|\frac{\partial^2}{\partial q_3^2}\right|n\right\rangle\right] \tag{4.36}$$

The vibrational angular momentum matrix elements may be expressed in terms of $|ijk\rangle$ as,

$$-\frac{\hbar^2}{\mu_{\text{symm}}}\left\langle ijk\left|\frac{1}{\mathbf{I}'(q_1)}\left[q_2\frac{\partial}{\partial q_3}-q_3\frac{\partial}{\partial q_2}\right]^2\right|lmn\right\rangle \tag{4.37}$$

which is expanded to give,

$$\begin{aligned}\left\langle i\left|\frac{1}{\mathbf{I}'(q_1)}\right|l\right\rangle\Bigg[&\left\langle j\left|q_2^2\right|m\right\rangle\left\langle k\left|\frac{\partial^2}{\partial q_3^2}\right|n\right\rangle-\delta_{kn}\left\langle j\left|q_2\frac{\partial}{\partial q_2}\right|m\right\rangle-\delta_{jm}\left\langle k\left|q_3\frac{\partial}{\partial q_3}\right|n\right\rangle\\&-2\left\langle j\left|q_2\frac{\partial}{\partial q_2}\right|m\right\rangle\left\langle k\left|q_3\frac{\partial}{\partial q_3}\right|n\right\rangle+\left\langle k\left|q_3^2\right|n\right\rangle\left\langle j\left|\frac{\partial^2}{\partial q_2^2}\right|m\right\rangle\Bigg]\end{aligned} \tag{4.38}$$

In the non-linear case, the 3$^{\text{rd}}$ order truncation of the Watson operator, $\hat{U}_w^{(3)}$, has matrix elements of form,

$$-\frac{\hbar^2}{8}\left\langle ijk\left|\hat{U}_w^{(3)}\right|lmn\right\rangle \tag{4.39}$$

where the truncation $\hat{U}_w^{(3)}$ is completely defined by the mass and structural parameters of the molecule.

The potential energy matrix elements are evaluated using an adaptation of the HEG quadrature scheme [40, 41, 84]. Assuming that the potential operator $\hat{V}$ can be expanded as a power series in vibrational $\mathbf{q}$ co-ordinates, the potential energy integral matrix truncated at first order is of form,

$$\begin{aligned}\left\langle ijk\left|\hat{V}\right|lmn\right\rangle &\approx \langle ijk\,|v_0|\,lmn\rangle+\langle ijk\,|v_1q_1|\,lmn\rangle+\langle ijk\,|v_2q_2|\,lmn\rangle+\langle ijk\,|v_3q_3|\,lmn\rangle\\&= v_0\delta_{il}\delta_{jm}\delta_{kn}+v_1\delta_{jm}\delta_{kn}X_{il}(q_1)+v_2\delta_{il}\delta_{kn}X_{jm}(q_2)\\&\quad+v_3\delta_{il}\delta_{jm}X_{kn}(q_3)\end{aligned} \tag{4.40}$$

where the matrix $\mathbf{X}(q_i)$ is constructed from the expectation values of the normal co-ordinate q_i,

$$X_{ab}(q_i) = \langle a \left| q_i \right| b \rangle \tag{4.41}$$

If $\mathbf{D}(q_i)$ is defined as the diagonalised form of $\mathbf{X}(q_i)$ such that $\mathbf{C}(q_i)$ are the corresponding eigenvectors, then,

$$\mathbf{X}(q_i) = \left[\mathbf{C}(q_i)\right]^T \mathbf{D}(q_i)\mathbf{C}(q_i) \tag{4.42}$$

The diagonal elements of $\mathbf{D}(q_i)$ are the quadrature points in the q_i co-ordinate. Therefore the potential energy integrals may be written as,

$$\begin{aligned} &\left\langle ijk \left| \hat{V}(\mathbf{X}(q_1), \mathbf{X}(q_2), \mathbf{X}(q_3)) \right| lmn \right\rangle \\ = \; &\mathbf{C}(q_1)\mathbf{C}(q_2)\mathbf{C}(q_3)\hat{V}(\mathbf{D}(q_1), \mathbf{D}(q_2), \mathbf{D}(q_3)) \left[\mathbf{C}(q_1)\right]^T \left[\mathbf{C}(q_2)\right]^T \left[\mathbf{C}(q_3)\right]^T \end{aligned} \tag{4.43}$$

It remains to briefly discuss the process by which the 1D integrals (*e.g.* $\left\langle a \left| \hat{X}_{q_i} \right| b \right\rangle$, where $\hat{X}_{q_i}$ is an arbitrary operator acting on $\psi(q_i)$) are evaluated. This integral is defined on a finite-element $q_i^h = [a, b]$ to be,

$$\left\langle a \left| \hat{X}_{q_i} \right| b \right\rangle = \int_a^b \psi_a^h(q_i) \hat{X}_{q_i} \psi_b^h(q_i) dq_i \tag{4.44}$$

Throughout this thesis, such integrals have been calculated using a 16 point Gaussian quadrature scheme. The previous integral is therefore evaluated as,

$$\begin{aligned} \left\langle a \left| \hat{X}_{q_i} \right| b \right\rangle &= \int_a^b \psi_a^h(q_i) \hat{X}_{q_i} \psi_b^h(q_i) dq_i \\ &= (b-a) \int_0^1 \psi_a^h(y) \hat{X}_y \psi_b^h(y) dy \\ &\approx (b-a) \sum_{j=1}^{n_g} \omega_j \psi_a^h(\rho_i) \hat{X}_{\rho_i} \psi_b^h(\rho_i) \end{aligned} \tag{4.45}$$

where ρ_i are the quadrature points in co-ordinate q_i defined on $[0,1]$ and ω_j are defined as,

$$\omega_j = \left[\sum_{k=0}^{5} q_k(y_j)^2\right]^{-1}, \qquad q_{ng}(y) = \sqrt{(2n+1)}P_{16}^{(a,0)}(1-2y) \tag{4.46}$$

Here y_j are defined in terms of the zeroes of polynomials and $P_{16}^{(a,0)}$ Jacobi polynomials [85]. The global integral (on the domain $[g_a, g_b]$) is then obtained by the summation of each finite-element integral (on the sub-domain of $[h_{j-1}, h_j]$),

$$\begin{aligned}\left\langle a \left| \hat{X}_{q_i} \right| b \right\rangle &= \int_{g_a}^{g_b} \psi_a^h(q_i)\hat{X}_{q_i}\psi_b^h(q_i)dq_i \\ &= \sum_{k=1}^{n}\int_{h_{j-1}}^{h_j} \psi_a^k(q_i)\hat{X}_{q_i}\psi_b^k(q_i)dq_i\end{aligned} \tag{4.47}$$

All calculations of 3D vibrational eigenfunctions reported in this thesis have been performed using FORTRAN programs of von Nagy-Felsobuki and co-workers (shqr_pcsf, vib32_cc_ajp, vib33_cc_ajp, vib34_cc_ajp) [86]. All code employed in this thesis is provided in Appendix C.

4.4.5. Vibration-Averaged Structures

Page and von Nagy-Felsobuki [87] have reported a method by which the vibration-averaged structures of a triatomic molecule can be calculated. By defining the following matrix integrals,

$$\begin{aligned}\langle q_1 \rangle &= \delta_{jm}\delta_{kn}\left\langle i \left| \hat{H}^{\text{vib}} \right| l \right\rangle \\ \langle q_2 \rangle &= \delta_{il}\delta_{kn}\left\langle j \left| \hat{H}^{\text{vib}} \right| m \right\rangle \\ \langle q_3 \rangle &= \delta_{il}\delta_{jm}\left\langle k \left| \hat{H}^{\text{vib}} \right| n \right\rangle\end{aligned} \tag{4.48}$$

the expectation values of $\hat{H}^{\text{vib}}$ in the 1D vibrational eigenvector basis may be determined. By use of the transformation matrices $\mathbf{L} : (f_1, f_2, f_3) \mapsto (r_1, r_2, r_3)$ of Searles and von Nagy-Felsobuki [70] and $\mathbf{A} : (w_1, w_2, w_3) \mapsto (r_1, r_2, r_3)$ of Wang *et al.* [71], the expectation values of the internal co-ordinates of the molecule may subsequently be calculated. This procedure has been implemented in two FORTRAN programs (vib_struct, vib_struct_lin) [88], given in Appendix C.

4.4.6. Vibrational States of $(^1\mathrm{A}_1)\mathrm{BeH}_2^{2+}$

Page and von Nagy-Felsobuki [80] have calculated the low-lying VBOs and the corresponding vibration-averaged structures of the ground states of $(^1\mathrm{A}_1)\mathrm{BeH}_2^{2+}$, $(^1\mathrm{A}')\mathrm{BeHD}^{2+}$ and $(^1\mathrm{A}_1)\mathrm{BeD}_2^{2+}$ using the numerical procedures outlined in this section. The PEF embedded in the nuclear Hamiltonian was that detailed in Chapter 3. These VBOs and vibration-averaged structures of $(^1\mathrm{A}_1)\mathrm{BeH}_2^{2+}$ are listed in Table 4.4. Vibration-averaged structures and VBOs of the low-lying vibrational states of $(^1\mathrm{A}')\mathrm{BeHD}^{2+}$ and $(^1\mathrm{A}_1)\mathrm{BeD}_2^{2+}$ are provided in Appendix D.

From Table 4.4 it is evident that the ten lowest vibrational states of $(^1\mathrm{A}_1)\mathrm{BeH}_2^{2+}$ can be assigned unequivocally using a single dominant configuration. It is also evident from Table 4.4 that for $(^1\mathrm{A}_1)\mathrm{BeH}_2^{2+}$ excitations in the symmetric bend mode are seldom observed in the lowest ten vibrational states. This is consistent with the reported vibrational states of the isoelectronic species $(^1\mathrm{A}_1)\mathrm{LiH}_2^{+}$ [83] and the isovalent species MgH_2^{2+} [87]. The fundamental frequencies of $(^1\mathrm{A}_1)\mathrm{BeH}_2^{2+}$ presented in Table 4.4 are also in reasonable agreement with the predicted trends regarding harmonic vibrational frequencies. For example, using the CCSD(T) method of Page and von Nagy-Felsobuki [80] the harmonic fundamental frequencies for the $|100\rangle$, $|010\rangle$ and $|001\rangle$ modes are 1243.7, 3549.4 and 1035.8 cm^{-1}, respectively. Similarly, the CCSD(T) harmonic ZPE of $(^1\mathrm{A}_1)\mathrm{BeH}_2^{2+}$ is 80.1 cm^{-1} higher than the IC-MRCI

Table 4.4 Low-lying VBOs, **f** expectation values and vibration-averaged structures of the lowest 10 vibrational states of $(^1A_1)BeH_2^{2+}$.

Assign.	Symmetry	Weight[a]	VBO ($/cm^{-1}$)	$\langle f_1 \rangle$ ($/a_0$)	$\langle f_2 \rangle$ ($/a_0$)	$\langle f_3 \rangle$ ($/a_0$)	$\langle R_{\text{Be-H}} \rangle$ ($/$Å)	$\langle \theta \rangle$ ($/^\circ$)
$\|000\rangle$	a_1	0.96	0.0[b]	0.073	−0.045	1.429−12[c]	1.647	29.2
$\|001\rangle$	b_2	0.88	948.3	0.274	−0.201	5.719−12	1.673	27.5
$\|100\rangle$	a_1	0.84	1169.9	0.478	−0.190	−1.752−12	1.679	28.5
$\|002\rangle$	a_1	0.73	1909.5	0.404	−0.360	2.705−12	1.691	26.5
$\|101\rangle$	b_2	0.68	2107.9	1.135	−0.517	−4.847−13	1.697	27.2
$\|200\rangle$	a_1	0.73	2328.0	1.007	−0.327	−3.281−12	1.709	28.1
$\|003\rangle$	b_2	0.60	2907.8	0.510	−0.515	−2.250−11	1.703	25.9
$\|102\rangle$	a_1	0.51	3098.4	1.580	−0.732	1.020−11	1.706	27.0
$\|201\rangle$	b_2	0.53	3287.2	1.710	−0.620	3.973−12	1.719	27.1
$\|010\rangle$	a_1	0.80	3323.6	0.301	−0.147	−1.408−12	1.665	30.7

[a]Calculated using equation (4.32).
[b]ZPE = 2834.3 cm^{-1}.
[c]1.429-12 denotes 1.429×10^{-12}.

fully anharmonic value. The larger difference between $|010\rangle$ fundamental frequencies can be understood in terms of the differences between CCSD(T) and IC-MRCI 1D PES curvatures.

The lowest ten vibrational states of $(^1\mathrm{A}')\mathrm{BeHD}^{2+}$ are more delocalised than are those of either $(^1\mathrm{A}_1)\mathrm{BeH}_2^{2+}$ or $(^1\mathrm{A}_1)\mathrm{BeD}_2^{2+}$. For example, the states with VBOs at 1505.7, 2167.3, 2270.5, 2577.7 and 2966.5 cm^{-1} are each principally composed from two dominant configurations. As for $(^1\mathrm{A}_1)\mathrm{BeH}_2^{2+}$, excited quanta in the symmetric bend mode of vibration are only observed in one of the lowest 10 vibrational states of $(^1\mathrm{A}')\mathrm{BeHD}^{2+}$, *viz.* the $|010\rangle$ fundamental vibration. The low-lying vibrational states of $(^1\mathrm{A}_1)\mathrm{BeD}_2^{2+}$ are assigned more definitively, as all excited vibrational states are each assigned to a single dominant configuration. The exception is the a_1 state with VBO at 2231.6 cm^{-1}. The latter state is predominantly composed from a mixture of the $|102\rangle$ and $|200\rangle$ configurations, which accounted for 77% of the normalised vibrational wave function.

The vibration-averaged structures included in Table 4.4 provide an indication of the effects of configuration mixing in the vibrational wave function. For example, for each of the lowest ten vibrational states of $(^1\mathrm{A}_1)\mathrm{BeH}_2^{2+}$, the vibration-averaged structures exhibit longer bond lengths (by *ca.* 0.05-0.1 Å) than those corresponding to the IC-MRCI PES minimum. Additionally, vibration-averaged bond angles range from *ca.* -3.5° to +1.3° with respect to the equilibrium *ab initio* value for the low-lying excited states. Hydrogenic isotopic substitution in $(^1\mathrm{A}_1)\mathrm{BeH}_2^{2+}$ has a negligible effect on the vibration-averaged structures. For instance, $\langle R_{\mathrm{Be\text{-}H}} \rangle$ for the ground vibrational state of $(^1\mathrm{A}')\mathrm{BeHD}^{2+}$ is 0.001 Å larger than that of $(^1\mathrm{A}_1)\mathrm{BeH}_2^{2+}$, while $\langle R_{\mathrm{Be\text{-}D}} \rangle$ for the ground vibrational state of $(^1\mathrm{A}')\mathrm{BeHD}^{2+}$ is 0.001 Å smaller than that of $(^1\mathrm{A}_1)\mathrm{BeD}_2^{2+}$. The expectation values $\langle \theta \rangle$ for the ground vibrational states of the three isotopomers are in exact agreement.

4.4.7. Vibrational States of $(^1\Sigma_g^+)BeHe_2^{2+}$

The algorithms detailed in this section have been applied to the $^1\Sigma_g^+$ ground state of $BeHe_2^{2+}$. The analytical PEF used in the computation of the potential energy matrix integrals is that of Page *et al.* [89], and has been described in Chapter 3. Low-lying $l = 0$ vibrational states of $(^1\Sigma_g^+)BeHe_2^{2+}$ are listed in Table 4.5 in terms of VBOs, symmetries, assignments and vibration-averaged structures. Only $\langle R_{\text{Be-H}} \rangle$ have been considered here, since all $\langle \theta \rangle$ values are 180° due to the symmetry of the PEF in the w_2 co-ordinate.

The low-lying vibrational states of $(^1\Sigma_g^+)BeHe_2^{2+}$ are observed to be closely spaced, indicative of the generally flat topology of the molecular PEF in the neighbourhood of the geometric minimum. This property of the vibrational spectrum appears to be typical of helide ions of form XHe_2^{2+}, and has been observed previously for X = C, Si, N, O [72, 90–92]. It is evident that these low-lying vibrational states are also dominated by excitations in the w_2 vibrational mode. For example, vibrational states with VBOs at 115.1, 286.2, 510.7, 784.9, 835.2 and 1014.7 cm^{-1} have each been assigned a primary configuration which includes a non-zero w_2 quantum. This is anticipated, due to the relative 1D PEF curvatures in the w_1, w_2 and w_3 co-ordinates, respectively. Nevertheless, each of the lowest 10 $l = 0$ vibrational states of $(^1\Sigma_g^+)BeHe_2^{2+}$ may be described using one or two primary configurations.

States with significant w_2 character are observed to be generally more multi-configurational than those consisting of w_1 and/or w_3 excitations. For example, the vibrational states with VBOs at 115.1 and 286.2 cm^{-1} are assigned predominantly to the $|020\rangle$ configuration term. Nevertheless, these states exhibit significant contribution from the $|040\rangle$ and $|160\rangle$ configuration terms, respectively. A similar trend is observed with respect to the states with VBOs at 510.7 and 784.9 cm^{-1}, both of which primarily exhibit $|040\rangle$ character. Conversely, the w_1 and w_3 fundamen-

Table 4.5 Low-lying VBOs, **w** expectation values and vibration-averaged bond lengths of $(^1\Sigma_g^+)BeHe_2^{2+}$ for $l = 0$.

Assign.	Symmetry	Weight[a]	VBO ($/cm^{-1}$)	$\langle w_1 \rangle$ (a_0)	$\langle w_2 \rangle$ (a_0)	$\langle w_3 \rangle$ (a_0)	$\langle R_{\text{Be-He}} \rangle$ (Å)
$\|000\rangle$	σ_g^+	0.93	0.0[b]	−0.010	4.976−09	1.426−12	1.433
$\|020\rangle$,$\|040\rangle$	σ_g^+	0.57,0.33	115.1	−0.144	1.028−08	5.159−13	1.394
$\|020\rangle$,$\|160\rangle$	σ_g^+	0.65,0.21	286.2	−0.188	−4.867−07	2.646−13	1.355
$\|040\rangle$,$\|140\rangle$	σ_g^+	0.59,0.20	510.7	−0.197	1.522−06	1.020−13	1.351
$\|100\rangle$	σ_g^+	0.92	699.2	0.045	7.180−08	4.024−13	1.457
$\|040\rangle$,$\|060\rangle$	σ_g^+	0.55,0.35	784.9	−0.205	1.249−04	1.979−12	1.348
$\|120\rangle$,$\|060\rangle$	σ_g^+	0.53,0.37	835.2	−0.083	−2.102−07	−5.006−13	1.401
$\|001\rangle$	σ_u^+	0.85	920.1	0.023	5.610−07	−4.396−12	1.447
$\|001\rangle$,$\|021\rangle$	σ_u^+	0.43,0.41	1004.0	−0.123	5.945−06	−1.951−13	1.383
$\|120\rangle$,$\|080\rangle$	σ_g^+	0.54,0.23	1014.7	−0.139	1.261−04	2.909−12	1.376

[a]Calculated using equation (4.32).
[b]ZPE = 870.1 cm^{-1}.

tal modes are observed to consist of the $|100\rangle$ and $|001\rangle$ terms with configuration weights of 0.92 and 0.85, respectively. All $l = 0$ vibrational states are such that strictly even (or zero) excited quanta are observed in the w_2 mode. Consequently, such states may freely mix in the 3D configuration expansion.

The relative 1D PEF curvatures in the w_1, w_2 and w_3 co-ordinates are also illustrated by the respective $\langle w \rangle$ expectation value. For example, the vibration-averaged bond lengths of each state listed in Table 4.5 are dominated by the contribution from $\langle w_1 \rangle$. Nevertheless, the effect of vibration-averaging for the ground state is relatively subtle, decreasing the Be-He separation by *ca.* 4.2 mÅ relative to the *ab initio* R_e value [89]. For all states dominated by w_2 excitations a decrease in $\langle R_{\text{Be-He}} \rangle$ relative to the vibrational ground state value is observed. Conversely, for the w_1 and w_3 fundamental modes, $\langle R_{\text{Be-He}} \rangle$ are 1.457 and 1.447 Å, respectively. Additionally the $|120\rangle$ σ_g^+ state with VBO at 835.2 cm^{-1}exhibits a $\langle R_{\text{Be-He}} \rangle$ value of 1.401 Å.

4.4.8. Vibrational Radiative Properties

The vibrational transition moment integrals for states $\langle a|$ and $|b\rangle$ in the 3D vibrational eigenfunction basis are of form [93],

$$\mu_\alpha(a,b) = \langle ijk\,|\mu_\alpha(\rho_1,\rho_2,\rho_3)|\,lmn\rangle \tag{4.49}$$

Throughout this thesis, the integrals of equation (4.49) have been calculated using the novel adapted HEG quadrature scheme developed by Sudarko *et al.* [72]. This procedure essentially entails the truncation of a convergent power series expansion of $\mu_\alpha(\rho_1,\rho_2,\rho_3)$ at 1^{st} order so that,

$$\begin{aligned}\langle ijk\,|\mu_\alpha(\rho_1,\rho_2,\rho_3)|\,lmn\rangle \approx \langle ijk\,|c_0|\,lmn\rangle + \langle ijk\,|c_1q_1|\,lmn\rangle \\ + \langle ijk\,|c_2q_2|\,lmn\rangle + \langle ijk\,|c_3q_3|\,lmn\rangle\end{aligned} \tag{4.50}$$

from which an expression for the transition moment analogous to equation (4.43) is obtained, with the exception that the potential operator is replaced by $\mu_\alpha(\rho_1,\rho_2,\rho_3)$. Thus, the vibrational transition moment integrals and potential energy matrix integrals are evaluated on a common quadrature grid. Since the Eckart frame is imposed on the molecule, the square dipole moment matrix integral may subsequently be calculated,

$$\mu_{a,b}^2 = \mu^2(a,b) = \mu_x^2 + \mu_y^2 \tag{4.51}$$

Equation (4.51) is used in order to calculate the Einstein coefficients of induced absorption (B_{ab}) and spontaneous emission (A_{ab}) [40],

$$B_{ab} = \frac{8\pi^3}{3h^2}\mu_{a,b}^2 \tag{4.52}$$

At thermal equilibrium, B_{ab} and A_{ab} are related according to,

$$N_a B_{ba} \rho_{v_{ab}} = N_b \left(A_{ab} + B_{ab} \rho_{v_{ab}} \right), \qquad \frac{N_a}{N_b} = \frac{\left(A_{ba} + B_{ba} \rho_{v_{ab}} \right)}{B_{ab} \rho_{v_{ab}}} \tag{4.53}$$

The spectral density of the external radiation field for a black radiating system, $\rho_{v_{ab}}$ satisfies Planck's law,

$$\rho_{v_{ab}} = \frac{8\pi h v_{ab}^3}{c^3} \frac{1}{\left(e^{hcv_{ab}/kT} - 1 \right)} \tag{4.54}$$

where v_{ab} is the frequency of the transition (/cm^{-1}) between states $\langle a|$ and $|b\rangle$, and c, k and T are the speed of light, Boltzmann's constant and temperature, respectively. The radiative lifetime of flourescence, τ_b^f, due to spontaneous emission in the absence of an external field is defined as,

$$\tau_b^f = \frac{1}{\sum_{a<b} A_{ba}} \tag{4.55}$$

Upon the addition of an external field, this expression becomes,

$$\tau_b^f = \frac{1}{\sum_a A_{ba} + \sum_a B_{ba} \rho_{v_{ab}} + \sum_{b\prime} B_{bb\prime} \rho_{v_{ab}}} \tag{4.56}$$

since induced transitions (*i.e.* absorptions) are now allowed. The vibrational band intensity (/cm molecule^{-1}) is defined as,

$$S_{ab} = \frac{\hbar v_{ab}}{c} \frac{N_A}{Q_v} \frac{1.012510 \times 10^6}{RT} B_{ba} e^{-hcv_{0a}/kT} \left(1 - e^{-hcv_{ab}/kT} \right) \tag{4.57}$$

where R is the universal gas constant, N_A is Avagadro's number and Q_v is the vibrational partition function.

The vibrational radiative properties of non-linear molecules reported in this thesis have been calculated using an existing FORTRAN program of von Nagy-

Felsobuki and co-workers (vibint_timef_djw) [94]. This program has been adapted in this work for the calculation of vibrational radiative properties of linear molecules (vibint_timef_linear) [95]. Both programs are given in Appendix C.

4.4.9. Vibrational Spectrum of $(^1A_1)BeH_2^{2+}$

Page and von Nagy-Felsobuki [80] have calculated vibrational radiative properties including square dipole matrix elements, Einstein coefficients, band strengths and radiative lifetimes of $(^1A_1)BeH_2^{2+}$, $(^1A')BeHD^{2+}$ $(^1A_1)BeH_2^{2+}$ using the methods detailed in this section, in conjunction with the analytical DMF described in Chapter 3. These properties are given in Table 4.6 for the lowest 10 vibrational states of $(^1A_1)BeH_2^{2+}$. Analogous data for $(^1A')BeHD^{2+}$ and $(^1A_1)BeD_2^{2+}$ are given in Appendix D.

It can be seen that for the ground state of $(^1A_1)BeH_2^{2+}$, the $|201\rangle \leftarrow |000\rangle$ transition possess the greatest band strength, with $S = 1.63 \times 10^{-12}$ cm molecule^{-1}. However, both the $|003\rangle \leftarrow |000\rangle$ and $|010\rangle \leftarrow |000\rangle$ transitions were of similar intensities, possessing band strengths of $S = 1.59 \times 10^{-12}$ and $S = 1.15 \times 10^{-12}$ cm molecule^{-1}, respectively. For $(^1A')BeHD^{2+}$ the existence of several vibrational states

Table 4.6 Vibrational Radiative Properties of $(^1A_1)BeH_2^{2+}$ at 296 K.

i	VBO ($/cm^{-1}$)	R^2 ($/a.u.^2$)	A_{0i} ($/s^{-1}$)	B_{0i} ($10^{16}cm^3erg^{-1}s^2$)	S_{0i} ($/cm\ molecule^{-1}$)	τ_i ($/s$)
1	948.3	4.26−01[a]	1.14+02	8.03+01	1.67−16	8.04−05
2	1169.9	1.10+00	5.51+02	2.06+02	5.32−16	1.26−04
3	1909.5	1.05+01	2.28+04	1.97+03	8.31−15	8.80−07
4	2107.9	8.84+02	2.60+06	1.67+05	7.76−13	3.60−07
5	2328.0	2.75−01	1.09+03	5.18+01	2.67−16	9.20−06
6	2907.8	1.32+03	1.02+07	2.48+05	1.59−12	6.00−08
7	3098.4	1.27+00	1.18+04	2.39+02	1.64−15	3.10−07
8	3287.2	1.19+01	1.33+05	2.25+03	1.63−12	2.10−07
9	3323.6	8.31+00	9.57+04	1.57+03	1.15−12	7.64−06

[a] 4.26-01 denotes 4.26×10^{-1}.

with similar band strengths is predicted. For example, the $|002\rangle$, ($|101\rangle, |001\rangle$), ($|101\rangle, |201\rangle$), ($|003\rangle, |201\rangle$) and ($|002\rangle, |102\rangle$) states of (^{1}A$'$)BeHD^{2+} each possess band strengths (with respect to transition to the ground vibrational state) of the order of 10^{-13} cm molecule^{-1}. For ($^1\Sigma_g^+$)BeD$_2^{2+}$ the vibrational transitions $|101\rangle \leftarrow |000\rangle$ and $|101\rangle \leftarrow |000\rangle$ have the greatest spectral band intensities, possessing band strengths of 1.66×10^{-12} and 1.72×10^{-13} cm molecule^{-1}, respectively.

4.4.10. Vibrational Spectrum of ($^1\Sigma_g^+$)BeHe$_2^{2+}$

Radiative properties of the low-lying $l = 0$ vibrational states, including square dipole matrix elements, Einstein coefficients, band strengths and radiative lifetimes have been calculated using methods developed in this section and are listed in Table 4.7. The embedded DMF is that of Page and von Nagy-Felsobuki [89] detailed in Chapter 3.

It is evident from Table 4.7 that the vibrational states in question exhibit band strengths of *ca.* $10^{-11} - 10^{-12}$ cm molecule^{-1}. However, states with non-zero w_1 quanta are observed to exhibit slightly larger band strengths. For instance, the largest S value (8.77×10^{-11} cm molecule^{-1}) in Table 4.7 corresponds

Table 4.7 Vibrational Radiative Properties of ($^1\Sigma_g^+$)BeHe$_2^{2+}$ at 296 K.

i	VBO (/cm^{-1})	R^2 (/a.u.^{2})	A_{0i} ($/s^{-1}$)	B_{0i} (10^{16} cm^3 erg^{-1} s^2)	S_{0i} (/cm molecule^{-1})	τ_i ($/s$)
1	115.1	7.42+05[a]	3.55+05	1.40+08	4.47−12	8.49−08
2	286.2	9.15+05	6.72+06	1.72+08	2.40−11	4.64−08
3	510.7	2.65+05	1.11+07	4.99+07	1.51−11	2.49−08
4	699.2	1.06+06	1.14+08	2.00+08	8.77−11	7.07−09
5	784.9	7.12+04	1.08+07	1.34+07	6.67−12	1.26−08
6	835.2	2.45+05	4.48+07	4.62+07	2.46−11	4.37−09
7	920.1	7.87+05	1.92+08	1.48+08	8.74−11	4.68−09
8	1004.0	6.33+04	2.01+07	1.19+07	7.70−12	1.35−08
9	1014.7	1.07+04	3.50+06	2.01+06	1.31−12	3.61−09

[a] 7.42+05 denotes 7.42×10^5.

to the $|100\rangle \leftarrow |000\rangle$ band. Similarly, the $(0.53 \times |120\rangle + 0.37 \times |060\rangle)$ state with VBO at 920.1 cm^{-1} exhibits a S value of 8.74×10^{-11} cm molecule^{-1}, with respect to transition to the ground vibrational state. Other states with similar band strengths (*i.e.* of the order of 10^{-11} cm molecule^{-1}), although dominated by configuration terms including excited w_2 quanta, also exhibit significant w_1 character. For instance, the $(0.65 \times |020\rangle + 0.21 \times |160\rangle)$ and $(0.59 \times |040\rangle + 0.20 \times |140\rangle)$ states with VBOs at 286.2 and 510.7 cm^{-1} exhibit respective band strengths of 2.40×10^{-11} and 1.51×10^{-11} cm molecule^{-1}, with respect to transition to the ground vibrational state.

4.5. A Rovibrational Hamiltonian for Non-linear Triatomic Molecules

The form of the pure molecular rotation operator of equation (4.16), $\hat{H}^{\text{rot}}$, may be conveniently written in matrix notation. The elements of $\hat{H}^{\text{rot}}$ spanned by the 3D vibrational eigenvectors $\langle\Psi_i|$ and $|\Psi_j\rangle$ are of form [23],

$$\hat{H}^{\text{rot}}_{ij} = \frac{1}{2}\langle A\rangle_{ij}\hat{\Pi}_x^2 + \frac{1}{2}\langle B\rangle_{ij}\hat{\Pi}_y^2 + \frac{1}{2}\langle C\rangle_{ij}\hat{\Pi}_z^2 + \frac{1}{2}\langle D\rangle_{ij}\left(\hat{\Pi}_x\hat{\Pi}_y + \hat{\Pi}_y\hat{\Pi}_x\right) \tag{4.58}$$

where [24, 25, 29, 70, 96–98],

$$\begin{aligned} \langle A\rangle_{ij} &= \langle\Psi_i|\,\mu_{xx}\,|\Psi_j\rangle \;\; \langle B\rangle_{ij} = \langle\Psi_i|\,\mu_{yy}\,|\Psi_j\rangle \\ \langle C\rangle_{ij} &= \langle\Psi_i|\,\mu_{zz}\,|\Psi_j\rangle \;\; \langle D\rangle_{ij} = \langle\Psi_i|\,\mu_{xy}\,|\Psi_j\rangle \end{aligned} \tag{4.59}$$

are the ij^{th} elements of the rotational constant matrices. The components of the angular momentum operators, $\hat{\Pi}_\alpha$ $(\alpha = x, y, z)$ are defined in the molecule-fixed

frame of reference and of form [99],

$$\hat{\Pi}_x = -i\cos\chi\left(\cot\theta\frac{\partial}{\partial\chi} - \frac{1}{\sin\theta}\frac{\partial}{\partial\phi}\right) - i\sin\chi\frac{\partial}{\partial\theta} \tag{4.60}$$

$$\hat{\Pi}_x = -i\sin\chi\left(\cot\theta\frac{\partial}{\partial\chi} - \frac{1}{\sin\theta}\frac{\partial}{\partial\phi}\right) - i\cos\chi\frac{\partial}{\partial\theta} \tag{4.61}$$

$$\hat{\Pi}_z = -i\frac{\partial}{\partial\chi} \tag{4.62}$$

where θ, ϕ and χ are the associated Euler angles of the n-unit vectors.

The Coriolis coupling operator of equation (4.16), $\hat{H}^{\text{cor}}$, may also be written in matrix notation. The matrix element $\hat{H}^{\text{cor}}_{ij}$ in the 3D vibrational eigenvector basis is of form [41],

$$\hat{H}^{\text{cor}}_{ij} = \frac{i}{\hbar}\langle F\rangle_{ij}\hat{\Pi}_z \tag{4.63}$$

Here the elements of $\mathbf{F}$ are parametrised in the vibrational $\mathbf{f}$ co-ordinates such that,

$$\langle F\rangle_{ij} = \left\langle \Psi_i \left| \frac{\hbar^2}{\mathbf{I}'(f_1)}\left(f_3\frac{\partial}{\partial f_2} - f_2\frac{\partial}{\partial f_3}\right)\right| \Psi_j \right\rangle \tag{4.64}$$

The 'full' normal co-ordinate rovibrational Hamiltonian for an arbitrary non-linear triatomic molecule may therefore be assembled [41],

$$\begin{aligned}\hat{H}^{\text{RV}}_{ij} = E_i\langle S\rangle_{ij} &+ \frac{1}{2}\langle A\rangle_{ij}\hat{\Pi}^2_x + \frac{1}{2}\langle B\rangle_{ij}\hat{\Pi}^2_y \\ &+ \frac{1}{2}\langle C\rangle_{ij}\hat{\Pi}^2_z + \frac{1}{2}\langle D\rangle_{ij}\left(\hat{\Pi}_x\hat{\Pi}_y + \hat{\Pi}_y\hat{\Pi}_x\right) + \frac{i}{\hbar}\langle F\rangle_{ij}\hat{\Pi}_z\end{aligned} \tag{4.65}$$

Here, E_i is the energy of the i^{th} vibrational state and $\langle S\rangle_{ij}$ is the ij^{th} element of the vibrational overlap matrix $\mathbf{S}$. The solution of the nuclear rovibrational Schrödinger equation (4.17) therefore equates to the diagonalisation of the Hamiltonian matrix defined in equation (4.65).

4.5.1. The Rovibrational Wave Function

The rovibrational eigenfunctions Ψ^{RV} of equation (4.17) are constructed from the product of the vibrational eigenfunctions Ψ_v^{vib} and the symmetric-top eigenfunctions, φ_{JKm}. Hence,

$$\Psi^{\mathrm{RV}}_{v,JKm} = \sum_{n,K} C_{nKJ} \Psi^{\mathrm{vib}}_n \varphi_{JKm} \tag{4.66}$$

The form of the symmetric-top eigenfunctions in rotational co-ordinates are,

$$\varphi_{JKm} = |JKm\rangle = \Theta_{JKm}(\theta) e^{im\phi} e^{iK\chi} \tag{4.67}$$

where $\Theta_{JKm}(\theta)$ are defined by Shaffer [100] and K and m are $(2J+1)$-fold degenerate (*i.e.* $K, m = -J, -J+1, \ldots, J-1, J$) and describe the rotational angular momenta in the laboratory and molecule fixed frames of reference, respectively. Equivalently,

$$\varphi_{JKm} = \left[\frac{2J+1}{8\pi^2}\right]^{1/2} \mathbf{D}^J_{Km} \tag{4.68}$$

where $\mathbf{D}^J_{Km}$ are the Wigner rotation matrices [99]. Due to orthonormality,

$$\langle JKm | J'K'm' \rangle = \delta_{JJ'} \delta_{KK'} \delta_{mm'} \tag{4.69}$$

Rovibrational eigenfunctions Ψ^{RV} of equation (4.17) are obtained by constructing the rovibrational 'super-matrix' in the Ψ^{RV} basis, $\left\langle \Psi^{\mathrm{RV}} \middle| \hat{H}^{\mathrm{RV}} \middle| \Psi^{\mathrm{RV}} \right\rangle$. In order to ensure all elements of this matrix remain real, φ_{JKm} are transformed to $\pm$ combinations, such that,

$$\left| R^+_{JKm} \right\rangle = \frac{1}{\sqrt{2}} \left(|JKm\rangle + |J(-K)m\rangle \right) \tag{4.70}$$

$$\left|R^{+}_{JKm}\right\rangle = \frac{1}{\sqrt{2}i}\left(|JKm\rangle - |J(-K)m\rangle\right) \tag{4.71}$$

where $K \geq 0$. This is achieved by use of the Wang transformation [75],

$$\begin{bmatrix} R^{-}_{JKm} \\ \vdots \\ R^{-}_{J2m} \\ R^{-}_{J1m} \\ J0m \\ R^{+}_{J1m} \\ R^{+}_{J2m} \\ \vdots \\ R^{+}_{JKm} \end{bmatrix} = \frac{1}{\sqrt{2}} \begin{bmatrix} i & 0 & \cdots & & 0 & -i \\ 0 & \ddots & & & \iddots & 0 \\ & & i & -i & & \\ \vdots & \cdots & 0 & \sqrt{2} & 0 & \cdots & \vdots \\ & & 1 & 0 & 1 & & \\ 0 & \iddots & & & \ddots & 0 \\ 1 & 0 & \cdots & & 0 & 1 \end{bmatrix} \begin{bmatrix} \varphi_{J(-K)m} \\ \vdots \\ \varphi_{J(-2)m} \\ \varphi_{J(-1)m} \\ \varphi_{J0m} \\ \varphi_{J1m} \\ \varphi_{J2m} \\ \vdots \\ \varphi_{JKm} \end{bmatrix} \tag{4.72}$$

The basis functions $\left|R^{\pm}_{JKm}\right\rangle$ are orthonormal by construction. Substitution of equations (4.70 - 4.71) into equation (4.66) yields,

$$\Psi^{\mathrm{RV}}_{v,JKm} = \sum_{n,K} C_{nKJ}\Psi^{\mathrm{vib}}_{n}\left|R^{\pm}_{JKm}\right\rangle \tag{4.73}$$

The non-zero elements of the angular momenta matrices in the $\left|R^{\pm}_{JKm}\right\rangle$ basis have been determined by Carney *et al.* [23] to be,

$$\left\langle R^{\mp}_{JKm}\left|\hat{\Pi}_z\right|R^{\pm}_{JKm}\right\rangle = \pm iK \tag{4.74}$$

$$\left\langle R^{\pm}_{JKm}\left|\hat{\Pi}^2_z\right|R^{\pm}_{JKm}\right\rangle = K^2 \tag{4.75}$$

$$\left\langle R^{\pm}_{JKm}\left|\hat{\Pi}^2\right|R^{\pm}_{JKm}\right\rangle = J(J+1) \tag{4.76}$$

$$\left\langle R^{\pm}_{J(K+2)m} \left| \hat{\Pi}_x^2 - \hat{\Pi}_y^2 \right| R^{\pm}_{JKm} \right\rangle = \frac{1}{2} \left[(J-K-1)(J-K)(J+K+1)(J+K+2) \right]^{1/2} \tag{4.77}$$

$$\left\langle R^{\pm}_{J(K-2)m} \left| \hat{\Pi}_x^2 - \hat{\Pi}_y^2 \right| R^{\pm}_{JKm} \right\rangle = \frac{1}{2} \left[(J+K-1)(J+K)(J-K+1)(J-K+2) \right]^{1/2} \tag{4.78}$$

$$\left\langle R^{\pm}_{J(K+2)m} \left| \hat{\Pi}_x \hat{\Pi}_y + \hat{\Pi}_y \hat{\Pi}_x \right| R^{\pm}_{JKm} \right\rangle = \mp \frac{1}{2} \left[(J-K-1)(J-K) (J+K+1)(J+K+2) \right]^{1/2} \tag{4.79}$$

$$\left\langle R^{\pm}_{J(K-2)m} \left| \hat{\Pi}_x \hat{\Pi}_y + \hat{\Pi}_y \hat{\Pi}_x \right| R^{\pm}_{JKm} \right\rangle = \pm \frac{1}{2} \left[(J+K-1)(J+K) (J-K+1)(J-K+2) \right]^{1/2} \tag{4.80}$$

Equations (4.74 - 4.80) are all independent of m, since the matrix elements are defined in the molecular frame of reference in the absence of external fields. The order of the rovibrational super-matrix is $\left[v_{\max} \times (2J_{\max} + 1) \right]^2$, where $v_{\max}$ and $J_{\max}$ denote the number of vibrational and rotational states employed. Diagonalisation of the super-matrix yields the rovibrational eigenvalues and eigenfunctions, the latter of which may be assigned using a configuration weight scheme analogous to equation (4.32). These assignments may subsequently be labelled using the $J_{K_a K_c}$ Mulliken convention [101], where K_a and K_c are the asymmetric signatures of the limiting prolate and oblate rotors, respectively. Both K_a and K_c may take the values $0, 1, 1, 2, 2, \ldots, J$. For molecules of C_{2v} and C_s symmetry, the asymmetric rotors are functions of J, whereas for molecules of D_{3h} symmetry the asymmetric rotors are functions of $|K|$.

All calculations of the rovibrational states of non-linear triatomic molecules reported in this thesis have been made using a FORTRAN program of von Nagy-Felsobuki and co-workers (hrovibfau_assignsw1) [102], which is given in Appendix C.

4.5.2. Rovibrational Radiative Properties

The probability of transition between two rovibrational states $\langle a| \equiv \Psi^{\mathrm{RV}}_{v_1,J_1K_1m_1}$ and $|b\rangle\, \Psi^{\mathrm{RV}}_{v_2,J_2K_2m_2}$ may be calculated using the $\mu^2_{a,b}$ matrix,

$$R^2 = \sum_{m_1}\sum_{m_2} \left|\left\langle \Psi^{\mathrm{RV}}_{v_1,J_1K_1m_1} \left|\mu_{\mathrm{sf}}\right| \Psi^{\mathrm{RV}}_{v_2,J_2K_2m_2} \right\rangle\right|^2 \tag{4.81}$$

where μ_{sf} here is the DMF transformed to the space-fixed frame of reference, as outlined by Zare [99]. Sudarko *et al.* [72] have derived the explicit form of equation (4.81) to be,

$$\begin{aligned}
R^2 = \frac{3}{8}\left[\frac{2J_1+1}{8\pi^2}\right]\left[\frac{2J_2+1}{8\pi^2}\right]\sum_{m_1}\sum_{m_2}\Bigg|\Bigg\langle \sum_{v_1}\Bigg[\sum_{K_1=J_1}^{K_1=1} C_{v_1,J_1K_1m_1}\Psi^{\mathrm{vib}}_{v_1}\left(i\left(|J_1K_1m_1\rangle - |J_1(-K_1)m_1\rangle\right)\right) + \\
\sqrt{2}C_{v_1,J_10_1m_1}\Psi^{\mathrm{vib}}_{v_1}\mathbf{D}^{J_1}_{m_10} + \sum_{K_1=1}^{K_1=J_1} C_{v_1,J_1K_1m_1}\Psi^{\mathrm{vib}}_{v_1}\left(\mathbf{D}^{J_1}_{m_1K_1} + \mathbf{D}^{J_1}_{m_1(-K_1)}\right)\Bigg] \\
\left|\mu_x\left(\mathbf{D}^1_{0(-1)} - \mathbf{D}^1_{01}\right) - i\mu_y\left(\mathbf{D}^1_{0(-1)} - \mathbf{D}^1_{01}\right)\right| \sum_{v_1}\Bigg[\sum_{K_1=J_1}^{K_1=1} C_{v_1,J_1K_1m_1}\Psi^{\mathrm{vib}}_{v_1}\left(i\left(|J_1K_1m_1\rangle - |J_1(-K_1)m_1\rangle\right)\right) + \\
\sqrt{2}C_{v_1,J_10_1m_1}\Psi^{\mathrm{vib}}_{v_1}\mathbf{D}^{J_1}_{m_10} + \sum_{K_1=1}^{K_1=J_1} C_{v_1,J_1K_1m_1}\Psi^{\mathrm{vib}}_{v_1}\left(\mathbf{D}^{J_1}_{m_1K_1} + \mathbf{D}^{J_1}_{m_1(-K_1)}\right)\Bigg]\Bigg\rangle\Bigg|^2
\end{aligned}$$

The associated spectral intensity (/cm molecule^{-1}) may then be calculated,

$$S^2_{ab} = \frac{8\pi^3}{3hc}\frac{C_AN_A}{Q_VQ_R}\frac{g_{\mathrm{nsi}}}{RT}v_{ab}\left[e^{-hcE_a/kT} - e^{-hcE_b/kT}\right]R^2_{ab} \tag{4.82}$$

where C_A is the isotopic abundance, g_{nsi} is the nuclear statistical weight of the initial state, Q_R is the rotational partition function and E_a and E_b are the energies of states $\langle a|$ and $|b\rangle$, respectively.

The rovibrational transition probabilities and associated spectral intensities reported in this thesis have been calculated using an existing FORTRAN program of von Nagy-Felsobuki and co-workers (rovint_xym3) [103], which is given in Appendix C.

4.5.3. Rovibrational Spectrum of $(^1A_1)BeH_2^{2+}$

The predicted rovibrational spectrum of $(^1A_1)BeH_2^{2+}$ is given in Figure 4.4, which includes all transitions with $v \leq 10$, $J \leq 5$ provided that the spectral line intensity, S_{ab} is greater than 1.0×10^{-20} cm molecule^{-1}. The inset of Figure 4.4 clearly shows the rotational branch structure of the spectrum.

Rovibrational energies, $J_{K_aK_c}$ assignments and corresponding configuration weights of the low-lying vibrational states of $(^1A_1)BeH_2^{2+}$ for $J \leq 4$ are listed in Table 4.8. It is evident from this table that for all rovibrational states for which $J \leq 3$, $J_{K_aK_c}$ assignments may be made unequivocally. For the $J = 4$ rovibrational states however, this is not always the case. For example, the 4_{22} states of the five lowest vibrational states each possess leading configuration weights less than 0.5. Nevertheless, manual inspection shows that these assignments constitute the main

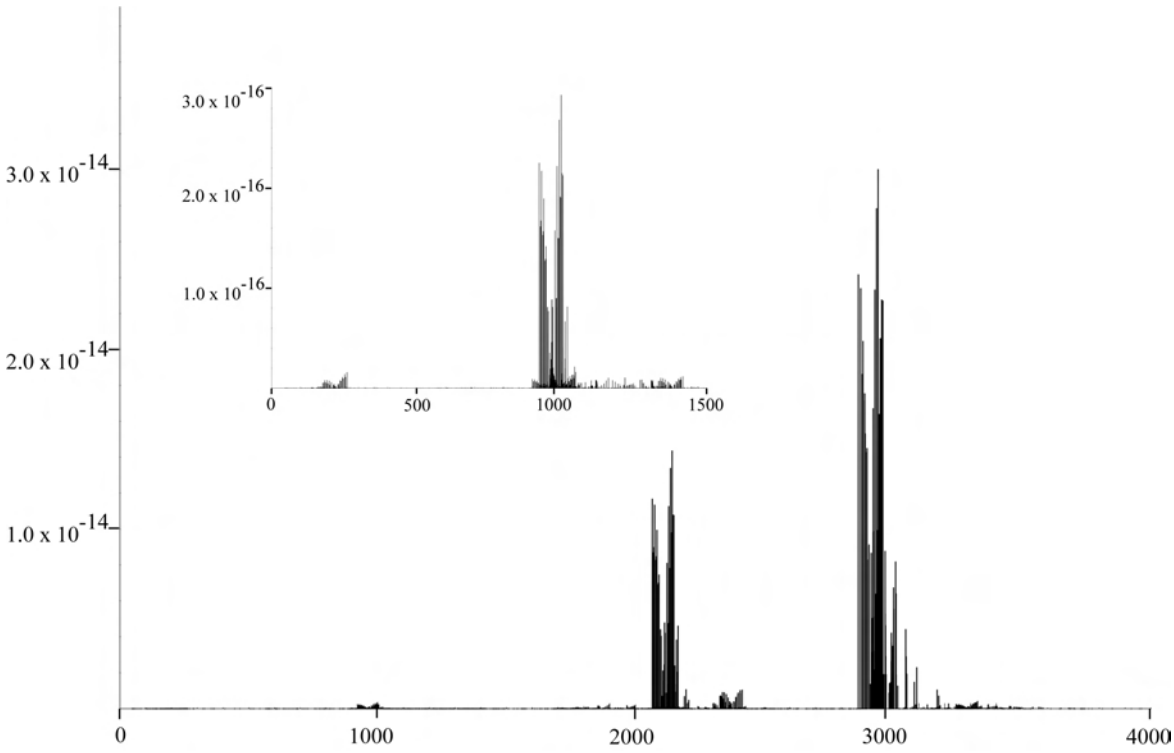

Figure 4.4 Rovibrational spectrum (at 296 K) of $(^1A_1)BeH_2^{2+}$ for $v \leq 10$, $J \leq 5$ and $S_{ab} \geq 1.0 \times 10^{-20}$. Transition frequencies and spectral intensities given in cm^{-1} and cm molecule^{-1}, respectively.

Table 4.8 Low-lying rovibrational energies[a] (/cm^{-1}) and assignments of (^{1}A$_1$)BeH$_2^{2+}$.

			$\|000\rangle$		$\|001\rangle$		$\|100\rangle$		$\|002\rangle$		$\|101\rangle$	
J	K_a	K_c	E^{RV}	Weight	E^{RV}	Weight	E^{RV}	Weight	E^{RV}	Weight	E^{RV}	Weight
1	0	1	7.9	1.00	955.9	1.00	1177.6	1.00	1917.1	1.00	2115.4	1.00
1	1	1	55.1	1.00	1009.2	1.00	1225.3	1.00	1975.4	1.00	2168.3	1.00
1	1	0	55.5	1.00	1009.6	1.00	1225.7	1.00	1975.8	1.00	2168.7	1.00
2	0	2	23.6	0.75	971.2	0.75	1193.0	0.75	1932.2	0.75	2130.6	0.75
2	1	2	70.4	1.00	1023.9	1.00	1240.4	1.00	1990.0	1.00	2183.0	1.00
2	1	1	71.5	1.00	1025.3	1.00	1241.4	1.00	1991.4	1.00	2184.2	1.00
2	2	1	212.6	1.00	1184.4	1.00	1384.4	1.00	2166.5	1.00	2342.8	1.00
2	2	0	212.6	0.75	1184.4	0.75	1384.4	0.75	2166.5	0.75	2342.8	0.75
3	0	3	47.2	0.63	994.1	0.63	1216.0	0.63	1954.8	0.63	2153.2	0.63
3	1	3	93.4	0.94	1046.1	0.94	1262.9	0.94	2011.9	0.94	2205.1	0.94
3	1	2	95.6	0.63	1048.8	0.63	1264.9	0.63	2014.7	0.63	2207.4	0.62
3	2	2	236.0	1.00	1207.1	1.00	1407.3	1.00	2189.0	1.00	2365.3	1.00
3	2	1	236.0	0.63	1207.1	0.63	1407.3	0.63	2189.1	0.63	2365.3	0.63
3	3	1	469.8	0.94	1471.6	0.94	1645.8	0.94	2482.9	0.94	2630.2	0.94
3	3	0	469.8	0.63	1471.6	0.62	1645.8	0.63	2482.9	0.62	2630.2	0.62
4	0	4	78.6	0.56	1024.5	0.56	1246.8	0.56	1984.9	0.56	2183.4	0.56
4	1	4	124.1	0.88	1075.7	0.88	1293.0	0.88	2041.1	0.87	2234.5	0.87
4	1	3	127.7	0.56	1080.2	0.56	1296.3	0.56	2045.8	0.56	2238.3	0.56
4	2	3	267.2	0.88	1237.4	0.87	1437.9	0.87	2219.1	0.87	2395.3	0.87
4	2	2	267.2	0.43	1237.4	0.42	1437.9	0.43	2219.1	0.42	2395.4	0.42
4	3	2	500.7	0.88	1501.6	0.87	1676.1	0.87	2512.6	0.87	2660.0	0.87
4	3	1	500.7	0.56	1501.6	0.56	1676.1	0.56	2512.6	0.56	2660.0	0.56
4	4	1	823.6	0.54	1868.1	0.54	2008.7	0.54	2925.3	0.54	3030.3	0.54
4	4	0	823.6	0.87	1868.1	0.87	2008.7	0.60	2925.3	0.87	3030.3	0.87

[a]Relative to the ZPE of 2834.3 cm^{-1}.

character of the rovibrational wave function.

4.6. Conclusion

Vibrational and rovibrational Hamiltonians for polyatomic molecules have been reviewed, with particular emphasis placed on those for triatomic molecules. The solution algorithm developed by von Nagy-Felsobuki and co-workers [40] for the calculation of vibrational/rovibrational spectra of triatomic molecules has been employed throughout this work. The normal co-ordinate vibrational Hamiltonians of von Nagy-Felsobuki and co-workers were therefore described in detail for both non-linear [70] and linear [71] triatomic species. Technical details relevant to these Hamiltonians, such as the quadrature algorithms used to calculate 1D vibrational eigenvectors and kinetic/potential/dipole moment matrix integrals were also discussed. A method for evaluating vibration-averaged structures was also given. The rovibrational Hamiltonian matrix elements for a non-linear molecule [25] were detailed, as were the rovibrational transition dipole matrix elements [72]. Vibrational and rovibrational wave functions have been assigned using a configuration weight schemes in terms of normal co-ordinates $\mathbf{q}$ and $J_{K_aK_c}$, respectively [40].

The vibrational spectra of $(^1\mathrm{A}_1)\mathrm{BeH}_2^{2+}$ and $(^1\Sigma_g^+)\mathrm{BeHe}_2^{2+}$ were subsequently reported. Analytical PEFs and DMFs of these species which were embedded in the respective nuclear Hamiltonians were developed in Chapter 3. The 3D vibrational states of both species were constructed using 20 vibrational basis functions in each of the q_i normal co-ordinates. Consequently, each 3D vibrational eigenfunction consisted of an 8000 term configuration expansion. The rovibrational spectrum of $(^1\mathrm{A}_1)\mathrm{BeH}_2^{2+}$ was reported for $v \leq 10$, $J \leq 5$ and $S_{ab} \geq 1.0 \times 10^{-20}$ cm molecule^{-1}. For $J \geq 4$ significant configuration mixing in the rovibrational wave function of $(^1\mathrm{A}_1)\mathrm{BeH}_2^{2+}$ was observed. As such, the assignments of these rovibrational states

could not be made without recourse to a manual inspection of the appropriate rovibrational eigenvector.

4.7. References

[1] M. Born, Gott. Nachr. Math. Phys. **KI**, 1 (1951).

[2] M. Born and K. Huang, *Dynamical Theory of Crystal Lattices* (Oxford University Press, London, 1954).

[3] See volume **58** of Spectrochim. Acta A (2002).

[4] H. Ebrahimi and M. Tafazzoli, Molecular Physics **105**, 2269 (2007).

[5] M. J. Bramley and T. Carrington, Jr., J. Chem. Phys. **99**, 8519 (1993).

[6] M. J. Bramley and N. C. Handy, J. Chem. Phys. **98**, 1378 (1993).

[7] I. N. Kozin, M. M. Law, J. M. Hutson, and J. Tennyson, J. Chem. Phys. **118**, 4896 (2003).

[8] S. Carter, N. Pinnavaia, and N. C. Handy, Chem. Phys. Lett. **240**, 400 (1995).

[9] D. Luckhaus, J. Chem. Phys. **118**, 8797 (2003).

[10] M. Mladenovic, Spectrochim. Acta A **58**, 795 (2002).

[11] D. W. Schwenke, J. Phys. Chem. **100**, 18884 (1996).

[12] D. W. Schwenke, J. Phys. Chem. **100**, 2867 (1996).

[13] H.-G. Yu, J. Chem. Phys. **117**, 2030 (2002).

[14] H.-G. Yu, J. Chem. Phys. **120**, 2270 (2004).

[15] E. Matyus, G. Czako, B. T. Sutcliffe, and A. G. Császár, J. Chem. Phys. **127**, 084102 (2007).

[16] S. N. Yurchenko, W. Thiel, and P. Jensen, J. Mol. Spec. **245**, 126 (2007).

[17] J. Pesonen, J. Theor. Comp. Chem. **4**, 1057 (2005).

[18] C. Eckart, Phys. Rev. **47**, 552 (1935).

[19] E. B. Wilson and J. B. Howard, J. Chem. Phys. **4**, 260 (1936).

[20] B. T. Darling and D. M. Dennison, Phys. Rev. **57**, 128 (1940).

[21] J. K. G. Watson, Mol. Phys. **15**, 479 (1968).

[22] J. K. G. Watson, Mol. Phys. **19**, 465 (1970).

[23] G. D. Carney, L. L. Sprandel, and C. W. Kern, Adv. Chem. Phys. **37**, 305 (1978).

[24] G. D. Carney and R. N. Porter, J. Chem. Phys. **65**, 3547 (1976).

[25] G. D. Carney, S. R. Langhoff, and L. A. Curtiss, J. Chem. Phys. **66**, 3724 (1977).

[26] W. Meyer, P. Botschwina, and P. G. Burton, J. Chem. Phys. **84**, 191 (1986).

[27] S. Miller and J. Tennyson, Chem. Phys. Lett. **145**, 117 (1988).

[28] S. Miller and J. Tennyson, J. Mol. Spec. **128**, 530 (1988).

[29] P. G. Burton, E. I. von Nagy-Felsobuki, and G. Doherty, Chem. Phys. Lett. **104**, 323 (1984).

[30] P. G. Burton and E. I. von Nagy-Felsobuki, Mol. Phys. **55**, 527 (1985).

[31] S. Carter and N. C. Handy, Mol. Phys. **47**, 1445 (1982).

[32] S. Carter and N. C. Handy, Mol. Phys. **52**, 1367 (1984).

[33] S. Carter and N. C. Handy, Mol. Phys. **57**, 175 (1986).

[34] S. Carter and N. C. Handy, Comp. Phys. Rep. **5**, 115 (1986).

[35] S. Carter and N. C. Handy, J. Chem. Phys. **87**, 4294 (1987).

[36] P. R. Bunker, Ann. Rev. Phys. Chem. **34**, 59 (1983).

[37] P. Jensen, Comp. Phys. Rep. **1**, 1 (1986).

[38] P. Jensen and P. R. Bunker, *Computational Molecular Spectroscopy* (Wiley, Chichester, 2000).

[39] Z. Bacic and J. C. Light, Ann. Rev. Phys. Chem. **40**, 469 (1989).

[40] D. J. Searles and E. I. von Nagy-Felsobuki, *Ab Initio Calculations of Vibrational Band Origins* (Elsevier, 1991).

[41] D. J. Searles and E. I. von Nagy-Felsobuki, *Lecture Notes in Chemistry* (Springer-Verlag, Berlin, 1993), vol. 61.

[42] B. T. Sutcliffe, *Methods in Computational Chemistry* (Plenum Press, New York, 1992), vol. 4, p. 33.

[43] B. T. Sutcliffe, S. Miller, and J. Tennyson, Comp. Phys. Comm. **51**, 73 (1988).

[44] J. R. Henderson, S. Miller, and J. Tennyson, J. Chem. Soc. Far. Trans. **86**, 1963 (1990).

[45] J. Tennyson, S. Miller, and J. R. Henderson, *Methods in Computational Chemistry* (Plenum Press, New York, 1992), vol. 4, p. 91.

[46] I. Hubac and M. Svrcek, *Methods in Computational Chemistry* (Plenum Press, New York, 1992), vol. 4, p. 145.

[47] D. W. Schwenke, J. Chem. Phys. **96**, 3426 (1992).

[48] D. W. Schwenke, Comp. Phys. Comm. **70**, 1 (1992).

[49] B. T. Sutcliffe, Mol. Phys. **48**, 561 (1983).

[50] E. K. C. Lai, Master's thesis, Indiana University, Bloomington, Indiana (1975).

[51] S. Carter, N. C. Handy, and B. T. Sutcliffe, Mol. Phys. **49**, 745 (1983).

[52] D. Cropek and G. D. Carney, J. Chem. Phys. **80**, 4280 (1984).

[53] M. Brommer, B. Weis, B. Follmeg, P. Rosmus, S. Carter, N. C. Handy, H.-J. Werner, and P. J. Knowles, J. Chem. Phys. **98**, 5222 (1993).

[54] J. Tennyson and A. van der Avoird, J. Chem. Phys. **77**, 5664 (1982).

[55] J. Tennyson and B. T. Sutcliffe, J. Chem. Phys. **77**, 4061 (1982).

[56] J. Tennyson and B. T. Sutcliffe, Mol. Phys. **51**, 887 (1984).

[57] B. T. Sutcliffe and J. Tennyson, Mol. Phys. **58**, 1053 (1986).

[58] J. R. Henderson, S. Miller, and J. Tennyson, Spectrochim. Acta A **44**, 1287 (1988).

[59] J. Tennyson, S. Miller, and J. R. Henderson, J. Chem. Soc. Farad. Trans. **2**, 1963 (1990).

[60] G. Czako, T. Furtenbacher, P. Barletta, A. G. Császár, V. Szalay, and B. T. Sutcliffe, Phys. Chem. Chem. Phys. **9**, 3407 (2007).

[61] R. Radau, Ann. Sci. École Normale Supérior **5**, 311 (1868).

[62] B. R. Johnson and W. P. Reinhardt, J. Chem. Phys. **85**, 4538 (1986).

[63] D. W. Schwenke, Chem. Phys. Lett. **189**, 91 (1992).

[64] P. Jensen, J. Mol. Spec. **132**, 429 (1988).

[65] P. Jensen and W. P. Kraemer, J. Mol. Spec. **129**, 172 (1988).

[66] P. Jensen, J. Mol. Spec. **128**, 478 (1988).

[67] P. Jensen, J. Mol. Spec. **133**, 438 (1989).

[68] G. D. Carney, Diss. Anstr. Int. **34B**, 1956 (1973).

[69] G. D. Carney and R. N. Porter, J. Chem. Phys. **60**, 4251 (1974).

[70] D. J. Searles and E. I. von Nagy-Felsobuki, J. Chem. Phys. **95**, 1107 (1991).

[71] F. Wang, F. R. W. McCourt, and E. I. von Nagy-Felsobuki, J. Mol. Struct. (Theochem) **497**, 227 (2000).

[72] Sudarko, J. M. Hughes, and E. I. von Nagy-Felsobuki, Aust. J. Phys. **53**, 665 (2000).

[73] D. J. Searles and E. I. von Nagy-Felsobuki, Am. J. Phys. **56**, 444 (1988).

[74] G. Strang and G. J. Fix, *An Analysis of the Finite Element Method* (Prentice-Hall, New-Jersey, 1973).

[75] S. C. Wang, Phys. Rev. **34**, 243 (1929).

[76] G. Doherty, M. J. Hamilton, P. G. Burton, and E. I. von Nagy-Felsobuki, Aust. J. Phys. **39**, 749 (1986).

[77] D. J. D. Wilson, Ph.D. thesis, The University of Newcastle, Australia (2003).

[78] Sudarko, Ph.D. thesis, The University of Newcastle, Australia (2000).

[79] D. J. Searles, F. Wang, J. A. Hayward, J. M. Hughes, D. J. D. Wilson, A. J. Page,

and E. I. von Nagy-Felsobuki, ONEDA_PADE_CS (Unpublished, 2008).

[80] A. J. Page and E. I. von Nagy-Felsobuki, Mol. Phys. **105**, 2527 (2007).

[81] G. Amat and L. Henry, Cah. Phys. **12**, 273 (1958).

[82] J. K. G. Watson, Mol. Phys. **79**, 943 (1993).

[83] A. J. Page and E. I. von Nagy-Felsobuki, J. Phys. Chem. A **111**, 4478 (2007).

[84] D. O. Harris, G. G. Engerholm, and W. D. Gwinn, J. Chem. Phys. **43**, 1515 (1965).

[85] P. J. Davis and I. Polonski, *Handbook of Mathematical Functions* (Dover, New York, 1965).

[86] D. J. Searles, F. Wang, J. A. Hayward, J. M. Hughes, D. J. D. Wilson, A. J. Page, and E. I. von Nagy-Felsobuki, SHQR_PCSF (Unpublished, 2008).

[87] A. J. Page and E. I. von Nagy-Felsobuki, Chem. Phys. (In press).

[88] A. J. Page and E. I. von Nagy-Felsobuki, VIB_STRUCT (Unpublished, 2008).

[89] A. J. Page, D. J. D. Wilson, and E. I. von Nagy-Felsobuki, Chem. Phys. Lett. **442**, 194 (2007).

[90] Sudarko and E. I. von Nagy-Felsobuki, J. Mol. Spec. **208**, 161 (2001).

[91] Sudarko, J. M. Hughes, and E. I. von Nagy-Felsobuki, Spectrochim. Acta A **58**, 747 (2002).

[92] Sudarko and E. I. von Nagy-Felsobuki, Phys. Chem. Chem. Phys. **6**, 4542 (2004).

[93] K. P. Huber and G. Herzberg, *Constants of Diatomic Molecules*, vol. IV of *Molecular Spectra and Molecular Structure* (Van Nostrand, New York, 1979).

[94] D. J. Searles, F. Wang, J. A. Hayward, J. M. Hughes, D. J. D. Wilson, A. J. Page, and E. I. von Nagy-Felsobuki, VIBINT_TIMEF_DJW (Unpublished, 2008).

[95] D. J. Searles, F. Wang, J. A. Hayward, J. M. Hughes, D. J. D. Wilson, A. J. Page, and E. I. von Nagy-Felsobuki, VIBINT_TIMEF_LINEAR (Unpublished, 2008).

[96] G. D. Carney and R. N. Porter, Phys. Rev. Lett. **45**, 537 (1980).

[97] P. G. Burton, E. I. von Nagy-Felsobuki, and G. Doherty, Chem. Phys. Lett. **104**, 323 (1984).

[98] F. Wang, D. J. Searles, and E. I. von Nagy-Felsobuki, J. Phys. Chem. **96**, 10580 (1992).

[99] R. N. Zare, *Angular Momentum* (John Wiley & Sons, New York, 1987).

[100] W. H. Shaffer, J. Mol. Spec. **1**, 69 (1957).

[101] H. W. Kroto, *Molecular Rotation Spectra* (John Wiley & Sons, London, 1975).

[102] D. J. Searles, F. Wang, J. A. Hayward, J. M. Hughes, D. J. D. Wilson, A. J. Page, and E. I. von Nagy-Felsobuki, HROVIB_ASSIGNSW1 (Unpublished, 2008).

[103] D. J. Searles, F. Wang, J. A. Hayward, J. M. Hughes, D. J. D. Wilson, A. J. Page, and E. I. von Nagy-Felsobuki, ROVINT_XYM3 (Unpublished, 2008).

CHAPTER 5

Ab Initio Investigation of Alkali Metal Hydride and Helide Ions

5.1. Introduction

A systematic study of the structures, stabilities and energetics of MH_2^+, $HMHe^+$ and MHe_2^+ for M = Li, Na and K is presented in this Chapter. The *ab initio* methods developed and benchmarked in Chapter 2 will be employed here for all electronic structure calculations. Particular emphasis will be placed upon the efficacy of isovalent arguments with respect to these species. Where possible, these data will be presented in and discussed relative to available theoretical [1–35] and experimental [35–38] data. These data have been reviewed in Chapter One. The *ab initio* study of the structures and energetics of these species will allow suitable candidates for rovibrational calculations to be gauged (see Figure 1.1). In particular, the investigation of the dissociative energetics and PES topologies of MH_2^+, $HMHe^+$ and MHe_2^+ using *ab initio* methods will provide an indication as to the most suitable candidates for a full rovibrational analysis. *Ab initio* rovibrational spectra of suitable species (*viz.* $(^1A_1)LiH_2^+$ and $(^1A_1)NaH_2^+$) will therefore be subsequently presented. All aspects of these *ab initio* rovibrational spectra have been calculated using methods and algorithms described in Chapters Three and Four. Data presented in this Chapter serve as an extension to the work of Page *et al.* [39–42], who have previously elucidated the structural and energetic trends of neutral alkali-metal hydrides and alkaline-earth metal hydrohelide/helide cations.

There has recently been a number of theoretical investigations dealing with

the spectroscopy of the ground state of LiH_2^+ (see references [21, 23] and references therein). Of all the molecular ions investigated in this thesis, $(^1A_1)LiH_2^+$ is the only one for which a rotationally-resolved spectrum has been identified experimentally thus far [36, 37]. Nevertheless, rovibrational spectra of a number of ion-quadrupole complexes similar in nature to LiH_2^+ have recently been reported [36, 37, 43]. Additionally, Page and von Nagy-Felsobuki have constructed *ab initio* rovibrational spectra of $(^1A_1)LiH_2^+$ [23] and $(^1A_1)NaH_2^+$ [34]. It is anticipated therefore that spectroscopic characterisation of alkali metal hydride and hydrohelide ions may occur in the near future. Theoretical prediction of vibrational/rovibrational properties of these species at this moment may therefore provide timely assistance for the characterisation of these ions. Molecular PESs and DMSs, vibrational/rovibrational transition frequencies, vibration-averaged structures and vibrational/rovibrational radiative data (*i.e.* band/line strengths) of $(^1A_1)LiH_2^+$ and $(^1A_1)NaH_2^+$ will be presented in Sections 5.6 and 5.7, respectively.

5.2. Computational Procedure

The UCCSD(T), IC-MRCI and IC-MRCI+Q methods and atomic basis sets employed presently are essentially those described in Chapter 2. In cases where helium was present, helium $1s$ electron density was excluded from the CASSCF optimisation. Thus a correct description of the electronic wave function in the asymptotic limit (in which the He $1s$ configuration is identically doubly occupied) was obtained. Conversely, hydrogen $1s$ electron density was included in all CASSCF active spaces. It is also noted that all *ab initio* results calculated in this work include BSSE and relativistic (DK2) correction and have been calculated using MOLPRO [44], unless states otherwise.

5.3. Alkali Metal Dihydride Cations: MH_2^+ (M = Li, Na, K)

Values of R_e, θ_e, D_e, ω_1, ω_2 and ω_3 of $(^1A_1)MH_2^+$ (M = Li, Na, K) calculated in this work are compared to previous theoretical and experimental data in Tables 5.1, 5.2 and 5.3, respectively. Several dissociative mechanisms have been considered for $(^1A_1)MH_2^+$, due to the nature of the bonding present in these ground state systems. In particular, potential well-depths corresponding to the dissociative reactions,

$$D_e(1) : (^1A_1)MH_2^+ \rightarrow (^1S_0)M^+ + (^1\Sigma_g^+)H_2 \tag{5.1}$$

$$D_e(2) : (^1A_1)MH_2^+ \rightarrow (^2\Sigma^+)MH^+ + (^2S_{1/2})H \tag{5.2}$$

$$D_e(3) : (^1A_1)MH_2^+ \rightarrow (^1S_0)M^+ + 2(^2S_{1/2})H \tag{5.3}$$

have been calculated for each species. Due to the number of reports concerning $(^1A_1)LiH_2^+$, comparison between the results of this work and previous *ab initio* results is limited to those which employed correlated methods.

From Table 5.1 it is evident that R_e calculated using UCCSD(T), IC-MRCI and IC-MRCI+Q are in excellent agreement, differing at most by 0.1 mÅ. The single- and multi-reference θ_e values calculated in this work are also in exact agreement. Furthermore, there is generally good agreement between UCCSD(T), IC-MRCI and IC-MRCI+Q equilibrium structures and those from previous theoretical investigations. For example, compared to the CCSD value of Davy *et al.* [9], the UCCSD(T) R_e value is *ca.* 14 mÅ smaller. Similarly, IC-MRCI and IC-MRCI+Q yield values of R_e are 2.9 mÅ smaller than the recent MRVB calculation of Kraemer and Špirko [21]. There is also good agreement between both single- and multi-reference values of R_e of this work with the FCI value of Page and von Nagy-Felsobuki [23] (see Chapter 3). The latter was calculated using CVTZ (Li) [45] and aug-cc-pVTZ (H) [46] basis sets, and is *ca.* 7 mÅ larger than the values of this work. Values of θ_e

Table 5.1 *Ab initio* equilibrium parameters of $(^1A_1)LiH_2^+$.

Method	R_e (/Å)	θ_e (/°)	D_e[a] (/kJmol^{-1})			Frequencies (/cm^{-1})		
			1	2	3	ω_1	ω_2	ω_3
UCCSD(T)[b]	2.0194	21.4	25.95	469.3	482.7	521	4087	864
IC-MRCI[b]	2.0192	21.4	25.97	469.3	482.7	521	4090	864
IC-MRCI+Q[b]	2.0192	21.4	24.51	469.3	482.7	506	4092	838
MP2[c]	2.1262	21.7					4178.77	
MP2[d]	2.1076	21.9	25.38					
MP2[e]	2.144	21.5	24.8					
MP2[f]	2.14	21.5	24.3					
CISD[g]	2.042	21.2						
CCSD[h]	2.034	21.5	24.6			502	4300	701
MRVB[i]	2.0221	21.5	25.80					
FCI[j]	2.027	21.4	25.67			487.9		738.8
Experiment[k]			27.21 ± 19.0					

[a] $D_e(1)$, $D_e(2)$ and $D_e(3)$ correspond to dissociative reactions (5.1), (5.2) and (5.3), respectively.
[b] This work.
[c] Includes BSSE correction, in conjunction with [10*s*] (H) [6*s*4*p*] (Li) basis sets; see reference [24].
[d] In conjunction with 6-311G basis sets; see reference [22].
[e] In conjunction with 6-311G(*d*,*p*) basis sets; see reference [29]. D_e value calculated using MP4.
[f] Includes BSSE correction, in conjunction with aug-cc-pVQZ basis sets; see reference [30].
[g] In conjunction with [6*s*3*p*1*d*] basis sets; see reference [1].
[i] In conjunction with [8*s*4*p*3*d*] (H) and [14*s*9*p*4*d*3*f*] (Li) basis sets; see reference [21].
[j] In conjunction with aug-cc-pVTZ (H) and CVTZ (Li) basis sets, respectively. Fundamental frequencies are fully anharmonic values; see reference [23].
[k] See reference [38].

calculated deviate from CCSD [9], MRVB [21] and FCI [23] values by 0.1°, regardless of the method employed. With respect to previously reported MP2 equilibrium structures, the R_e and θ_e values of this work are generally 90-130 mÅ and 0.1-0.4° smaller, respectively.

It is observed that UCCSD(T), IC-MRCI and IC-MRCI+Q yield deeper potential well-depths, relative to all reported values of D_e calculated using MP2 [22, 24, 29, 30]. The same observation is made with respect to the CCSD D_e value reported by Davy *et al.* [9]. The well-depths reported by Kraemer and Špirko (MRVB) [21] and Page and von Nagy-Felsobuki (FCI) [23] are closer to those of this work. For instance, the former $D_e(1)$ value differs by -0.15, -0.17 and 0.29 kJ mol^{-1} relative to UCCSD(T), IC-MRCI and IC-MRCI+Q values, respectively.

Similarly, the FCI $D_e(1)$ value differs from UCCSD(T), IC-MRCI and IC-MRCI+Q values by -0.28, -0.03 and 0.16 kJ mol^{-1}, respectively. Wu [38] reported the only experimental $D_0(1)$ value of $(^1\mathrm{A}_1)\mathrm{LiH}_2^+$ available in the literature. The error reported in this measurement is of a similar magnitude to the value of $D_0(1)$ itself, and therefore renders any comparison meaningless. Nevertheless, a $D_0(1)$ value of 20.72 kJ mol^{-1} has been reported [36] using the MRVB PES of Kraemer and Špirko [21]. This value compares well to the ZPE-corrected UCCSD(T), IC-MRCI and IC-MRCI+Q D_e values of 19.52, 19.52 and 18.32 kJ mol^{-1}, respectively. Similarly, the FCI PES of Page and von Nagy-Felsobuki [23] yields a $D_0(1)$ value of 19.92 kJ mol^{-1}.

The results of this work indicate that the minimum-energy structure of $(^1\mathrm{A}_1)\mathrm{NaH}_2^+$ is of C_{2v} symmetry, in concurrence with previously reported data. The equilibrium structure of $(^1\mathrm{A}_1)\mathrm{NaH}_2^+$ calculated using UCCSD(T), IC-MRCI and IC-MRCI+Q are also in excellent agreement. For instance, the largest difference in R_e and θ_e calculated using these methods is 2.6 mÅ and 0.1°, respectively. Nevertheless, the single- and multi-reference methods employed presently predict an equilibrium structure disparate to those from previous investigations in a quantitative sense. For example, the R_e values of this work are *ca.* 1-150 mÅ smaller than all previously reported HF and MP2 values, with the exception of the SCF MO result of Switalski *et al.* [28]. The latter approach employed a model core potential and yielded an R_e value of 2.38 Å. There is better agreement between the description of θ_e provided here and those reported previously. For example, UCCSD(T), IC-MRCI and IC-MRCI+Q θ_e values differ from reported MP2 values [29, 30, 35] by -0.2-0.5°. Similarly, the correlated methods of this work give θ_e values *ca.* 0.5-1.2° larger than HF values [11, 26, 27].

The $[(^1\mathrm{A}_1)\mathrm{NaH}_2^+ \rightarrow (^1\mathrm{S}_0)\mathrm{Na}^+ + (^1\Sigma_g^+)\mathrm{H}_2(v = 0)]$ dissociation energy

Table 5.2 *Ab initio* equilibrium parameters of $(^1A_1)NaH_2^+$.

Method	R_e (/Å)	θ_e (/°)	D_e[a] (/kJmol^{-1})			Frequencies (/cm^{-1})		
			1	2	3	ω_1	ω_2	ω_3
UCCSD(T)[b]	2.4208	17.8	14.66	463.9	471.4	364	4215	458
IC-MRCI[b]	2.4182	17.7	16.48	460.3	467.7	399	4232	420
IC-MRCI+Q[b]	2.4195	17.8	14.72	465.8	473.3	393	4162	414
SCF MO[c]	2.38	18.0						
HF[d]	2.541	16.6	13.6			260	4577	439
HF[e]	2.458	17.4	12.0			306	4518	558
HF[f]	2.475	17.3	13			286	4522	502
MP2[g]	2.5081	17.9	14				4218.78	
MP2[h]	2.427	17.7	12.3					
MP2[i]	2.463	17.3	10.31			304	4458	533
MP2[j]	2.45	17.5	12.6					
Experiment[j]			10.3 ± 0.8					

[a] $D_e(1)$, $D_e(2)$ and $D_e(3)$ correspond to dissociative reactions (5.1), (5.2) and (5.3), respectively.
[b] This work.
[c] In conjunction with a model core potential; see reference [28].
[d] In conjunction with 6-31G(d) basis sets; see reference [26].
[e] In conjunction with [3s2p] (H) and [6s5p1d] (Na) basis sets; see reference [11].
[f] In conjunction with [5s3p1d] (H) and 6-311G* (Na) basis sets; see reference [27].
[g] Includes BSSE correction, in conjunction with [10s] (H) [6s4p] (Li) basis sets; see reference [24].
[h] In conjunction with 6-311G(d,p) basis sets; see reference [29]. D_e value calculated using MP4 result.
[i] In conjunction with 6-311+G(3df,2p) basis sets; see reference [35]. Experimental result is D_0 value.
[j] Includes BSSE correction, in conjunction with aug-cc-pVQZ basis sets; see reference [30].

(*i.e.* $D_0(1)$) has been measured experimentally by Bushnell *et al.* [35] to be 10.3 ± 0.8 kJ mol^{-1}. Using a fully anharmonic UCCSD(T) PES/vibrational wave function (see §5.7), $D_0(1)$ is calculated to be 10.3 kJ mol^{-1}, a value that is in excellent with experiment [35]. By comparing harmonic/anharmonic $D_0(1)$ values, a quantitative measure of the effects of anharmonicity on the molecular PES may be gauged. For example, UCCSD(T) harmonic frequencies listed in Table 5.2 yield a $D_0(1)$ value of 10.83 kJ mol^{-1}. Similarly, the IC-MRCI and IC-MRCI+Q $D_0(1)$ values are calculated to be 12.58 and 11.30 kJ mol^{-1}, respectively. The latter data illustrate the effect of size-extensivity on the PES curvature in the locality of the geometric minimum. Curtiss and Pople [26] previously reported D_0 to be 10.3

kJ mol^{-1} using HF/6-31G(d). This method neglected the effects of correlation in both (^{1}A$_1$)NaH$_2^+$ and the dissociation products however, and so it is likely that this agreement is fortuitous. There is reasonable agreement between the MP2 D_0 values reported by Barbatti *et al.* [29] (MP2/6-311G(d,p)) and Vitillo *et al.* [30] (MP2/6-311+G(3df,2p)) and the CCSD(T) value of this work, with these values agreeing to within *ca.* 1 kJ mol^{-1}. From consideration of the data presented in Table 5.2 it is concluded that a reasonable description of the molecular wave function is attained using UCCSD(T). That is, little is gained with respect to molecular equilibrium parameters when multi-reference effects are taken into account.

The data in Table 5.2 concerning the harmonic fundamental frequencies of (^{1}A$_1$)NaH$_2^+$ suggest that the ^{1}A$_1$ PES is particularly sensitive with respect to the *ab initio* wave function employed. This is particularly evident upon comparison of correlated and non-correlated ω_2 fundamental frequencies. This fundamental mode essentially corresponds to ω_e in the H$_2$ subunit. It is evident that the CCSD(T) ω_2 value is generally 200-250 cm^{-1} smaller than previously reported HF values, and *ca.* 140 cm^{-1} smaller than the MP2/6-311+G(3df,2p) value reported by Bushnell *et al.* [35]. For comparison, ω_e(H$_2$) calculated using CCSD/aug-cc-pVQZ is 4399 cm^{-1}. This implies that the anisotropy of the Na$^+$-H$_2$ interaction is less pronounced than those of the Li$^+$-H$_2$ [23] and Mg^{2+}-H$_2$ [47] interactions. For these isovalent and isoelectronic series ω_2 were calculated to be 4277 and 3951 cm^{-1}, respectively, using an equivalent CCSD(T) method.

Equilibrium parameters of the ^{1}A$_1$ ground state of KH$_2^+$ are compared to previously reported theoretical and experimental data in Table 5.3. The method employed presently yield (^{1}A$_1$)KH$_2^+$ equilibrium parameters which are in good agreement. For example, the largest discrepancies observed for R_e and θ_e values are 15.9 mÅ and 0.1° and occur using UCCSD(T) and IC-MRCI. It is observed that there

Table 5.3 *Ab initio* equilibrium parameters of $(^1A_1)KH_2^+$.

Method	R_e (/Å)	θ_e (/°)	D_e[a] (/kJmol^{-1})			Frequencies (/cm^{-1})		
			1	2	3	ω_1	ω_2	ω_3
UCCSD(T)[b]	2.8935	14.8	8.734	461.1	465.5	320	4259	416
IC-MRCI[b]	2.9094	14.7	8.359	459.1	477.6	320	4323	421
IC-MRCI+Q[b]	2.8974	14.8	8.637	463.4	470.9	313	4243	412
MP2[c]	3.186	13.8	4.90					
MP2[d]	3.06	13.9	6.1					
Experiment[e]			6.07 ± 0.8					

[a] $D_e(1)$, $D_e(2)$ and $D_e(3)$ correspond to dissociative reactions (5.1), (5.2) and (5.3), respectively.
[b] This work.
[c] In conjunction with 6-311G(*d*,*p*) basis sets; see reference [29]. D_e value calculated using MP4 result.
[d] Includes BSSE correction, in conjunction with aug-cc-pVQZ basis sets; see reference [30].
[e] In conjunction with 6-311+G(3*df*,2*p*) basis sets; see reference [35]. Experimental result is D_0 value.

are only two previously published *ab initio* equilibrium structures available, both of which were calculated with MP2. For example, Curtiss and Pople [26] employed MP2/6-311G(*d*,*p*) to report R_e and θ_e to be 3.186 Å and 13.8°, respectively. Similarly, Vitillo *et al.* [30] employed MP2/aug-cc-pVQZ to report R_e and θ_e to be 3.06 Å and 13.9°. The single- and multi-reference methods employed in this work predict that the $^1A_1$ ground state is significantly more tightly bound than do either of the previous MP2 methods. For example, R_e calculated using UCCSD(T), IC-MRCI and IC-MRCI+Q is *ca.* 160-290 mÅ smaller than those calculated using MP2/6-311G(*d*,*p*) and MP2/aug-cc-pVQZ.

Comparison of the potential well-depth for equation (5.1) also leads to this conclusion. For example, using UCCSD(T), IC-MRCI and IC-MRCI+Q $D_e(1)$ is 8.734, 8.359 and 8.637 kJ mol^{-1}, respectively. As such, IC-MRCI underestimates $D_e(1)$ by 0.375 and 0.278 kJ mol^{-1}, relative to UCCSD(T) and IC-MRCI+Q. Nevertheless, these values are *ca.* 3.4-3.8 kJ mol^{-1} larger than the MP2/6-311G(*d*,*p*) value [26] and *ca.* 2.2-2.6 kJ mol^{-1} larger than the MP2/aug-cc-pVQZ value [30]. Bushnell *et al.* [35] have reported an experimental $D_0(1)$ for the $[(^1A_1)KH_2^+ \rightarrow (^1S_0)K^+ +$

$(^1\Sigma_g^+)H_2(v=0)]$ dissociation channel of 6.07 ± 0.8 kJ mol^{-1}. Vitillo *et al.* [30] have reported D_0 to be 5.5 kJ mol^{-1}, a result within the limits of experimental error. Using UCCSD(T), IC-MRCI and IC-MRCI+Q, $D_0(1)$ was calculated to be 5.157, 4.375 and 5.228 kJ mol^{-1}, respectively. As such, these methods yield $D_0(1)$ values *ca.* -0.11, -0.89 and -0.04 kJ mol^{-1} outside the limits of experimental error. The relative magnitudes of the $D_0(1)$ values of this work and that of Vitillo *et al.* [30] are therefore indicative of the relative magnitudes of the ZPE corrections.

Comparison of successive binding energies corresponding to the dehydrogenation of $(^1A_1)LiH_2^+$, $(^1A_1)NaH_2^+$ and $(^1A_1)KH_2^+$ (*i.e.* equations (5.2) and (5.3), respectively) yields further insight into the dissociative natures of these complexes. Such a comparison is made in Table 5.4. If it is assumed that the two M-H bonds in these species are identical, then the energy binding a single hydrogen to the metal ion is half the value of $D_e(3)$. The difference, Δ, between this energy and $D_e(2)$ therefore gives an indication of the relative binding strengths of the two hydrogens. It is inferred from Table 5.4 that for the $^1A_1$ ground states of LiH_2^+, NaH_2^+ and KH_2^+ the binding of the second hydrogen is substantially weaker than the first. For instance, $\bar{\Delta}$ using UCCSD(T), IC-MRCI and IC-MRCI+Q for these species are *ca.* -455.8, -455.7 and -451.1 kJ mol^{-1}, respectively. It is also inferred from this comparison that the relative binding strengths of M-H_1 and M-H_2 are relatively constant for M = Li, Na and K. That is, the binding energy of the two M-H bonds in each of these

Table 5.4 Binding energies (/kJ mol^{-1}) for successive hydrogenation of M^+ ions (M = Li, Na, K).

	$(^2A_1)LiH_2^+$			$(^2A_1)NaH_2^+$			$(^2A_1)KH_2^+$		
Method	$D_e(2)$	$D_e(3)$	Δ^a	$D_e(2)$	$D_e(3)$	Δ^a	$D_e(2)$	$D_e(3)$	Δ^a
UCCSD(T)	469.3	482.7	-455.8	463.9	471.4	-456.3	461.1	465.5	-456.8
IC-MRCI	469.3	482.7	-455.8	460.3	467.7	-453.0	459.1	477.6	-440.5
IC-MRCI+Q	469.3	482.7	-455.9	465.8	473.3	-458.3	463.4	470.9	-456.0

[a] $\Delta = D_e(3) - 2D_e(2)$. $D_e(2)$ and $D_e(3)$ correspond to dissociative reactions (5.2) and (5.3), respectively. It is assumed that both M-H bonds are identical.

species is relatively independent of atomic number M.

5.4. Alkali Metal Hydrohelide Cations: $HMHe^+$ (M = Li, Na, K)

Equilibrium structures and energetics of the ground state hydrohelide species $HMHe^+$ (M = Li, Na, K) have been considered in this work. Equilibrium parameters including R_e, θ_e and dissociative potential well-depths D_e have been calculated using UCCSD(T), IC-MRCI and IC-MRCI+Q, and are given in Table 5.5. The values of IE_1 for Li, Na and K are less than that of IE_1 for He. Consequently, the dissociative products resulting from alkali metal hydrohelide species will invariably include neutral He. Similarly, dissociation of $HMHe^+$ (M = Li, Na, K) into [M^+ + HeH] is also not a probable reaction. This is due primarily to the relative abilities of M^+ and H to chemically bind helium, which in turn are determined by the relative polarisabilities of M^+ and H. Following these considerations, the only dissociative reactions considered in this work for $HMHe^+$ are,

$$D_e(1) : HMHe^+ \rightarrow (^2\Sigma^+)MH^+ + (^1S_0)He \tag{5.4}$$

$$D_e(2) : HMHe^+ \rightarrow (^1S_0)M^+ + (^2S_{1/2})H + (^1S_0)He \tag{5.5}$$

No theoretical or experimental data of an alkali metal hydrodelide cation has been reported in the literature to date.

From Table 5.5 it is evident that the single- and multi-reference methods employed in this work yield quantitatively consistent equilibrium structures for the $^2\Sigma^+$ ground state of $HLiHe^+$. For example, UCCSD(T), IC-MRCI and IC-MRCI+Q each predict this species to be linear at equilibrium, with R_e(M-H) being 2.1942, 2.1944 and 2.1941 Å, respectively. The R_e(Li-He) values calculated using these methods are also in excellent agreement, differing by at most 0.4 mÅ. The ground state

Table 5.5 *Ab initio* equilibrium parameters of $HMHe^+$, M = Li, Na, K.

Method	R_e (M-H) (/Å)	R_e (M-He) (/Å)	θ_e (/°)	$D_e{}^a$ (/kJmol^{-1})	
				1	2
		$(^2\Sigma^+)HLiHe^+$			
UCCSD(T)	2.1942	1.9036	180.0	7.464	20.87
IC-MRCI	2.1944	1.9036	180.0	7.483	20.90
IC-MRCI+Q	2.1941	1.9032	180.0	6.741	20.15
		$(^2\Sigma^+)HNaHe^+$			
UCCSD(T)	2.5911	2.3322	180.0	3.814	11.35
IC-MRCI	2.5941	2.3343	180.0	3.720	12.92
IC-MRCI+Q	2.5916	2.3330	180.0	3.799	11.30
		$(^2A')HKHe^+$			
UCCSD(T)	3.0592	2.8506	80.3	2.098	6.433
IC-MRCI	3.0926	2.8764	81.3	3.656	7.335
IC-MRCI+Q	3.0682	2.8560	80.5	1.934	6.420

[a] $D_e(1)$ and $D_e(2)$ correspond to dissociation reactions (5.4) and (5.5), respectively.

of $HNaHe^+$ has also been determined to be of $C_{\infty v}$ symmetry. The R_e values with respect to both M-H and M-He bonds calculated using UCCSD(T), IC-MRCI and IC-MRCI+Q are also in excellent agreement. For instance, the largest discrepancy between these methods with respect to R_e(M-H) is 3 mÅ, observed using UCCSD(T) and IC-MRCI. These methods also yield the largest difference for R_e(M-He), being only 2.1 mÅ. The ground state of $HKHe^+$ arises from an identical metal ion configuration to those of $(^2\Sigma^+)HLiHe^+$ and $(^2\Sigma^+)HNaHe^+$. Nevertheless, the lowest energy point on the $HKHe^+$ PES corresponds to a C_s equilibrium structure. This conclusion has been reached using both single- and multi-reference wave functions. For example, θ_e for $(^2A')HKHe^+$ using UCCSD(T), IC-MRCI and IC-MRCI+Q are 80.3, 81.3 and 80.5°, respectively, and as such are in excellent agreement. There is greater discrepancy in the calculated equilibrium K-H and K-He bond lengths. For instance, R_e(M-H) calculated using these methods are 3.0592, 3.0926 and 3.0682 Å, and so exhibit a maximum deviation of 33.4 mÅ. This deviation is of a similar order of magnitude with respect to R_e(M-He), with a value of 25.8 mÅ. In both cases, the

maximum deviation occurs between UCCSD(T) and IC-MRCI data.

The current consensus is that $HMHe^+$ (for main-group elements M) essentially exist as a HM^+-He complex, with the H and He bound covalently and electrostatically to the metal, respectively [40, 41]. This trend is not observed for the ground states of $HMHe^+$ (M = Li, Na, K). Indeed, comparison of the R_e(M-H) and R_e(M-He) values for these species suggests that He is more tightly bound to the central M^+ ion relative to H, contrary to established trends in the main-group hydrodelide ions [40, 41]. Nevertheless, the bonding observed in $(^2\Sigma^+)HMHe^+$ is not reflected in the respective diatomic hydride fragments. For example, the equilibrium bond length of $(^2\Sigma^+)MH$ (M = Li, Na, K) are calculated to be 1.5980, 1.8899 and 2.2501 Å, respectively, using UCCSD(T). The converse is the case for the diatomic helide fragment ions $(^1\Sigma^+)MHe^+$, for which R_e are 1.8977, 2.3272 and 2.8492 Å, respectively.

Opposing trends are also observed with respect to potential well-depths for equations (5.4) and (5.5). If the difference between $D_e(1)$ and $D_e(2)$ is interpreted as the binding energy of the M-H bond, then data in Table 5.5 suggest that the M-H bond is stronger than the M-He bond. For instance, $D_e(1)$ and $D_e(2)$ for $(^2\Sigma^+)HLiHe^+$ are *ca.* 7 and 20 kJ mol^{-1}, respectively. Similarly, these data for $(^2\Sigma^+)HNaHe^+$ are *ca.* 3.8 and 12 kJ mol^{-1}, whereas for $(^2\Sigma^+)HKHe^+$ values of *ca.* 2 and 7 kJ mol^{-1} are observed. Dissociative potential well-depth data therefore imply that the M-H bond is of greater strength compared to the M-He bond. These data complement those of Page and co-workers [40, 41] with respect to ground state $HMHe^+$ (M = Be, Mg, Ca). Such a conclusion is however contradictory to that obtained from consideration of the equilibrium structures alone.

In order to further elucidate these trends observed in the structures and stabilities of $(^2\Sigma^+)HMHe^+$, constrained angle optimisations have been performed in

the manner of Page and von Nagy-Felsobuki [41]. In particular, R_e(M-H) and R_e(M-He) have been determined over the range $60^\circ \leq \theta \leq 180^\circ$ using increments in θ of 10°. These minimum energy paths (MEPs) and corresponding R_e(M-H) and R_e(M-He) values are given in Figure 5.1. This figure illustrates succinctly the nature of the bonding in these ground state ions to be extremely fluxional. For instance, while the MEP for $(^2\Sigma^+)$HLiHe$^+$ exhibits a minimum energy structure corresponding to $\theta = 180^\circ$, it is evident that the topology of the MEP is such that a large change in bond angle brings about an almost negligible change in energy. For example, at room temperature θ may fluctuate by as much as *ca.* 105°. An analogous observation is made with respect to the ground state of HNaHe$^+$, which also exhibits a linear minimum energy structure. In this case, θ may fluctuate by as much as *ca.* 120°. The ground state of HKHe$^+$ exhibits a non-linear minimum energy structure, as shown in Figure 5.1. Nevertheless, the ^{2}A$'$-$^2\Sigma^+$ barrier height is 1.70 and 1.53 cm^{-1} using UCCSD(T) and IC-MRCI+Q, respectively. As such $(^2$A$')$HKHe$^+$ is unable to support a bound vibrational state in the bond angle co-ordinate. It is also inferred from Figure 5.1 that both R_e(M-H) and R_e(M-He) are extremely variable for $(^2\Sigma^+)$HLiHe$^+$ and $(^2\Sigma^+)$HNaHe$^+$. For example, for $60^\circ \leq \theta \leq 180^\circ$ the optimal M-H and M-He values may vary by up to *ca.* 0.13 and 1.09 Å (HLiHe$^+$) and 0.10 and 0.17 Å (HNaHe$^+$), relative to the minimum energy structure, respectively. Similarly, for the ground state of HKHe$^+$, R_e(M-H) and R_e(M-He) may vary by up to 0.03 and 0.04 Å, respectively.

It is concluded that the ground state PESs of HMHe$^+$ (M = Li, Na, K) are extremely flat, particularly in the H-M-He bond angle co-ordinate. The UCCSD(T), IC-MRCI and IC-MRCI+Q approaches employed in this work provided consistent descriptions of the structures and energetics of these species. It is also concluded that multi-reference effects, with respect to R_e, θ_e and D_e, are only appreciable for

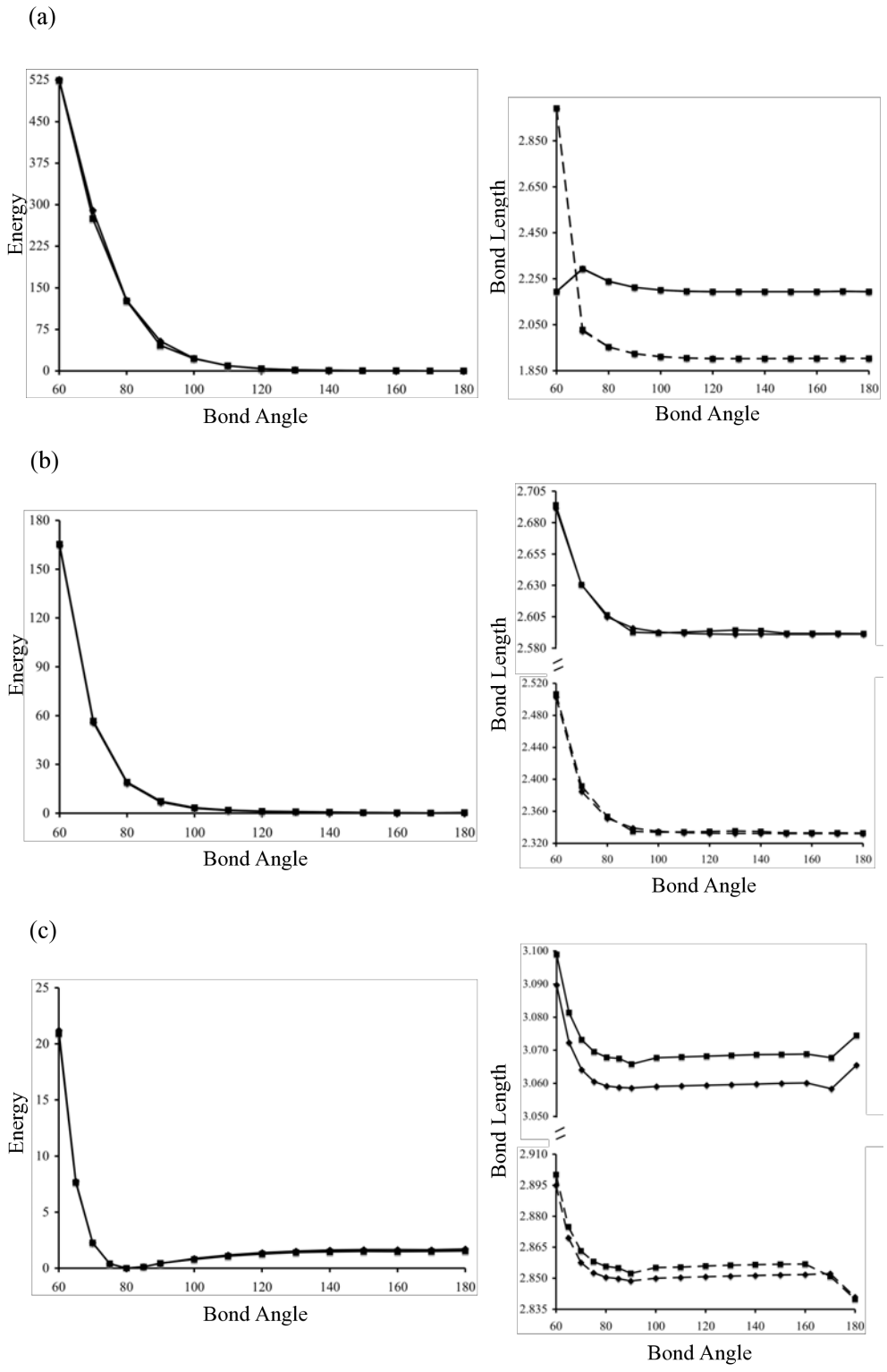

Figure 5.1 Optimised molecular energies (/cm^{-1}) of: (a) HLiHe$^+$; (b) HNaHe$^+$, and; (c) HKHe$^+$ as a function of bond angle (/°) using UCCSD(T) (diamonds) and IC-MRCI+Q (squares). Optimised M-H (full lines) and M-He (dashed lines) bond lengths (/Å) of each species are also presented.

the ground state of $HKHe^+$. Nevertheless, an agreement of less than 1 cm^{-1} was observed in the $^2A'$-$^2\Sigma^+$ barrier height for this molecule. From this analysis of the ground state PESs of $HMHe^+$ it is concluded that these species would not be suitable for a normal co-ordinate vibrational analysis.

5.5. Alkali Metal Dihelide Cations: MHe_2^+ (M = Li, Na, K)

Equilibrium parameters, including R_e, θ_e and D_e have been calculated for the ground states of $LiHe_2^+$, $NaHe_2^+$ and KHe_2^+. These data are given in Table 5.6. Binding energies have been calculated for two dissociative processes, *viz.*

$$MHe_2^+ \rightarrow (^2\Sigma^+)MHe^+ + (^1S_0)He \tag{5.6}$$

$$MHe_2^+ \rightarrow (^1S_0)M^+ + 2(^1S_0)He \tag{5.7}$$

for M = Li, Na and K.

From Table 5.6 it is evident that single- and multi-reference methods of this work yield R_e values in good agreement with previously reported *ab initio* data. For example, compared to the MP2/6-311+G(3*df*,3*pd*) R_e value of Sapse *et al.* [32], values of this work generally differ by *ca.* 2 mÅ. Compared to the CCSD(T)/cc-pV5Z value of Marinetti *et al.* [33], this agreement is better than 1 mÅ. Results of this work indicate that the minimum energy structure of the ground state of $LiHe_2^+$ is of $D_{\infty h}$ symmetry. This is contrary to the calculations of Sapse *et al.* [32] and Marinetti *et al.* [33], who reported a $^1A_1$ minimum energy state for $LiHe_2^+$, with θ_e being 112.62° and 106°, respectively. Nevertheless, Marinetti *et al.* [33] also located a $D_{\infty h}$ structure energetically very close to the C_{2v} structure. These workers ultimately concluded that the 'true' ground state structure could not be decided using their chosen methods, due to the extremely flat curvature of PES

Table 5.6 *Ab initio* equilibrium parameters of MHe_2^+, M = Li, Na, K.

Method	R_e (/Å)	θ_e (/°)	D_e[a] (/kJmol^{-1})	
			1	2
		$LiHe_2^+$		
UCCSD(T)[b]	1.9001	180.0	7.552	15.347
IC-MRCI[b]	1.9004	180.0	7.580	14.921
IC-MRCI+Q[b]	1.8997	180.0	6.890	15.580
MP2[c]	1.902	112.62	7.385	14.77
CCSD(T)[d]	1.9	106		
		$NaHe_2^+$		
UCCSD(T)[b]	2.3283	87.4	3.852	7.797
IC-MRCI[b]	2.3360	92.0	3.719	8.377
IC-MRCI+Q[e]	2.3318	91.0	3.764	7.793
MP2[c]	2.343	122.79	4.565	9.129
CCSD(T)[d]	2.32	180.0		7.893
		KHe_2^+		
UCCSD(T)[b]	2.8471	64.7	2.148	4.270
IC-MRCI[b]	2.8719	65.6	2.021	4.039
IC-MRCI+Q[b]	2.8466	65.0	1.873	4.109
CCSD(T)[d]	2.831	180.0		4.399

[a] $D_e(1)$ and $D_e(2)$ correspond to dissociation reactions (5.6) and (5.7), respectively.
[b] This work.
[c] In conjunction with 6-311+G(3*df*,3*pd*) basis sets; see reference [32].
[d] Include BSSE correction, in conjunction with cc-pV5Z ($LiHe_2^+$, $NaHe_2^+$) and aug-cc-pV5Z (KHe_2^+) basis sets; see reference [33].

with respect to the bond angle co-ordinate. This conclusion has also been reached in this work. For example, using UCCSD(T) and IC-MRCI+Q respectively, it is observed that a fluctuation in θ of *ca.* $\pm 70°$ results in a change of only 1 cm^{-1} in the energy of $LiHe_2^+$.

Discrepancies in calculated θ_e values are also observed for the ground state of $NaHe_2^+$. For example, UCCSD(T), IC-MRCI and IC-MRCI+Q predict θ_e to be 87.4, 92.0 and 91.0°, and so are in good agreement. However, Sapse *et al.* [32] calculated θ_e to be 122.79° using MP2/6-311+G(3*df*,3*pd*). Similarly, Marinetti *et al.* [33] employed CCSD(T)/cc-pV5Z, giving a θ_e value of 180°. The latter authors also acknowledged the existence of a non-linear structure energetically adjacent to that of the $^1\Sigma_g^+$ structure. It is therefore anticipated that the PES curvature with respect

to the He-Na-He bond angle co-ordinate will be particularly flat. Nevertheless, all methods employed in this work predict the $^1A_1$ state to be the lowest in energy. In addition, the $^1A_1$-$^1\Sigma_g^+$ barrier height has been calculated using UCCSD(T) and IC-MRCI+Q to be 1.33 and 1.28 cm^{-1}, respectively. As such, neither the $^1A_1$ or $^1\Sigma_g^+$ states of $NaHe_2^+$ are able to support a bound vibrational state in the He-M-He bond angle co-ordinate.

Despite these differences in *ab initio* θ_e values for $NaHe_2^+$, good agreement is achieved with respect to R_e. For example, UCCSD(T), IC-MRCI and IC-MRCI+Q values differ by at most 7.7 mÅ. These results agree with the values of Sapse *et al.* [32] and Marinetti *et al.* [33] to within 14.7 and 16 mÅ, respectively. Similarly, the binding energies for reactions (5.6) and (5.7) calculated in this work are also in good agreement with those calculated previously. For example, Sapse *et al.* [32] predicted $D_e(1)$ to be 0.713, 0.846 and 0.801 kJ mol^{-1} larger than UCCSD(T), IC-MRCI and IC-MRCI+Q values, respectively. Better agreement is achieved between the results of this work and the CCSD(T)/cc-pV5Z value of Marinetti *et al.* [33] for this binding energy. For example, the latter value differs from UCCSD(T), IC-MRCI and IC-MRCI+Q data by 0.096, -0.484 and 0.100 kJ mol^{-1}, respectively.

For the ground state of KHe_2^+ the results of this work may only be compared to the CCSD(T)/aug-cc-pV5Z values of Marinetti *et al.* [33]. It is evident from Table 5.6 that UCCSD(T) and IC-MRCI+Q yield R_e values larger than this CCSD(T)/aug-cc-pV5Z value by *ca.* 10 mÅ. This difference for IC-MRCI is *ca.* 30 mÅ. As such, the inclusion of the +Q corrections to the IC-MRCI energy has a marked effect with respect to R_e. This was not observed for the ground states of $LiHe_2^+$ and $NaHe_2^+$. Nevertheless, θ_e values calculated in this work are in good agreement, differing by at most 0.9°. No binding energy for equation (5.6) has been reported in the literature to date. Good agreement is found between the methods

employed in this work with respect to this binding energy. For example, $D_e(1)$ calculated using IC-MRCI differs from the UCCSD(T) value by -0.127 kJ mol^{-1}. The inclusion of the size-extensivity correction decreases this IC-MRCI value by another 0.148 kJ mol^{-1}. A similar agreement is observed for $D_e(2)$ - IC-MRCI and IC-MRCI+Q values are 0.231 and 0.161 kJ mol^{-1} smaller than the UCCSD(T) value. The latter is in good agreement with the CCSD(T)/aug-cc-pV5Z value of Marinetti *et al.* [33], differing by only -0.129 kJ mol^{-1}.

Both single- and multi-reference wave functions employed presently predict the ground electronic state of KHe_2^+ to be of C_{2v} symmetry. Conversely, Marinetti *et al.* [33] predicted a linear minimum energy structure. The $^1A_1$-$^1\Sigma_g^+$ barrier height of the ground state of KHe_2^+ has been calculated to be 5.14 and 5.54 cm^{-1} using UCCSD(T) and IC-MRCI+Q, respectively. There is therefore a distinct resemblance to the $(^1A_1)NaHe_2^+$ PES in the bond angle co-ordinate. The data of this work are therefore consistent with that of Marinetti *et al.* [33] concerning the curvature of the ground state PESs of MHe_2^+ (M = Li, Na, K).

A comparison of the relative energies required for the successive addition of helium atoms to the Li^+, Na^+ and K^+ ions is pertinent to the present discussion. As such, comparison of Δ for the ground states of $LiHe_2^+$, $NaHe_2^+$ and KHe_2^+ is made in Table 5.7. The assumption that the two M-He bonds in each species are identical is therefore implicit in this comparison. It is obvious from Table 5.7 that Δ is sensitive to the *ab initio* method used in its calculation. For instance, for $LiHe_2^+$, Δ(UCCSD(T)) and Δ(IC-MRCI) are 0.242 and -0.239 kJ mol^{-1}, respectively. The quantitative similarity between binding energies for equations (5.6) and (5.7) is also noticeable. Using UCCSD(T), IC-MRCI and IC-MRCI+Q $\bar{\Delta}$ of $LiHe_2^+$, $NaHe_2^+$ and KHe_2^+ are 0.601, 0.432 and 0.111 kJ mol^{-1}, respectively. Two conclusions may be drawn from this data. Firstly, for each species in question the binding energy of

Table 5.7 Binding energies (/kJ mol^{-1}) for successive helium addition of M^+ ions (M = Li, Na, K).

	$LiHe_2^+$			$NaHe_2^+$			KHe_2^+		
Method	$D_e(2)$	$D_e(3)$	Δ^a	$D_e(2)$	$D_e(3)$	Δ^a	$D_e(2)$	$D_e(3)$	Δ^a
UCCSD(T)	7.552	15.347	0.242	3.852	7.797	0.093	2.148	4.270	-0.027
IC-MRCI	7.580	14.921	-0.239	3.719	8.377	0.939	2.021	4.039	-0.002
IC-MRCI+Q	6.890	15.580	1.800	3.764	7.793	0.264	1.873	4.109	0.363

[a] $D_e(1)$ and $D_e(2)$ correspond to dissociative reactions (5.6) and (5.7), respectively. Δ D_e values are defined as $D_e(2) - 2D_e(1)$ and it is assumed both M-He bonds are identical.

the second helium atom is greater than that of the first helium atom. Secondly, the magnitude of this difference is dependent on the polarisability of the M^+ ion. In particular, the strength of the M-He_2 bond compared to the M-He_1 bond decreases with increasing M^+ polarisability.

From this discussion of the structures and stabilities of the MHe_2^+ (M = Li, Na and K), it is evident that these ground state PESs are extremely sensitive to the *ab initio* method employed. That is, the symmetry of the lowest energy state is determined largely by the *ab initio* method and basis set used. This conclusion recapitulates that reached by Marinetti *et al.* [33] in their investigation of these species. It is noted however that the ground state PESs of MHe_2^+ would be amenable to a scattering co-ordinate vibrational analysis. However, good agreement (particularly with respect to R_e, θ_e and $^1A_1$-$^1\Sigma_g^+$ barrier heights) was observed between single- and multi-reference wave functions employed in the present work for each species. It is also inferred from the previous discussion that multi-reference effects appear to have a generally minimal impact on the structures and dissociative energetics of these ground state dihelide ions.

5.6. *Ab Initio* Property Surfaces and Rovibrational Spectrum of $(^1A_1)LiH_2^+$

Page and von Nagy-Felsobuki [23] employed all-electron FCI in conjunction with triple-ζ basis sets to calculate analytical property surfaces and subsequently rovibrational spectra of $(^1A_1)LiH_2^+$, $(^1A')LiHD^+$ and $(^1A_1)LiD_2^+$. The discrete PES and DMS of $(^1A_1)LiH_2^+$, and their respective analytical representations have been presented and discussed in Chapter Three. The $P(5,5)$ OGL PEF was employed in order to compute the 1D vibrational eigenfunctions of each species. The corresponding eigenvalues are included in Appendix E. A total of 1000 finite-elements were employed over integration domains of $[-1.76a_0, 5.0a_0]$ (t_1), $[-0.648a_0, 4.0a_0]$ (t_2) and $[-4.0a_0, 4.0a_0]$ (t_3) for the numerical solution of each nuclear Schrödinger equation. All 1D eigenvectors included in the configurational basis set decayed appropriately in the classical forbidden region of the potential.

Low-lying vibrational states of $(^1A_1)LiH_2^+$, $(^1A')LiHD^+$ and $(^1A_1)LiD_2^+$ are detailed in Table 5.8 in terms of the VBOs, assignments and vibration-averaged structures. In the case of $(^1A_1)LiH_2^+$, each of the lowest 10 vibrational states could be assigned unequivocally using the configuration weight scheme detailed in Chapter Four. It is therefore concluded that a more definitive description of the character of the vibrational wave function is realised using the configuration weight scheme rather than using the configuration density description employed by Page and von Nagy-Felsobuki [23]. For example, Page and von Nagy-Felsobuki reported that the a_1 vibrational states with VBOs at 1550.9 and 2124.8 cm^{-1} were primarily composed of $[0.26 \times |200\rangle + 0.15 \times |100\rangle]$ and $[0.28 \times |300\rangle + 0.09 \times |400\rangle + 0.09\,|600\rangle]$ configurations, respectively, using the configuration densities assignment scheme introduced in Chapter Four. As anticipated from the 1D vibrational calculations of $(^1A_1)LiH_2^+$, low-lying bound vibrational states are composed mainly from linear combinations of 1D eigenfunctions in the t_1 and t_3 excited normal modes.

Table 5.8 Structural properties of low-lying vibrational states of $(^1A_1)LiH_2^+$, $(^1A')LiHD^+$ and $(^1A_1)LiD_2^+$.

i	VBO ($/cm^{-1}$)	Assign $\|t_1t_2t_3\rangle$	Sym.	Weight[a]	$R_{Li\text{-}H}$ ($/Å$)	$R_{Li\text{-}D}$ ($/Å$)	$\langle\theta\rangle$ ($/^\circ$)
			$(^1A_1)LiH_2^+$				
0	0.0	$\|000\rangle$	a_1	0.89	2.089		23.4
1	487.9	$\|100\rangle$	a_1	0.72	2.053		24.0
2	738.8	$\|001\rangle$	b_2	0.82	2.093		24.6
3	1003.7	$\|200\rangle$	a_1	0.54	1.956		24.5
4	1305.9	$\|101\rangle$	b_2	0.70	2.063		24.9
5	1550.9	$\|200\rangle$	a_1	0.51	2.200		24.6
6	1586.1	$\|002\rangle$	a_1	0.69	2.090		25.1
7	1891.3	$\|201\rangle$	b_2	0.58	1.925		25.4
8	2124.8	$\|300\rangle$	a_1	0.52	2.122		25.0
9	2234.0	$\|102\rangle$	a_1	0.65	2.098		25.4
			$(^1A')LiHD^+$				
0	0.0	$\|000\rangle$	a'	0.89	2.100	2.097	20.6
1	390.9	$\|100\rangle$	a'	0.68	2.147	2.156	20.1
2	640.9	$\|001\rangle$	a''	0.76	2.116	2.113	19.4
3	805.1	$\|200\rangle$,$\|100\rangle$	a'	0.47,0.29	2.179	2.180	19.9
4	1067.1	$\|101\rangle$	a''	0.58	2.141	2.138	19.2
5	1248.3	$\|200\rangle$	a'	0.54	2.203	2.195	19.9
6	1367.2	$\|002\rangle$	a'	0.63	2.093	2.125	18.9
7	1532.3	$\|201\rangle$,$\|101\rangle$	a''	0.43,0.28	2.163	2.151	19.2
8	1714.1	$\|300\rangle$	a'	0.53	2.224	2.211	19.8
9	1837.1	$\|102\rangle$,$\|112\rangle$	a'	0.47,0.24	2.115	2.131	18.9
			$(^1A_1)LiD_2^+$				
0	0.0	$\|000\rangle$	a_1	0.89		2.094	20.6
1	357.6	$\|100\rangle$	a_1	0.68		2.158	20.1
2	486.4	$\|001\rangle$	b_2	0.79		2.113	19.4
3	722.0	$\|100\rangle$	a_1	0.51		2.194	19.8
4	880.3	$\|101\rangle$	b_2	0.61		2.152	19.3
5	1007.7	$\|002\rangle$	a_1	0.67		2.105	18.8
6	1108.0	$\|200\rangle$	a_1	0.57		2.213	19.7
7	1285.3	$\|101\rangle$	b_2	0.51		2.177	19.2
8	1455.6	$\|102\rangle$	a_1	0.57		2.139	18.8
9	1515.8	$\|300\rangle$	a_1	0.54		2.227	19.7

[a] See text.
[b] $(^1A_1)LiH_2^+$ ZPE = 2679.4 cm^{-1}.
[c] $(^1A')LiHD^+$ ZPE = 2324.8 cm^{-1}.
[d] $(^1A_1)LiD_2^+$ ZPE = 1918.0 cm^{-1}.

Use of the configuration weight scheme generally yields a more definitive description of the low-lying vibrational states of $(^1A')LiHD^+$ and $(^1A_1)LiD_2^+$. In particular, each of the vibrational states of $(^1A_1)LiD_2^+$ listed in Table 5.8 are attributed to a single dominant configuration term. In contrast, Page and von Nagy-Felsobuki [23] reported that the vibrational states of $(^1A_1)LiD_2^+$ with VBOs at 357.6, 880.3, 1107.7, 1285.3 and 1455.6 cm^{-1} were composed primarily from two configurations. These workers also reported that the states of $(^1A_1)LiD_2^+$ with VBOs at 722.0 and 1515.8 and 1591.3 cm^{-1} were further delocalised, the major terms in these configurations being $[0.26 \times |100\rangle + 0.20 \times |200\rangle + 0.03 \times |400\rangle]$ and $[0.30 \times |300\rangle + 0.09 \times |400\rangle + 0.09 \times |510\rangle]$, respectively. Nevertheless, for $(^1A')LiHD^+$ the states with VBOs at 805.1, 1532.3 and 1837.1 cm^{-1} necessitated the use of two configuration terms for a satisfactory description of the wave function to be obtained.

Using the multi-reference PES of Martinazzo *et al.* [5], Bieske and co-workers [37] recently calculated the intermolecular stretch and bend frequencies of $(^1A_1)LiD_2^+$ to be 365 and 503 cm^{-1}, respectively. The corresponding values calculated in the present work are comparable with these values, differing by *ca.* -7 and -17 cm^{-1}, respectively. For comparison, these same frequencies calculated by Bulychev *et al.* [22] were 329.8 and 447.2 cm^{-1}. Comparison of the lowest excited vibrational energies of $(^1A_1)LiH_2^+$ calculated here with those calculated by Bulychev *et al.* [22] shows a similar trend. For instance, the energy of the lowest excited a_1 vibrational state of $(^1A_1)LiH_2^+$ calculated in this work is *ca.* 88 cm^{-1} higher, whilst the energy of the lowest excited b_2 state calculated here is *ca.* 150 cm^{-1} higher. For the ground state of $(^1A_1)LiD_2^+$, the vibration-averaged D-D bond length was calculated to be 0.775 Å. This value is in good agreement with the D-D bond length calculated on the MRCI PES of Martinazzo *et al.* [5], the latter being 0.751 Å.

The vibration-averaged H-H bond length in the LiH_2^+ vibrational ground state is 0.847 Å, and so is slightly larger than that for LiD_2^+. Emmeluth *et al.* [36] reported an experimental $R_{\text{H-H}}$ value of 0.90 Å using the assumption of zero inertial defect. This experimental value is substantially larger than both the value of this work and the accepted $R_{\text{H-H}}$ for the free H_2 molecule, and has been attributed to the influence of the large amplitude bending/hindered rotations of the molecule on the effective molecular B and C constants. The vibration-averaged bond angle of the $(^1A_1)LiH_2^+$ ground state is 1.9° larger than the FCI optimised value [23]. This is ascribed to the presence of the a_1 bend mode of vibration in the overall vibrational configuration interaction. Isotopic substitution in the H-H molecular subunit had only a minor effect with respect to vibration-averaged equilibrium structures.

It is to be expected that elements of $\mathbf{F}$ would be small using an Eckart-Watson Hamiltonian. This is generally the case for the three isotopomers considered in this work. For instance, the Coriolis matrix elements are generally of the order of $10^{-11}-10^{-17}$, $10^{-14}-10^{-16}$, and $10^{-11}-10^{-17}$ cm^{-1} for $(^1A_1)LiH_2^+$, $(^1A')LiHD^+$ and $(^1A_1)LiD_2^+$, respectively. Also, the diagonal elements of $\mathbf{F}$ are at least one order of magnitude smaller relative to those off the diagonal in all cases. The values of the ground state rotational constants for $(^1A_1)LiH_2^+$, $(^1A')LiHD^+$ and $(^1A_1)LiD_2^+$ are also as expected for a near-prolate top (*i.e.* $\langle A\rangle_{ii} >> \langle B\rangle_{ii} \approx \langle C\rangle_{ii}$). These values manifest themselves in the asymmetry parameter (κ) values of $(^1A_1)LiH_2^+$, $(^1A')LiHD^+$ and $(^1A_1)LiD_2^+$, which are -0.996, -0.987 and -0.994, respectively. The rotational constants $\langle A\rangle_{11}$, $\langle B\rangle_{11}$ and $\langle C\rangle_{11}$ of $(^1A_1)LiD_2^+$ calculated in the present work also compare favourably with those corresponding to the equilibrium structure of Martinazzo *et al.* [5], differing by 1.4, -0.2 and -0.2 cm^{-1}, respectively.

Bieske and co-workers *et al.* [36, 37] have observed several rovibrational transition frequencies of $(^1A_1)LiH_2^+$ and $(^1A_1)LiD_2^+$ in the H-H/D-D stretch bands. Com-

parison between these data and results of this work is therefore possible. Table 5.9 gives comparisons between experimental and theoretical transition frequencies of $(^1A_1)LiH_2^+$ for the $K = 0, 1, 2$ and 3 manifolds for $J \leq 5$. More extensive listings ($J \leq 10$) for $(^1A_1)LiH_2^+$ and comparisons for $(^1A_1)LiD_2^+$ ($K = 0, 1, 2$ and $J \leq 10$) are provided in Appendix E. It is observed that for $(^1A_1)LiH_2^+$, the FCI PEF of this work yields rovibrational transition frequencies which are in good agreement with experiment. For $(^1A_1)LiH_2^+$ the maximum discrepancy between experiment and theoretical values is *ca.* 10, 10, 8 and 7 cm^{-1} for $K = 0, 1, 2$ and 3, respectively. A similar level of accuracy is attained for $(^1A_1)LiD_2^+$, with the largest differences for the $K = 0$ and 1 manifolds being *ca.* 5 cm^{-1}. For $K = 2$ the largest discrepancy is *ca.* 7 cm^{-1}. The FCI PEF therefore yields transition frequencies accurate to within *ca.* 0.1-0.2% of experimental values. It is also possible to directly compare the performance of the FCI PEF *via* the rovibrational level spacings. All rovibrational levels in the D-D stretching band of $(^1A_1)LiD_2^+$ for $K = 0, 1, 2$ and $J \leq 10$ are in excellent agreement with experimental data. To summarise this comparison, the largest differences in the $K = 0$ manifold for the R and P branches are 0.7 and 0.5 cm^{-1}, respectively. The largest differences here arise from the highest J values considered *viz.* the $\Delta\left(9_{0,9} \leftarrow 8_{0,8}, 10_{0,10} \leftarrow 9_{0,9}\right)$ and $\Delta\left(8_{0,8} \leftarrow 9_{0,9}, 9_{0,9} \leftarrow 10_{0,10}\right)$ spacings. Similar differences are observed in the comparison of the level spacings for $K = 1$. For the $K = 1$ R, P and Q branches, the largest deviations in rovibrational level spacings from experiment are 0.7, 0.5 and 0.2 cm^{-1}, respectively. Within the $K = 2$ manifold, the largest difference in the R branch level spacings is 1.0 cm^{-1}, while for the P branch the largest difference is 0.6 cm^{-1}.

The vibrational band origins, square dipole matrix elements, Einstein A and B coefficients, band strengths and radiative lifetimes of the LiH_2^+, $LiHD^+$ and LiD_2^+ electronic ground states are presented in Table 5.10. Rovibrational transition

Table 5.9 Comparison of experimental and *ab initio* rovibrational transition frequencies (/cm^{-1}) of LiH_2^{+}[a] for the $K = 0$, 1, 2 and 3 manifolds.

Trans.			Exp.	Theor.	Δ	Trans.			Exp.	Theor.	Δ	Trans.			Exp.	Theor.	Δ
									$K = 0$								
R Branch						P Branch						Q Branch					
$1_{0,1}$	←	$0_{0,0}$	4058.3	4064.0	5.6	$0_{0,0}$	←	$1_{0,1}$		4053.9							
$2_{0,2}$	←	$1_{0,1}$	4063.3	4069.1	5.8	$1_{0,1}$	←	$2_{0,2}$	4043.4	4048.9	5.5						
$3_{0,3}$	←	$2_{0,2}$	4068.1	4074.3	6.1	$2_{0,2}$	←	$3_{0,3}$	4038.4	4043.9	5.6						
$4_{0,4}$	←	$3_{0,3}$	4073.0	4079.4	6.5	$3_{0,3}$	←	$4_{0,4}$	4033.3	4039.1	5.7						
$5_{0,5}$	←	$4_{0,4}$	4077.8	4084.7	6.9	$4_{0,4}$	←	$5_{0,5}$	4028.3	4034.3	6.0						
									$K = 1$								
$2_{1,2}$	←	$1_{1,1}$	4059.1	4064.5	5.5	$1_{1,0}$	←	$2_{1,1}$	4039.2	4044.4	5.1	$1_{1,1}$	←	$1_{1,0}$	4049.2	4054.4	5.2
$2_{1,1}$	←	$1_{1,0}$	4059.4	4064.8	5.4	$1_{1,1}$	←	$2_{1,2}$	4039.5	4044.6	5.1	$1_{1,0}$	←	$1_{1,1}$	4049.5	4054.7	5.2
$3_{1,3}$	←	$2_{1,2}$	4063.9	4069.6	5.8	$2_{1,1}$	←	$3_{1,2}$	4034.2	4039.4	5.2	$2_{1,2}$	←	$2_{1,1}$	4048.8	4054.2	5.4
$3_{1,2}$	←	$2_{1,1}$	4064.3	4070.0	5.7	$2_{1,2}$	←	$3_{1,3}$	4034.6	4039.8	5.2	$2_{1,1}$	←	$2_{1,2}$	4049.8	4055.1	5.3
$4_{1,4}$	←	$3_{1,3}$	4068.6	4074.8	6.1	$3_{1,2}$	←	$4_{1,3}$	4029.1	4034.5	5.4	$3_{1,3}$	←	$3_{1,2}$	4048.3	4054.0	5.6
$4_{1,3}$	←	$3_{1,2}$	4069.3	4075.3	6.1	$3_{1,3}$	←	$4_{1,4}$	4029.7	4035.0	5.3	$3_{1,2}$	←	$3_{1,3}$	4050.1	4055.6	5.5
$5_{1,5}$	←	$4_{1,4}$	4073.4	4079.9	6.6	$4_{1,3}$	←	$5_{1,4}$	4024.0	4029.6	5.6	$4_{1,3}$	←	$4_{1,4}$	4047.6	4056.4	8.8
$5_{1,4}$	←	$4_{1,3}$	4074.1	4080.6	6.5	$4_{1,4}$	←	$5_{1,5}$	4024.8	4030.3	5.6						
									$K = 2$								
$3_{2,2}$	←	$2_{2,1}$	4052.8	4057.9	5.2	$2_{2,0}$	←	$3_{2,1}$	4023.2	4027.8	4.6						
$3_{2,1}$	←	$2_{2,0}$	4052.8	4057.9	5.2	$2_{2,1}$	←	$3_{2,2}$	4023.2	4027.8	4.6						
$4_{2,3}$	←	$3_{2,1}$	4057.6	4063.2	5.6	$3_{2,1}$	←	$4_{2,2}$	4018.3	4023.1	4.8						
$4_{2,2}$	←	$3_{2,2}$	4057.6	4063.2	5.6	$3_{2,2}$	←	$4_{2,3}$	4018.3	4023.1	4.8						
$5_{2,4}$	←	$4_{2,3}$	4062.4	4068.5	6.1	$4_{2,2}$	←	$5_{2,3}$	4013.3	4018.5	5.1						
$5_{2,3}$	←	$4_{2,2}$	4062.4	4068.5	6.1	$4_{2,3}$	←	$5_{2,4}$	4013.3	4018.5	5.1						
									$K = 3$								
$4_{3,2}$	←	$3_{3,1}$	4039.7	4048.9	9.2												
$4_{3,1}$	←	$3_{3,0}$	4039.7	4048.9	9.2												
$5_{3,3}$	←	$4_{3,2}$	4044.4	4054.8	10.4												
$5_{3,2}$	←	$4_{3,1}$	4044.4	4054.8	10.4												

[a]Experimental data from reference [36]. All transitions given in terms of $J_{K_aK_c}$.

Table 5.10 Radiative properties of low-lying vibrational states of $(^1A_1)LiH_2^+$, $(^1A')LiHD^+$ and $(^1A_1)LiD_2^+$.

i	VBO ($/cm^{-1}$)	μ^2 ($/au^2$)	A_{0i} ($/s^{-1}$)	B_{0i} ($/10^{-16}$ cm^3 erg^{-1} s^2)	S_{0i} ($/cm molecule^{-1})	τ ($/s$)
				$(^1A_1)LiH_2^+$		
1	487.9	2.34+01	8.54+02	4.42+03	3.87−15	6.42−04
2	738.8	3.59+01	4.54+03	6.76+03	9.61−15	1.91−04
3	1003.7	2.33+00	7.39+02	4.39+02	8.66−16	2.00−04
4	1305.9	1.73+01	1.21+04	3.25+03	8.39−15	3.55−05
5	1550.9	3.49−01	4.09+02	6.58+01	2.02−16	7.70−05
6	1586.1	2.73+00	3.42+03	5.14+02	1.61−15	4.40−05
7	1891.3	1.30+00	2.75+03	2.45+02	9.15−16	1.37−05
8	2124.8	4.54−02	1.37+02	8.56+00	3.60−17	3.66−05
9	2234.0	8.59−01	3.00+03	1.62+02	7.15−16	1.11−05
				$(^1A')LiHD^+$		
1	390.9	1.88+01	3.52+02	3.54+03	2.15−15	1.02−03
2	640.9	3.15+01	2.61+03	5.94+03	6.66−15	3.03−04
3	805.1	3.80+00	6.22+02	7.15+02	1.03−15	3.18−04
4	1067.1	7.89+00	3.01+03	1.49+03	2.89−15	9.39−05
5	1248.3	4.10−01	2.50+02	7.72+01	1.76−16	1.25−04
6	1367.2	6.77+00	5.42+03	1.27+03	3.18−15	5.21−05
7	1532.3	5.78−01	6.52+02	1.09+02	3.05−16	3.61−05
8	1714.1	4.20−02	6.63+01	7.91+00	2.48−17	6.11−05
9	1837.1	3.34−01	6.50+02	6.29+01	2.12−16	2.44−05
				$(^1A_1)LiD_2^+$		
1	357.6	1.76+01	2.532+02	3.32+03	1.65−15	1.17−03
2	486.4	2.41+01	8.686+02	4.53+03	3.36−15	6.75−04
3	722.0	1.36+00	1.608+02	2.57+02	3.03−16	4.63−04
4	880.3	1.07+01	2.295+03	2.02+03	2.95−15	1.45−04
5	1007.7	1.90+00	6.102+02	3.58+02	6.03−16	1.82−04
6	1108.0	1.29−03	5.489−01	2.42−01	4.50−19	2.19−04
7	1285.3	4.60−01	3.060+02	8.66+01	1.87−16	5.97−05
8	1455.6	3.70−01	3.581+02	6.97+01	1.71−16	4.72−05
9	1515.8	2.25−04	2.457−01	4.24−02	1.08−19	1.13−04

frequencies, spectral line intensities and their respective assignments of the LiH_2^+, $LiHD^+$ and LiD_2^+ electronic ground states were calculated for $v \leq 4$ and $J \leq 4$ and $T = 296$ K. It should be noted that the J selection rules can be disregarded here, since values of R_{ab}^2 have been calculated exactly (that is, using the 'full rovibrational wave function and the spatially transformed DMF). These rovibrational transitions and line strengths are shown in Figure 5.2, using a line intensity threshold of 1.0×10^{-30} cm molecule^{-1}. For $(^1A_1)LiH_2^+$, $(^1A')LiHD^+$ and $(^1A_1)LiD_2^+$ 305,

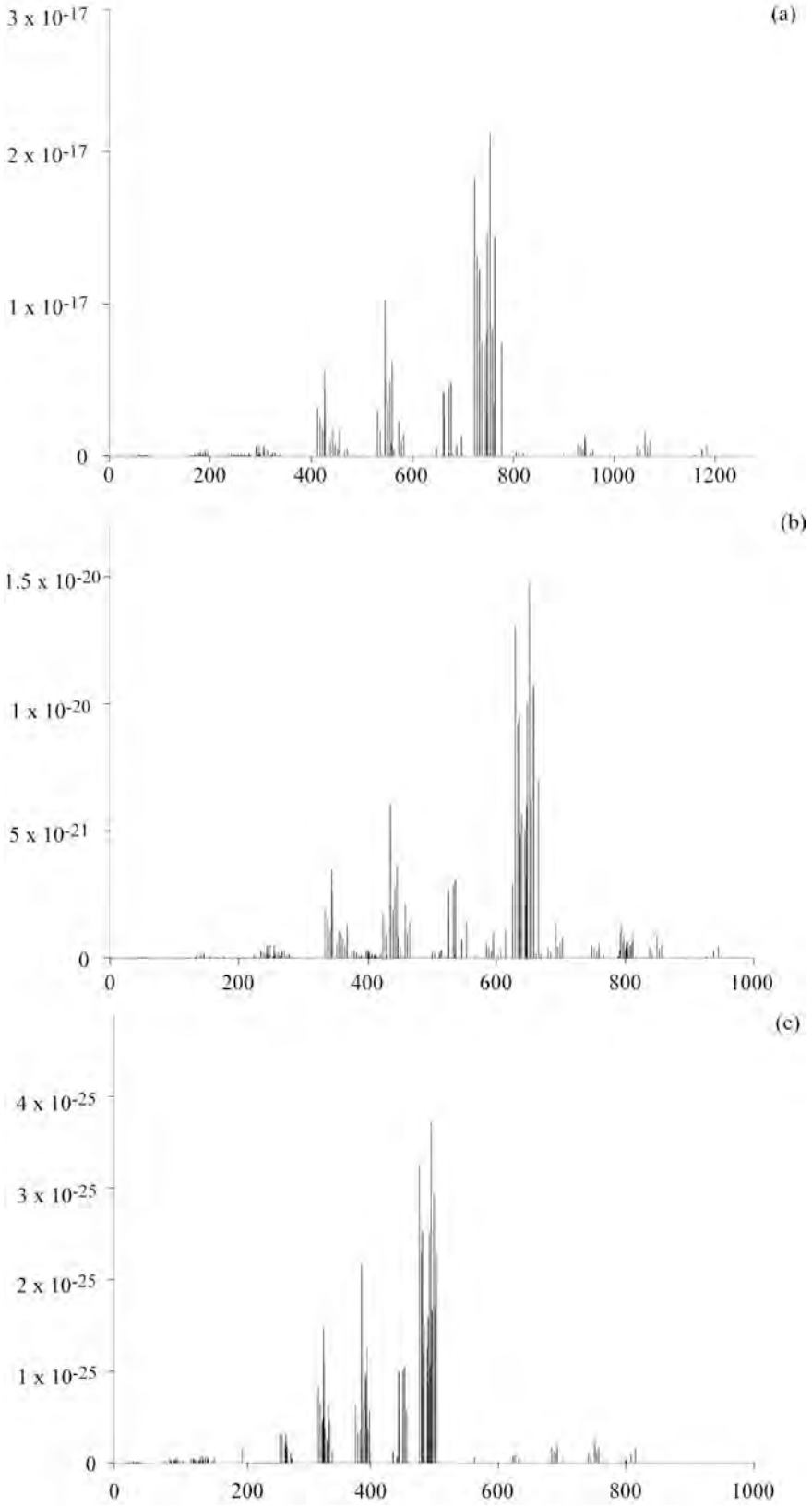

Figure 5.2 *Ab initio* rovibrational spectra for $v \leq 4$, $J \leq 4$ and $S_{ab} \geq 1.0 \times 10^{-30}$ at 296 K: (a) $(^1A_1)LiH_2^+$, 305 lines; (b) $(^1A')LiHD^+$, 514 lines, and; (c) $(^1A_1)LiD_2^+$, 233 lines. Transition frequencies and intensities given in cm^{-1} and cm $molecule^{-1}$, respectively.

514 and 233 transitions are shown, respectively. It is evident that $(^1A_1)LiH_2^+$ possessed the most intense rovibrational transitions, the most intense of which has been assigned to the $2_{0,2} \leftarrow 3_{0,3}$ transition of the $|001\rangle$ band ($v = 754.1$ cm^{-1}, $S_{ab} = 2.12 \times 10^{-17}$ cm molecule^{-1}). The $LiHD^+$ and LiD_2^+ ground states also exhibit their most intense bands for the $2_{0,2} \leftarrow 3_{0,3}$ rotational transition in the $|001\rangle$ band. These transitions occur at 651.8 and 495.4 cm^{-1}, with spectral line intensities of 1.47×10^{-20} and 3.72×10^{-23} cm molecule^{-1}, respectively. The most prominent rovibrational transitions for $(^1A_1)LiH_2^+$, $(^1A')LiHD^+$ and $(^1A_1)LiD_2^+$ are listed more extensively in Appendix E.

5.7. *Ab Initio* Property Surfaces and Rovibrational Spectrum of $(^1A_1)NaH_2^+$

Page and von Nagy-Felsobuki [34] have employed the CCSD(T) method developed in this work in the construction of *ab initio* rovibrational spectra of $(^1A_1)NaH_2^+$, $(^1A')NaHD^+$ and $(^1A_1)NaD_2^+$. These spectra were calculated using discrete PES and DMS grids consisting of 118 and 90 CCSD(T) points, respectively. The discrete PES was represented analytically *via* a $P(6,6)$ Padé expansion of the OGL variable with $\sigma_{85-88,91-99} = 0$ using SVD. The μ_y and μ_x component DMSs were fitted using 7$^{\text{th}}$ order internal displacement co-ordinate power series expansions. Each analytical function was constructed using methods described in Chapter Three. The discrete property surfaces are given in Appendix E, as are the respective analytical representations (FORTRAN format). Two-dimensional contour projections of the $(^1A_1)NaH_2^+$ PEF and DMF are also given in Appendix E.

The 1D vibrational eigenfunctions of $(^1A_1)NaH_2^+$, $(^1A')NaHD^+$ and $(^1A_1)NaD_2^+$ were calculated using a FEM grid consisting of 1000 elements over the t_1, t_2 and t_3 mode domains. These domains were $[-3.0a_0, 4.5a_0]$, $[-0.75a_0, 5.0a_0]$ and $[-2.5a_0, 2.5a_0]$, respectively. It was therefore ensured that all 1D basis func-

tions decayed appropriately in the classically forbidden regions of the PES. Moreover, it was ensured that all corresponding eigenvalues were converged to within the residual error of the PES. One-dimensional vibrational eigenvalues of $(^1A_1)NaH_2^+$, $(^1A')NaHD^+$ and $(^1A_1)NaD_2^+$ are listed in Appendix E.

The low-lying VBOs of $(^1A_1)NaH_2^+$ are detailed in Table 5.11, as are the respective assignments and vibration-averaged structures. Each state listed in this table has been assigned using a single dominant configuration, excepting the state with VBO at 1096.9 cm^{-1}. The latter vibrational state is predominantly composed of the $|200\rangle$ and $|300\rangle$ configurations. For the fundamental $|100\rangle$ and $|001\rangle$ modes, configuration mixing in the vibrational wave function is limited. For example, the weights of the $|100\rangle$ and $|001\rangle$ terms in these states are 0.71 and 0.82, respectively. Similarly, the $|010\rangle$ term in the a_2 bend fundamental (with VBO at 4114.2 cm^{-1}) exhibited a configuration weight of 0.77. There is more configuration mixing in the low-lying overtone bands (as expected). For instance, the a_1 with VBOs at 705.8 and 1508.8 cm^{-1} correspond to the $|200\rangle$ and $|300\rangle$ bands, respectively. These states are more delocalised, with the predominant terms having configuration weights of 0.52 and 0.56, respectively.

The effects of vibration-averaging on the equilibrium Na-H bond length is quite noticeable in the vibrational ground state of $(^1A_1)NaH_2^+$. Comparison of data from Tables 5.2 and 5.11 indicate that $\langle R\rangle$ is *ca.* 0.1 Å larger than R_e, which corresponds to the PES minimum. The change in H-Na-H bond angle is more tempered, with $\langle\theta\rangle$ being 0.7° smaller than θ_e. For the a_1 breathe and b_2 asymmetric stretch fundamental modes, $\langle R\rangle$ values are 2.563 and 2.477 Å, thus deviating from the ground state values by 0.063 and -0.023 Å, respectively. Contractions in $\langle\theta\rangle$ of 0.3 and 1.0° are also observed for the $|100\rangle$, $|001\rangle$ states, respectively. This illustrates the effects of configuration interaction in the vibrational wave function on observable quanti-

Table 5.11 Structural properties of low-lying vibrational states of $(^1A_1)NaH_2^+$, $(^1A')NaHD^+$ and $(^1A_1)NaD_2^+$.

i	VBO ($/cm^{-1}$)	Assign $\|t_1t_2t_3\rangle$	Sym.	Weight[a]	$R_{\text{Na-H}}$ ($/Å$)	$R_{\text{Na-D}}$ ($/Å$)	$\langle\theta\rangle$ ($/^\circ$)
			$(^1A_1)NaH_2^+$				
0	0.0[b]	$\|000\rangle$	a_1	0.88	2.500		17.1
1	341.0	$\|100\rangle$	a_1	0.71	2.563		16.8
2	646.0	$\|001\rangle$	b_2	0.82	2.477		16.1
3	705.8	$\|200\rangle$	a_1	0.52	2.591		16.7
4	1057.8	$\|101\rangle$	b_2	0.73	2.523		16.0
5	1096.9	$\|200\rangle$, $\|300\rangle$	a_1	0.56,0.36	2.611		16.7
6	1428.9	$\|002\rangle$	a_1	0.72	2.433		15.9
7	1484.3	$\|201\rangle$	b_2	0.63	2.554		16.0
8	1508.9	$\|300\rangle$	a_1	0.56	2.631		16.7
9	1905.8	$\|102\rangle$	a_1	0.68	2.484		15.8
			$(^1A')NaHD^+$				
0	0.0[c]	$\|000\rangle$	a'	0.87	2.499	2.499	17.0
1	264.7	$\|100\rangle$	a'	0.67	2.558	2.560	16.7
2	530.2	$\|001\rangle$	a''	0.59	2.527	2.552	16.3
3	558.2	$\|200\rangle$, $\|400\rangle$	a'	0.31, 0.24	2.552	2.534	16.4
4	827.3	$\|101\rangle$, $\|301\rangle$	a''	0.46, 0.18	2.562	2.585	16.3
5	871.9	$\|101\rangle$, $\|001\rangle$	a''	0.44, 0.20	2.578	2.545	16.3
6	1134.3	$\|201\rangle$, $\|101\rangle$	a''	0.39, 0.17	2.553	2.583	16.1
7	1178.2	$\|002\rangle$, $\|600\rangle$	a'	0.44, 0.20	2.556	2.555	16.1
8	1223.7	$\|002\rangle$, $\|012\rangle$	a'	0.42, 0.22	2.522	2.509	16.0
9	1461.7	$\|301\rangle$, $\|501\rangle$	a''	0.30, 0.24	2.575	2.600	16.1
			$(^1A_1)NaD_2^+$				
0	0.0[d]	$\|000\rangle$	a_1	0.87		2.498	17.0
1	229.5	$\|100\rangle$	a_1	0.64		2.568	16.6
2	405.2	$\|001\rangle$	b_2	0.77		2.500	16.0
3	464.6	$\|100\rangle$, $\|200\rangle$	a_1	0.54,0.38		2.606	16.5
4	669.8	$\|101\rangle$	b_2	0.61		2.545	15.9
5	715.0	$\|200\rangle$	a_1	0.60		2.625	16.4
6	869.5	$\|002\rangle$	a_1	0.65		2.472	15.6
7	942.2	$\|101\rangle$, $\|201\rangle$	b_2	0.48,0.44		2.574	15.9
8	980.9	$\|300\rangle$	a_1	0.55		2.639	16.4
9	1176.4	$\|102\rangle$	a_1	0.58		2.511	15.6

[a] See text.
[b] $(^1A_1)NaH_2^+$ ZPE = 2561.4 cm^{-1}.
[c] $(^1A')NaHD^+$ ZPE = 2213.7 cm^{-1}.
[d] $(^1A_1)NaD_2^+$ ZPE = 1814.2 cm^{-1}.

ties. These data cumulatively suggest that the analytical $(^1A_1)NaH_2^+$ PES exhibits a relatively small curvature in the immediate neighbourhood of the PES minimum. Comparison of the fundamental frequencies in Table 5.11 with harmonic values also supports conclusion. For example, the $|100\rangle$, $|001\rangle$ and $|010\rangle$ VBOs differ from the CCSD(T) ω_1, ω_2 and ω_3 values by -9.3, -202.8 and 77.6 cm^{-1}, respectively. The exaggerated difference in the fundamental a_1 bend mode is typical of MH_2^{n+} species [23, 40, 41] and illustrates the high anharmonicity present in the a_1 breathe 1D PES co-ordinate.

Extensive configuration mixing is observed for the low-lying vibrational states of $(^1A')NaHD^+$, which are presented in Table 5.11. For example, only the ground state and the $|100\rangle$ and $|001\rangle$ fundamental modes have been assigned using a single dominant term. The weights of the primary configurations in the latter two states are 0.67 and 0.59, respectively, suggesting that a greater degree of delocalisation is present in the vibrational wave function of $(^1A')NaHD^+$ than those of $(^1A_1)NaH_2^+$ and $(^1A_1)NaD_2^+$. The characters of all other vibrational states listed in Table 5.11 are more multi-configurational in nature, and have been described using two dominant configurations. Vibration-averaged structures of $(^1A')NaHD^+$ are also indicative of a flat PES in the region of the minimum. For example, $\langle R\rangle$(Na-H) and $\langle R\rangle$(Na-D) are identical for the ground vibrational state. For comparison, the same differences for $(^1A')LiHD^+$ and $(^1A')MgHD^+$ have been calculated to be 0.004 and 0.0783 Å [23, 47].

Each of the lowest 10 states of $(^1A_1)NaD_2^+$ has been assigned using a single dominant configuration, except for the a_1 and b_2 states corresponding to the VBOs at 464.58 and 942.24 cm^{-1}, respectively. The latter vibrational states were found to be composed primarily from $[0.54 \times |100\rangle + 0.38 \times |200\rangle]$ and $[0.48 \times |101\rangle + 0.44 \times |201\rangle]$ terms, respectively. As for $(^1A_1)NaH_2^+$, the fundamen-

tal vibrational states of $(^1A_1)NaD_2^+$ have been assigned most definitively. For example, the fundamental a_1 breathe and b_2 asymmetric stretch modes include $|100\rangle$ and $|001\rangle$ configuration weights of 0.67 and 0.59, respectively. These vibrational states are therefore more delocalised than the analogous states for $(^1A_1)NaH_2^+$. The vibrational overtone bands for $(^1A_1)NaD_2^+$ also possess more multi-configurational character than the fundamental states. For example, the $|002\rangle$ term exhibits a configuration weight of 0.65 in the lowest b_2 asymmetric stretch overtone (VBO = 869.5 cm^{-1}). Similarly, the second overtone in the a_1 breathe mode includes the $|300\rangle$ term with a configuration weight of 0.55. For the ground vibrational state of $(^1A_1)NaD_2^+$, isotopic substitution results in a contraction of 0.0014 Å in the $\langle R\rangle$(Na-D) value, compared to $(^1A')NaHD^+$, as expected. The effect of this isotopic substitution is negligible with respect to $\langle\theta\rangle$.

All rovibrational states of $(^1A_1)NaH_2^+$, $(^1A')NaHD^+$ and $(^1A_1)NaD_2^+$ for $v \leq 10$, $J \leq 5$ have been calculated in this work. These states are included in Appendix E. Rotational constant, centrifugal distortion and Coriolis coupling matrix elements spanned by the lowest ten vibrational states of each species have also been evaluated. The κ asymmetry parameters for the ground vibrational states of $(^1A_1)NaH_2^+$, $(^1A')NaHD^+$ and $(^1A_1)NaD_2^+$ have been calculated to be -0.952, -0.950 and -0.947, respectively. As such, each species is a near-prolate top. All rovibrational states have been assigned using the $J_{K_aK_c}$ assignment scheme.

Vibrational radiative properties, including vibration transition moments, Einstein A and B coefficients, vibration band strengths and radiative lifetimes have been calculated for the low-lying vibrational states of $(^1A_1)NaH_2^+$, $(^1A')NaHD^+$ and $(^1A_1)NaD_2^+$. These data are given in Table 5.12. It is evident from this table that the $|001\rangle$ states of $(^1A_1)NaH_2^+$, $(^1A')NaHD^+$ and $(^1A_1)NaD_2^+$ are of the greatest intensity, exhibiting S values of 6.24×10^{-12}, 2.75×10^{-12} and 1.34×10^{-12} cm molecule^{-1},

Table 5.12 Radiative properties of low-lying vibrational states of $(^1A_1)NaH_2^+$, $(^1A')NaHD^+$ and $(^1A_1)NaD_2^+$.

i	VBO ($/cm^{-1}$)	μ^2 ($/au^2$)	A_{0i} ($/s^{-1}$)	B_{0i} ($/10^{-16}$ cm^3 erg^{-1} s^2)	S_{0i} ($/cm molecule^{-1}$)	τ ($/s$)
				$(^1A_1)NaH_2^+$		
1	341.0	3.38+04	4.20+05	6.36+06	3.07−12	6.13−07
2	646.0	3.06+04	2.59+06	5.76+06	6.24−12	3.29−07
3	705.8	1.26+04	1.39+06	2.38+06	2.84−12	1.56−07
4	1057.8	1.41+04	5.22+06	2.65+06	4.88−12	5.54−08
5	1096.9	6.96+02	2.88+05	1.31+05	2.50−13	5.64−08
6	1428.9	9.35+02	8.55+05	1.76+05	4.40−13	1.86−07
7	1484.3	8.95+03	9.18+06	1.69+06	4.38−12	1.52−08
8	1508.9	7.15+00	7.71+03	1.35+03	3.56−15	2.64−08
9	1905.8	2.04+03	4.43+06	3.84+05	1.28−12	1.75−08
				$(^1A')NaHD^+$		
1	264.7	2.71+04	1.58+05	5.11+06	1.50−12	8.87−07
2	530.2	1.95+04	9.11+05	3.67+06	2.75−12	3.67−07
3	558.2	1.53+04	8.33+05	2.88+06	2.30−12	3.81−07
4	827.3	3.20+03	5.69+05	6.03+05	7.50−13	1.24−07
5	871.9	6.46+03	1.34+06	1.22+06	1.60−12	1.13−07
6	1134.3	4.37+03	2.00+06	8.23+05	1.42−12	5.13−08
7	1178.2	3.38+03	1.73+06	6.36+05	1.14−12	5.96−08
8	1223.7	1.09+03	6.25+05	2.05+05	3.83−13	6.49−08
9	1461.7	1.29+03	1.27+06	2.44+05	5.45−13	2.32−08
				$(^1A_1)NaD_2^+$		
1	229.5	2.68+04	1.02+05	5.05+06	1.04−12	1.05−06
2	405.2	1.53+04	3.18+05	2.87+06	1.34−12	1.42−06
3	464.6	9.02+03	2.84+05	1.70+06	9.44−13	3.80−07
4	669.8	8.17+03	7.70+05	1.54+06	1.32−12	2.70−07
5	715.0	2.61+02	2.99+04	4.91+04	4.54−14	2.00−07
6	869.5	1.56+03	3.22+05	2.94+05	3.36−13	7.20−07
7	942.2	5.01+03	1.31+06	9.43+05	1.17−12	8.00−08
8	980.9	4.52−01	1.34+02	8.51+01	1.10−16	1.10−07
9	1176.4	1.56+03	7.94+05	2.93+05	4.58−13	8.01−08

respectively. It is therefore anticipated that these bands would be dominant in the simulated *ab initio* rovibrational spectra of these species.

These bands are observed in Figure 5.3, which depicts the *ab initio* rovibrational spectra of $(^1A_1)NaH_2^+$, $(^1A')NaHD^+$ and $(^1A_1)NaD_2^+$ for $v \leq 10$ and $J \leq 5$. The rovibrational spectrum of $(^1A_1)NaH_2^+$ features several bands of similar intensity in the region 500-1750 cm^{-1}. The most intense transitions however have been assigned to the $|001\rangle \leftarrow |000\rangle$ (∼650-750 cm^{-1}), $|101\rangle \leftarrow |000\rangle$ (∼1000-1100 cm^{-1})

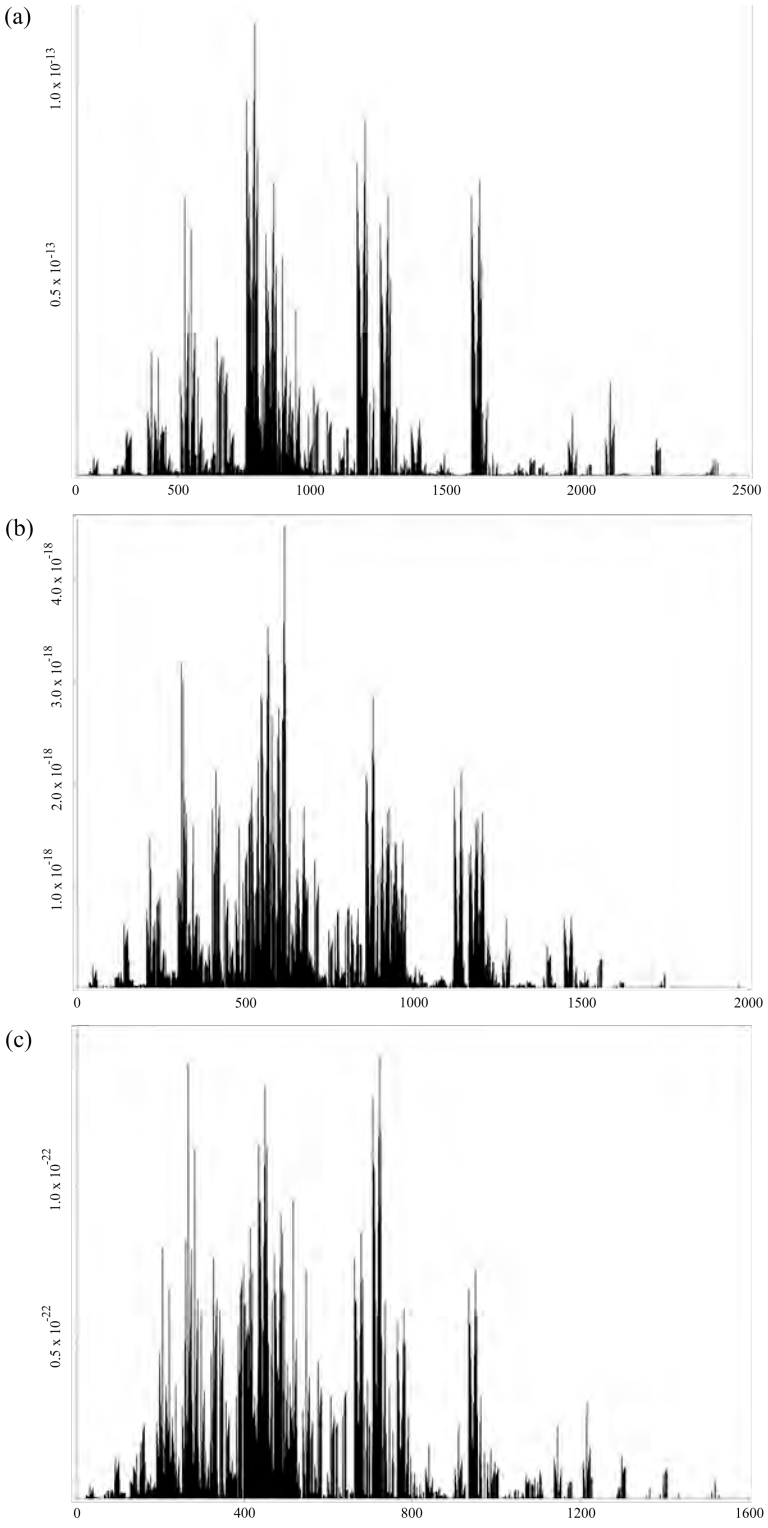

Figure 5.3 *Ab initio* rovibrational spectra for $v \leq 10$, $J \leq 5$ and S_{ab} at 296 K: (a) $(^1\mathrm{A}_1)\mathrm{NaH}_2^+$ ($S_{ab} = 1 \times 10^{-20}$), 7764 lines; (b) $(^1\mathrm{A}')\mathrm{NaHD}^+$ ($S_{ab} = 1 \times 10^{-20}$), 4855 lines, and; (c) $(^1\mathrm{A}_1)\mathrm{NaD}_2^+$ ($S_{ab} = 1 \times 10^{-25}$), 4162 lines. Frequencies and intensities given in cm^{-1} and cm $\mathrm{molecule}^{-1}$, respectively.

and $|201\rangle \leftarrow |000\rangle$ ($\sim$1450-1550 cm^{-1}) bands. Assignments of the most prominent transitions are given explicitly in Table 5.13. The rovibrational spectrum of

Table 5.13 Assignments of prominent transitions in the *ab initio* rovibrational spectra of $(^1A_1)NaH_2^+$, $(^1A')NaHD^+$ and $(^1A_1)NaD_2^+$. Frequencies and intensities given in cm^{-1} and cm molecule^{-1}, respectively.

Initial					Final					
$\|t_1t_2t_3\rangle$	J	K_a	K_c		$\|t_1t_2t_3\rangle$	J	K_a	K_c	Freq.	Intensity
$(^1A_1)NaH_2^+$										
$\|001\rangle$	5	0	5	$\leftarrow$	$\|000\rangle$	4	0	4	661.9	1.16−13
$\|001\rangle$	4	0	4	$\leftarrow$	$\|000\rangle$	5	0	5	631.8	9.62−14
$\|001\rangle$	4	0	4	$\leftarrow$	$\|000\rangle$	3	0	3	658.6	9.62−14
$\|101\rangle$	5	0	5	$\leftarrow$	$\|000\rangle$	4	0	4	1072.8	9.09−14
$\|001\rangle$	5	1	4	$\leftarrow$	$\|000\rangle$	4	1	3	672.3	8.36−14
$\|001\rangle$	3	0	3	$\leftarrow$	$\|000\rangle$	4	0	4	634.5	8.29−14
$\|001\rangle$	5	1	5	$\leftarrow$	$\|000\rangle$	4	1	4	671.9	8.08−14
$\|101\rangle$	4	0	4	$\leftarrow$	$\|000\rangle$	5	0	5	1042.9	7.99−14
$\|201\rangle$	5	0	5	$\leftarrow$	$\|000\rangle$	4	0	4	1499.0	7.57−14
$\|101\rangle$	4	0	4	$\leftarrow$	$\|000\rangle$	3	0	3	1069.7	7.51−14
$(^1A')NaHD^+$										
$\|101\rangle, \|001\rangle$	5	0	5	$\leftarrow$	$\|100\rangle$	4	0	4	617.4	4.54−18
$\|101\rangle, \|001\rangle$	4	0	4	$\leftarrow$	$\|100\rangle$	3	0	3	615.4	3.59−18
$\|001\rangle$	5	0	5	$\leftarrow$	$\|000\rangle$	4	0	4	568.1	3.54−18
$\|001\rangle$	5	1	4	$\leftarrow$	$\|000\rangle$	4	1	3	571.2	3.27−18
$\|001\rangle$	5	1	5	$\leftarrow$	$\|000\rangle$	4	1	4	571.0	3.22−18
$\|100\rangle$	5	1	4	$\leftarrow$	$\|000\rangle$	5	0	5	310.7	3.18−18
$\|101\rangle, \|001\rangle$	5	1	4	$\leftarrow$	$\|100\rangle$	4	1	3	620.7	3.16−18
$\|101\rangle, \|001\rangle$	5	1	5	$\leftarrow$	$\|100\rangle$	4	1	4	620.5	3.11−18
$\|001\rangle$	5	1	4	$\leftarrow$	$\|100\rangle$	5	0	5	316.2	3.02−18
$\|001\rangle$	4	0	4	$\leftarrow$	$\|000\rangle$	5	0	5	547.6	2.87−18
$(^1A_1)NaD_2^+$										
$\|101\rangle, \|201\rangle$	5	0	5	$\leftarrow$	$\|100\rangle$	4	0	4	720.8	1.42−22
$\|100\rangle$	5	1	4	$\leftarrow$	$\|000\rangle$	5	0	5	265.3	1.39−22
$\|101\rangle$	5	0	5	$\leftarrow$	$\|100\rangle$	4	0	4	448.6	1.32−22
$\|101\rangle, \|201\rangle$	4	0	4	$\leftarrow$	$\|100\rangle$	5	0	5	705.2	1.28−22
$\|101\rangle, \|201\rangle$	5	1	5	$\leftarrow$	$\|100\rangle$	4	1	4	724.1	1.18−22
$\|100\rangle, \|200\rangle$	4	1	3	$\leftarrow$	$\|100\rangle$	4	0	4	265.4	1.17−22
$\|101\rangle, \|201\rangle$	5	1	4	$\leftarrow$	$\|100\rangle$	4	1	3	724.4	1.16−22
$\|101\rangle, \|201\rangle$	4	0	4	$\leftarrow$	$\|100\rangle$	3	0	3	719.2	1.16−22
$\|101\rangle$	4	0	4	$\leftarrow$	$\|100\rangle$	5	0	5	433.0	1.14−22
$\|101\rangle$	5	1	5	$\leftarrow$	$\|100\rangle$	4	1	4	452.5	1.13−22

$(^1A')NaHD^+$ exhibits two predominant bands located at $\sim$550-650 cm^{-1} and $\sim$300-400 cm^{-1}. The most intense lines have been also characterised in Table 5.13. These

transitions have been assigned to the $[|101\rangle, |001\rangle] \leftarrow |100\rangle$ and $|001\rangle \leftarrow |000\rangle$ bands, respectively. The rovibrational spectrum of $(^1A_1)NaD_2^+$ is dominated by three bands of intensity *ca.* 1.5×10^{-22} in the 300-500 cm^{-1} region. Nevertheless, the most intense transitions have been assigned unequivocally. In particular, transitions from the $|100\rangle \leftarrow |000\rangle$ ($\sim$250-350 cm^{-1}), $[|001\rangle, |201\rangle] \leftarrow |000\rangle$ ($\sim$450-550 cm^{-1}) and $[|101\rangle, |201\rangle] \leftarrow |000\rangle$ ($\sim$700-800 cm^{-1}) bands have been assigned.

5.8. Conclusion

A detailed and systematic investigation of the structures, stabilities and energetics of ground state MH_2^+, $HMHe^+$ and MHe_2^+ (M = Li, Na, K) has been presented. Both single- and multi-reference methods were employed to calculate equilibrium parameters including R_e, θ_e and D_e and elucidate trends therein. The results of this work concerning the dihydride cations of Li, Na and K indicate that these species result from a charge-quadrupole interaction between the metal ion and the H_2 molecular subunit. This fact is now well established in the literature. Trends in terms of R_e, θ_e, D_e, ω_1, ω_2 and ω_3 have been ascribed largely to the relative ionic radii, and the consequent strength of this charge-quadrupole interaction. Values of D_0 of MH_2^+ are generally in good or excellent agreement with available experimental data. The geometric structures of the ground states of the hydrohelide/helide cations are extremely fluxional with respect to the central bond angle co-ordinate. In the case of the hydrohelide monocations of Li, Na and K, a substantial variation in M-H and M-He bond lengths is also observed. It is consequently concluded that a concept such as 'equilibrium structure' for such species is of limited value. The ground state PESs of MHe_2^+ are also extremely sensitive to the *ab initio* methods by which they are modelled. Indeed, the symmetry of the state itself is seen to be determined by the level of theory employed in this approximation.

FCI and CCSD(T) have been employed to construct analytical PEFs and DMFs of $(^1A_1)LiH_2^+$ and $(^1A_1)NaH_2^+$, respectively. The molecular property surfaces of the former species were developed in Chapter Three. Discrete CCSD(T) PES and DMS grids of $(^1A_1)NaH_2^+$ consisted of 118 and 90 points, respectively. The analytical $(^1A_1)NaH_2^+$ PES consisted of a $P(6,6)$ approximant (with $\sigma_{85-88,91-99} = 0$ using SVD) in conjunction with the OGL expansion variable. Similarly, 7^{th} order power series expansions of the internal displacement co-ordinates were employed for analytical μ_x and μ_y component DMFs.

Vibration band origins and vibration-averaged structures for $(^1A_1)MH_2^+$, $(^1A')MHD^+$ and $(^1A_1)MD_2^+$ (M = Li, Na) were calculated using variational algorithms detailed in Chapter Four. The character of ground and excited state vibrational eigenvectors were assessed using a configuration weight assignment scheme. In the cases of $(^1A')LiHD^+$ and $(^1A')NaHD^+$, it was observed that the low-lying vibrational states possessed a relatively delocalised nature. Conversely, the lowest vibrational states of $(^1A_1)LiH_2^+$, $(^1A_1)LiD_2^+$, $(^1A_1)NaH_2^+$ and $(^1A_1)NaD_2^+$ could be assigned using a single dominant configuration. The rovibrational wave functions of all isotopomeric species could be assigned unequivocally using normal modes of vibration and the $J_{K_aK_c}$ assignment scheme. For $(^1A_1)LiH_2^+$ and $(^1A_1)LiD_2^+$, calculated rovibrational transition frequencies in the H-H stretch bands were calculated to be within *ca.* 0.1-0.2% of recent experimental values. Vibrational radiative properties, such as vibration transition moments, Einstein A and B coefficients, vibration band strengths, radiative lifetimes and rovibrational spectral intensities were calculated using methods outlined in Chapter Four.

5.9. References

[1] D. J. Searles and E. I. von Nagy-Felsobuki, Phys. Rev. A **43**, 3365 (1991).

[2] E. Bodo, F. A. Gianturco, R. Martinazzo, A. Forni, A. Famulari, and M. Raimondi, J. Phys. Chem. A **104**, 11972 (2000).

[3] E. Bodo, F. A. Gianturco, and R. Martinazzo, J. Phys. Chem. A **105**, 10994 (2001).

[4] E. Bodo, F. A. Gianturco, R. Martinazzo, and M. Raimondi, J. Phys. Chem. A **105**, 10986 (2001).

[5] R. Martinazzo, G. F. Tantardini, E. Bodo, and F. A. Gianturco, J. Chem. Phys. **119**, 11241 (2003).

[6] R. Martinazzo, E. Bodo, F. A. Gianturco, and M. Raimondi, Chem. Phys. **287**, 335 (2003).

[7] C. Sanz, E. Bodo, and F. A. Gianturco, Chem. Phys. **314**, 135 (2005).

[8] H. S. Lee, Y. S. Lee, and G. H. Jeung, J. Phys. Chem. A **103**, 11080 (1999).

[9] R. Davy, E. Skoumbourdis, and T. Kompanchenko, Mol. Phys. **97**, 1263 (1999).

[10] A. Russek, R. Snyder, and R. J. Furlan, Phys. Rev. A **39**, 6158 (1989).

[11] D. A. Dixon, J. L. Gole, and A. Komornicki, J. Phys. Chem. **92**, 1378 (1988).

[12] B. H. Cardelino, W. H. Eberhardt, and R. F. Borkman, J. Chem. Phys. **84**, 3230 (1986).

[13] P. Hobza and P. von Ragué-Schleyer, Chem. Phys. Lett. **105**, 630 (1984).

[14] J. B. Collins, P. von Ragué-Schleyer, J. S. Binkley, J. A. Pople, and L. Radom, J. Am. Chem. Soc. **98**, 3436 (1976).

[15] E. Kochanski, Chem. Phys. Lett. **28**, 471 (1974).

[16] R. C. Raffenetti and K. Ruedenberg, J. Chem. Phys. **59**, 5978 (1973).

[17] W. A. Lester Jr, J. Chem. Phys. **54**, 3171 (1971).

[18] W. A. Lester Jr, J. Chem. Phys. **53**, 1511 (1970).

[19] N. K. Ray, J. Chem. Phys. **52**, 463 (1970).

[20] A. A. Wu and F. O. Ellison, J. Chem. Phys. **47**, 1458 (1967).

[21] W. P. Kraemer and V. Špirko, Chem. Phys. **330**, 190 (2006).

[22] V. P. Bulychev, K. M. Bulanin, and M. O. Bulanin, Opt. Spectrosc. **96**, 205 (2004).

[23] A. J. Page and E. I. von Nagy-Felsobuki, J. Phys. Chem. A **111**, 4478 (2007).

[24] D. M. Bishop and S. M. Cybulski, Chem. Phys. Lett. **230**, 177 (1994).

[25] W. Kutzelnigg, V. Staemmler, and C. Hoheisel, Chem. Phys. **1**, 27 (1973).

[26] L. A. Curtiss and J. A. Pople, J. Phys. Chem. **92**, 894 (1988).

[27] M. F. Falcetta, J. L. Pazun, M. J. Dorko, D. Kitchen, and P. E. Siska, J. Phys. Chem. **97**, 1011 (1993).

[28] J. D. Switalski, J. T. J. Huang, and M. E. Schwartz, J. Chem. Phys. **60**, 2252 (1974).

[29] M. Barbatti, G. Jalbert, and M. A. C. Nascimento, J. Chem. Phys. **114**, 2213 (2001).

[30] J. G. Vitillo, A. Damin, A. Zecchina, and G. Ricchiardi, J. Chem. Phys. **122**, 114311 (2005).

[31] I. Tamássy-Lentei and J. Szaniszló, J. Mol. Struct. (THEOCHEM) **501-502**, 403 (2000).

[32] A.-M. Sapse, A. Dumitra, and D. C. Jain, J. Clust. Sci. **14**, 21 (2003).

[33] F. Marinetti, E. C. E. Bodo, F. A. Gianturco, E. Yurtsever, M. Yurtsever, and E. Yildirim, Theor. Chim. Acta **118**, 53 (2007).

[34] A. J. Page and E. I. von Nagy-Felsobuki, J. Chem. Phys. (Submitted).

[35] J. E. Bushnell, P. R. Kemper, and M. T. Bowers, J. Phys. Chem. **98**, 2044 (1994).

[36] C. Emmeluth, B. L. J. Poad, C. D. Thompson, G. H. Weddle, and E. J. Bieske, J. Chem. Phys. **126**, 204309 (2007).

[37] C. D. Thompson, C. Emmeluth, B. L. J. Poad, G. H. Weddle, and E. J. Bieske, J. Chem. Phys. **125**, 044310 (2006).

[38] C. H. Wu, J. Chem. Phys. **71**, 783 (1979).

[39] A. J. Page, D. J. D. Wilson, and E. I. von Nagy-Felsobuki, Chem. Phys. Lett. **429**, 335 (2006).

[40] A. J. Page, D. J. D. Wilson, and E. I. von Nagy-Felsobuki, Chem. Phys. Lett. **442**, 194 (2007).

[41] A. J. Page and E. I. von Nagy-Felsobuki, Phys. Chem. Chem. Phys. **10**, 1285 (2008).

[42] A. J. Page and E. I. von Nagy-Felsobuki, J. Mol. Struct. (THEOCHEM) **853**, 53 (2008).

[43] C. Emmeluth, B. L. J. Poad, C. D. Thompson, G. Weddle, E. J. Bieske, A. A. Buchachenko, T. A. Grinev, and J. Klos, J. Chem. Phys. **127**, 164310 (2007).

[44] H.-J. Werner, P. J. Knowles, R. Lindh, F. R. Manby, M. Schütz, P. Celani, T. Korona, G. Rauhut, R. D. Amos, A. Bernhardsson, et al., MOLPRO, *version 2006.1* (2006), see http://www.molpro.net.

[45] M. A. Iron, M. Oren, and J. M. L. Martin, Mol. Phys. **101**, 1345 (2003).

[46] T. H. Dunning, J. Chem. Phys. **90**, 1007 (1989).

[47] A. J. Page and E. I. von Nagy-Felsobuki, Chem. Phys. **351**, 37 (2008).

CHAPTER 6

Ab Initio Investigation of Alkaline-Earth Metal Hydride and Helide Ions

6.1. Introduction

A detailed *ab initio* study of the structures and stabilities of ground state MH_2^{n+}, $HMHe^{n+}$ and MHe_2^{n+} for M = Be, Mg, Ca and $n = 1, 2$ is presented in this Chapter. In particular, single- and multi-reference *ab initio* methods will be employed to characterise the equilibrium structures, dissociation energies and harmonic vibration frequencies of these species. These data will be presented and compared with available theoretical [1–20] data in §6.3, 6.4 and 6.5, respectively. A comprehensive review of experimental and theoretical data concerning the species of interest has been presented in Chapter One. Page *et al.* [15, 17, 21] have previously elucidated the structural and energetic trends of Be, Mg and Ca hydrohelide and helide ions. This discussion will be extended to the respective dihydrides in §6.3. Particular emphasis will be placed upon the efficacy of isovalent and isoelectronic arguments [22, 23] with respect to these species. Electron density analyses will also be utilised to elucidate the relative structural and energetics trends in the respective mono- and dications.

A systematic study of the structures and energetics of MH_2^{n+}, $HMHe^{n+}$ and MHe_2^{n+} will allow those species suitable for full rovibrational analyses to be determined (see Figure 1.1). The *ab initio* method employed here is that developed and benchmarked in Chapter 2. Page and von Nagy-Felsobuki have constructed *ab initio* rovibrational spectra for $(^1A_1)BeH_2^{2+}$ [5] and $(^1A_1)MgH_2^{2+}$ [7] from single- and

multi-reference property surfaces. These efforts will be extended to the ground states of $(^2\Sigma^+)$HBeHe^{2+}, $(^2\Sigma^+)$HMgHe^{2+} and $(^1\Sigma_g^+)$MgHe$_2^{2+}$ in this work. Hence, molecular PEFs and DMFs of the ground states of these species will be presented in §6.7. These property surfaces have been constructed using methods described in Chapter Three. Vibrational and rovibrational data, including vibration-averaged structures of these species will be presented and discussed in §6.8, 6.9 and 6.10, respectively. Vibrational and rovibrational radiative data (*i.e.* band and line strengths) will also be presented in §6.8, 6.9 and 6.10, respectively. All vibrational and rovibrational data have been calculated according to the algorithms developed and described in Chapter Four.

The principle aim of this investigation is to provide information regarding the structural and energetic properties of this interesting class of molecules. Furthermore, comparison and discussion of trends with respect to these properties will provide insight into underlying mechanisms. Experimental spectroscopy of molecular hydride, hydrohelide and helide ions is presently a burgeoning field of research. This is particularly the case with respect to ground state ion-quadrupole complexes of form MH_2^{n+} [24–27]. *Ab initio* data concerning the vibrational and rovibrational structures and spectra may therefore be timely in assisting the experimental detection and characterisation of such species.

6.2. Computational Procedure

The UCCSD(T), IC-MRCI and IC-MRCI+Q methods and atomic basis sets employed presently are essentially those described in Chapter Two. In cases where helium was present, helium $1s$ electron density was excluded from the CASSCF optimisation. Thus a correct description of the electronic wave function in the asymptotic limit (in which the He $1s$ configuration is identically doubly occupied)

is obtained. Conversely, hydrogen 1s electron density was included in all CASSCF active spaces. It is also noted that all *ab initio* results calculated in this work include BSSE and relativistic (DK2) correction and have been calculated using MOLPRO [28], unless stated otherwise. All MO, NO and electron density plots presented in this thesis have been constructed using MOLDEN [29].

6.3. Alkaline-Earth Metal Dihydride Cations: MH_2^{n+} (n = 1, 2)

6.3.1. MH_2^+ (M = Be, Mg, Ca)

Equilibrium parameters of $(^2A_1)BeH_2^+$, $(^2A_1)MgH_2^+$ and $(^2A_1)CaH_2^+$ including R_e, θ_e, ω_1, ω_2 and ω_3 have been calculated and are presented in Table 6.1.

With respect to the $^2A_1$ ground state of BeH_2^+ there is excellent agreement between single- and multi-reference equilibrium parameters calculated in this work. In particular, it is evident that the UCCSD(T), IC-MRCI and IC-MRCI+Q θ_e values are in exact agreement, whereas the largest discrepancy in R_e calculated with these methods is 0.4 mÅ. The VBCI calculations of Poshusta *et al.* [1, 30] yielded significantly larger equilibrium bond lengths and smaller bond angles than those of this work, as is anticipated. In addition, the fundamental vibration frequencies of $(^2A_1)BeH_2^+$ reported by Poshusta *et al.* [1, 30] also differ substantially from those of this work, most notably in the ω_1 and ω_3 modes. These correspond directly to the Be-H stretch modes, and therefore these differences are consistent with those observed in R_e. The MRCI/cc-pVQZ results of Hinze *et al.* [2] are in closer agreement with those of this work. For example, the values of R_e calculated using MRCI are *ca.* 20 mÅ smaller than those values reported here. These two sets of θ_e values are also in better agreement, differing by *ca.* 0.3°. It is noted that the $(^2A')BeH_2^+$ PES minimum calculated by Hinze *et al.* [2] corresponded to equilibrium Be-H bond

Table 6.1 *Ab initio* equilibrium parameters of $(^2A_1)MH_2^+$, M = Be, Mg, Ca.

Method	R_e (/Å)	θ_e (/°)	D_e[a] (/kJmol^{-1})			Frequencies (/cm^{-1})		
			1	2	3	ω_1	ω_2	ω_3
			BeH_2^+					
UCCSD(T)[b]	1.8161	24.4	37.68	188.1	494.4	1158	3862	911
IC-MRCI[b]	1.8159	24.4	35.42	187.4	494.1	1184	3898	932
IC-MRCI+Q[b]	1.8163	24.4	36.04	188.0	494.7	1162	3872	913
VBCI[c]	2.76	17.1	16.4			790	4600	590
VBCI[d]	2.20	20.5	10.6			240	4582	
MRCI[e]	1.794	24.72	39.76					
MRCI+Q[e]	1.794	24.72						
			MgH_2^+					
UCCSD(T)[b]	2.6387	16.3	9.867	265.5	466.6	691	4147	796
IC-MRCI[b]	2.6847	15.9	13.76	267.9	465.6	666	4223	792
IC-MRCI+Q[b]	2.6528	16.2	8.920	268.0	464.7	683	4158	793
MRCI[f]	2.748	15.8	9.2			180	4313	410
			CaH_2^+					
UCCSD(T)[b]	3.1892	13.4	4.79	258.9	461.5	519	4188	763
IC-MRCI[b]	3.3417	12.8	1.69	254.9	458.4	493	4205	763
IC-MRCI+Q[b]	3.1670	13.6	2.83	257.4	459.6	505	4169	752
MRCI[g]	3.33	12.8	6.75					

[a] $D_e(1)$, $D_e(2)$ and $D_e(3)$ correspond to dissociative reactions (6.1), (6.2) and (6.3), respectively.
[b] This work.
[c] In conjunction with GTOs; see reference [30].
[d] See reference [1].
[e] Core-corrected values, calculated in conjunction with cc-pVQZ basis sets; see reference [2]. The R_e values correspond to $^2A_1$ PES minima. The corresponding C_s minima exhibits symmetry breaking in the Be-H bonds. Explicitly, R_e(Be-H$_1$) = 1.798 and R_e(Be-H$_2$) = 1.790 Å.
[f] Employing a SA-MCSCF reference wave function, in conjunction with [9s9p7d4f] (Mg) and [6s4p2d] (H) basis sets; see reference [8].
[g] In conjunction with [7s6p6d1f] (Ca) and cc-pV5Z (H) basis sets; see reference [11].

lengths which differed by 8 mÅ. According to Hinze *et al.* [2] this symmetry breaking was a result of the interaction between two $^1A_1$ states and a $^1B_2$ state, all of which transform as $^1A'$ states in C_s symmetry. No such symmetry breaking was observed in the present work. As such, it is possible that the symmetry breaking observed by Hinze *et al.* [2] was a product of the active space employed in their CASSCF/MRCI wave function, which included only the 1s, 2s and 2p orbitals of Be and H.

For the $^2A_1$ ground state of MgH_2^+, the results of the present work may

only be compared with those of Bauschlicher [8]. In addition, no experimental data concerning $(^2A_1)MgH_2^+$ have been reported, despite the experimental work of Ding *et al.* [24] concerning the spectroscopy of $(^2A_1)MgD_2^+$. Bauschlicher [8] employed MRCI in conjunction with a state-averaged MCSCF (SA-MCSCF) reference determinant. The relative magnitudes of the R_e values calculated by Bauschlicher [8] and those calculated here are as anticipated, and may be explained with recourse to the sizes of the respective basis sets employed. The effects of the +Q correction to the IC-MRCI energy are noticeable with respect to the equilibrium parameters of $(^2A_1)MgH_2^+$. For example, R_e decreases by *ca.* 30 mÅ and θ_e increases by 0.3° upon inclusion of the +Q term. Similar effects in the calculated harmonic frequencies and dissociative well-depths (*vide infra*) are also noticed. These fluctuations indicate that the CCSD(T) and IC-MRCI+Q data concerning these equilibrium parameters are in good agreement.

This is also evident with respect to the $^2A_1$ ground state of CaH_2^+. For example, from Table 6.1 it can be seen that the addition of the +Q correction to the IC-MRCI energy corresponds to a decrease of *ca.* 0.18 Å in the R_e(Ca-H) value. As such, the IC-MRCI+Q and UCCSD(T) equilibrium parameters for $(^2A_1)CaH_2^+$ are in good agreement, exhibiting differences in R_e and θ_e values of *ca.* 20 mÅ and 0.1°, respectively. To date the only equilibrium structure of $(^2A_1)CaH_2^+$ reported in the literature is that of Czuchaj *et al.* [11], who employed MRCI in conjunction with $[7s6p6d1f]$ and cc-pV5Z [31] basis sets for Ca and H, respectively. There is a substantial difference between the latter R_e values and those of this work (as anticipated). These differences are *ca.* 200 mÅ, and are ascribed to the relative sizes of the contracted basis sets employed. Better agreement is observed with respect to the equilibrium bond angles, with the largest difference being 0.8°.

In order that the dissociative behaviours of the $^2A_1$ ground states of BeH_2^+,

MgH_2^+ and CaH_2^+ be better understood, the dissociative mechanisms,

$$D_e(1) : (^2A_1)MH_2^+ \rightarrow (^2S_{1/2})M^+ + (^1\Sigma_g^+)H_2 \quad (6.1)$$

$$D_e(2) : (^2A_1)MH_2^+ \rightarrow (^1\Sigma^+)MH^+ + (^2S_{1/2})H \quad (6.2)$$

$$D_e(3) : (^2A_1)MH_2^+ \rightarrow (^2S_{1/2})M^+ + 2(^2S_{1/2})H \quad (6.3)$$

have been considered in this work. Potential well-depths for each of these reactions are listed in Table 6.1. It is evident from Table 6.1 that each species is most weakly bound with respect to the $[M^+ + (^1\Sigma_g^+)H_2]$ dissociative products (*i.e.* equation (6.1)). For instance, this well-depth for $(^2A_1)BeH_2^+$ is calculated to be *ca.* 36 kJ mol^{-1}, whereas those corresponding to equations (6.2) and (6.3) are *ca.* 188 and 494 kJ mol^{-1}, respectively. Similarly, for the ground state of MgH_2^+, these respective well-depths are *ca.* 10, 267 and 465 kJ mol^{-1}, whilst for $(^2A_1)CaH_2^+$ they are *ca.* 4, 255 and 460 kJ mol^{-1}. These data suggest that each of the BeH_2^+, MgH_2^+ and CaH_2^+ ground states arise from the interaction between the metal ion charge and the H_2 subunit quadrupole moment. This fact has been established for each species in previous investigations [2, 8, 11] and will be discussed at greater length in this work (*vide infra*). The ω_2 fundamental frequencies for $(^2A_1)BeH_2^+$, $(^2A_1)MgH_2^+$ and $(^2A_1)CaH_2^+$, which essentially correspond to $\omega_e(H_2)$, also suggest that these species exist as ion-molecule complexes. For example, ω_2 for these species are calculated to be *ca.* 3850, 4150 and 4200 cm^{-1}, respectively. For comparison, the value of $\omega_e(H_2)$ calculated using CCSD/aug-cc-pVQZ is 4399 cm^{-1}.

6.3.2. MH_2^{2+} (M = Be, Mg, Ca)

Values of R_e, θ_e, D_e, ω_1, ω_2 and ω_3 for the ground states BeH_2^{2+}, MgH_2^{2+} and CaH_2^{2+} have been calculated using UCCSD(T), IC-MRCI and IC-MRCI+Q. It is

evident from Table 6.2 that the single- and multi-reference equilibrium parameters are in exact agreement for the $^1A_1$ ground state of BeH_2^{2+}. These results are also in excellent agreement with previously published data. For example, the differences in R_e values calculated in this work and the CCSD(T)/MRCI values of Page and von Nagy-Felsobuki [5] are of the order of 0.1 mÅ. The latter method employed augmented, core-correlated quadruple-ζ basis sets. Similarly, the discrepancy in θ_e with these respective methods is 0.1°. The MRCI R_e value reported by Valtazanos *et al.* [4] is smaller than the values of this work by *ca.* 15 mÅ, and was calculated using double-ζ basis sets.

There is also good agreement between single- and multi-reference equilibrium structures for $(^1A_1)MgH_2^{2+}$. For example, R_e and θ_e values calculated using UCCSD(T), IC-MRCI and IC-MRCI+Q agree to within 2.5 mÅ and 0.1°, respectively. The only previously reported structure determined using a correlated approach is that of Simandiras and Nicolaides [9], who employed MP2 in conjunction with $[9s7p3d1f]$ and $[3s2p]$ basis sets for Mg and H, respectively. At this level of theory, the ground state of MgH_2^{2+} exhibits R_e and θ_e values *ca.* 1 mÅ and 0.1° larger than those of this work, respectively. Conversely, the predicted equilibrium H_2 subunit bond lengths of this work are *ca.* 10 and 9 mÅ larger than the HF and MP2 values of Simandiras and Nicolaides [9], respectively.

The discrepancy between UCCSD(T), IC-MRCI and IC-MRCI+Q equilibrium structures of $(^1A_1)CaH_2^{2+}$ and the MP2 structure of Simandiras and Nicolaides [9] is more noticeable. For example, the equilibrium Ca - H bond lengths agree to within 30 mÅ, whereas θ_e values agree to within *ca.* 0.2°. Nevertheless, the single- and multi-reference R_e values of this work are in excellent agreement, differing by *ca.* 4 mÅ. The equilibrium bond angles calculated using these methods are in exact agreement.

Table 6.2 *Ab initio* equilibrium parameters of $(^1A_1)MH_2^{2+}$, M = Be, Mg, Ca.

Method	R_e (/Å)	θ_e (/°)	D_e[a] (/kJmol^{-1})			Frequencies (/cm^{-1})		
			1	2	3	ω_1	ω_2	ω_3
			BeH_2^{2+}					
UCCSD(T)[b]	1.6093	29.3	230.8	522.9	687.6	1469	3372	1132
IC-MRCI[b]	1.6093	29.3	230.8	522.8	687.5	1467	3372	1130
IC-MRCI+Q[b]	1.6093	29.3	230.9	522.9	687.7	1469	3372	1132
CCSD(T)[c]	1.609	29.4	231.0					
MRCI[d]	1.594	28.7	212.3					
MRCI[c]	1.609	29.4	230.9					
			MgH_2^{2+}					
UCCSD(T)[b]	2.0297	22.1	97.01	484.9	553.8	1071	3767	957
IC-MRCI[b]	2.0332	22.0	95.51	471.9	538.0	1287	3826	1153
IC-MRCI+Q[b]	2.0321	22.0	92.76	481.3	550.2	1084	3802	966
SCF[e]	2.048	21.9	90.8			871	4133	782
MP2[e]	2.034	22.2	95.0			844	4067	794
			CaH_2^{2+}					
UCCSD(T)[b]	2.4635	17.7	47.61	472.0	504.4	838	4026	872
IC-MRCI[b]	2.4676	17.7	42.73	476.5	491.2	829	4021	866
IC-MRCI+Q[b]	2.4647	17.7	45.07	472.1	505.1	836	4029	871
SCF[e]	2.350	17.2	39.3			698	4372	497
MP2[e]	2.491	17.5	43.1			628	4304	527

[a] $D_e(1)$, $D_e(2)$ and $D_e(3)$ correspond to dissociative reactions (6.4), (6.5) and (6.6), respectively.
[b] This work.
[c] Includes BSSE correction, in conjunction with aug-CVQZ (Be) [15, 32] and aug-cc-pVQZ (H) [31, 33] basis sets; see reference [5].
[d] In conjunction with an augmented double-ζ Dunning-Hay basis set [34]; see reference [4].
[e] In conjunction with [9*s*7*p*3*d*1*f*] (Mg), [9*s*8*p*3*d*] (Ca) and [3*s*2*p*] (H) basis sets; see reference [9].

The natures of the $^1A_1$ ground states of BeH_2^{2+}, MgH_2^{2+} and CaH_2^{2+} necessitate a thorough analysis of the possible dissociative mechanisms. As such, binding energies corresponding to the dissociative reactions,

$$D_e(1) : (^1A_1)MH_2^{2+} \rightarrow (^1S_0)M^{2+} + (^1\Sigma_g^+)H_2 \tag{6.4}$$

$$D_e(2) : (^1A_1)MH_2^{2+} \rightarrow (^2\Sigma^+)MH^{2+} + (^2S_{1/2})H \tag{6.5}$$

$$D_e(3) : (^1A_1)MH_2^{2+} \rightarrow (^1S_0)M^{2+} + 2(^2S_{1/2})H \tag{6.6}$$

have been considered. These data are presented in Table 6.2. The values of $D_e(1)$

indicate that the $(^1A_1)MH_2^{2+}$ complexes (M = Mg, Ca) are most weakly bound with respect to the dissociation products $[M^{2+} + (^1\Sigma_g^+)H_2]$, as was the case for $(^2A_1)MH_2^+$. For instance, the former of these species exhibits potential well-depths of *ca.* 92, 480 and 545 kJ mol^{-1} for reactions (6.4), (6.5) and (6.6), respectively, whereas these respective well-depths for $(^1A_1)CaH_2^{2+}$ are *ca.* 42, 472 and 500 kJ mol^{-1}. This is not the case for $(^1A_1)BeH_2^{2+}$, since $IE_2(Be)$ is smaller than $IE_1((^1\Sigma_g^+)H_2)$. Consequently, the $[Be^+ + (^1\Sigma^+)H_2^+]$ dissociation channel is 25.85, 25.92 and 25.78 kJ mol^{-1} lower in energy than the $(^1A_1)BeH_2^{2+}$ potential minimum using UCCSD(T), IC-MRCI and IC-MRCI+Q, respectively. Conversely, these same dissociation channels for $(^1A_1)MH_2^{2+}$ (M = Mg, Ca) are thermodynamically stable, and correspond to potential well-depths of 149.39, 138.12 and 145.95 kJ mol^{-1} (M = Mg) and 408.99, 422.19 and 414.81 kJ mol^{-1} (M = Ca), using UCCSD(T), IC-MRCI and IC-MRCI+Q, respectively.

It is inferred from these trends in dissociation energies that the $(^1A_1)MH_2^{2+}$ complexes essentially result from the anisotropic interaction between the H_2 quadrupole moment and the M^{2+} charge, in the same manner as for the monocations. This inference is corroborated by an investigation of the IC-MRCI density of each species (*vide infra*). The calculated harmonic vibration frequencies also provide support for this conclusion. For instance, the ω_2 harmonic frequency of $(^1A_1)BeH_2^{2+}$ is calculated to be 3372 cm^{-1} using all correlated methods employed here. The harmonic frequencies of $(^1A_1)MgH_2^{2+}$ and $(^1A_1)CaH_2^{2+}$ listed in Table 6.2 are also indicative of a ion-quadrupole interaction between the Mg^{2+}/Ca^{2+} ion and H_2. For example, $\omega_2(MgH_2^{2+})$ and $\omega_2(CaH_2^{2+})$ are calculated to be *ca.* 3800 and 4020 cm^{-1}, respectively. The distinct increases in $D_e(1)$, $D_e(2)$ and $D_e(3)$ values for MH_2^{2+}, compared to those of MH_2^+, are also noted here.

6.3.3. Isovalent Comparisons

Each of $(^2A_1)MH_2^+$ (M = Be, Mg, Ca) arise from the interaction between the metal ion charge and the H_2 quadrupole moment, as previously stated. These metal ions possess [RG]ns^1 configurations. An identical interaction leads to the formation of the $(^1A_1)MH_2^{2+}$ complexes, with the metal ions possessing [RG] configurations. That each species in both the $(^2A_1)MH_2^+$ and $(^1A_1)MH_2^{2+}$ series exhibit symmetrically identical ground state equilibrium structures is anticipated. Because of this, it is appropriate to investigate trends evident in the dissociative energies and harmonic fundamental frequencies in the context of isovalent arguments.

Comparison of successive binding energies corresponding to the dehydrogenation of $(^2A_1)MH_2^+$ and $(^1A_1)MH_2^{2+}$ (*i.e.* equations (6.2)/(6.5) and (6.3)/(6.6) for $n = 1/2$, respectively) yields insight into the dissociative natures of these complexes. Use of the logic applied to $(^1A_1)MH_2^+$ (M = Li, Na, K) pertaining to Δ in Chapter 5 provides an indication of the relative binding energies of the two hydrogens in MH_2^{n+} (M = Be, Mg, Ca). These data are provided in Table 6.3, from which it is inferred that for the $^1A_1$ ground states of BeH_2^{2+}, MgH_2^{2+} and CaH_2^{2+} the binding of the second hydrogen is weaker than the first. This is also the case for $(^2A_1)MgH_2^+$ and $(^2A_1)CaH_2^+$, for which Δ values are calculated to be *ca.* -70 and -55 kJ mol^{-1}. However, the converse is the case for the $^2A_1$ ground state of BeH_2^+, for which Δ is 118.1 kJ mol^{-1}. Nevertheless, it is noted that these differences in binding energies decrease monotonically down the group, independently of charge.

In order to better understand these observed trends in the binding energies of isovalent MH_2^{n+} species, electron density analyses have been performed. The maximum electron density (MED) path along an arbitrary X-Y bond (denoted $\rho(\mathbf{R})$) may be employed to assess the degree of binding [22, 23, 35–38] in MH_2^{n+} ($n = 1, 2$). According to the nomenclature of Frenking *et al.* [22], the point at which the gradient

Table 6.3 Binding energies (/kJ mol^{-1}) for successive hydrogenation of M^{n+} ions (M = Be, Mg, Ca).

	$D_e(2)$	$D_e(3)$	Δ^a	$D_e(2)$	$D_e(3)$	Δ^a	$D_e(2)$	$D_e(3)$	Δ^a
Method	$(^2A_1)BeH_2^+$			$(^2A_1)MgH_2^+$			$(^2A_1)CaH_2^+$		
UCCSD(T)	188.1	494.4	118.1	265.5	466.6	-64.5	258.9	461.5	-56.2
IC-MRCI	187.4	494.1	119.3	267.9	465.6	-70.1	254.9	458.4	-51.3
IC-MRCI+Q	188.0	494.7	118.7	268.0	464.7	-71.3	257.4	459.6	-55.3
	$(^1A_1)BeH_2^{2+}$			$(^1A_1)MgH_2^{2+}$			$(^1A_1)CaH_2^{2+}$		
UCCSD(T)	522.9	687.6	-358.1	484.9	553.8	-416.0	472.0	504.4	-439.6
IC-MRCI	522.8	687.5	-358.1	471.9	538.0	-405.8	476.5	491.2	-461.8
IC-MRCI+Q	522.9	687.7	-358.2	481.3	550.2	-412.3	472.1	505.1	-439.1

$^a\Delta = D_e(3) - 2D_e(2)$. $D_e(2)$ and $D_e(3)$ correspond to dissociative reactions (6.2)/(6.5) and (6.3)/(6.6) for $n = 1/2$, respectively. It is assumed that both M^{n+}-H bonds are identical.

of $\rho(\mathbf{R})$ vanishes, denoted $\rho(\mathbf{R}_b) = \rho_b$, corresponds to a saddle point of the MED of rank and signature $(3, +1)$. The latter is a sufficient condition for the existence of a chemical bond between two nuclei. Thus, the values ρ_b and $\mathbf{R}_b$ may be used to gauge the strength and polarity of any chemical bond. To place the MED data of the species investigated presently in context, it is noted here for comparison that the typical ρ_b for a covalent bond is *ca.* 1.5-3.0 e Å^{-3} [23, 36–38]. Electron density plots for MH_2^{n+} (M = Be, Mg, Ca) have been generated using IC-MRCI, and are included in Appendix F. The corresponding MEDs along the M^{n+}- H_2 midpoint vector are also given in Appendix F. The MED data pertinent to the present discussion has been collated in Table 6.4, where they are accompanied by the polarisability of each metal ion. Plots of the IC-MRCI bonding NOs and $-\nabla^2\rho(\mathbf{R})$ of all species investigated in this Chapter are also included in Appendix F.

Values of ρ_b and $\mathbf{R}_b$ for the ground states of MH_2^{n+} indicate that the strength of the M^{n+}-H_2 interaction is inversely proportional to the polarisability of the M^{n+} ion. For example, $\alpha(Be^+)$ and $\alpha(Be^{2+})$ are 24.46 and 0.05 a_0^3, respectively, whereas ρ_b for $(^2A_1)BeH_2^+$ and $(^1A_1)BeH_2^{2+}$ are 0.21 and 0.42 e Å^{-3}, respectively. Identical observations are made with respect to the Mg and Ca species given in

Table 6.4 IC-MRCI values of ρ_b and $\mathbf{R}_b$ for MH_2^{n+} and $\alpha(M^{n+})$ (M = Be, Mg, Ca; $n = 1, 2$).

	$\alpha(M^{n+})$ ($/a_0^3$)	ρ_b (/e Å^{-3})	$\mathbf{R}_b/R_e$ [a]
$(^2A_1)BeH_2^+$	24.46	0.21	0.37
$(^2A_1)MgH_2^+$	35.61	0.06	0.47
$(^2A_1)CaH_2^+$	81.65	0.03	0.49
$(^1A_1)BeH_2^{2+}$	0.05	0.42	0.39
$(^1A_1)MgH_2^{2+}$	0.48	0.18	0.48
$(^1A_1)CaH_2^{2+}$	3.19	0.13	0.53

[a] $\mathbf{R}_b$ and R_e are defined along the vector joining M^{n+} and the midpoint of the H_2 bond, relative to M^{n+}.

Table 6.4. For example, the ratios $\rho_b(MH_2^+)$:$\rho_b(MH_2^{2+})$ for M = Mg and Ca are 1:3 and 1:4.3, respectively. Nevertheless, the polarity of each respective M^{n+}-H_2 interaction appears to be largely independent of the polarisability of the metal ion. This is indicated by the relative magnitudes of the $\mathbf{R}_b/R_e$ ratios for these species. For instance, $\mathbf{R}_b/R_e$ for MH_2^{2+} (M = Be, Mg, Ca) are only 5, 2 and 8% larger than those of MH_2^+, respectively. As such, these data complement the equilibrium parameters and dissociative potential well-depths listed in Tables 6.1 and 6.2.

6.4. Alkaline-Earth Metal Hydrohelide Cations: $HMHe^{n+}$ (n = 1, 2)

6.4.1. $HMHe^+$ (M = Be, Mg, Ca)

Ab initio values of R_e, θ_e, ω_1, ω_2 and ω_3 of $HBeHe^+$, $HMgHe^+$ and $HCaHe^+$ have been calculated and are compared to available theoretical data in Table 6.5. No experimental data concerning a molecular hydrohelide ion of an alkaline-earth metal has been reported in the literature. In addition, Page and von Nagy-Felsobuki [21] have reported the only known investigation into the structures and stabilities of $HMgHe^+$ and $HCaHe^+$ using *ab initio* methods. Of particular interest in the present context is the quasi-linear nature of the $^1A'$ ground state of

Table 6.5 *Ab initio* equilibrium parameters of $HMHe^+$, M = Be, Mg, Ca.

Method	R_e (M-H) (/Å)	R_e (M-He) (/Å)	θ_e (/°)	$D_e{}^a$ (/kJmol^{-1})		Frequencies (/cm^{-1})		
				1	2	ω_1	ω_2	ω_3
			$(^1\Sigma^+)$HBeHe$^+$					
UCCSD(T)[b]	1.2997	1.5176	180.0	36.26	342.5	1045	277	2141
IC-MRCI[b]	1.2997	1.5179	180.0	36.33	342.2	1216	283	2047
IC-MRCI+Q[b]	1.2997	1.5177	180.0	35.67	342.0	1064	278	2013
B3LYP[c]	1.302	1.525	180.0	31.84				
MP2[c]	1.294	1.519	180.0	28.45				
QCISD[c]	1.305	1.529	180.0	27.20				
CCSD(T)[d]	1.2998	1.5178	180.0	36.30				
CCSD(T)[c]	1.305	1.529	180.0	27.20				
MRCI[d]	1.2998	1.5181	180.0	36.27				
MRCI+Q[d]	1.2998	1.5175	180.0	35.69				
			$(^1\Sigma^+)$HMgHe$^+$					
UCCSD(T)[b]	1.6493	2.1665	180.0	7.806	208.0	664	194	1570
IC-MRCI[b]	1.6512	2.1779	180.0	7.255	200.4	662	192	1594
IC-MRCI+Q[b]	1.6494	2.1689	180.0	7.716	206.6	664	194	1574
			$(^1A')$HCaHe$^+$					
UCCSD(T)[b]	1.9215	2.6271	113.4	4.016	211.6			
IC-MRCI[b]	1.9260	2.6441	115.1	3.899	202.4			
IC-MRCI+Q[b]	1.9210	2.6309	113.3	4.103	206.7			

[a] $D_e(1)$ and $D_e(2)$ correspond to dissociation reactions (6.7) and (6.8), respectively.
[b] This work.
[c] In conjunction with 6-311++G(2*df*,2*pd*) basis sets; see reference [18].
[d] Includes BSSE correction, in conjunction with aug-CVQZ (Be) [15, 32] and aug-cc-pVQZ [31, 33] basis sets; see reference [5].

$HCaHe^+$ (*vide infra*).

Single- and multi-reference methods employed in this work predict a linear equilibrium geometry for the ground state of $HBeHe^+$. These results therefore agree with all previously published theoretical data. The *ab initio* methods employed here predict identical equilibrium structures with respect to R_e(Be-H). Moreover, the largest deviation in R_e(Be-He) is 0.3 mÅ, between UCCSD(T) and IC-MRCI values. Good agreement between current and previous values of is also observed with respect to R_e(Be-H). There is excellent agreement between all equilibrium aspects of $(^1\Sigma^+)$HBeHe$^+$ calculated here and those of Page *et al.* [5], who employed CCSD(T) and IC-MRCI in conjunction with aug-CVQZ (Be) [15, 32] and aug-cc-pVQZ (H, He)

basis sets. For example, R_e(Be-H) and R_e(Be-He) values typically deviate by *ca.* 0.1 mÅ and 0.5 Å, respectively. Predictably, the lower-order correlated methods, such as QCISD and DFT, give larger R_e(Be-He) values than CCSD(T) and IC-MRCI by a margin of *ca.* 10 mÅ. Page *et al.* [17] constructed the first full-dimensional PES of the $^1\Sigma^+$ ground state of $HBeHe^+$ using IC-MRCI. The analytical representation of this surface is shown in Figure 6.1. This PEF is provided as a FORTRAN subroutine in Appendix F, along with the discrete IC-MRCI PES grid.

The potential energy surface minimum for $HMgHe^+$ also corresponds to a $^1\Sigma^+$ equilibrium structure. For example, the present methods yield R_e(Mg-H) and R_e(Mg-He) values of *ca.* 1.65 and 2.17 Å, respectively. These data suggest that the Mg^+ ion exhibits greater affinity to the hydrogen than to the helium. The relative magnitudes of the ω_1 and ω_3 harmonic vibration frequencies of $(^1\Sigma^+)HMgHe^+$also indicate this trend, since these frequencies correspond to the fundamental M-He and M-H stretch modes, respectively. A similar observation is made with respect to the ω_1 and ω_3 harmonic vibration frequencies for $(^1\Sigma^+)HBeHe^+$, and the relative magnitudes of the equilibrium Be-H and Be-He bond lengths.

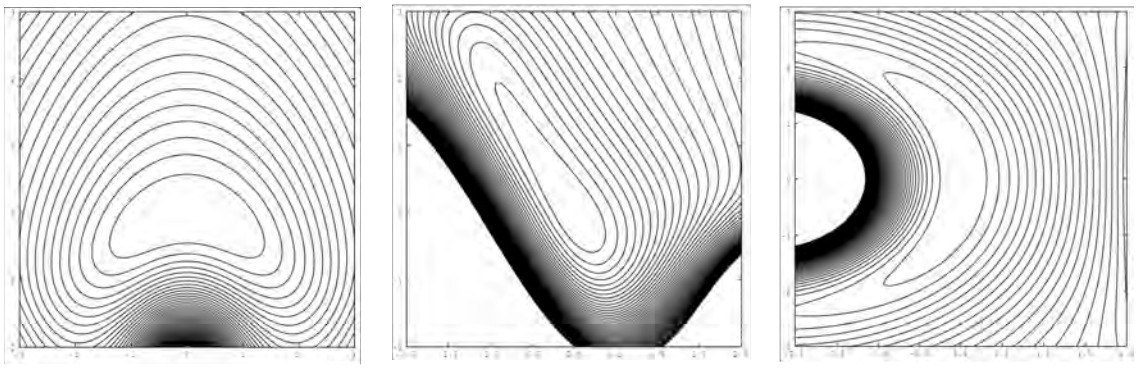

Figure 6.1 Two-dimensional projections of the (4,4) DUN Padé IC-MRCI+BSSE PEF of $(^1\Sigma^+)HBeHe^+$ [17] (in a_0): (a) w_2 (x) versus w_1 (y); (b) w_4 (x) versus w_1 (y), and; (c) w_4 (x) versus w_2 (y). Contours are spaced at increments of 20 kJ mol^{-1}.

All methods employed in this work predict a ^{1}A$'$ equilibrium structure for the ground state of HCaHe$^+$. For example, employing UCCSD(T), IC-MRCI and IC-MRCI+Q yields θ_e values of 113.4, 115.1 and 113.3°, respectively. Good agreement between these methods is also attained with respect to R_e(Ca-H), with the largest discrepancy being 5.0 mÅ. The +Q correction to the IC-MRCI energy is observed to have a noticeable effect with respect to the value of R_e(Ca-He), reducing it by 13.2 mÅ. *Ab initio* harmonic vibration frequencies have not been calculated for (^{1}A$'$)HCaHe$^+$, due to the highly fluxional nature of the PES in the H-Ca-H bend co-ordinate. This was illustrated by Page and von Nagy-Felsobuki [21], who constructed the MEP for the H-Ca-He bend co-ordinate of (^{1}A$'$)HCaHe$^+$ by performing a series of constrained angle optimisations. These workers subsequently determined the ^{1}A$'$-$^1\Sigma^+$ barrier height to be 115.02 and 117.15 cm^{-1} using UCCSD(T) and IC-MRCI+Q. As such, the bend co-ordinate PES is unable to support a bound vibrational state. This will be the subject of greater discussion in subsequent Sections.

The values of IE$_1$ and IE$_2$ for Be, Mg and Ca are less than that of IE$_1$ for He. The dissociation products of all Be, Mg and Ca molecular helide ions investigated in this work would therefore be expected to include neutral He. Dissociation of HMHe$^+$ (M = Be, Mg, Ca) into [M$^+$ + HeH] is also not likely to be a realistic process, due to the relative polarisabilities of M$^+$ and H, and the subsequent abilities of these species to chemically bind helium. As such, potential well-depths corresponding to the dissociative reactions,

$$D_e(1) : (^1\Sigma^+)\text{HMHe}^+ \rightarrow (^1\Sigma^+)\text{MH}^+ + (^1\text{S}_0)\text{He} \tag{6.7}$$

$$D_e(2) : (^1\Sigma^+)\text{HMHe}^+ \rightarrow (^2\text{S}_{1/2})\text{M}^+ + (^2\text{S}_{1/2})\text{H} + (^1\text{S}_0)\text{He} \tag{6.8}$$

have been calculated so that the dissociative properties of HMHe$^+$ may be assessed.

From Table 6.5 it is evident that the relative magnitudes of $D_e(1)$ and $D_e(2)$ for $(^1\Sigma^+)$HBeHe$^+$ are different by an approximate order of magnitude. This suggests that $(^1\Sigma^+)$HBeHe$^+$ exists essentially as a complex of the form HBe$^+$-He. This is confirmed by the study of Page *et al.* [5], who calculated the Be-H and Be-He bond orders to be 1.002 and 0.126, respectively, using RHF. Thus, H and Be$^+$ share a covalent bond, whereas the Be-He bond arises from an electrostatic interaction. This conclusion is in agreement with that of Antoniotti *et al.* [18]. A similar trend in binding energies is evident for $(^1\Sigma^+)$HMgHe$^+$. For example, $D_e(1)$ and $D_e(2)$ values calculated using the methods of this work are *ca.* 8 and 200 kJ mol^{-1}, respectively. As such, it is estimated that the strength of the Mg$^+$-He bond is approximately 3% of that of the Mg$^+$-H bond. A similar analysis for $(^1A')$HCaHe$^+$ gives an estimated Ca$^+$-He bond strength of *ca.* 2%. From these data a concomitant decrease in M$^+$-He bond orders would therefore be expected.

These trends with respect to HMHe$^+$ helium binding energies may be understood with recourse to an AO density analysis of the electronic wave function of each species. In particular, a successive decrease of M$^+$ p-orbital density in the HOMO/LUMO is observed for M = Be, Mg and Ca. This is complemented by a successive increase in M$^+$ s-orbital character with increasing M atomic number. Following the arguments developed by Breckenridge *et al.* [39–41] (with respect to species such as BeHe$^+$, BeHe^{2+}, MgHe$^+$ and MgHe^{2+}) these fluctuating M$^+$ p/s orbital populations are seen to result in an increased repulsive 'σ/σ' interaction between the MH$^+$ unit and He. Conversely, the magnitude of the quadrupole/induced-dipole attractive forces experienced at small distances between MH$^+$ and He diminishes with increasing M atomic number.

6.4.2. $HMHe^{2+}$ (M = Be, Mg, Ca)

Equilibrium parameters including R_e(M-H), R_e(M-He), θ_e, ω_1, ω_2 and ω_3 of $HMHe^{2+}$ (M = Be, Mg, Ca) have been calculated using UCCSD(T), IC-MRCI and IC-MRCI+Q. These data are presented in Table 6.6.

No experimental or theoretical data for $HMHe^{2+}$ (M = Be, Mg, Ca) have been reported in the literature to date. Nevertheless, the methods of this work predict PES minima corresponding to equilibrium structures for each species. From comparison with data in Table 6.5 it is apparent that the spatial symmetry of the ground state of $HMHe^{n+}$ is independent of the charge for $n = 1, 2$. As such, both $HBeHe^{2+}$ and $HMgHe^{2+}$ exhibit $^2\Sigma^+$ structures, where as the ground state of $HCaHe^{2+}$ exhibits an equilibrium structure of C_s symmetry.

Table 6.6 shows that the single- and multi-reference methods of this work yield consistent results with respect to the ground state structures of $HMHe^{2+}$. For example, the largest deviations between UCCSD(T), IC-MRCI and IC-MRCI+Q values of R_e(Be-H) and R_e(Be-He) are 0.2 mÅ and 0.2 mÅ, respectively. These deviations for $(^2\Sigma^+)HMgHe^{2+}$ are 1.2 mÅ and 0.6 mÅ, while for $(^2A')HCaHe^{2+}$ they are 8.9 mÅ and 7.5 mÅ, respectively. These methods also yield θ_e values for the latter species in agreement to within 0.6°.

The motivations discussed previously regarding the dissociative processes of $HMHe^+$ have been employed in the investigation of the dissociative mechanisms of the respective dications. As such, the dissociative reactions,

$$D_e(1) : (^2\Sigma^+)HMHe^{2+} \rightarrow (^2\Sigma^+)MH^{2+} + (^1S_0)He \tag{6.9}$$

$$D_e(2) : (^2\Sigma^+)HMHe^{2+} \rightarrow (^1S_0)M^{2+} + (^2S_{1/2})H + (^1S_0)He \tag{6.10}$$

have been considered in this work. For $(^2\Sigma^+)HBeHe^{2+}$ the $D_e(1)$ and $D_e(2)$ values

Table 6.6 *Ab initio* equilibrium parameters of $HMHe^{2+}$, M = Be, Mg, Ca.

Method	R_e (M-H) (/Å)	R_e (M-He) (/Å)	θ_e (/°)	D_e[a] (/kJmol^{-1})		Frequencies (/cm^{-1})		
				1	2	ω_1	ω_2	ω_3
			$(^2\Sigma^+)HBeHe^{2+}$					
UCCSD(T)	1.8002	1.4429	180.0	79.67	244.4	845	132	1072
IC-MRCI	1.8002	1.4427	180.0	79.76	244.3	880	167	1120
IC-MRCI+Q	1.8004	1.4429	180.0	78.87	244.5	841	144	1031
			$(^2\Sigma^+)HMgHe^{2+}$					
UCCSD(T)	2.1778	1.9039	180.0	29.96	98.65	535	96	503
IC-MRCI	2.1790	1.9043	180.0	29.54	84.61	851	174	618
IC-MRCI+Q	2.1779	1.9045	180.0	29.44	97.88	521	120	448
			$(^2A')HCaHe^{2+}$					
UCCSD(T)	2.5855	2.3675	121.7	13.71	45.81			
IC-MRCI	2.5944	2.3750	121.1	13.30	38.25			
IC-MRCI+Q	2.5867	2.3703	121.2	13.83	51.57			

[a] $D_e(1)$ and $D_e(2)$ correspond to dissociation reactions (6.9) and (6.10), respectively.

listed in Table 6.6 are indicative of significantly different energetics with respect to $(^1\Sigma^+)HBeHe^+$. In particular, these data suggest that the Be^{2+}-He interaction in $(^2\Sigma^+)HBeHe^{2+}$ is stronger than the Be^+-He interaction in $(^1\Sigma^+)HBeHe^+$. For example, reactions (6.7) and (6.9) correspond to potential well-depths of *ca.* 36 and 79 kJ mol^{-1}, respectively. The ω_1:ω_3 ratios of these two species complement these dissociative data, since they are indicative of the relative potential curvatures in the [BeH^{n+} + He] dissociative channels. By averaging the UCCSD(T), IC-MRCI and IC-MRCI+Q ω_1 and ω_3 values, these ratios are *ca.* 1:1.86 and 1:1.25 for $(^1\Sigma^+)HBeHe^+$and $(^2\Sigma^+)HBeHe^{2+}$, respectively. A similar analysis has been applied to compare $(^1\Sigma^+)HMgHe^+$and $(^2\Sigma^+)HMgHe^{2+}$. In this case the difference between the mono- and di-cationic species is more noticeable. For instance, the binding energies corresponding to (6.7) and (6.9) are *ca.* 7 and 30 kJ mol^{-1}. The binding energy of the atomisation reactions (6.8) and (6.10) are *ca.* 205 and 90 kJ mol^{-1}, respectively. The ω_1:ω_3 ratios for the magnesium species are also exaggerated compared to the beryllium analogues. Using mean values of ω_1 and ω_3, these

ratios are *ca.* 1:2.38 and 1:0.82 for $(^1\Sigma^+)$HMgHe$^+$and $(^2\Sigma^+)$HMgHe^{2+}, respectively.

6.4.3. Isovalent Comparisons

From comparison of Tables 6.5 and 6.6 it is evident that the isovalent pairs ($(^1\Sigma^+)$HBeHe$^+$, $(^1\Sigma^+)$HMgHe$^+$) and ($(^2\Sigma^+)$HBeHe^{2+}, $(^2\Sigma^+)$HMgHe^{2+}) exhibit equilibrium structures of identical symmetries, in agreement with the Walsh rules. Moreover, the increase in M-H and M-He bond lengths in both pairs may be largely ascribed to the relative ionic radii of Be^+/Mg^+ and Be^{2+}/Mg^{2+}. Nevertheless, the ground state equilibrium bond angle of both HCaHe$^+$ and HCaHe^{2+} are significantly different than both ($(^1\Sigma^+)$HBeHe$^+$, $(^1\Sigma^+)$HMgHe$^+$) and ($(^2\Sigma^+)$HBeHe^{2+}, $(^2\Sigma^+)$HMgHe^{2+}), respectively. This occurs in both cases despite each species possessing the same valence shell occupation. Nevertheless, no stationary point on the ground state PES of either HCaHe$^+$ or HCaHe^{2+} has been located [21]. The optimisation algorithm of Page and von Nagy-Felsobuki [21] has been employed in this work to construct MEPs for the ground states of HMgHe^{2+} and HCaHe^{2+}. The resultant PESs are compared to those of $(^1\Sigma^+)$HMgHe$^+$ and $(^1A')$HCaHe$^+$ in Appendix F. It is obvious from this comparison that no stable linear conformation for HCaHe^{2+} exists. However, HMgHe^{2+} resides in a relatively deep potential well, in a similar fashion to HMgHe$^+$. Page and co-workers [17, 21] have rationalised these discrepant equilibrium structures using qualitative MO arguments, *viz.* comparison of the energies and symmetries of the lowest unoccupied MO energies in the diatomic fragment ions BeH$^+$, MgH$^+$and CaH$^+$.

Similar trends are noticed with the relative atom-diatom potential well-depths of the ($(^1\Sigma^+)$HBeHe$^+$, $(^1\Sigma^+)$HMgHe$^+$, $(^1A')$HCaHe$^+$) and ($(^2\Sigma^+)$HBeHe^{2+}, $(^2\Sigma^+)$HMgHe^{2+}, $(^2A')$HCaHe^{2+}) isovalent series. For instance, from Tables 6.5 it is observed that the potential well-depths of equations (6.7) for $(^1\Sigma^+)$HBeHe$^+$,

($^1\Sigma^+$)HMgHe$^+$and (^{1}A$'$)HCaHe$^+$ are *ca.* 36, 7 and 4 kJ mol^{-1}, respectively. Similarly, for ($^2\Sigma^+$)HBeHe^{2+}, ($^2\Sigma^+$)HMgHe^{2+}and (^{2}A$'$)HCaHe^{2+} these well-depths are *ca.* 79, 29 and 13 kJ mol^{-1}, respectively. From these data it may be inferred that both the M-He and M-H bond strengths decrease with increasing M^{2+} polarisability. This trend appears to be independent of the metal ion charge.

Electron density analyses have been performed for the ground states of HMHe^{n+} so that these trends observed with respect to structures and energetics may be elucidated further. Electron density plots for HMHe^{n+} ($n = 1, 2$) have been calculated using IC-MRCI and are given in Appendix F. The corresponding MEDs along the internuclear vectors are also given in Appendix F. Pertinent data relative to the present context are listed in Table 6.7. These data support the previous inference with respect to the relative M-H and M-He bond strengths of HMHe^{n+} ($n = 1, 2$). For example, a monotonic decrease in ρ_b(M-H) and ρ_b(M-He) is observed for both the mono- and dications, indicating that the degree of binding is inversely proportional to the M$^+$ polarisability. In the case of the dications, comparison of the relative values of ρ_b(M-H) and ρ_b(M-He) for each species indicates that the HeM^{2+}-H nature of these complexes also decreases with increasing polarisability of M. For example, both ($^2\Sigma^+$)HBeHe^{2+} and ($^2\Sigma^+$)HMgHe^{2+} are such that ρ_b(M-H)$<$ ρ_b(M-He), whereas for (^{2}A$'$)HCaHe^{2+} these values are 0.08 and 0.09

Table 6.7 IC-MRCI values of ρ_b and $\mathbf{R}_b$ for HMHe^{n+} (M = Be, Mg, Ca; $n = 1, 2$).

	ρ_b (M-H) (/e Å^{-3})	$\mathbf{R}_b/R_e$ (M-H)[a] (/Å)	ρ_b (M-He) (/e Å^{-3})	$\mathbf{R}_b/R_e$ (M-He)[a] (/Å)
($^1\Sigma^+$)HBeHe$^+$	0.74	0.42	0.23	0.40
($^1\Sigma^+$)HMgHe$^+$	0.43	0.52	0.07	0.49
(^{1}A$'$)HCaHe$^+$	0.43	0.68	0.04	0.54
($^2\Sigma^+$)HBeHe^{2+}	0.25	0.39	0.40	0.48
($^2\Sigma^+$)HMgHe^{2+}	0.12	0.47	0.15	0.49
(^{2}A$'$)HCaHe^{2+}	0.08	0.54	0.09	0.56

[a]Displacement along the M-H/M-He bond relative to M.

e $\mathrm{\AA}^{-3}$, respectively.

6.5. Alkaline-Earth Metal Dihelide Cations: MHe_2^{n+} (n = 1, 2)

6.5.1. MHe_2^+ (M = Be, Mg, Ca)

Equilibrium structures and harmonic vibration frequencies of the $^2A_1$ ground states of $BeHe_2^+$, $MgHe_2^+$ and $CaHe_2^+$ have been calculated using UCCSD(T), IC-MRCI and IC-MRCI+Q. These data are presented in Table 6.8. No alkaline-earth metal dihelide ion has been identified or characterised experimentally to date. Therefore, the results of this work may only be compared with previous *ab initio* values.

It is evident from Table 6.8 that the UCCSD(T), IC-MRCI and IC-MRCI+Q equilibrium parameters of $BeHe_2^+$ of this work are in excellent agreement with those reported by Page *et al.* [15] using the same correlated approaches. The latter investigation employed aug-CVQZ (Be) [15, 32] and aug-cc-pVQZ (H, He) [31, 33] basis sets. For example, R_e values calculated using CCSD(T), IC-MRCI and IC-MRCI+Q differ by *ca.* 8.0, 8.0 and 5.0 mÅ, respectively. Similar accuracy is observed with respect to values of θ_e. The MP2 values of Bu and Zhong [13] and Page *et al.* [15], the former of which employed 6-311+G(3*df*,3*pd*) basis sets, give slightly larger values of R_e and θ_e, as anticipated. There is greater variance between the *ab initio* binding energies of this work and those reported in the literature. This is particularly the case for the first of the following dissociation reactions,

$$(^2A_1)MHe_2^+ \rightarrow (^2\Sigma^+)MHe^+ + (^1S_0)He \tag{6.11}$$

$$(^2A_1)MHe_2^+ \rightarrow (^2S_{1/2})M^+ + 2(^1S_0)He \tag{6.12}$$

With respect to equation (6.11), UCCSD(T), IC-MRCI and IC-MRCI+Q yield well-

Table 6.8 *Ab initio* equilibrium parameters of $(^2A_1)MHe_2^+$, M = Be, Mg, Ca.

Method	R_e (/Å)	θ_e (/°)	D_e[a] (/kJmol^{-1})		Frequencies (/cm^{-1})		
			1	2	ω_1	ω_2	ω_3
			$BeHe_2^+$				
UCCSD(T)[b]	2.9336	59.7	1.601	3.101	78	35	67
IC-MRCI[b]	2.9263	59.9	2.073	2.604	59	14	58
IC-MRCI+Q[b]	2.9253	60.3	0.905	3.401	83	64	61
MP2[c]	3.085	61.3	1.8923	2.2228	69	25	60
MP2[d]	3.020	60.6	1.3334	2.6002	89.4	46.4	64.2
CCSD(T)[d]	2.942	60.1	1.6310	3.1608	82.2	43.4	70.6
IC-MRCI[d]	2.934	59.9	1.3322	2.7877	65.9	23.3	71.1
IC-MRCI+Q[d]	2.920	60.2	1.7998	3.2085	67.3	23.7	68.1
			$MgHe_2^+$				
UCCSD(T)[b]	3.5048	50.9	0.917	1.742	49	28	44
IC-MRCI[b]	3.5896	49.6	0.653	1.461	13	58	43
IC-MRCI+Q[e]	3.5062	51.3	0.873	1.155	56	36	48
MP2[c]	3.600	51.9			23	46	43
MP2[e]	3.602	52.47	2.0455		21.45	45.85	42.65
			$CaHe_2^+$				
UCCSD(T)[b]	4.2857	39.5	0.500	0.910	41	67	31
IC-MRCI[b]	4.3367	43.8	0.444	0.763	33	40	27
IC-MRCI+Q[b]	4.2291	41.4	0.555	0.729	41	57	33
B3LYP[f]	4.05	57.8	0.013		62.3	33.1	54.3

[a] $D_e(1)$ and $D_e(2)$ correspond to dissociation reactions (6.11) and (6.12), respectively.
[b] This work.
[c] In conjunction with 6-311+G(3*df*,3*pd*) basis sets; see reference [13, 14].
[d] In conjunction with aug-CVQZ (Be) [15, 32] and aug-cc-pVQZ basis sets. MP2, CCSD(T) and IC-MRCI+Q values are BSSE corrected; see reference [15].
[e] In conjunction with the 6-311+G(3*df*,3*pd*) basis set; see reference [19].
[b] In conjunction with the 6-311+G(3*df*) basis set; see reference [20].

depths of 1.601, 2.073 and 0.905 kJ mol^{-1}, respectively. Although this UCCSD(T) result is in good agreement with the corresponding CCSD(T) value of Page *et al.* [15], the difference in the results of the multi-reference methods are more noticeable, being *ca.* 0.7 kJ mol^{-1}. Nevertheless, the topological curvature of the IC-MRCI+Q molecular PES constructed by Page *et al.* [15] is extremely small in the dissociative regions. Indeed, the dissociative potential wall in the He-Be-He bend co-ordinate is *ca.* 25 cm^{-1}, as can be seen from Figure 6.2. As such, the dissociative energetics of this molecule are likely to be extremely sensitive to the *ab initio* method employed. The

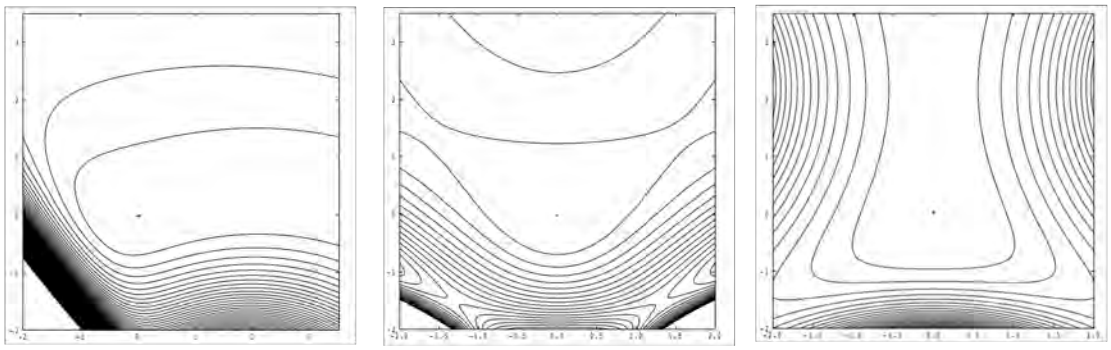

Figure 6.2 Two-dimensional projections of the IC-MRCI+Q+BSSE (4,4) Padé SPF PEF of $(^2A_1)BeHe_2^+$ [15] (in a_0): (a) t_2 (x) versus t_1 (y); (b) t_3 (x) versus t_1 (y), and; (c) t_3 (x) versus t_2 (y). Contours are spaced at increments of 1 kJ mol^{-1}.

IC-MRCI+Q PEF of Page *et al.* [15] is given as a FORTRAN subroutine in Appendix F, as is the IC-MRCI+Q discrete PES. The shallow nature of the $(^2A_1)BeHe_2^+$ PES is also apparent upon comparison of harmonic vibration frequencies. For example, it can be seen from Table 6.8 that each fundamental mode exhibits a frequency less than *ca.* 100 cm^{-1}, irrespective of the method employed. These data provide further indication as to the extremely weak nature of the bonding exhibited by the ground state of $BeHe_2^+$.

In a similar manner to the molecular dihydride cations discussed in §6.3, the increase in the equilibrium R_e(M-He) values observed with the increasing polarisability of M is ascribed to the increasing ionic radii of the central metal ion. Nevertheless, the bonding in the ground states of MHe_2^+ are significantly different in nature to that of MH_2^+. From Table 6.8 it is evident that UCCSD(T) and IC-MRCI+Q give consistent equilibrium parameters of $MgHe_2^+$ to within 1.4 mÅ (R_e) and 0.4° (θ_e). The +Q correction to the IC-MRCI wave function decreases the value of R_e by *ca.* 80 mÅ. However, these equilibrium structures differ significantly from those calculated by Sapse *et al.* [19] and Bu *et al.* [13, 14] who employed MP2/6-311+G(3*df*,3*pd*). For example, the latter R_e values are *ca.* 100 mÅ larger than those

of this work. The single- and multi-reference methods employed presently therefore suggest a more tightly bound complex than has been previously reported. This fact is also evident upon comparison of the potential well-depths for equation (6.11) calculated in this work and the MP2/6-311+G(3*df*,3*pd*) value. Explicitly, the latter value is *ca.* 1.0-1.5 kJ mol^{-1} larger than the values reported in this work.

The only equilibrium structure for $(^2A_1)CaHe_2^+$ reported in the literature is that of Jalbout and Solimannejad [20], who employed B3LYP/6-311+G(3*df*). According to this method and those employed in the present work, the ground state of $CaHe_2^+$ is extremely weakly bound with respect to equation (6.11). For example, this well-depth using B3LYP/6-311+G(3*df*) is calculated to be 0.013 kJ mol^{-1}. Using UCCSD(T), IC-MRCI and IC-MRCI+Q, this well-depth is an order of magnitude larger at *ca.* 0.5 kJ mol^{-1}. There are similar discrepancies with respect to the equilibrium parameters of $(^2A_1)CaHe_2^+$. For instance, the values of R_e and θ_e calculated in this work are *ca.* 0.2-0.3 Å larger and *ca.* 18-14° smaller than the values of Jalbout and Solimannejad [20], respectively. Wilson and von Nagy-Felsobuki [42–47] have discussed and established the shortcomings of applying DFT to helium bonding with respect to small TM-helide cations.

6.5.2. MHe_2^{2+} (M = Be, Mg, Ca)

Equilibrium parameters for the ground states of MHe_2^{2+} (M = Be, Mg, Ca) have been calculated using UCCSD(T), IC-MRCI and IC-MRCI+Q. These data are collated in Table 6.9. Potential well-depths corresponding to the dissociative reactions

$$MHe_2^{2+} \rightarrow (^1\Sigma^+)MHe^{2+} + (^1S_0)He \quad (6.13)$$

$$MHe_2^{2+} \rightarrow (^1S_0)M^{2+} + 2(^1S_0)He \quad (6.14)$$

Table 6.9 *Ab initio* equilibrium parameters of MHe_2^{2+}, M = Be, Mg, Ca.

Method	R_e (/Å)	θ_e (/°)	D_e[a] (/kJmol^{-1})		Frequencies (/cm^{-1})		
			1	2	ω_1	ω_2	ω_3
			$(^1\Sigma_g^+)BeHe_2^{2+}$				
UCCSD(T)[b]	1.4373	180.0	85.04	175.1	729	101	1004
IC-MRCI[b]	1.4373	180.0	85.10	175.9	765	102	1021
IC-MRCI+Q[b]	1.4373	180.0	84.30	174.1	738	102	1010
HF[c]	1.44	180.0	74.1				
CCSD(T)[d]	1.4373	180.0	84.98		730.8	13.7	995.2
IC-MRCI[d]	1.4372	180.0	85.01		727.1	105.2	1010
IC-MRCI+Q[d]	1.4373	180.0	84.24				
			$(^1\Sigma_g^+)MgHe_2^{2+}$				
UCCSD(T)[b]	1.8960	180.0	31.46	63.56	446	47	508
IC-MRCI[b]	1.8964	180.0	29.05	62.48	448	48	513
IC-MRCI+Q[b]	1.8936	180.0	30.66	62.88	450	47	510
MP2[e]	1.911	135.9	27.90	56.15	413	45	453
			$(^1A_1)CaHe_2^{2+}$				
UCCSD(T)[b]	2.3667	106.0	13.85	27.91			
IC-MRCI[b]	2.3516	109.9	14.17	36.20			
IC-MRCI+Q[b]	2.3419	108.1	14.60	28.60			

[a] $D_e(1)$ and $D_e(2)$ correspond to dissociation reactions (6.13) and (6.14), respectively.
[b] This work.
[c] See reference [16].
[d] R_e, θ_e and D_e values are corrected for basis set superposition error, calculated in conjunction with the aug-CVQZ (Be) [15, 32] and aug-cc-pVQZ (He) basis sets. CCSD(T) ω values are harmonic and neglect basis set superposition error correction. IC-MRCI ω values are anharmonic and include basis set superposition error correction; see reference [17].
[e] In conjunction with the 6-311+G(3*df*,3*pd*) basis set; see reference [13].

have been considered here.

With respect to the $^1\Sigma_g^+$ ground state of $BeHe_2^{2+}$, comparison is only possible with theoretical values since no experimental data for $(^1\Sigma_g^+)BeHe_2^{2+}$ is available. The UCCSD(T), IC-MRCI+Q and IC-MRCI $(^1\Sigma_g^+)BeHe_2^{2+}$ equilibrium structures are in exact agreement. Furthermore, these equilibrium bond lengths are in excellent agreement with the CCSD(T), IC-MRCI and IC-MRCI+Q values reported by Page *et al.* [17], with the largest difference between R_e values being 0.1 mÅ. The inclusion of correlation in the description of the $(^1\Sigma_g^+)BeHe_2^{2+}$ ground state therefore has a negligible effect on the equilibrium geometry in the region of the minimum of PES.

For instance, optimised UCCSD(T), IC-MRCI and IC-MRCI+Q structures differ from the HF structure of Harrison *et al.* [16] by *ca.* -3.0 mÅ. In this investigation the $(^1\Sigma_g^+)BeHe_2^{2+}$ ground state did not exhibit an energy conformer with a non-linear equilibrium structure.

The only previously reported equilibrium structure of the ground state of $MgHe_2^{2+}$ is that of Bu and Zhong [48], who used BSSE corrected MP2/6-311+G(3*df*,3*pd*). It is evident from Table 6.9 that using all methods of this work R_e is *ca.* 20 mÅ smaller than the MP2/6-311+G(3*df*,3*pd*) [48] value. Conversely, the potential well-depths calculated in this work for the ground state of $MgHe_2^{2+}$ are larger than the MP2/6-311+G(3*df*,3*pd*) [48] values, for both equations (6.13) and (6.14). For instance, for the former dissociative reaction it is seen from Table 6.9 that the potential well-depths calculated in this work differ from the MP2/6-311+G(3*df*,3*pd*) [48] value by *ca.* 2.5-3.5 kJ mol^{-1}. For the latter reaction, this difference is *ca.* 7 kJ mol^{-1}. It is therefore concluded that the single- and multi-reference wave functions employed here predict the $^1\Sigma_g^+$ ground state of $MgHe_2^{2+}$ to be more strongly bound than has been previously reported. The largest discrepancy between the results of this work and those of Bu and Zhong [48] is that observed with respect to the θ_e value for $(^1\Sigma_g^+)MgHe_2^{2+}$. In particular, using MP2/6-311+G(3*df*,3*pd*), Bu and Zhong [48] determined this bond angle to be 135.9°. However, no potential minimum corresponding to a non-linear equilibrium structure could be located using UCCSD(T) or IC-MRCI+Q (*vide infra*). The ω_1 fundamental frequencies calculated for $(^1\Sigma_g^+)MgHe_2^{2+}$ differ from the MP2/6-311+G (3*df*,3*pd*) [48] value by *ca.* 40 cm^{-1}. For ω_2 these differences are *ca.* 3 cm^{-1}, whilst for ω_3 these differences are an order of magnitude larger, being *ca.* 60 cm^{-1}.

The *ab initio* equilibrium structures of the ground state of $CaHe_2^{2+}$ reported by Page and von Nagy-Felsobuki [21] are the only data available for this species.

From Table 6.9 it is evident that these equilibrium structures are reasonably consistent, with R_e and θ_e values agreeing to within *ca.* 10 mÅ and 4°, respectively. These data indicate the sensitivity of the molecular PES topology with respect to the *ab initio* method employed. The $^1A_1$ ground state of $CaHe_2^{2+}$ exhibits a quasi-linear structure, and so is consistent with its isoelectronic analogue $(^1A')HCaHe^+$. However, the $^1A_1$-$^1\Sigma_g^+$ potential barrier for $CaHe_2^{2+}$ is substantially smaller. Page and von Nagy-Felsobuki [21] have reported this barrier to be 3.53 and 2.85 cm^{-1} using UCCSD(T) and IC-MRCI+Q, respectively, suggesting that the fluxional nature of these helide ions increases proportionally with helium substitution.

6.5.3. Isovalent Comparisons

It is appropriate to compare the properties of isovalent series $(^2A_1)BeHe_2^+$, $(^2A_1)MgHe_2^+$, $(^2A_1)CaHe_2^+$), $(^1\Sigma_g^+)BeHe_2^{2+}$, $(^1\Sigma_g^+)MgHe_2^{2+}$ and $(^1A_1)CaHe_2^{2+}$). From Table 6.8 it is seen that the ground states of $BeHe_2^+$, $MgHe_2^+$ and $CaHe_2^+$ correspond to equilibrium structures of C_{2v} symmetry. However, these structures exhibit quantitatively different equilibrium geometries. For example, R_e values for $(^2A_1)BeHe_2^+$, $(^2A_1)MgHe_2^+$ and $(^2A_1)CaHe_2^+$ are *ca.* 2.9, 3.5 and 4.2 Å, respectively. There is a complementary decrease in θ_e for this series also. In particular, θ_e for $(^2A_1)BeHe_2^+$, $(^2A_1)MgHe_2^+$ and $(^2A_1)CaHe_2^+$ have been calculated to be *ca.* 60, 50 and 40°, respectively. It is inferred from these data that the electrostatic nature of the M-He bond increases with increasing M^{n+} polarisability, independently of charge (n = 1, 2).

This conclusion is also reached upon consideration of the potential well-depths corresponding to equations (6.11) and (6.13). For example, for the former dissociation reaction these potential well-depths have been calculated to be *ca.* 1.5, 1.0 and 0.5 kJ mol^{-1}, respectively, whereas for the latter the well-depths are *ca.* 3.0, 1.5 and 1.0 kJ mol^{-1}. These binding energies are quantitatively very similar to the

atomisation energies for each species (*i.e.* equations (6.12) and (6.14)). The relative binding energies of both helium atoms to the metal ion may be assessed using the Δ values listed in Table 6.10. It is seen from this table that for MHe_2^+ both M^+-He bonds are almost identical in an energetic sense. For example, for $BeHe_2^+$, $MgHe_2^+$ and $CaHe_2^+$ exhibit Δ values of *ca.* 1, 0.5 and 0.1 kJ mol^{-1}, respectively. This is contrary in nature to the trends observed in §6.3.3, with respect to the ground states of $BeHe_2^+$, $MgHe_2^+$ and $CaHe_2^+$.

Similar trends to those observed with respect to the ground state structures of the hydrohelide species discussed in §6.4 are also evident. For example, both ($BeHe_2^+$, $MgHe_2^+$) and ($BeHe_2^{2+}$, $MgHe_2^{2+}$) exhibit symmetrically identical ground states. The ground state equilibrium structure of $CaHe_2^{2+}$ differs from those of $BeHe_2^{2+}$ and $MgHe_2^{2+}$, despite possessing the same valence shell occupation. Page *et al.* [17, 21] have argued that these structures arise from the relative energies and symmetries of the lowest unoccupied MO energies in the diatomic fragment ions $BeHe^{2+}$, $MgHe^{2+}$ and $CaHe^{2+}$, respectively. These differences are also illustrated by the comparison of the MEPs in the He-M-He bend co-ordinate, which have been constructed using the same constrained-angle optimisation approach employed for $HMgHe^{n+}$ and $HCaHe^{n+}$. These MEPs are included in Appendix F.

In order to further illustrate these bonding trends for the ground states of

Table 6.10 Binding energies (/kJ mol^{-1}) for successive helium addition of M^+ ions (M = Be, Mg, Ca).

	$BeHe_2^+$			$MgHe_2^+$			$CaHe_2^+$		
Method	$D_e(2)$	$D_e(3)$	Δ^a	$D_e(2)$	$D_e(3)$	Δ^a	$D_e(2)$	$D_e(3)$	Δ^a
UCCSD(T)	1.601	3.101	-0.101	0.917	1.742	-0.091	0.500	0.910	-0.091
IC-MRCI	2.073	2.604	-1.542	0.653	1.461	0.155	0.444	0.763	-0.124
IC-MRCI+Q	0.905	3.401	1.592	0.873	1.155	-0.591	0.555	0.729	-0.380

[a] $D_e(1)$ and $D_e(2)$ correspond to dissociative reactions (6.11) and (6.12), respectively. Δ D_e values are defined as $D_e(2) - 2D_e(1)$ and it is assumed both M-He bonds are identical.

MHe_2^+ and MHe_2^{2+}, densities and MEDs have been calculated using IC-MRCI. These are depicted in Appendix F, and summarised in terms of ρ_b and $\mathbf{R}_b/R_e$ in Table 6.11. It is evident that the dependence of bond strength on the polarisability of the metal ion is replicated in these data. For example, ρ_b for MHe_2^{2+} are 0.34, 0.15 and 0.09 e Å^{-3}, respectively. The data in Table 6.11 succinctly convey the weakness of the MHe_2^+ bonding. For example, $BeHe_2^+$, $MgHe_2^+$ and $CaHe_2^+$ exhibit ρ_b values of 0.02, 0.01 and 4.09×10^{-3} e Å^{-3}, respectively. Using the present nomenclature for what constitutes a chemical bond, it is concluded that the ground states of MHe_2^+ (M = Be, Mg, Ca) are the result of purely dispersive and electrostatic interactions.

Table 6.11 IC-MRCI values of ρ_b and $\mathbf{R}_b$ for MHe_2^{n+} (M = Be, Mg, Ca; $n = 1, 2$).

	ρ_b (/e Å^{-3})	$\mathbf{R}_b/R_e$ [a] (/Å)
$(^2A_1)BeHe_2^+$	0.02	0.54
$(^2A_1)MgHe_2^+$	0.01	0.58
$(^2A_1)CaHe_2^+$	4.09×10^{-3}	0.62
$(^1\Sigma_g^+)BeHe_2^{2+}$	0.34	0.41
$(^1\Sigma_g^+)MgHe_2^{2+}$	0.15	0.50
$(^1A_1)CaHe_2^{2+}$	0.09	0.56

[a]Displacement along the M-He bond relative to M.

6.6. Isoelectronic Comparisons of Helide Species

The limitations of the isoelectronic argument have been established previously with respect to main-group [23, 35] and TM [42, 43] helide ion chemistry. It is therefore constructive to determine the efficacy of this argument in the context of the alkaline earth metal helide ions. Although MH_2^+ and $HMHe^{2+}$ are isoelectronic, it is not feasible to consider these species in an isoelectronic sense. This conclusion has been reached following the discussion presented in this Chapter concerning the disparate natures of the bonding mechanisms in the respective species. As such,

the present isoelectronic discussion will be limited to comparisons between species of form $HMHe^+$ and MHe_2^{2+}.

Data pertinent to the consideration of the isoelectronic comparison between the ground states of $HMHe^+$ and MHe_2^{2+} are reiterated in Table 6.12, for convenience. Without loss of generality, all isoelectronic comparisons are made using IC-MRCI+Q. It is immediate that there is little consistency between the isoelectronic species $HMHe^+$ and MHe_2^{2+}. For example, the ground states of $HBeHe^+$ and $BeHe_2^{2+}$ exhibit R_e(Be-He) values of 1.5177 and 1.4373 Å, respectively, and thus differ by 80.4 mÅ. The dissociative potential well-depths with respect to the loss of a single helium atom are 35.67 and 84.30 kJ mol^{-1}, respectively. These data indicate that $(^1\Sigma_g^+)BeHe_2^{2+}$ is significantly more tightly bound than $(^1\Sigma^+)HBeHe^+$. The values of ρ_b(Be-He) for $(^1\Sigma^+)HBeHe^+$ and $(^1\Sigma_g^+)BeHe_2^{2+}$, calculated to be 0.23 and 0.34 eÅ^{-3}, respectively, support this conclusion. Nevertheless, the polarity of the Be-He bonds in these species, indicated by the relative values of $\mathbf{R}_b$(Be-He), are 0.61 and 0.59 Å, respectively.

Similar inconsistencies in structural and energetic parameters are observed for the isoelectronic $(^1\Sigma^+)HMgHe^+$ and $(^1\Sigma_g^+)MgHe_2^{2+}$. For example, the respective R_e(Mg-He) values are 2.1689 and 1.8936 Å, respectively, and so exhibit a difference of 275.3 mÅ. Similarly, the removal of a single helium atom from both species corresponds to well-depths of 7.806 and 30.66 kJ mol^{-1}, values differing by an approximate factor of 4. With respect to IC-MRCI MED data, the discrepancies for these species are also exaggerated with respect to the beryllium analogues. For instance, ρ_b(Mg-He) are calculated to be 0.07 and 0.15 eÅ^{-3}, respectively. It is estimated therefore that the Mg-He bond strength in $(^1\Sigma^+)HMgHe^+$ is approximately double that in $(^1\Sigma_g^+)MgHe_2^{2+}$. However, $\mathbf{R}_b$(Mg-He) are reasonably consistent, with $(^1\Sigma^+)HMgHe^+$ and $(^1\Sigma_g^+)MgHe_2^{2+}$ exhibiting values of 1.07 and 0.95 Å, respectively.

Table 6.12 Comparison of $HMHe^+$ and MHe_2^{2+} using IC-MRCI+Q, M = Be, Mg, Ca.

	R_e(M-He) (/Å)	θ_e (/°)	D_e[a] (/kJ mol^{-1})	ρ_b(M-He)[b] (/e Å^{-3})	$\mathbf{R}_b$(M-He)[b] (/Å)
$(^1\Sigma^+)$HBeHe$^+$	1.5177	180.0	35.67	0.23	0.61
$(^1\Sigma_g^+)$BeHe$_2^{2+}$	1.4373	180.0	84.30	0.34	0.59
$(^1\Sigma^+)$HMgHe$^+$	2.1689	180.0	7.806	0.07	1.07
$(^1\Sigma_g^+)$MgHe$_2^{2+}$	1.8936	180.0	30.66	0.15	0.95
$(^1A')$HCaHe$^+$	2.6309	113.3	4.103	0.04	1.44
$(^1A_1)$CaHe$_2^{2+}$	2.3419	108.1	14.60	0.09	1.32

[a]Corresponds to dissociation into $[(^1\Sigma^+)MH^+ + (^1S_0)He]$ and $[(^1\Sigma^+)MHe^{2+} + (^1S_0)He]$, respectively.
[b]IC-MRCI values.

A comparison of R_e(Mg-He) and $\mathbf{R}_b$(Mg-He) reveals that the polarity of the Mg-He bonds in both $(^1\Sigma^+)$HMgHe$^+$ and $(^1\Sigma_g^+)$MgHe$_2^{2+}$are shifted towards the helium nucleus, relative to the analogous beryllium species.

Both $(^1A')$HCaHe$^+$ and $(^1A_1)$CaHe$_2^{2+}$ exhibit non-linear equilibrium structures, with bond angles of 113.3 and 108.1°, respectively. Nevertheless, Page and von Nagy-Felsobuki [21] reported IC-MRCI+Q $^1A'$-$^1\Sigma^+$ and $^1A_1$-$^1\Sigma_g^+$ barrier heights for HCaHe$^+$ and CaHe$_2^{2+}$ of 117.15 and 2.85 cm^{-1}, respectively. These data illustrate the differences in the PES topology in the X-Ca-Y bond angle co-ordinate. Identical trends in R_e, D_e, ρ_b and $\mathbf{R}_b$ observed for isoelectronic beryllium and magnesium species are also evident for $(^1A')$HCaHe$^+$ and $(^1A_1)$CaHe$_2^{2+}$. For example, R_e(Ca-He) values for these two species differ by 289.0 mÅ, respectively, whereas the D_e values differ by *ca.* 10.50 kJ mol^{-1}. The latter figure corresponds to a factor of *ca.* 3.5. Both ρ_b(Ca-He) and $\mathbf{R}_b$(Ca-He) here are indicative of extremely weakly bound complexes. Nevertheless, ρ_b(Ca-He) for $(^1A')$HCaHe$^+$ is approximately half that for $(^1A_1)$CaHe$_2^{2+}$. It is interesting to note here that R_e(Ca-He) and $\mathbf{R}_b$(Ca-He) values indicate that the polarity of the Ca-He bond in both species is centred on the helium nucleus. For the beryllium and magnesium species presently under

discussion, the converse is the case.

6.7. *Ab Initio* Property Surfaces of MH_2^{2+}, $HMHe^{2+}$ (M = Mg, Be) and $MgHe_2^{2+}$

From the discussion presented in this Chapter it is evident that not all species of form MH_2^{n+}, $HMHe^{n+}$ and MHe_2^{n+} (M = Be, Mg, Ca and $n = 1, 2$) are suitable candidates for vibrational and rovibrational calculations. For example, it is generally observed from §6.3, 6.4 and 6.5 that the dications exhibit equilibria that are more thermodynamically stable compared to the respective monocations. This was particularly evident for the hydrohelide and dihelide ions. Similarly, the ground states of $HCaHe^{n+}$ and $CaHe_2^{n+}$ (n = 1, 2) are also deemed unsuitable for a normal co-ordinate vibrational analysis, due to their fluxional nature. Consequently, vibrational and rovibrational calculations have been limited to the ground states of MgH_2^{2+}, $HMHe^{2+}$ (M = Be, Mg) and $MgHe_2^{2+}$ in this Chapter.

Page and von Nagy-Felsobuki [7] reported an analytical PEF and DMF of the $^1A_1$ ground state of MgH_2^{2+} using the CCSD(T) method employed in this work. This method has been applied here to the $^2\Sigma^+$ and $^1\Sigma_g^+$ ground states of $HMgHe^{2+}$ and $MgHe_2^{2+}$, and the $^2\Sigma^+$ ground state of $HBeHe^{2+}$. Analytical PEFs and DMFs of these species have also been developed in this work. Page and von Nagy-Felsobuki also developed *ab initio* property surfaces for $(^1A_1)BeH_2^{2+}$ [5] and $(^1\Sigma_g^+)BeHe_2^{2+}$ [17] using IC-MRCI in conjunction with aug-CVQZ (Be) and aug-cc-pVQZ (H,He) basis sets. These surfaces were presented in Chapter Three, and rovibrational and vibrational spectra for these respective species were presented in Chapter Four. Discrete and analytical property surfaces for these molecules are detailed in Table 6.13. Discrete PES grids of $(^1A_1)MgH_2^{2+}$, $(^2\Sigma^+)HMHe^{2+}$ (M = Be, Mg) and $(^1\Sigma_g^+)MgHe_2^{2+}$ are included in Appendix F, as are their analytical representations. The latter are

provided as FORTRAN subroutines. Two-dimensional contour plots of all surfaces are also provided in Appendix F.

The analytical PEFs for $(^2\Sigma^+)$HBeHe^{2+}, $(^2\Sigma^+)$HMgHe^{2+} and $(^1\Sigma_g^+)$MgHe$_2^{2+}$ outlined in Table 6.13 exhibit $(\chi^2)^{1/2}$ values of 14.88, 10.97 and 10.95 cm^{-1}, respectively. As such, the accuracy of these fitted surfaces (with respect to the discrete *ab initio* grid) in the region employed for numerical integration may be questionable. However, these $(\chi^2)^{1/2}$ values serve to illustrate the difference between purely statistical and topological accuracies. For example, $\left(\overline{(\chi^2)^{1/2}}, \max\left[(\chi^2)^{1/2}\right]\right)$ for points on the $P(5,5)$ OGL $(^2\Sigma^+)$HBeHe^{2+} PEF with energies V such that $V < 3000$, $3000 < V < 6000$, $6000 < V < 9000$, $9000 < V < 12000$ and $12000 < V < 15000$ cm^{-1} are (2.19, 0.64), (2.41, 0.35), (3.95, 0.69), (9.22, 1.50) and (4.61, 1.74) cm^{-1}, respectively. The deviation between *ab initio* and fitted PES points therefore increases in the more geometrically remote areas of the PES domain. This observation is also made with respect to the $(^2\Sigma^+)$HMgHe^{2+} and $(^1\Sigma_g^+)$MgHe$_2^{2+}$ PEFs outlined in Table 6.13. In the context of the calculation of low-lying vibrational states, these increasing deviations are relatively insignificant, due to the rapid decay of the vibrational wave function in these areas of the PES domain.

6.8. *Ab Initio* Rovibrational Spectrum of $(^1\mathrm{A}_1)$MgH$_2^{2+}$

Low-lying *ab initio* 1D vibrational eigenvalues, VBOs, configuration assignments and vibration-averaged structures for the ground electronic state of $(^1\mathrm{A}_1)$MgH$_2^{2+}$, $(^1\mathrm{A}')$MgHD^{2+} and $(^1\mathrm{A}_1)$MgD$_2^{2+}$ are given in Appendix F. The numerical solution to the 1D nuclear Schrödinger equations for these species employed normal co-ordinate domains of [-2.0 a_0, 4.0 a_0] (t_1), [-1.0 a_0, 5.0 a_0] (t_2) and [-2.25 a_0, 2.25 a_0] (t_3).

Table 6.13 Property surfaces of MH_2^{2+}, $HMHe^{2+}$ and MHe_2^{2+} (M = Be, Mg).

Species	Ansatz	Reference	Potential Energy Surface				
			# Points	Function	Variable	SVD	$(\chi^2)^{1/2}$ (/cm^{-1})
$(^1A_1)BeH_2^{2+}$	IC-MRCI+BSSE[a]	[5]	89	$P(6,5)$	OGL	$\sigma_{65,67-69,71-83} = 0$	5.20
$(^2\Sigma^+)HBeHe^{2+}$	CCSD(T)+DK2+BSSE	This work	112	$P(5,5)$	OGL	$\sigma_{83,86-99} = 0$	14.88
$(^1\Sigma_g^+)BeHe_2^{2+}$	IC-MRCI+BSSE[a]	[17]	87	$P(6,5)$	EOGL	$\sigma_{60,62,65-74} = 0$	6.90
$(^1A_1)MgH_2^{2+}$	CCSD(T)+DK2+BSSE	[7]	96	$P(6,5)$	OGL	$\sigma_{70-83} = 0$	4.89
$(^2\Sigma^+)HMgHe^{2+}$	CCSD(T)+DK2+BSSE	This work	96	$P(5,4)$	EOGL	$\sigma_{66,69-74} = 0$	10.97
$(^1\Sigma_g^+)MgHe_2^{2+}$	CCSD(T)+DK2+BSSE	This work	100	$P(6,5)$	SPF	$\sigma_{56,58,61,62,64-74} = 0$	10.95
			Dipole Moment Surface				
			# Points	Power Series Order		$(\chi^2)^{1/2}$ (/a.u.)	
				μ_x	μ_y	μ_x	μ_y
$(^1A_1)BeH_2^{2+}$	IC-MRCI+BSSE[a]	[5]	73	7	6	2.09×10^{-4}	1.93×10^{-3}
$(^2\Sigma^+)HBeHe^{2+}$	CCSD(T)+DK2+BSSE	This work	91	6	6	4.46×10^{-3}	8.41×10^{-4}
$(^1\Sigma_g^+)BeHe_2^{2+}$	IC-MRCI+BSSE[a]	This work	57	5	5	9.20×10^{-4}	1.16×10^{-3}
$(^1A_1)MgH_2^{2+}$	CCSD(T)+DK2+BSSE	[7]	69	7	6	3.71×10^{-4}	1.16×10^{-3}
$(^2\Sigma^+)HMgHe^{2+}$	CCSD(T)+DK2+BSSE	This work	93	6	6	3.65×10^{-3}	2.33×10^{-7}
$(^1\Sigma_g^+)MgHe_2^{2+}$	CCSD(T)+DK2+BSSE	This work	91	6	6	1.11×10^{-2}	6.26×10^{-6}

[a]In conjunction with aug-CVQZ [15, 32] (Be) and aug-cc-pVQZ [31, 33] (H,He) basis sets.

A single dominant configuration is assigned to each of the lowest ten vibrational states of $(^1A_1)MgH_2^{2+}$. Moreover, none of these states possess leading configurations with excited quanta in the t_2 co-ordinate, a fact ascribed to the relative 1D PES curvatures in the t_1, t_2 and t_3 co-ordinates. As expected, the ground vibrational state of $(^1A_1)MgH_2^{2+}$ is composed primarily from the $|000\rangle$ configuration, which exhibits a weight of 0.94. Similarly, for the fundamental t_1 and t_3 modes (with VBOs at 754.6 and 796.9 cm^{-1}, respectively), the $|100\rangle$ and $|001\rangle$ configurations possess weights of 0.83 and 0.85, respectively. A single dominant configuration ($|010\rangle$ with a weight of 0.74) also comprises the fundamental t_2 vibration (with VBO at 3704.4 cm^{-1}). The inclusion of anharmonic effects in the fundamental modes of vibration may be gauged *via* the comparison between the anharmonic and harmonic frequencies. The respective differences in for the t_1, t_2 and t_3 fundamental modes are 36.9, 246.3 and 29.3 cm^{-1}. The relatively large difference observed between the fundamental t_2 frequencies is typical of alkali and alkaline-earth metal dihydride cations [5, 7].

Compared to $(^1A_1)MgH_2^{2+}$ there is significantly more configuration mixing present in the lowest 10 vibrational states of $(^1A')MgHD^{2+}$. For instance, the states of a' symmetry with VBOs at 1313.4, 1578.1, 1700.4, 1880.9 and 2301.3 cm^{-1} are each composed from two primary configurations. The t_1 and t_3 fundamental vibrations of $(^1A')MgHD^{2+}$ are also more delocalised than are those of $(^1A_1)MgH_2^{2+}$, having $|100\rangle$ and $|001\rangle$ configuration weights of 0.70 and 0.68. The $|010\rangle$ configuration is more dominant in the t_2 fundamental mode, having a configuration weight of 0.84. The lowest ten vibrational states of $(^1A_1)MgD_2^{2+}$ are each composed primarily from a single configuration. In addition, the t_1, t_2 and t_3 fundamental vibrational states of $(^1A_1)MgD_2^{2+}$ are composed almost entirely from the $|100\rangle$, $|010\rangle$ and $|001\rangle$ configurations, respectively. Several near-degenerate vibrational states exist

in the vibrational spectrum of $(^1A_1)MgD_2^{2+}$. For example, the b_2 $(0.85 \times |001\rangle)$ and a_1 $(0.84 \times |100\rangle)$ states have VBOs at 550.1 and 552.4 cm^{-1}, respectively. This near-degeneracy is also observed for the b_2 $(0.70 \times |101\rangle)$ and a_1 $(0.65 \times |002\rangle)$ states with VBOs at 1105.8 and 1108.6 cm^{-1}.

Radiative properties, including transition moments R^2, Einstein A and B coefficients, band strengths S and radiative lifetimes τ of the lowest 10 vibrational states have been calculated for $(^1A_1)MgH_2^{2+}$, $(^1A')MgHD^{2+}$ and $(^1A_1)MgD_2^{2+}$ at 296 K. These data are given in Appendix F. The rovibrational spectra of $(^1A_1)MgH_2^{2+}$, $(^1A')MgHD^{2+}$ and $(^1A_1)MgD_2^{2+}$ have also been calculated for the lowest 10 vibrational states and $J \leq 5$. These spectra are shown in Figure 6.3. The most prominent rovibrational transitions predicted for the ground states of $(^1A_1)MgH_2^{2+}$, $(^1A')MgHD^{2+}$ and $(^1A_1)MgD_2^{2+}$ have been assigned and are listed in Appendix F.

From Figure 6.3 it can be seen that the calculated rovibrational spectrum of the ground state of $(^1A_1)MgH_2^{2+}$ is dominated by three bands with intensities of the order of 10^{-13} cm $molecule^{-1}$. These bands correspond to the $|001\rangle$, $|101\rangle$ and $|003\rangle$ vibrational states. The *ab initio* rovibrational spectrum of $(^1A')MgHD^{2+}$, features several bands of similar intensities. The most intense band observable for $(^1A')MgHD^{2+}$ is assigned as the $|001\rangle$ state, located at *ca.* 750-850 cm^{-1}. The rovibrational spectrum of $(^1A_1)MgD_2^{2+}$ exhibits three prominent bands, located at 550-650, 1100-1200 and 1700-1800 cm^{-1}. Each of the bands observed in Figure 6.3 have been assigned unequivocally, despite the existence of near-degeneracies. For example, the band located at 550-650 cm^{-1} is assigned to the $|001\rangle$ state, despite the near-degeneracy of this state with the $|100\rangle$ state. The band located at 1100-1200 cm^{-1} is assigned to be the $|101\rangle$ state, despite this states near-degeneracy with the $|002\rangle$ state. The band at 1700-1800 cm^{-1} is assigned to the $|003\rangle$ state.

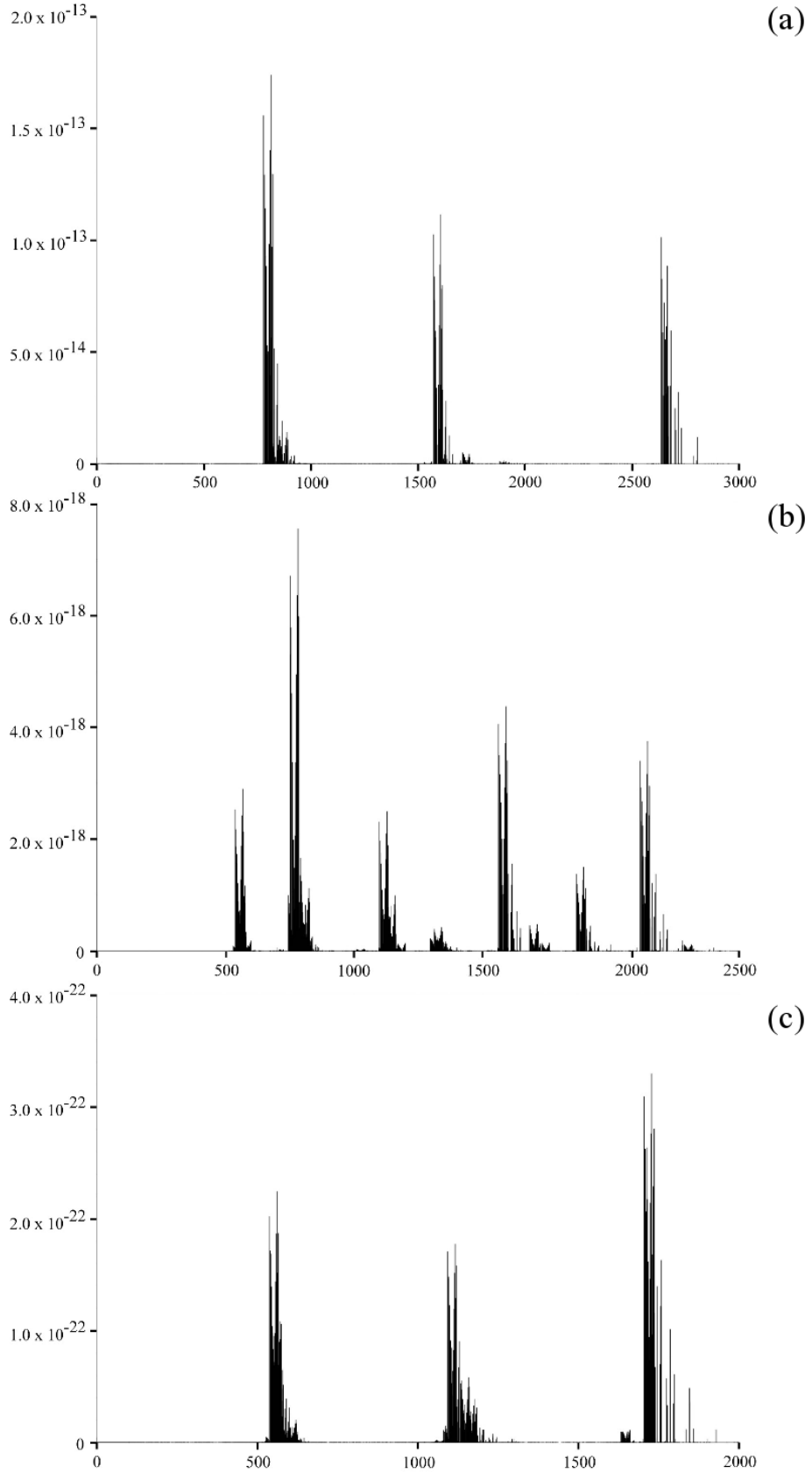

Figure 6.3 *Ab initio* rovibrational spectra for $v \leq 10$, $J \leq 5$ and $S_{ab} \geq 1.0 \times 10^{-30}$ at 296 K: (a) $(^1\mathrm{A}_1)\mathrm{MgH}_2^{2+}$; (b) $(^1\mathrm{A}')\mathrm{MgHD}^{2+}$, and; (c) $(^1\mathrm{A}_1)\mathrm{MgD}_2^{2+}$. Transition frequencies and intensities given in cm^{-1} and cm $\mathrm{molecule}^{-1}$, respectively.

6.9. *Ab Initio* Vibrational Spectra of $(^2\Sigma^+)HMHe^{2+}$ (M = Be, Mg)

Vibrational structural and radiative properties of the $^2\Sigma^+$ ground states of $HBeHe^{2+}$ and $HMgHe^{2+}$ have been calculated using the solution algorithm of von Nagy-Felsobuki and co-workers [49, 50] for $l = 0$. The 1D vibrational Schrödinger equations for $(^2\Sigma^+)HBeHe^{2+}$ were solved using integration domains of $[-2.0a_0, 5.0a_0]$, $[-4.0a_0, 4.0a_0]$ and $[-2.0a_0, 2.5a_0]$ in the w_1, w_2 and w_3 modes, respectively. These domains in the case of $(^2\Sigma^+)HMgHe^{2+}$ were $[-2.0a_0, 5.0a_0]$, $[-5.0a_0, 5.0a_0]$ and $[-2.5a_0, 3.0a_0]$, respectively.

The low-lying $l = 0$ vibrational states of $(^2\Sigma^+)HBeHe^{2+}$ are dominated by excitations in the w_2 vibrational co-ordinate. For example, from Table 6.14 it is evident that the vibrational states with VBOs at 215.5, 475.2, 760.2, 981.5, 1062.2 1233.2 and 1264.2 cm^{-1} exhibit significant w_2 character. Nevertheless, the assignment of each of the ten lowest vibrational states is made using only one or two dominant configuration terms. The prominent contribution from excited w_2 quanta in this spectrum is attributed to the relative 1D PEF curvatures. Moreover, the same term in the CI is seen to occur with comparable weights in adjacent vibrational states. The three lowest $l = 0$ excited vibrational states illustrate this point. These states are assigned using $|020\rangle$, $[|020\rangle, |040\rangle]$ and $|040\rangle$ terms, respectively. The respective configuration weights of these terms are 0.74, [0.54,0.36] and 0.58. The pair of states (predominantly of $|120\rangle$ character) with VBOs at 981.5 and 1233.6 cm^{-1} also exhibit this phenomenon. Vibration-averaged structures of $(^2\Sigma^+)HBeHe^{2+}$ yield insight into the topology of the molecular PEF in the region of the geometrical equilibrium. It is observed that the vibrational ground state exhibits $\langle R_{\text{Be-H}} \rangle$ and $\langle R_{\text{Be-He}} \rangle$ values of 1.794 and 1.457 Å, respectively. These values differ by *ca.* -6 and 14 mÅ from the *ab initio* PES minimum, respectively.

With respect to transition to the ground vibrational state, it is observed

Table 6.14 *Ab initio* ($l = 0$) vibrational spectra of $(^2\Sigma^+)$HMHe^{2+} (M = Be, Mg).

i	Assign.	Weight[a]	VBO (/cm^{-1})	$\langle R_{\text{M-H}}\rangle$ (/Å)	$\langle R_{\text{M-He}}\rangle$ (/Å)	R^2 (/a.u.^{2})	A_{0i} ($/s^{-1}$)	B_{0i} ($/10^{16}$ cm^3 erg^{-1} s^2)	S_{0i} (/cm molecule^{-1})	τ_i ($/s$)
						$(^2\Sigma^+)$HBeHe^{2+}				
0	$\|000\rangle$	0.97	0.0[b]	1.794	1.457					
1	$\|020\rangle$	0.74	215.5	1.685	1.433	4.27+00[c]	1.34+01	8.04+02	1.04−16	1.88−03
2	$\|020\rangle$,$\|040\rangle$	0.54,0.36	475.2	1.608	1.419	1.03+00	3.48+01	1.95+02	7.71−17	8.59−04
3	$\|040\rangle$	0.58	760.0	1.539	1.412	1.57−02	2.17+00	2.96+00	2.03−18	3.82−04
4	$\|100\rangle$	0.88	769.9	1.798	1.501	7.18−01	1.03+02	1.35+02	9.39−17	1.78−03
5	$\|120\rangle$,$\|021\rangle$	0.59,0.30	981.5	1.683	1.479	7.10+00	2.10+03	1.34+03	1.20−15	1.45−04
6	$\|001\rangle$	0.88	1048.3	1.851	1.463	5.49+01	1.98+04	1.03+04	9.96−15	4.65−05
7	$\|060\rangle$	0.41	1062.2	1.480	1.414	6.25−03	2.35+00	1.18+00	1.15−18	1.89−04
8	$\|120\rangle$,$\|040\rangle$	0.51,0.24	1233.6	1.630	1.460	4.90−01	2.88+02	9.23+01	1.05−16	4.52−05
9	$\|021\rangle$	0.65	1264.2	1.721	1.442	5.50+00	3.48+03	1.04+03	1.21−15	3.23−05
						$(^2\Sigma^+)$HMgHe^{2+}				
0	$\|000\rangle$	0.93	0.0[c]	2.160	1.932					
1	$\|020\rangle$,$\|021\rangle$	0.69,0.23	119.5	2.052	1.924	2.89+02	1.55+02	5.44+04	1.66−15	7.63−05
2	$\|020\rangle$,$\|040\rangle$	0.57,0.42	311.7	2.013	1.932	1.04+02	9.91+02	1.97+04	2.77−15	2.50−05
3	$\|100\rangle$	0.73	397.9	2.155	2.004	8.98+00	1.78+02	1.69+03	3.34−16	1.68−04
4	$\|120\rangle$,$\|140\rangle$	0.51,0.26	502.4	2.032	1.980	1.90+02	7.54+03	3.57+04	9.50−15	1.23−05
5	$\|040\rangle$,$\|060\rangle$	0.58,0.26	559.5	1.997	1.946	8.47−01	4.65+01	1.60+02	4.84−17	1.35−05
6	$\|120\rangle$,$\|160\rangle$	0.50,0.26	687.5	2.023	1.973	2.18+01	2.22+03	4.10+03	1.58−15	6.15−06
7	$\|001\rangle$	0.73	736.5	2.242	1.935	7.77−01	9.73+01	1.46+02	6.07−17	1.87−04
8	$\|200\rangle$	0.53	761.5	2.164	2.081	7.09+00	9.82+02	1.34+03	5.76−16	8.65−05
9	$\|040\rangle$,$\|060\rangle$	0.42,0.40	835.2	1.987	1.951	1.20+01	2.19+03	2.26+03	1.08−15	6.25−06

[a] See text.
[b] $(^2\Sigma^+)$HBeHe^{2+} ZPE = 991.8 cm^{-1}.
[c] 4.27+00 denotes 4.27×10^{00}.
[d] $(^2\Sigma^+)$HMgHe^{2+} ZPE = 619.2 cm^{-1}.

that the most intense transitions for $(^2\Sigma^+)$HBeHe^{2+} are those from states of w_3 character. For example, the two most intense bands in the vibrational spectrum of $(^2\Sigma^+)$HBeHe^{2+} are the $|001\rangle$ and $|021\rangle$ bands, which exhibit S values of 9.96×10^{-15} and 1.21×10^{-15} cm molecule^{-1}, respectively. Conversely, the $|100\rangle \leftarrow |000\rangle$ transition exhibits a band strength of 9.39×10^{-17} cm molecule^{-1}, and so is comparatively weak. This transition is relatively persistent however, exhibiting a τ value of 1.78×10^{-3} s. The only state in the $l = 0$ vibrational spectrum with a greater radiative lifetime is the $|020\rangle$ state with VBO at 215.5 cm^{-1}, for which τ is 1.88×10^{-3} s.

The structural and radiative parameters for the low-lying $l = 0$ vibrational states of $(^2\Sigma^+)$HMgHe^{2+} are listed in Table 6.14. It is evident that there is more extensive delocalisation of the low-lying vibrational wave functions than for $(^2\Sigma^+)$HBeHe^{2+}. For example, the states with VBOs at 119.5, 311.7, 502.4, 559.5, 687.5 and 835.2 cm^{-1} are each assigned using two dominant configuration terms. The first two excited vibrational states of $(^2\Sigma^+)$HMgHe^{2+} succinctly illustrate the effects of vibrational CI. For example, these states correspond to the VBOs at 119.5 and 311.7 cm^{-1}, but both consist primarily of the $|020\rangle$ configuration term. Nevertheless, the $|021\rangle$ and $|040\rangle$ terms, respectively, possess configuration weights similar to that of the $|020\rangle$ term, respectively. This property is also observed in the $|120\rangle$ states with VBOs at 502.4 and 687.5 cm^{-1}. These states exhibit contributions from the $|140\rangle$ and $|160\rangle$ terms, respectively. Each of these latter terms correspond to configuration weights of 0.26. Compared to the *ab initio* equilibrium bond lengths, the vibration-averaged Mg-H and Mg-He bond lengths differ by 17 and 28 mÅ. It is therefore inferred that the ground state vibrational wave function decays relatively quickly. This decay is itself a reflection of the surprisingly steep curvature of the molecular PEF in the neighbourhood of the equilibrium structure. Values of $\langle R_{\text{Mg-H}} \rangle$

are seen to decrease (from those of the ground state) for all vibrational states of w_2 character given in Table 6.14. This is not the case with respect to $\langle R_{\text{Mg-He}} \rangle$. For example, the states with VBOs at 559.5 and 835.2 cm^{-1} exhibit $\langle R_{\text{Mg-He}} \rangle$ values of 1.946 and 1.951 Å, respectively. Both $\langle R_{\text{Mg-H}} \rangle$ and $\langle R_{\text{Mg-He}} \rangle$ are seen to increase in all excited vibrational states of w_1 and w_3 character.

The low-lying $l = 0$ vibrational spectrum of $(^2\Sigma^+)$HMgHe^{2+} includes several bands of similar intensity. For instance, the bands at 119.5, 311.7, 502.4, 687.5 and 835.2 cm^{-1} each possess S values of *ca.* 10^{-15} cm molecule^{-1}. Similarly, the bands at 397.9 and 761.5 cm^{-1} exhibit band strengths of *ca.* 10^{-16} cm molecule^{-1}, respectively. The radiative lifetimes of the low-lying vibrational states are generally smaller than those of $(^2\Sigma^+)$HBeHe^{2+} by *ca.* a factor of 10-100. It is evident from Table 6.14 that the most persistent bands in this $(^2\Sigma^+)$HMgHe^{2+} spectrum are the $|001\rangle$ and $|100\rangle$ bands, which possess τ values of 1.87×10^{-4} and 1.68×10^{-4} s, respectively.

6.10. *Ab Initio* Vibrational Spectrum of $(^1\Sigma_g^+)$MgHe$_2^{2+}$

The low-lying $l = 0$ vibrational spectrum of the $^1\Sigma_g^+$ ground state of MgHe$_2^{2+}$ has been calculated using the solution algorithm of von Nagy-Felsobuki and co-workers [49, 50]. Associated structural and radiative properties are given in Table 6.15. The 1D vibrational Schrödinger equations of $(^1\Sigma_g^+)$MgHe$_2^{2+}$ in the w_1, w_2 and w_3 co-ordinates were solved numerically using integration domains of $[-2.0a_0, 5.5a_0]$, $[-4.0a_0, 4.0a_0]$ and $[-1.75a_0, 1.75a_0]$, respectively.

The low-lying VBOs of $(^1\Sigma_g^+)$MgHe$_2^{2+}$ are closely spaced in energy, as seen from Table 6.15. Moreover, the lowest four excited states are almost entirely dominated from excitations in w_2. These excitations are also observed to be relatively delocalised. For instance, the states with VBOs at 54.8 and 133.9 cm^{-1} are described

Table 6.15 *Ab initio* ($l = 0$) vibrational spectrum of $(^1\Sigma_g^+)\mathrm{MgHe}_2^{2+}$.

i	Assign.	Symmetry	Weight[a]	VBO ($/\mathrm{cm}^{-1}$)	$\langle R_{\text{Mg-He}} \rangle$ ($/\text{Å}$)	R^2 ($/\text{a.u.}^2$)	A_{0i} ($/s^{-1}$)	B_{0i} ($/10^{16}$ cm^3 erg^{-1} s^2)	S_{0i} ($/\text{cm molecule}^{-1}$)	τ_i ($/\text{s}$)
0	$\|000\rangle$	σ_g^+	0.94	0.0[b]	1.902					
1	$\|020\rangle$,$\|040\rangle$	σ_g^+	0.61,0.37	54.8	1.832	7.13−01[c]	3.67−02	1.34+02	5.51−19	2.39−02
2	$\|020\rangle$,$\|060\rangle$	σ_g^+	0.65,0.26	133.9	1.814	9.17−02	6.90−02	1.73+01	3.55−19	2.30−02
3	$\|040\rangle$	σ_g^+	0.63	240.7	1.810	1.22−02	5.31−02	2.29+00	1.22−19	1.99−02
4	$\|040\rangle$,$\|060\rangle$	σ_g^+	0.49,0.44	367.7	1.801	1.91−03	2.98−02	3.60−01	3.54−20	1.53−02
5	$\|100\rangle$	σ_g^+	0.91	383.0	1.939	1.57−01	2.77+00	2.96+01	3.08−18	1.25−02
6	$\|001\rangle$	σ_u^+	0.86	432.8	1.934	9.99+00	2.54+02	1.88+03	2.29−16	2.44−03
7	$\|120\rangle$	σ_g^+	0.57	443.1	1.879	3.20−03	8.73−02	6.03−01	7.58−20	1.10−02
8	$\|021\rangle$	σ_u^+	0.49	475.9	1.852	8.99−04	3.04−02	1.69−01	2.33−20	2.58−03
9	$\|060\rangle$	σ_g^+	0.57	504.5	1.803	3.25−03	1.31−01	6.12−01	9.05−20	1.12−02

[a]See text.
[b]ZPE = 449.9 cm^{-1}.
[c]7.13-01 denotes 7.13×10^{-01}.

predominantly by the $|020\rangle$ term, in conjunction with the $|040\rangle$ and $|060\rangle$ terms, respectively. Conversely, the $|100\rangle$ and $|001\rangle$ configuration terms constitute the majority of the w_1 and w_3 fundamental modes, exhibiting weights of 0.91 and 0.86, respectively. The vibration-averaged Mg-He bond length for the vibrational ground state is 1.902 Å, a value only 6 mÅ larger than R_e calculated using UCCSD(T). This indicates directly the interplay between PEF topology and the asymptotic decay of the ground state vibrational wave function. For the w_1 and w_3 fundamental modes, $\langle R_{\text{Mg-He}} \rangle$ is 1.939 and 1.934 Å. This corresponds to respective increases of 37 and 32 mÅ relative to the ground vibrational state (as anticipated).

The transitions between the ground state and the fundamental w_3 and w_1 exhibit the greatest band strengths for all states considered. Explicitly, these band strengths are 2.29×10^{-16} and 3.08×10^{-18} cm molecule^{-1}. This is not only consistent with expectations for a $D_{\infty h}$ molecule, but is also reflective of extent to which configuration mixing is limited in these states. Excited states with considerable w_2 character in the $(^1\Sigma_g^+)\text{MgHe}_2^{2+}$ vibrational spectrum generally correspond to much weaker transitions, with respect to the ground vibrational state. For example, the $|040\rangle$ bands (VBOs=240.7 and 367.7 cm^{-1}) and the $|060\rangle$ band (VBO=504.5 cm^{-1}) each exhibit band strengths of *ca.* 10^{-20} cm molecule^{-1}. Each of the lowest 10 vibrational states in the $(^1\Sigma_g^+)\text{MgHe}_2^{2+}$ $l = 0$ spectrum exhibit radiative lifetimes of *ca.* $10^{-2} - 10^{-3}$ s, with respect to transition to the ground vibrational state.

6.11. Conclusion

A systematic investigations of the structures, stabilities and dissociative energetics of ground state MH_2^{n+}, HMHe^{n+} and MHe_2^{n+} (M = Be, Mg, Ca; n = 1, 2) has been presented. Both single- and multi-reference methods were employed to calculate equilibrium parameters including R_e, θ_e, D_e, ω_1, ω_2 and ω_3. The ground

states of MH_2^{n+} were found to arise from the charge-quadrupole interaction with the molecule constituents. This finding has been established previously in the literature, and is consistent with those concerning isoelectronic alkali-metal species. Trends in R_e, θ_e, D_e, ω_1, ω_2 and ω_3 have been analysed with recourse to both isovalent and isoelectronic arguments. Additionally, bonding characteristics derived from electron density analyses have been discussed in this context. The limitations in the application of both arguments have therefore been shown in this investigation. The geometric equilibria of the ground states of $HMHe^+$ are observed to be extremely fluxional with respect to the H-M-He bond angle co-ordinate. A similar conclusion was reached for the alkaline-earth dihelide monocations. However, the respective bonding of the H and He in both $HMHe^+$ and $HMHe^{2+}$ appeared to be charge-dependent. Despite the weak bonding characteristically observed for these hydrohelide and helide monocations, the corresponding dications each exhibit thermodynamically stable equilibria.

The UCCSD(T) method employed in this thesis was employed to construct discrete PES and DMS grids of $(^1A_1)MgH_2^{2+}$, $(^2\Sigma^+)HMHe^{2+}$ (M = Be, Mg) and $(^1\Sigma_g^+)MgHe_2^{2+}$. The subsequent analytical representations of these discrete grids were employed in the calculation of vibrational and rovibrational spectra. In particular, the rovibrational spectrum of $(^1A_1)MgH_2^{2+}$ was calculated for $v \leq 10$, $J \leq 5$. All rovibrational states were assigned using normal modes and $J_{K_aK_c}$, respectively. Zero angular momentum (*i.e.* $l = 0$) pure vibrational spectra of $(^2\Sigma^+)HMHe^{2+}$ (M = Be, Mg) and $(^1\Sigma_g^+)MgHe_2^{2+}$ were also calculated.

6.12. References

[1] R. D. Poshusta, D. W. Klint, and A. Liberles, J. Chem. Phys. **55**, 252 (1971).

[2] J. Hinze, Mol. Phys. **96**, 711 (1999).

[3] A. J. Page and E. I. von Nagy-Felsobuki, unpublished, 2008.

[4] P. Valtazanos and C. A. Nicolaides, Chem. Phys. Lett. **172**, 254 (1990).

[5] A. J. Page and E. I. von Nagy-Felsobuki, Mol. Phys. **105**, 2527 (2007).

[6] D. G. Musaev and O. P. Charkin, Z. Strukt. Khim. **31**, 190 (1990).

[7] A. J. Page and E. I. von Nagy-Felsobuki, Chem. Phys. **351**, 37 (2008).

[8] C. W. Bauschlicher, Chem. Phys. Lett. **201**, 11 (1993).

[9] E. D. Simandiras and C. A. Nicolaides, Chem. Phys. Lett. **185**, 529 (1991).

[10] S. Petrie, J. Phys. Chem. A **106**, 7034 (2002).

[11] E. Czuchaj, M. Krośnicki, and H. Stoll, Mol. Phys. **98**, 419 (2000).

[12] M. Krośnicki and J. Czub, Theor. Chem. Acc. **115**, 322 (2006).

[13] X. Bu and C. Zhong, Chem. Phys. Lett. **392**, 181 (2004).

[14] X. Bu, C. Zhong, and A. F. Jalbout, Chem. Phys. Lett. **387**, 410 (2004).

[15] A. J. Page, D. J. D. Wilson, and E. I. von Nagy-Felsobuki, Chem. Phys. Lett. **429**, 335 (2006).

[16] S. W. Harrison, L. J. Massa, and P. Solomon, Chem. Phys. Lett. **16**, 57 (1972).

[17] A. J. Page, D. J. D. Wilson, and E. I. von Nagy-Felsobuki, Chem. Phys. Lett. **442**, 194 (2007).

[18] P. F. Paola Antoniotti and F. Grandinetti, Int. J. Mass. Spec. **228**, 415 (2003).

[19] A.-M. Sapse, A. Dumitra, and D. C. Jain, J. Clust. Sci. **14**, 21 (2003).

[20] A. F. Jalbout and M. Solimannejad, J. Mol. Struct. (THEOCHEM) **640**, 21 (2003).

[21] A. J. Page and E. I. v. Nagy-Felsobuki, Phys. Chem. Chem. Phys. **10**, 1285 (2008).

[22] G. Frenking and D. Cremer, Structure and Bonding **73**, 17 (1990).

[23] G. Frenking, W. Koch, and J. F. Liebman, *From Atoms to Molecules: Isoelectronic Analogues* (VCH Publishers, New York, 1989).

[24] L. N. Ding, M. A. Young, P. D. Kleiber, W. C. Stwalley, and A. M. Lyyra, J. Phys. Chem. **97**, 2181 (1993).

[25] C. Emmeluth, B. L. J. Poad, C. D. Thompson, G. H. Weddle, and E. J. Bieske, J. Chem. Phys. **126**, 204309 (2007).

[26] C. D. Thompson, C. Emmeluth, B. L. J. Poad, G. H. Weddle, and E. J. Bieske, J. Chem. Phys. **125**, 044310 (2006).

[27] C. Emmeluth, B. L. J. Poad, C. D. Thompson, G. Weddle, E. J. Bieske, A. A. Buchachenko, T. A. Grinev, and J. Klos, J. Chem. Phys. **127**, 164310 (2007).

[28] H.-J. Werner, P. J. Knowles, R. Lindh, F. R. Manby, M. Schütz, P. Celani, T. Korona, G. Rauhut, R. D. Amos, A. Bernhardsson, et al., MOLPRO, *version 2006.1* (2006),

see http://www.molpro.net.

[29] G. Schaftenaar and J. Noordik, MOLDEN*: A pre- and post-processing program for molecular and electronic structures. J. Comput.-Aided Mol. Design, 14 (2000) 123-134.*

[30] R. D. Poshusta, J. A. Haugen, and D. F. Zetik, J. Chem. Phys. **51**, 3343 (1969).

[31] T. H. Dunning, J. Chem. Phys. **90**, 1007 (1989).

[32] M. A. Iron, M. Oren, and J. M. L. Martin, Mol. Phys. **101**, 1345 (2003).

[33] D. E. Woon and T. H. Dunning, J. Chem. Phys. **100**, 2975 (1994).

[34] T. H. Dunning and P. J. Hay, *Methods of Electronic Structure Theory* (1977), vol. 3, p. 1.

[35] G. Frenking, W. Koch, J. Gauss, and D. Cremer, J. Am. Chem. Soc. **110**, 8007 (1988).

[36] G. Frenking, W. Koch, D. Cremer, J. Gauss, and J. F. Liebman, J. Phys. Chem. **93**, 3397 (1989).

[37] W. Koch, G. Frenking, J. Gauss, D. Cremer, and J. R. Collins, J. Am. Chem. Soc. **109**, 5917 (1987).

[38] W. Koch, G. Frenking, and B. T. Luke, Chem. Phys. Lett. **139**, 149 (1987).

[39] K. L. Burns, D. Bellert, A. W.-K. Leung, and W. H. Breckenridge, J. Chem. Phys. **114**, 7877 (2001).

[40] A. W. K. Leung and W. H. Breckenridge, J. Chem. Phys. **111**, 9197 (1999).

[41] A. W. K. Leung, R. R. Julian, and W. H. Breckenridge, J. Chem. Phys. **111**, 4999 (1999).

[42] D. J. D. Wilson, Ph.D. thesis, The University of Newcastle, Australia (2003).

[43] D. J. D. Wilson, C. J. Marsden, and E. I. von Nagy-Felsobuki, Phys. Chem. Chem. Phys. **5**, 252 (2003).

[44] D. J. D. Wilson, C. J. Marsden, and E. I. von Nagy-Felsobuki, J. Phys. Chem. A **106**, 7348 (2002).

[45] D. J. D. Wilson, C. J. Marsden, and E. I. von Nagy-Felsobuki, Chem. Phys. **284**, 555 (2002).

[46] D. J. D. Wilson and E. I. von Nagy-Felsobuki, Phys. Chem. Chem. Phys. **8**, 3399 (2006).

[47] D. J. D. Wilson and E. I. von Nagy-Felsobuki, Mol. Phys. **103**, 507 (2005).

[48] X. Bu and C. Zhong, J. Mol. Struct. (THEOCHEM) **726**, 99 (2005).

[49] D. J. Searles and E. I. von Nagy-Felsobuki, *Ab Initio Calculations of Vibrational*

Band Origins (Elsevier, 1991).

[50] D. J. Searles and E. I. von Nagy-Felsobuki (Springer-Verlag, Berlin, 1993), vol. 61.

CHAPTER 7

Conclusion and Future Research

7.1. Introduction

The principle aim of this work was to investigate the structures, stability and spectroscopy of Group-I and II hydrides and helides. It is hoped that these calculations will provide timely assistance in the experimental identification and characterisation of these ions. This has been illustrated in this work with respect to the rovibrational spectra of $(^1A_1)LiH_2^+$ and $(^1A_1)LiD_2^+$.

High level *ab initio* electronic structure methods were employed to investigate MH_2, MH_2^{n+}, $HMHe^{n+}$ and MHe_2^{n+} (M = Li, Be, Na, Mg, K, Ca; n = 1, 2). Trends associated with the equilibrium parameters of these species were rationalised with recourse to qualitative MO arguments. The attributes and limitations of the isoelectronic and isovalent reasoning were also discussed with respect to the equilibrium properties of $HMHe^{n+}$ and MHe_2^{n+}. These latter arguments were found to be of limited use in this context. This conclusion is consistent with previous investigations of main group and transition metal helide ions (these investigations have been reviewed in previous chapters).

7.2. Structure and Stability of Group-I and II Metal Hydrides and Helides

In order to determine the efficacy of various electronic structure methods with respect to Group-I and II hydrides and helides, atomic properties of Li, Be, Na, Mg, K and Ca including IE_1, α and electronic transition frequencies were cal-

culated. The relativistic ANO-RCC basis sets were found to provide a relatively efficient and accurate description of the ground state electronic wave functions of these atoms. The inclusion of the DK2 relativistic correction was shown to generally improve atomic properties. As expected, post-HF methods were generally necessary for anything other than qualitative agreement with experiment. Moreover, excitations greater than singles and doubles in the correlated wave function were found to be beneficial with respect to calculated atomic properties. To this end, UCCSD(T) and IC-MRCI(+Q) were deemed to be the most suitable methods with respect to both efficiency and accuracy.

The UCCSD(T) and IC-MRCI(+Q) methods were employed to investigate the low-lying states of MH_2 and the ground states of MH_2^{n+}. The lowest $^2A_1$ and $^2\Sigma^-$ states of MH_2 were found to be purely repulsive, in agreement with previous predictions. The main factor determining the structure and stability of the $^1B_1$ and $^2B_2$ excited states of MH_2 was the relative orientations and occupations of the valence p atomic orbital of the metal and the H_2 $1\sigma_u$ orbital. The presence of occupied p orbitals in the metal ligand also increased the stability of the $D_{\infty h}$ excited states. The ground states of MH_2^{n+} were found to be the result of the charge-quadrupole interaction between the metal ion and the H_2 molecular subunit. This fact is now well established in the literature. Trends in terms of equilibrium parameters have been ascribed largely to the relative ionic radii, and the consequent strength of this charge-quadrupole interaction.

The equilibrium structures and stabilities of the ground states of $HMHe^{n+}$ and MHe_2^{n+} were also investigated using UCCSD(T) and IC-MRCI(+Q). The structures of the ground states of $HMHe^+$ were extremely fluxional with respect to the central bond angle co-ordinate. A substantial variation in M-H and M-He bond lengths of these species was also observed. The concept of an 'equi-

librium structure' for such species is therefore of limited value. The ground state PESs of MHe_2^+ were also extremely sensitive to the *ab initio* method by which they were modelled. Indeed, in the case of $LiHe_2^+$, $NaHe_2^+$ and KHe_2^+, the symmetry of the state itself was seen to be determined by the level of theory employed in this approximation. The respective bonding of the H and He in both $HMHe^+$ and $HMHe^{2+}$ appeared to be charge-dependent in the case of Be, Mg and Ca. Despite the weak bonding characteristically observed for the Group-II hydrohelide and helide monocations, the corresponding dications each exhibited thermodynamically stable equilibria, and resided in relatively deep potential wells.

7.3. Molecular Property Surfaces

The development of accurate molecular property surfaces critically depends on the knowledge of the molecular equilibrium structure. To this end, the results of the electronic structure calculations of Group-I and II hydrides and helides were employed in the construction of molecular PESs. In particular, PESs of $(^1A_1)LiH_2^+$, $(^1A_1)NaH_2^+$, $(^1A_1)BeH_2^{2+}$, $(^1A_1)MgH_2^{2+}$, $(^1A_1)BeHe_2^+$, $(^1\Sigma_g^+)BeHe_2^{2+}$, $(^1\Sigma^+)HBeHe^+$, $(^2\Sigma^+)HBeHe^{2+}$, $(^1\Sigma_g^+)MgHe_2^{2+}$ and $(^2\Sigma^+)HMgHe^{2+}$ were developed using correlated methods. For each species, a number of grid points (distributed about the equilibrium structure) were selected, at which electronic energies were calculated. The design of the discrete energy grid affects the accuracy of the final analytical PEF. In this work, points were selected to be coincident with the numerical quadrature points that were subsequently used in vibrational and rovibrational calculations. Analytical PEFs were generated using a least-squares regression algorithm.

Functional forms of molecular DMSs are required for the calculation of vibrational and rovibrational radiative properties. In this work, analytical DMFs (in terms of internal displacement expansion co-ordinates) were generated in an

analogous manner to that employed for the construction of PEFs. Similarly, the design of each discrete DMS grid was based on that of the respective discrete PES grid. All dipole moments were calculated using standard electronic structure programs, and employed the Eckart framework. Analytical DMFs of $(^1A_1)LiH_2^+$, $(^1A_1)NaH_2^+$, $(^1A_1)BeH_2^{2+}$, $(^1A_1)MgH_2^{2+}$, $(^1\Sigma_g^+)BeHe_2^{2+}$, $(^2\Sigma^+)HBeHe^{2+}$, $(^1\Sigma_g^+)MgHe_2^{2+}$ and $(^2\Sigma^+)HMgHe^{2+}$ were generated in this manner.

7.4. Calculation of Vibrational and Rovibrational States and Spectra

The solution of the 'pure' vibrational Schrödinger equation requires the vibrational Hamiltonian to be derived in a suitable co-ordinate system that ensures the absence of singularities in the resultant formulation. The rectilinear normal co-ordinate vibrational Hamiltonians of von Nagy-Felsobuki and co-workers were employed in this work. Separate Hamiltonians for non-linear and linear species were therefore employed. Initially, three 1D vibrational eigenfunctions were calculated *via* the solution of the respective 1D vibrational Schrödinger equations. The trial 3D vibrational wave functions were then constructed as CI expansions of these 1D basis functions. The Hamiltonian matrix was diagonalised using variational algorithms. The HEG quadrature scheme was employed in the calculation of all necessary matrix integrals. In this work, the solution algorithm of von Nagy-Felsobuki and co-workers has been extended in three ways:

(i) The solution of the 3D vibrational problem for linear triatomic molecules has been implemented;

(ii) A method by which vibration-averaged structures of triatomic molecules can be calculated has been developed and implemented;

(iii) The calculation of vibration transition moment integrals, and hence vibra-

tional radiative properties, for linear triatomic molecules has been implemented.

Vibrational radiative properties and spectra of $(^1A_1)LiH_2^+$, $(^1A_1)NaH_2^+$, $(^1A_1)BeH_2^{2+}$, $(^1A_1)MgH_2^{2+}$, $(^1\Sigma_g^+)BeHe_2^{2+}$, $(^2\Sigma^+)HBeHe^{2+}$, $(^1\Sigma_g^+)MgHe_2^{2+}$ and $(^2\Sigma^+)HMgHe^{2+}$ were subsequently calculated.

Rovibrational energies and wave functions of non-linear triatomic molecules were calculated using a rovibrational 'super-matrix'. The trial rovibrational wave functions were constructed as the products of vibrational and rotational basis functions. The rovibrational 'super-matrix' was then diagonalised using fully variational methods. For $(^1A_1)LiH_2^+$ and $(^1A_1)LiD_2^+$, rovibrational transition frequencies for $J \leq 10$ and $0 \leq K \leq 3$ calculated in this manner were within *ca.* 0.1-0.2% of experimental values. Rovibrational transition probabilities were calculated using an adapted HEG quadrature scheme. Subsequently, *ab initio* rovibrational spectra of $(^1A_1)LiH_2^+$, $(^1A_1)NaH_2^+$, $(^1A_1)BeH_2^{2+}$and $(^1A_1)MgH_2^{2+}$ were calculated.

7.5. Future Research

Further research arising from this study may centre on the following.

(i) The Electronic Structure Methodology

The accurate calculation of molecular properties using *ab initio* electronic structure methods is a continuing field of research. Ongoing developments in computer hardware (*e.g.* parallel architectures, improvements in cpu/memory capacity), software (*e.g.* linear scaling methods, sparse-matrix factorisation methods) and computational methods (*e.g.* multi-reference CC, CC(n) methods) will be the main aspects driving the advancement of molecular electronic structure calculations. The recent extension of the cc basis sets to Group-I

and II metals will also assist in the accurate calculation of Group-I and II molecular species.

(ii) The Thermodynamic Stability of Group II Metal Hydride and Helide Dications

More extensive investigation of the dissociative processes of MH_2^{2+}, $HMHe^{2+}$ and MHe_2^{2+} (M = Be, Mg, Ca) is recommended. In particular, investigation of the dissociation channels corresponding to H^+ and He^+ loss for these dications would provide definitive evidence regarding the relative stability of these species and their respective monocations. This data would also further assist in identifying those molecular candidates most suitable for further rovibrational analysis (*vide infra*).

(iii) The Multi-Dimensional Finite-Element Method

The 3D vibrational wave functions employed in this work were constructed as CI expansions of 1D vibrational basis functions. The latter were calculated using a FEM algorithm. While this CI approach provides a convenient assignment scheme for the final vibrational wave functions, errors inherent in the 1D approximation are incorporated into the final vibrational eigenspectrum. The use of a 3D finite-element algorithm would remove these approximations and so improve the accuracy of the ultimate vibrational eigenspectrum.

(iv) Ab Initio Investigation of Group-I and II Metal Hydrides and Helides

This work centered on the *ab initio* calculation of electronic and vibrational structures of Group-I and II metal hydrides and helides. The topologies of the ground state PESs of several helide ions investigated in this work were unsuitable for vibrational calculations using a rectilinear normal co-ordinate Hamiltonian. These systems would however be amenable to a scattering coor-

dinate analysis. The calculation of rovibrational spectra of more electron-dense dihydride ions, such as KH_2^+ and CaH_2^{2+}, may also be timely. The rotational solution algorithm of von Nagy-Felsobuki and co-workers is at present limited to non-linear triatomic molecules. Extension of this code to the linear case would make the calculation of rovibrational spectra of such species as $(^1\Sigma_g^+)HBeHe^+$, $(^2\Sigma^+)HBeHe^{2+}$ and $(^2\Sigma^+)HMgHe^+$ feasible.

(v) Ab Initio Spectra of Large Molecular Systems

All vibrational calculations presented in this work were performed using an Eckart-Watson Hamiltonian in conjunction with rectilinear normal coordinates. It was observed that this approach delivers accurate vibrational and rovibrational properties for triatomic molecules under two provisos. Firstly, it is required that the PES exhibits a single, well-defined, deep potential minimum. The molecule must also undergo small amplitude vibrations around some well-defined equilibrium structure. Further development of the solution algorithm of von Nagy-Felsobuki and co-workers (for example to tetra-atomic molecules) would facilitate the calculation of more complex molecular spectra.